UNIVERSITÀ DEGLI STUDI DI NAPOLI "FEDERICO II"
SCUOLA POLITECNICA E DELLE SCIENZE DI BASE

DIPARTIMENTO DI INGEGNERIA INDUSTRIALE
Corso di Dottorato di Ricerca in Ingegneria Industriale - XXX Ciclo

Ph.D. Thesis

AERODYNAMIC LIFT AND DRAG BREAKDOWN IN STEADY AND UNSTEADY FLOWS

MARIO OSTIERI

Supervisor:
Prof. Renato Tognaccini

Coordinator:
Prof. Michele Grassi

December 2017

Contact information:
Mario Ostieri
Università degli Studi di Napoli "Federico II"
Department of Industrial Engineering
Piazzale Tecchio 80, 80125, Naples
Italy
email: mario.ostieri@unina.it

ABSTRACT

The analysis of the aerodynamic force is a crucial aspect for the design of an aircraft. Furthermore, innovative applications like devices inspired by natural flight, windmills, drones etc. also require an accurate analysis of the forces they experience. Design requirements result in more and more complex flows, and different phenomena interaction can change significantly the distribution of the aerodynamic forces. Designers are typically interested in a physical decomposition of the aerodynamic force that allows estimating the contributions of the different phenomena that occur around the body. During last decades, many breakdown methods have been developed in steady flows to decompose aerodynamic drag in order to obtain a decomposition in viscous, wave and lift-induced drag components. Moreover, the recent interest in unsteady aerodynamics requires the physical decomposition of the whole aerodynamic force (lift and drag), with the necessity for the extension of aerodynamic force analysis methods to the unsteady regime.

In this dissertation the author analyzes an unconventional aerodynamic force exact expression, valid in compressible unsteady viscous flow. The method links the aerodynamic force generation to local flow variables which are non-zero only in localized zones of the flow, i.e. boundary layers, viscous wakes, shock waves and shock wakes. The application of this theory is focused on the case of Computational Fluid Dynamics (CFD) simulations.

The first part of this thesis is dedicated to the analysis of steady flows. A rigorous definition of the lift-induced drag component is proposed and numerically proved. The drag breakdown in profile and lift-induced drag components is analyzed for the flow around an elliptic wing, with the analysis of the lift-induced

drag generation. An alternative aerodynamic force expression is then developed to overcome numerical issues that occurs at high transonic regime. A first viscous-wave profile drag breakdown is also proposed. Applications are shown in the case of an airfoil, an elliptic wing, and a realistic transonic aircraft configuration. Comparisons with classical drag breakdown methods are also presented. A discussion on the improvements in the lift-induced drag analysis is provided. Finally to overcome some discrepancies with previous drag breakdown methods a new wave drag definition is derived.

The second part of this thesis is focused on the analysis of unsteady flows. A link between present nonlinear theory and classical linear inviscid results is found. This link allows for a new definition of dynamic force derivatives. Present decomposition is applied to incompressible flows around an oscillating flat plate at low and high Reynolds number. In addition, a new mixed inertial-non inertial formula is derived, which allows for more accurate results when dealing with numerical solutions obtained by moving rigid grid methods. The theoretical link allowed for a definition of reversible and irreversible parts of the aerodynamic force in both incompressible and compressible flows. Finally, the method is applied to the analysis of a numerical solution around a pitching airfoil and is validated with a comparison with a recent unsteady drag breakdown method.

To Elena

CONTENTS

NOMENCLATURE

a	=	non dimensional rotation center
$\boldsymbol{a}$	=	local acceleration vector
$\mathcal{AR}$	=	wing aspect ratio
$2b$	=	plate length
$\boldsymbol{b}$	=	arbitrary vector
$C(k)$	=	Theodorsen's complex function
$\tilde{C}(k)$	=	$D(k) + ikD(k)$
C_{D_0}	=	zero-lift drag coefficient
$C_{D_{i_{msk}}}$	=	lift-induced drag coefficient by Maskell's formula
$C_{D_{i\ell}}$	=	lift-induced drag coefficient by Lamb vector
$C_{d_{irr}}$	=	irreversible part of the aerodynamic force, drag coefficient
$C_{d_{nf}}$, $C_{D_{nf}}$	=	near field drag coefficient
$C_{d_{pr}}$, $C_{D_{pr}}$	=	profile drag coefficient
$C_{d_{rev}}$	=	reversible part of the aerodynamic force, drag coefficient
$C_{d_{v\ell}}$, $C_{D_{v\ell}}$	=	viscous drag coefficient by Lamb vector breakdown
$C_{d_{v\Delta s}}$, $C_{D_{v\Delta s}}$	=	viscous drag coefficient by entropy breakdown
$C_{d_{w\ell}}$, $C_{D_{w\ell}}$	=	wave drag coefficient by Lamb vector breakdown
$C_{d_{w\Delta s}}$, $C_{D_{w\Delta s}}$	=	wave drag coefficient by entropy breakdown
c_r	=	root chord
C_l, C_d, C_L, C_D	=	lift and drag coefficients
C_{l_α},$C_{l_{\dot{\alpha}}}$, $C_{l_{\ddot{\alpha}}}$	=	dynamic force derivatives
$\bar{C}_{l_\alpha}$,$\bar{C}_{l_{\dot{\alpha}}}$	=	dynamic force derivatives by Fourier analysis
$C_{l_{\ell\alpha}}$, $C_{l_{S_{far}\alpha}}$	=	α derivative of C_{l_ℓ} and $C_{l_{S_{far}}}$ by Fourier analysis
$C_{l_{nf}}$, $C_{l_{nf}}$	=	near field lift coefficient
$C_{l_{rev}}$	=	reversible part of the aerodynamic force, lift coefficient
C_p	=	pressure coefficient

d	=	space dimension
$D(k), E(k)$	=	complex functions
D_{fric}	=	friction drag
D_i	=	lift-induced drag
D_m	=	motion drag
D_p	=	pressure drag
D_{pa}	=	acoustic propagation drag
d_{pr}, D_{pr}	=	profile drag
D_{sp}	=	spurious drag
D_{uns}	=	Gariépy et al. unsteady drag
e	=	span efficiency
$F(k)$, $\tilde{F}(k)$	=	$\Re[C(k)]$, $\Re[\tilde{C}(k)]$
$\boldsymbol{F}$	=	aerodynamic force
$\boldsymbol{F}_a$	=	Wu's full aerodynamic force expression
$\boldsymbol{F}_{au}$	=	Wu's aerodynamic force expression inertial frame
$\boldsymbol{F}_b$	=	Mele and Tognaccini full aerodynamic force expression
$\boldsymbol{F}_{bu}$	=	aerodynamic force expression non inertial frame
$\boldsymbol{F}_c$	=	steady aerodynamic force expression by surface integrals
$\boldsymbol{F}_{cct}$	=	unsteady compressible correction term
$\boldsymbol{F}_{cu}$	=	aerodynamic force expression mixed inertial-non inertial frame
$\boldsymbol{F}_{ext}$	=	external forces
$\boldsymbol{F}_{fric}$	=	friction force
$\boldsymbol{F}_{irr}$	=	irreversible part of the aerodynamic force
$\boldsymbol{F}_{nf}$,$\boldsymbol{F}_{ff}$	=	near field and far field aerodynamic force expressions
$\boldsymbol{F}_L$	=	Longitudinal contribution to aerodynamic force
$\boldsymbol{F}_{\ell_T}$	=	vortex force due to $\boldsymbol{V}_T$
$\boldsymbol{F}_m$	=	apparent force
$\boldsymbol{F}_p$	=	pressure force
$\boldsymbol{F}_{rev}$	=	reversible part of the aerodynamic force
$\boldsymbol{F}_{S_T}$	=	surface integral contribution due to $\boldsymbol{V}_T$

$\boldsymbol{F}_T$	=	transverse contribution to aerodynamic force
$\boldsymbol{F}_t$, $\boldsymbol{F}_{t'}$, $\boldsymbol{F}_{t''}$	=	unsteady contribution to aerodynamic forces
$\boldsymbol{F}_{tb}$	=	contribution to aerodynamic force
g	=	$g(\Delta s/R, \Delta H/V_\infty^2)$ drag breakdown function
$\boldsymbol{f}_S$	=	surface external forces distribution
$\boldsymbol{f}_{vol}$	=	volume external forces distribution
h	=	enthalpy
h	=	mesh average size parameter
H	=	total enthalpy
I	=	hydrodynamic impulse
j	=	Liu compressible Lamb vector definition
$\boldsymbol{i}_x$,$\boldsymbol{i}_y$,$\boldsymbol{i}_z$	=	x, y and z axis versors
$\boldsymbol{\ell}$	=	Lamb vector
$\boldsymbol{\ell}^*$	=	$\tilde{\boldsymbol{\omega}} \times \tilde{\boldsymbol{V}}$
l, L	=	Lift
$\boldsymbol{m}_\rho$	=	compressible correction term
M_∞	=	freestream Mach number
$\boldsymbol{n} = [n_x, n_y, n_z]^T$	=	unit normal vector
p	=	pressure
p_d	=	dynamic pressure
p_t	=	total pressure
$\boldsymbol{r} = \boldsymbol{x}/(d-1)$	=	modified position vector
$\boldsymbol{r} = \boldsymbol{x}/(d-1)$	=	modified position vector
R	=	gas constant
R^+	=	Riemmann invariant
Re_∞	=	freestream Reynolds number
S_{far}, S_b, S_W	=	far field, body and wake plane surfaces
T	=	temperature OR oscillation period
$\boldsymbol{U}$	=	inertial frame translational velocity
$\boldsymbol{v}$	=	$(u, v)^T$ perturbation velocity

u_{irr}	=	irreversible velocity
u_{rev}, $u_{rev,s}$	=	reversible velocities
$\boldsymbol{V} = (V_\infty + u, v, w)^T$	=	velocity vector
V_∞	=	freestream velocity
$\boldsymbol{V}_T$	=	$\boldsymbol{U} + \boldsymbol{\Omega} \times \boldsymbol{r'}$
$\boldsymbol{V}_\phi, \boldsymbol{V}_\psi$	=	longitudinal and transversal velocity components
$\boldsymbol{x}$	=	position vector
x, y, z	=	cartesian coordinates
x_w	=	wake plane position
$\boldsymbol{x}_w$	=	wake plane position vector
w_a	=	perturbation z-velocity component on the flat plate
z_a	=	instantaneous geometry of the flat plate
α, $\bar{\alpha}$	=	pitching law motion and amplitude
β	=	$\sqrt{1 - M_\infty^2}$ compressibility correction parameter
$\boldsymbol{\delta}_{\rho V}$	=	contribution to aerodynamic force
$\Delta C_D(C_L)$	=	lift depending profile drag
μ	=	dynamic viscosity
$\boldsymbol{\Delta}_\mu$	=	contribution to aerodynamic force
$\boldsymbol{\Delta}_{\mu t}$	=	contribution to aerodynamic force in turbulent flow
σ	=	$\dfrac{\partial v}{\partial y} + \dfrac{\partial w}{\partial z}$
$\boldsymbol{\tau}_R$	=	Reynolds stress tensor
$\boldsymbol{\tau}_v$	=	viscous stress tensor
$\mathcal{V}$	=	computational domain
λ	=	velocity induced by γ_w on the body
φ	=	potential of perturbation velocity $\boldsymbol{v}$
γ_0	=	quasi-steady vorticity
γ_1	=	$\gamma_b - \gamma_0$
γ_b, γ_w	=	bound and free vorticity
γ_{flux}	=	Noca flux form function
γ_{pv}	=	gas heat capacity ratio

Γ	=	body circulation
Γ_ϕ, Γ_C, Γ_ψ	=	Liu longitudinal and transversal body circulation definitions
ψ	=	stream function
ξ, η	=	integration variables
$\bar{\eta}$	=	η/b angular velocity
$\bar{\omega}$	=	angular frequency
$\boldsymbol{\omega}$	=	vorticity
$\boldsymbol{\Omega}$	=	inertial frame
ρ	=	density
$\mathcal{Q}_\psi$, $\mathcal{Q}_W$	=	Liu transversal function
$\bar{f}$	=	ensemble averaged quantity
$\tilde{f}$	=	ensemble averaged quantity

Superscripts

$'$	=	moving frame quantity OR ensemble fluctuation
$''$	=	mixed inertial-non inertial quantity OR Favre fluctuation

Subscripts

a, au, b, bu, c, cu irr, rev	=	contributions of $\boldsymbol{F}_a$, $\boldsymbol{F}_{au}$, $\boldsymbol{F}_b$, $\boldsymbol{F}_{bu}$, $\boldsymbol{F}_c$, $\boldsymbol{F}_{cu}$, $\boldsymbol{F}_{irr}$, $\boldsymbol{F}_{rev}$
ℓ	=	vortex force contribution
m_ρ, $m_{\rho c}$, S_{far}, S_b, t, τ	=	contributions of $\boldsymbol{F}_{m_\rho}$, $\boldsymbol{F}_{m_{\rho c}}$ $\boldsymbol{F}_{S_{far}}$, $\boldsymbol{F}_{S_b}$, $\boldsymbol{F}_t$, $\boldsymbol{F}_\tau$

Different nomenclatures Left: cited nomenclature - Right: present nomenclature

$\boldsymbol{F}_B$	=	$\boldsymbol{F}_{tb}$
$\boldsymbol{F}_\Sigma$	=	$\boldsymbol{\Delta}_\mu$
Σ_I	=	S_W
$\Sigma_I \bigcup \Sigma_J$	=	S_{far}
x_s	=	x_w

LIST OF FIGURES

LIST OF TABLES

GENERAL INTRODUCTION

If we look up to the sky, and we analyze the shapes of the so-many aircrafts that fly over our heads, the shape is still the same since so-many years.

After the introduction of the winglets, by the NASA [1], with an effective reduction of the fuel consumption, there hasn't been a very strong innovation capable of attracting the interest of the bigger aircraft companies.

While aircraft design has become stagnant, in its way to think about a "new" aircraft model, aerodynamics is facing through new applications and implications, arisen in last years from new demands and new natural aspects.

Following the introduction of Computational Fluid Dynamics (CFD), and, more generally, of numerical methods, the story of design has moved from the need of experiments to the necessity of reduced costs, leading, where possible, to a reduced number of practical tests. CFD provides large amounts of data, with a constantly increasing trend, and the development of more advanced computational tolls aim at the full simulation of the entire physics around a body immersed in a fluid. While industrial applications could only rely on Reynolds Averaged Navier Stokes (RANS) simulations, nowadays more precise applications are becoming affordable in industry (Large Eddy Simulations (LES), Detached Eddy Simulations (DES) ...)

We can read on "The Bridge, National Academy of Engineering": [2] *Computational Fluid Dynamics (CFD) is routinely used today in a wide variety of disciplines and industries, including aerospace, automotive, power generation, chemical manufacturing, polymer processing, petroleum exploration, medical research, meteorology, and astrophysics. The use of CFD in the process industries has led to reductions in the cost of product and process development and optimization activities (by reducing down time), reduced the need for physical experimentation, shortened time to market, improved design reliability, increased conversions and yields, and facilitated the resolution of environmental, health, and right-to-operate issues. It follows that the economic benefit of using CFD has been substantial, although detailed economic analyses are rarely reported* .

At the same time, Experimental Fluid Dynamics (EFD) has succeeded in renewing itself with innovative methods to enlarge the amount of information provided by each test. Particle Image Velocimetry (PIV) is increasingly becoming an useful, reliable and always cheaper tool with which all the flow field around a body can be analyzed.

We can read on "Annual Review of Fluid Mechanics": [3] *Particle-image velocimetry has developed rapidly during the last decade. It is now clear that the basic two-dimensional technique is capable of providing accurate, high-quality measurements of instantaneous fields in a variety of laboratory-scale flows of gases and liquids spanning the range from millimeters per second to several hundred meters per second. Interrogation methods depend upon the image density, with the greatest demands for interrogation time coming from high-density photographs. The computation time required to process a photograph is now reasonable using appropriate laboratory computers, and the computation needed to process a single low-image-density video frame can be handled by relatively small computers. As the analysis of the images becomes less demanding, one can anticipate extensions of the technique to measurements involving hundreds or even thousands of frames of data. In particular, kinematic recording of vector fields, stereographic recording, and holographic recording are generalizations that will become more common as processing times decreased.*

Theoretical aerodynamics, even though tried to renew itself, could not follow the rise and power of such tools. Aircraft design nowadays cannot live without CFD and EFD, and optimization, of what we already know, is performed with those tools.

However technology, with its demands, changes and new applications require new knowledge; new knowledge requires new and more advanced theories.

In particular the diffusion of unmanned aerial vehicles and drones is now widespread in the society. The demand increasingly asks for devices smaller and faster, with a growing difficulty in analyzing the very complex flow field around these bodies, which operate in a very different aerodynamic regime with respect to aircrafts.

Wind turbines, as well, are spreading throughout our territory. No more only in open fields like countryside, or offshore. New applications are focusing on city windmills, on the top of buildings. Their design, especially for what concerns vertical axis wind turbines, requires a very deep knowledge of complex phenomena like dynamic stall and

unsteady aerodynamics and so on which are no more only an exclusive subject of research of rotorcraft designers.

Finally, to give another example, interest is growing towards the knowledge of bird flight, insect flights, fish swimming, i.e. about natural propulsion. Nature cannot stop to surprise humankind, demonstrating a strong capability of taking benefit from very complex phenomena in a way so natural, but so hard to reproduce technically. This consequently motivate intense research efforts on flapping wings.

These innovative applications require not only the record of data, but, when possible, also predictive theoretical models to uncover the physics of what is happening, how it is happening and why it is happening.

Even if demands are different, what joins these different research areas is the capability of obtaining so much data. But how these record could become useful?

Flow visualization is surely a tool important during the design, but is only a qualitative way to understand how design could be improved.

At the same time, while all designers know that optimization is clearly related to force generation (reduction of drag, increasing of efficiency, propulsion generation etc.), they don't know how to quantify and relate the flow data to the force itself.

The classical method to compute aerodynamic force, very simple in its application, only requires pressure and viscous shear stresses on the body. What happens on the body seems to be the only pilot for the force quantification, as the flow field around it is only a boring optional of the physical phenomenon.

Recent theoretical studies, moved from the known, but not deeply analyzed, link between the flow field and the aerodynamic force, found new force theories, expressed in force formulae, that clearly state that the force depends on what happens in the flowfield and not only on the flow variables on the body. Such unconventional methods succeed in linking the flow physics to the force generation, and allow for a quantitative, rather than qualitative, employment of the data acquired for the phenomenon object of the study, both from experimental and numerical methods.

This dissertation will regard one of these innovative force theories, based on the the analysis of the vorticity field around a moving body. Physical interpretations will

be shown, design implications, and even strong links between this general non linear aerodynamic force theory with the previous classical inviscid theories of the first stage of theoretical aerodynamics will be discussed.

The applications of this method will be mostly related to the core subject of aerodynamics efforts, i.e. aircraft design. The force decomposition will be the principal topic of the dissertation, even if some applications to other phenomena such low-Reynolds number unsteady aerodynamics will be analyzed. Numerical applications will be performed by analyzing CFD numerical data, even if this general force theory can be applied also to EFD numerical data.

1

THE AERODYNAMIC FORCE

Contents

1.1 From Newton's laws to the near field formula

In classical mechanics, body dynamics is ruled by Newton's laws. This is also the case of a body immersed in a fluid flow. When a body moves through, or it is invested by the fluid, it experiences a force. This force can be computed by Newton's second law. We can write

$$m\boldsymbol{a} = -\boldsymbol{F}_{fl} + \boldsymbol{F}_{ext} \ , \tag{1.1}$$

where $\boldsymbol{F}_{fl}$ is the force experienced by the body, due to the fluid, m is the body mass, and $\boldsymbol{F}_{ext}$ is the sum of the external forces. For example, considering a flying bird, m is the bird's mass, $\boldsymbol{F}_{ext}$ is given by the weight, $\boldsymbol{F}_{fl}$ is the force exerted by the air upon the bird's body.

Our aim is to measure this force $\boldsymbol{F}_{fl}$. Thanks to equation (1.1), measuring the body acceleration $\boldsymbol{a}$ and the external forces, it is possible to predict the force exerted by the fluid. This methods is, for example, applicable in wind tunnel tests, where $\boldsymbol{a}$ is imposed (usually 0, in steady flows), and measuring the external forces different from the fluid one (for example, the reaction exerted by the joint), it is possible to find how much force the fluid exerts on the body.

Another possibility is to obtain the force exerted by the fluid from a momentum balance in the fluid itself, i.e. gathering quantitative informations about the flow structure and properties.

Again, Newton's second law is necessary, to find the fluid *momentum balance*. If we consider a material fluid volume $\mathcal{V}_m(t)$, constituted by a continuum of fluid particles, for every particle we can write $\boldsymbol{F} = \rho \boldsymbol{V} \mathrm{d}\mathcal{V}$ (we are supposing valid the continuum hypothesis), where ρ is the particle density, $\boldsymbol{V}$ is its velocity and $\boldsymbol{F}$ is the sum of all the forces applied to the single fluid particle, even the forces due to the other particles.

If we consider Newton's third law, all the forces between particles cancel each other. In this way, for the complete system of particles, the sum of the forces is given by the

sum of the external forces applied to the system itself. We can write

$$\boldsymbol{F}_{ext} = \frac{d}{dt} \int\limits_{\mathcal{V}_m(t)} \rho \boldsymbol{V} \, \mathrm{d}\mathcal{V} \ , \tag{1.2}$$

where

$$\frac{d}{dt} \int\limits_{\mathcal{V}_m(t)} \rho \boldsymbol{V} \, \mathrm{d}\mathcal{V} = \int\limits_{\mathcal{V}_m(t)} \boldsymbol{f}_{vol} \, \mathrm{d}\mathcal{V} - \int\limits_{\partial\mathcal{V}_m(t)} \boldsymbol{f}_S \, \mathrm{d}S \ . \tag{1.3}$$

The LHS hand side of equation (1.3) represents the "continuous sum" of the momentum variation of the fluid particles, while the RHS represents the general volume and surface distributions of the external forces. For a boundary point, with a local surface plane whose versor is $\boldsymbol{n}$, the surface forces $\boldsymbol{F}_S$ can be found considering the general stress tensor $\boldsymbol{\tau}$, i.e. $-\boldsymbol{f}_S = \boldsymbol{n} \cdot \boldsymbol{\tau}$. Finally, the momentum balance can be written as

$$\frac{d}{dt} \int\limits_{\mathcal{V}_m(t)} \rho \boldsymbol{V} \, \mathrm{d}\mathcal{V} = \int\limits_{\mathcal{V}_m(t)} \rho \boldsymbol{f}_{vol} \, \mathrm{d}\mathcal{V} + \int\limits_{\partial\mathcal{V}_m(t)} \boldsymbol{n} \cdot \boldsymbol{\tau} \, \mathrm{d}S \ . \tag{1.4}$$

The material fluid volume $\mathcal{V}_m(t)$, as sketched in figure 1.1, is composed by an external material surface $S_{far_m}(t)$ and the body surface S_b, so the last term can be splitted in

$$\int\limits_{\partial\mathcal{V}_m(t)} \boldsymbol{n} \cdot \boldsymbol{\tau} \, \mathrm{d}S = \int\limits_{S_{far_m}t)} \boldsymbol{n} \cdot \boldsymbol{\tau} \, \mathrm{d}S + \int\limits_{S_b(t)} \boldsymbol{n} \cdot \boldsymbol{\tau} \, \mathrm{d}S \ .$$

The last term, defined as the action of the body over the fluid system, is the opposite of $\boldsymbol{F}_{fl}$! This is the classical formula for the aerodynamic force; it is the so-called *near field* formula, since its computation requires only the body stress tensor evaluation. We will refer to it with $\boldsymbol{F}_{nf}$:

$$\boldsymbol{F}_{nf} \equiv - \int\limits_{S_b(t)} \boldsymbol{n} \cdot \boldsymbol{\tau} \, \mathrm{d}S \ .$$

In the case of the Newtonian fluid model (we will make this assumption from now on), that is $\boldsymbol{\tau} = -p\boldsymbol{I} + \boldsymbol{\tau}_v$, where $\boldsymbol{I}$ is the unit normal tensor and $\boldsymbol{\tau}_v = 2\mu \left[\boldsymbol{\nabla V} + \boldsymbol{\nabla V}^T \right]$,

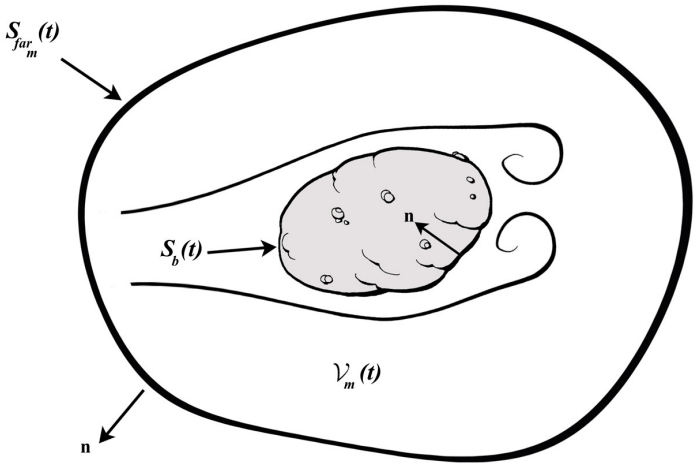

Figure 1.1 A generic body immersed in a fluid.

is the dissipative stress tensor, near field formula becomes

$$\boldsymbol{F}_{nf} = \int_{S_b(t)} (p\boldsymbol{n} - \boldsymbol{n} \cdot \boldsymbol{\tau}_v) \, \mathrm{d}S \; . \tag{1.5}$$

This formula allows for computing the aerodynamic force by body surface properties, not accounting for what is "loading" on the body. It is the typical formula applied in Computational Fluid Dynamics (CFD) and Experimental Fluid Dynamics (EFD). In the first case body solution is usually directly given by the solver, while in the second case, body pressure and shear stresses can be taken into account by proper sensors. Moreover, the application of the near field formula to compute aerodynamic force in experimental applications is not trivial, due to the difficulty of the measurements on the body.

1.2 Far field formula

Momentum balance gives us the chance to find another expression for the aerodynamic force. This time force expression will not depend on body physical variables.

Splitting the stress tensor integral in equation (1.4) in a body integral and a "far" integral, and taking into account of the near field force definition, we can write

$$\begin{aligned}\boldsymbol{F} = -\int\limits_{S_b(t)} \boldsymbol{n}\cdot\boldsymbol{\tau}\,\mathrm{d}S = -\frac{d}{dt}\int\limits_{\mathcal{V}_m(t)} \rho\boldsymbol{V}\,\mathrm{d}\mathcal{V} + \int\limits_{\mathcal{V}_m(t)} \rho\boldsymbol{f}_{vol}\,\mathrm{d}\mathcal{V} + \\ + \int\limits_{S_{far_m}(t)} (\boldsymbol{n}\cdot\boldsymbol{\tau}_v - p\boldsymbol{n})\,\mathrm{d}S \equiv \boldsymbol{F}_{ff}\ .\end{aligned} \tag{1.6}$$

This aerodynamic force expression is dependent on what happens "outside" the body. Typically it is called *far field* formula, since, historically, was initially found in the steady case only, where, in the hypothesis of negligible gravitational effects, the force is given only by an integral on the "far" surface S_{far}.

This nomenclature should not be valid in the unsteady regime, since it relies on the integration of the local momentum all over the fluid domain.

In fluid dynamic it is usually cumbersome the approach based on material surfaces, by which the "history" of the fluid motion is taken into account into the surface $S_{far_m}(t)$ variation in time.

It is easier to set an arbitrary volume. At a time t, let's take a volume $\mathcal{V}(t) = \mathcal{V}_m(t)$, whose boundary is composed by the far surface $S_{far}(t)$ and the body surface $S_b(t)$. The first approach is called "Lagrangian" point of view, while the second is called "Eulerian" point of view. Applying the Reynolds stress theorem, we find

$$\boldsymbol{F}_{ff} = -\int\limits_{\mathcal{V}(t)} \frac{\partial\rho\boldsymbol{V}}{\partial t}\,\mathrm{d}\mathcal{V} - \int\limits_{\partial\mathcal{V}(t)} \boldsymbol{n}\cdot\rho\boldsymbol{V}\boldsymbol{V}\,\mathrm{d}S + \int\limits_{S_{far}(t)} (\boldsymbol{n}\cdot\boldsymbol{\tau}_v - p\boldsymbol{n})\,\mathrm{d}S + \int\limits_{\mathcal{V}(t)} \rho\boldsymbol{f}_{vol}\,\mathrm{d}\mathcal{V}\ . \tag{1.7}$$

This is again a "farfield" formula, but it even presents a body surface integral!

An equivalent form of equation (1.7) can be obtained again applying the differential form of the Reynolds stress theorem. In fact, given $\frac{D}{Dt} = \frac{\partial}{\partial t} + \boldsymbol{V} \cdot \boldsymbol{\nabla}$, where $\frac{D}{Dt}$ is the material derivative, we have

$$\boldsymbol{F}_{ff} = -\int_{\mathcal{V}} \rho \boldsymbol{a} \, \mathrm{d}\mathcal{V} - \int_{S_{far}} (p\boldsymbol{n} - \boldsymbol{n} \cdot \boldsymbol{\tau}_v) \, \mathrm{d}S \, , \tag{1.8}$$

where $\boldsymbol{a} = \frac{D\boldsymbol{V}}{Dt}$ is the local fluid acceleration.

The farfield expression historically gave the chance to researchers and designers to develop theories and methods to obtain physical interpretations on the aerodynamic force generation.

It was, for example, the starting point for the Kutta-Joukowskij [4, 5] theorem demonstration. The farfield approach was also the way by which first formulae for a physical drag breakdown were obtained [6, 7]. In some applications and developments, where the pressure term is replaced in some way [8, 9], the farfield approach is applied to experimental sets where it is easier to measure flow velocity "far" from the body. Furthermore, moving from a body point of view to a "far" point of view, is the key to obtain informations from the "fluid".

Starting from farfield formula, in fact, it could be possible to relate aerodynamic force generation to local flow variables in many different ways.

Modern force breakdown methods rely on this link. That is, obtaining a physical force breakdown from local fluid informations.

1.3 What is the subject of this dissertation

It was important to start from *what* is the fluid force in order to arrive to the subject of this dissertation. The force breakdown concept is surely not innovative. Even from the near field formula (1.5) it is already possible to obtain a "breakdown". Basically we can

introduce

$$\boldsymbol{F}_{nf} = \int_{S_b(t)} (p\boldsymbol{n} - \boldsymbol{n} \cdot \boldsymbol{\tau}_v) \, \mathrm{d}S \equiv \boldsymbol{F}_p + \boldsymbol{F}_{fric} \, , \tag{1.9}$$

where $\boldsymbol{F}_p$ is the part of the force due to body pressure, *pressure force*, and $\boldsymbol{F}_{fric}$ is the part of the force due to the body viscous stresses, the *friction force*. This breakdown, even if interesting, is not related to the "flow phenomena" that happens around the body. It is useful to decompose the aerodynamic force along the freestream direction and the other directions. The force component parallel to the freestream velocity is the aerodynamic drag, while the component perpendicular to the freestream direction is the aerodynamic lift. The remaining component is the side force. As concerning aerodynamic drag, typically in aeronautical application, another breakdown is considered. The flow viscosity modifies the pressure distribution, generating the so-called form drag. The sum of form drag and friction drag is the viscous drag, so directly linked to irreversible effects due to the viscosity. When we consider a lifting body, another drag component arises, the lift-induced drag, since the trailing vortex system, that accompanies the production of lift, changes pressure distribution resulting in an additional drag contribution [10, 11]. Finally, at transonic and supersonic speeds, an additional drag contribution is due to the appearance of shock waves, the wave drag. This decomposition in viscous, lift-induced and wave drag has a deeper physical insight, directly linking each drag component to their sources. Aerodynamic designers are therefore interested in this *physical* breakdown, in order to adopt ad-hoc solutions to mitigate the effects of each of these flow phenomena. To cite an example, we can read in [12] by Van Dam, referring to the pressure drag: *Note that the total pressure drag is the result of three quite different flow phenomena; (1) boundary-layer displacement effect, (2) trailing vortex system, and (3) shock waves. The design approaches typically followed to reduce/minimize each of these pressure drag components tend to be quite different. For instance, varying the wing span has a dramatic effect on the trailing vortex system and, hence, the induced drag, but, this does not play a significant role in the boundary-layer development and, hence, the form drag.* As explained by Van Dam, while pressure drag accounts for various physical effects, induced drag can

be directly influenced by technical design approach, which is applied directly on the flow phenomena that generates drag. At the same way, wave and viscous drag can be directly reduced by other approaches.

Accuracy in the force computation, expecially the drag component, is another crucial design aspect. Indeed, as discussed by Van Dam [12], reporting an application performed by Meredith [13], "a one percent increase in the lift-to-drag ratio (L/D) during takeoff is equivalent to a 2800 lb increase in payload for a generic twin engine subsonic transport airplane on a long-range mission or approximately 200 lb in payload (or 1 passenger) per drag count" (1 drag count = 0.0001). Even if CFD is currently a powerful and common design tool, drag computation by CFD analyses can strongly be affected by numerical errors and approximations. The problem was addressed by Slooff [14] in 1986, where mesh sizes, and so CFD analyses, differently from current possibilities, were strongly influenced by the limited availability computational resources. Nowadays this issue, partially solved by the increasing computational power, is yet to be overcome, given the recent interest in more and more complex flows. These needs led to the development, in the last decades, of many "farfield methods" to perform a breakdown, to obtain more accurate methods for the force computation, and to opportunely analyze and understand how and where force is generated.

Given these assumptions, the subject of this dissertation can be introduced. In this thesis, an unconventional aerodynamic force formula, based on the local vorticity field will be discussed and analyzed. The thesis will be structured in this way:

- Chapter 2: an analysis of the state of the art, concerning farfield methods, and more generally aerodynamic force analysis, is discussed.
- Chapter 3: an exact unconventional aerodynamic force formula is derived. Extension to turbulent flows and other properties previously demonstrated by the research team in which the author is active will be discussed.
- Chapter 4: the analysis of steady flows by means of present aerodynamic force formula is discussed, with contributions in which the author participated. Among all the presented results, a rigorous definition of lift-induced drag in compressible

viscous flows is discussed, solving a long waited issue, as described by Spalart [15], whom wrote on Journal of Fluid Mechanics: "An ambition which will have to wait is a rigorous definition of induced drag in viscous flows". These results, together with its drag breakdown implications, have been already published on *AIAA Journal*, in the article "Vorticity based breakdown of the aerodynamic force in three-dimensional compressible flows" by Mele, Ostieri and Tognaccini [16]. Furthemore, full drag breakdown in viscous, wave and drag components has been introduced by means of Lamb vector integrals, and applied to a transonic aircraft configuration. These results have been already published on *Journal of Aircraft*, in the article "Aircraft lift and drag decomposition in transonic flows" by Mele, Ostieri and Tognaccini [17].

- Chapter 5: unsteady flows are analyzed, with contributions in which the author participated. As concerning incompressible flows, the analysis of the oscillating flat plate flow has been proposed. A mixed inertial non-inertial unconventional exact force formula is derived, and its link with the classic linear inviscid theory is discussed. Thanks to this link, a method to correctly compute and decompose the dynamic force derivatives in airfoil flows is derived. These results have been very recently published (November 2017) on *AIAA Journal*, in the article "Linear and nonlinear decomposition of the aerodynamic force acting on an oscillating plate" by Ostieri, Mele and Tognaccini [18]. Force breakdown in reversible and irreversible contributions is also discussed and defined, starting from the link with inviscid theories. The definition has been extended to compressible flows. This decomposition has been recently discussed in the conference paper "Two alternative drag breakdowns in unsteady flows" by Ostieri, Tognaccini, Bailly and Destarac, at AIMETA - XXIII Conference, 4th-7th September 2017, Salerno, Italy [19]; it will be further discussed at AIAA SciTech 2018 Conference, Kissemmee, USA, 8th-12th January, in the conference paper "Aerodynamic force and Lamb vector field in compressible unsteady flows" [20].

2

AERODYNAMIC FORCE BREAKDOWN: A REVIEW

Contents

This chapter reports a review of the existing aerodynamic force breakdown methods. The author choose to split the methods in 3 section: farfield methods, thermodynamic methods and vortical methods. Even if this is not strictly rigorous, since second and third sections can be someway included in the first, it seemed to be the clearest way to split different methods for the analysis and the breakdown of the aerodynamic force.

2.1 Farfield methods

2.1.1 Betz (1925): profile drag

Betz was the first to introduce a farfield method to physically decompose the aerodynamic force, in particular drag [21], in experimental applications. Assuming a reference frame $O(xyz)$, where x is aligned with the freestream velocity, and (x, z) is the symmetry plane, Betz found, for incompressible steady flows, a formula to compute aircraft profile drag:

$$D_{pr} = \int_{S_W} (p_{t_\infty} - p_t)\, \mathrm{d}S - \frac{\rho}{2} \int_{S_w} (u' - u)\,(2u_\infty - u' - u) \tag{2.1}$$

where u is the x component of the velocity $\boldsymbol{V} = (u, v, w)$, S_W is a wake plane, p_t the total pressure, and u' a "potential flow" x-velocity for the flow outside the vortical region.

The formula is composed by two terms. The first depends on the total pressure loss in the aircraft wake. The second term, dependent on u', is usually negligible with respect to the first one.

This formula is valid with the wake plane S_W far enough to have the velocity parallel to the freestream, and stagnation temperature losses negligible in all the flowfield.

2.1.2 Jones (1936): an improvement of Betz method

Jones overcome the limits of Betz' method due to the introducation of potential flow velocity u' [22]. He found, for incompressible steady flows

$$D_{pr} = p_{d_\infty} \int_{S_w} 2\sqrt{p_d^* - p^*} \left(1 - \sqrt{p_d^*}\right) \mathrm{d}S \tag{2.2}$$

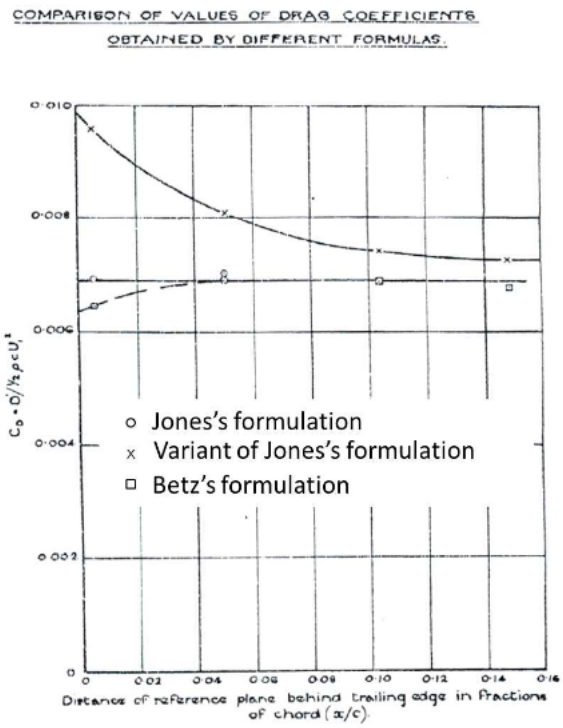

Figure 2.1 Variation of Betz and Jones profile drag formulation with wake plane distance from the body TE, Hart K-1442 experimental set.

where $p_d = \frac{1}{2}\rho u^2$ is the dynamic pressure and the superscript * indicates nondimensionalization with respect to p_{d_∞}.

The wake plane is assumed far enough to have a velocity parallel to the freestream and static pressure equal to p_∞.

Since outside the vortical region, in the wake plane, $p_d^* = 1$, the integration could be limited to the wake boundary. Attention had to be given to the zones where $p_d^* - p^*$ becomes negative, when moving the wake plane close to the TE.

A comparison between Betz's and Jones' formulations is shown in figure 2.1, applied to an Hart K-1442 airplane experimental set. Both formulae give the same results, except when S_W is placed very close to the trailing edge.

2.1.3 Maskell (1972): induced drag

Maskell introduced a method to compute the lift-induced drag in steady incompressible flows [23]. Let us assume a wake plane S_W, far enough from the body TE, orthogonal to the freestream velocity. A similar plane is usually called a Trefftz plane, that is a plane where u variations are negligible (u is the x component of the velocity $\boldsymbol{V} = (u, v, w)$). Under these hypothesis, we can assume a two-dimensional flow on each of these planes S_W. A flow potential ϕ and a stream function ψ for every plane are introduced. Given these assumptions, Maskell developed the following formula to compute lift-induced drag:

$$D_i = \rho \int_{S_W} (\psi \omega_x - \phi \sigma) \, \mathrm{d}S \tag{2.3}$$

where $\sigma = \dfrac{\partial v}{\partial y} + \dfrac{\partial w}{\partial z}$.

He also proposed a modification of Betz's theory, to correct its formula to take into account of wind tunnel blockage. Indeed the model tested during an experiment is not immersed in an infinite fluid domain but it is placed within a finite test section, and this aspect can affect significantly the force computation.

Kusunose, in his review book on lift-induced drag [24], proposed two methods to compute the stream function ψ. The first method requires the direct solution of the ψ Poisson problem $\nabla^2 \psi = -\omega_x$ by a numerical solver. The second method computes ψ in terms of the general solution of the previous problem through the Green's function method.

2.2 Thermodynamic methods

2.2.1 Oswatitsch (1956): the entropy drag

Oswatitsch [25] introduced the entropy drag concept to deal with profile drag. From thermodynamic considerations, Oswatitsch assumed that the profile drag is produced by entropy production, clearly linking profile drag generation to irreversible processes.

He introduced the following formula to compute profile drag in steady compressible

flows:

$$D_{pr} = \frac{T_\infty}{u_\infty} \int\limits_{S_w} \rho u \Delta s \, \mathrm{d}S \ . \tag{2.4}$$

Kusunose [24] applied this method to compute and decompose profile drag in viscous and wave components, when applied to experimental measurements. He was able to split the shock wake zone from the viscous wake zone, since, typically, they have different vorticity scales. The splitting was thus possible thanks to the introduction of a numerical vorticity magnitude cutoff. This methodology, in any case, does not take into account for boundary layer entrainment after the shock wave, and in complex applications, where shock wakes and viscous wakes strongly interact, cannot be directly applied.

2.2.2 Van Der Vooren and Destarac (2004)

Van der Vooren and Destarac, summarizing a work started at the beginning of the 90's [26], introduced a full breakdown of aerodynamic drag [27].

Breakdown starts from thermodynamic considerations, directly linking to entropy drag concept introduced by Oswatitsch. In this case, the method is conceived and developed for CFD applications, where it is assumed that flow information are available in all the flow field.

Considering the x component of the velocity u, where x is again aligned with the freestream, from thermodynamic considerations it can be developed the following relation

$$u = u_\infty \sqrt{1 + \frac{2\Delta H}{u_\infty^2} - \frac{2}{(\gamma_{pv} - 1)\, M_\infty^2} \left[\left(\frac{p}{p_\infty} \right)^{\frac{\gamma_{pv} - 1}{\gamma_{pv}}} e^{\frac{(\gamma_{pv} - 1)\, \Delta s}{\gamma_{pv} R}} - 1 \right] - \frac{v^2 + w^2}{V_\infty^2}} \ , \tag{2.5}$$

where R is the gas constant, γ_{pv} is the heat capacity ratio of the gas, $H = h + \frac{1}{2}V^2$ is the total enthalpy ($h = \frac{\gamma_{pv}}{\gamma_{pv} - 1}\frac{p}{\rho}$ is the enthalpy) and s is the entropy.

Assuming that, on a wake plane S_W far enough from the TE, there are no other

viscous contributions, no transverse velocities and static pressure equal to the freestream pressure p_∞, it can be introduced the *irreversible velocity* u_{irr} [28]:

$$u_{irr} = u_\infty \sqrt{1 + \frac{2\Delta H}{u_\infty^2} - \frac{2}{(\gamma_{pv} - 1)\, M_\infty^2} \left[e^{\dfrac{(\gamma_{pv} - 1)\, \Delta s}{\gamma_{pv} R}} - 1 \right]} \,. \tag{2.6}$$

To define the viscous-wave drag breakdown it has to be introduced the viscous volume $\mathcal{V}_v$, i.e. the region of the flows which includes the boundary layer and the viscous wake. At the same way, the wave volume $\mathcal{V}_w$ is the region of the flow which surrounds the shock wave. With some algebra the viscous and wave drag are so defined:

$$D_v = \int_{\mathcal{V}_v} \boldsymbol{\nabla} \cdot \left[\rho \left(u_{irr} - u_\infty \right) \boldsymbol{V} \right] \mathrm{d}\mathcal{V}, \qquad D_w = \int_{\mathcal{V}_w} \boldsymbol{\nabla} \cdot \left[\rho \left(u_{irr} - u_\infty \right) \boldsymbol{V} \right] \mathrm{d}\mathcal{V} \,. \tag{2.7}$$

Viscous and wave volumes can be numerically identified by using proper numerical sensors. A review of typical sensors, developed during the years, is reported in [29].

Induced drag is defined as the complementary part of viscous and wave drag with respect to near field formula. Considering the x components of friction and pressure forces defined in equation (1.9)

$$D_p = \int_{S_b} p \boldsymbol{n} \, \mathrm{d}S \,, \qquad D_f = - \int_{S_b} \boldsymbol{n} \cdot \boldsymbol{\tau}_v \, \mathrm{d}S \,, \tag{2.8}$$

we have

$$D_i = - \int_{\mathcal{V}_v \bigcup \mathcal{V}_w} \boldsymbol{\nabla} \cdot \left[\rho \left(u - u_{irr} \right) \boldsymbol{V} + \left(p - p_\infty \right) \boldsymbol{i}_x - \boldsymbol{\tau}_v \cdot \boldsymbol{i}_x \right] \mathrm{d}\mathcal{V} - D_p - D_f \,. \tag{2.9}$$

The sum of present viscous, wave and lift-induced drag is defined and farfield drag, $D_{ff} = D_i + D_w + D_v$, theoretically equal to the near field drag D_{nf} given present definitions. Differences resulting from computational errors instead can be significant. This difference is called spurious drag, i.e. $D_{sp} = D_{ff} - D_{nf}$. So the final numerical balance is $D_{nf} =$

$D_i + D_v + D_w + D_{sp}$.

The major drawback of this method is clearly related to the lack of a link between local flow variables and lift-induced drag definition, even if present formula assures the perfect balance between near field and farfield drag.

The introduction of volume definitions of viscous and wave drag, i.e. a relation between local flow variables and aerodynamic force generation, allows to introduce the *midfield* force concept. We call *midfield* force expression a force formula that relates the aerodynamic force to local flow variables, which are non-zero only in localized region of the flow. Aerodynamic force generation can be so related to the local variation of particular flow variables. Present viscous and wave drag definition, for example, being direct function of the irreversible velocity u_{irr}, are clearly related to the local entropy variations and total enthalpy variations, with the second one typically negligible for turbulent flows and power-off conditions (the Prandtl number is $Pr \approx 1$, where $Pr = \mu c_p/k$, μ is the molecular viscosity, c_p is the isobaric heat capacity and k is the thermal conductivity). Drag is thus generated in a very limited region of the flow.

The fact that numerical integrations can be confined to only a narrow zone of the flow allows to cancel a large amount of numerical error in the drag computation. The numerical artificial viscosity of the CFD simulations produces a so-called spurious entropy, i.e. an entropy due only to numerical effects. Denoting with $\mathcal{V}_{sp}$ the complementary part of $\mathcal{V}_v \bigcup \mathcal{V}_w$, Van der Vooren and Destarac [7] proposed the following formula of the spurious drag:

$$D_{sp} = \int_{\mathcal{V}_{sp}} \boldsymbol{\nabla} \cdot \left[\rho \left(u_{irr} - u_\infty\right) \boldsymbol{V}\right] \, \mathrm{d}\mathcal{V} \; . \tag{2.10}$$

The contribution is theoretically 0 in the zones outside viscous and wave volumes; on the contrary it is significant in numerical applications, being function of the irreversible velocity, i.e. the (spurious) entropy variation in $\mathcal{V}_c$. This contribution can be explained by the fact that, typically, mesh refinement decreases with the distance from the body. Viscous and wave regions are narrow and close the body, while $\mathcal{V}_c$ contains all the coarse mesh zones, that presents higher numerical approximations and so a great amount of spurious entropy. In any case, the spurious entropy produced in viscous and wave volumes,

anyway different than 0, is not taken into account in this definition.

Present method has been widely refined during the years. A one-vector formulation has been proposed to avoid irreversible velocity calculation, by means of an ad-hoc reversible velocity, since the irreversible velocity can be ill-defined in particular regions of the flow. An extension to the analysis of propeller has also been proposed by Mehéut [30].

A generalization to the jet-propelled configuration has also been proposed by Van Der Vooren and Destarac [7]. Viscous and wave volume have also to be considered around the nacelle. Furthermore, a drag contribution due to the additive through-flow arises.

An example of application is shown in figure 2.2. Computed drag polars with propeller on and propeller off configurations of the DLR-ALVAST twin engine transport aircraft [31] are compared with near field drag computations and experimental results obtained with the ONERA-SIMA wind tunnel.

Finally, Destarac analyzed the problem of spurious induced drag production in CFD numerical simulations [32, 33], due to the farfield boundary condition. Farfield boundary condition, theoretically has to be applied at the far infinity from the body, however in numerical applications is applied at a finite distance. This discrepancy between theory and numerical simulations generates a spurious lift-induced drag component, more significant in two-dimensional flows. Thanks to the present lift-induced drag definition, Destarac explained the spurious positive induced drag production in two-dimensional flows, that can be avoided by applying a vortical correction to the farfield boundary condition. The same phenomenon, in three-dimensional flow, turns in a negative induced drag spurious production.

This method is currently widely adopted as a design tool in the aerospace industry. Indeed, to account for the industrial need for accurate drag prediction, the American Institute for Aeronautics and Astronautics organized Drag Prediction Workshops (DPW) [34, 35, 36, 37, 38, 39] to give the possibility to companies, universities and research centers to discuss and propose numerical drag computations on common configurations. NASA proposed a Common Research Model (CRM) [40], which, starting from the $4th$ Drag Prediction Workshop, has become the standard transonic configuration to test drag

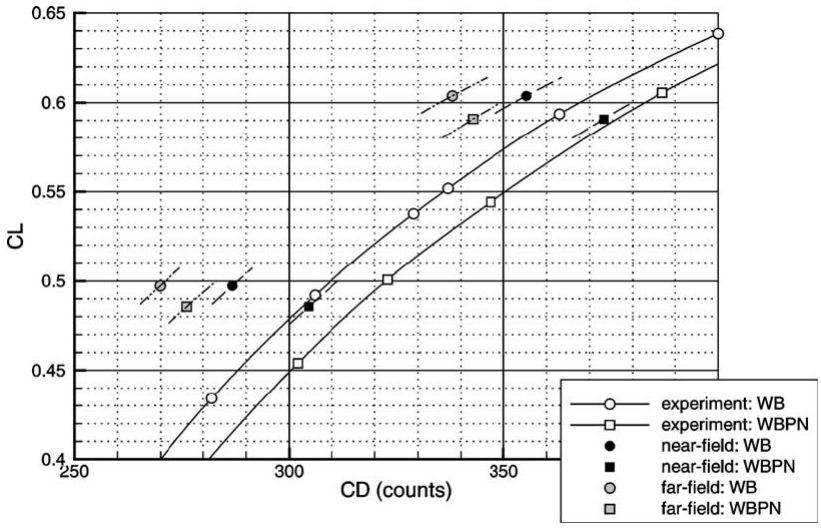

Figure 2.2 Van Der Vooren and Destarac drag breakdown method. Application to Wing-Body (WB) and Wing-Body-Propeller-Nacelle (WBPN) configurations of the DLR-ALVAST twin engine transport aircraft configuration. Simulation were performed at $M_\infty = 0.75$, $Re_\infty = 4.3 \cdot 10^6$, $\kappa - \omega$ turbulence model. Extracted from [7].

computation. Hue [41, 42, 43] proposed application of Van Der Vooren and Destarac drag decomposition method on the CRM wing body horizontal tail configuration and wing body configuration. Figure 2.3 reports the computed drag coefficient with the near field formula and present method on the wing body configuration, at $M_\infty = 0.85$, $Re_\infty = 5 \cdot 10^6$ and $C_L = 0.5$ (cruise condition). The spurious drag contribution has been canceled. Present method gives always a lower drag value, and converges more rapidly than near field drag. Table 2.1 reports the computed drag breakdown, where $L1 - L6$ are the grid levels. $L1$ is the coarsest grid level, while $L6$ is the finest one.

2.2.3 Paparone and Tognaccini (2003)

Paparone and Tognaccini [6] proposed an alternative drag breakdown method. Differently from Van der Vooren and Destarac irreversible velocity definition, they choose to adopt

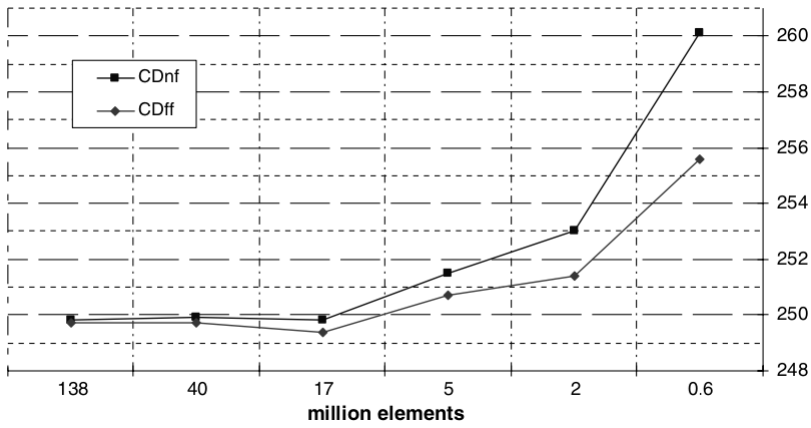

Figure 2.3 NASA CRM wing-body configuration, $M_\infty = 0.85$, $Re_\infty = 5 \cdot 10^6$, $C_L = 0.5$, grid convergence study with common Multiblock grids, wing-body configuration, near field and far field drag vs mesh refinement. Extacted from [43].

Grid level	$L1$	$L2$	$L3$	$L4$	$L5$	$L6$
C_L	0.5001	0.4995	0.5003	0.4993	0.5001	0.5004
$C_{D_{nf}}$	260.0	253.0	251.5	249.8	249.9	249.7
C_{D_f}	113.9	113.9	114.2	114.7	114.8	115.0
C_{D_v}	159.3	156.6	155.9	155.4	155.3	155.2
C_{D_w}	4.8	3.9	3.8	3.7	3.8	3.9
C_{D_i}	91.5	90.9	90.9	90.4	90.6	90.6
$C_{D_{ff}}$	255.6	251.4	250.7	249.4	249.7	249.7
$C_{D_{sp}}$	4.4	1.6	0.8	0.4	0.2	0

Table 2.1 NASA CRM, $M_\infty = 0.85$, $Re_\infty = 5 \cdot 10^6$, $C_L = 0.5$, grid convergence study with common Multiblock grids, drag breakdown. Extracted from [43].

another strategy. First of all, equation (2.5) can be rewritten in the following form

$$u = u_\infty \sqrt{1 + \frac{2\Delta H}{u_\infty^2} - \frac{2}{(\gamma_{pv} - 1)\, M_\infty^2} \left[\left(\frac{\Delta p}{p_\infty} \right)^{\frac{\gamma_{pv} - 1}{\gamma_{pv}}} e^{\frac{(\gamma_{pv} - 1)\, \Delta s}{\gamma_{pv} R}} - 1 \right]} \,. \tag{2.11}$$

This formula is function of Δs, ΔH and Δp. It can be expanded in series up to the second order terms, neglecting higher order terms, i.e.

$$\begin{aligned} \frac{u}{u_\infty} =& 1 + f_{p1} \left(\frac{\Delta p}{p_\infty} \right) + f_{p2} \left(\frac{\Delta p}{p_\infty} \right)^2 + f_{s1} \left(\frac{\Delta s}{R} \right) + f_{p2} \left(\frac{\Delta s}{R} \right)^2 + f_{H1} \left(\frac{\Delta H}{u_\infty^2} \right) + \\ &+ f_{H2} \left(\frac{\Delta H}{u_\infty^2} \right)^2 + f_{sH} \left(\frac{\Delta s}{R} \frac{\Delta H}{u_\infty^2} \right) + f_{sp} \left(\frac{\Delta s}{R} \frac{\Delta p}{p_\infty} \right) + f_{pH} \left(\frac{\Delta p}{p_\infty} \frac{\Delta H}{u_\infty^2} \right) + \\ &+ \mathcal{O} \left[\left(\frac{\Delta s}{R} \right)^3, \left(\frac{\Delta H}{u_\infty^2} \right)^3, \left(\frac{\Delta p}{p_\infty} \right)^3 \right] \dots \,. \end{aligned} \tag{2.12}$$

Pressure contributions are typically associated to aerodynamic lift and lift-induced drag, while enthalpy contributions are negligible in turbulent power-off conditions. Finally, first and second order terms associated to entropy variation give the entropy drag. The entropy first order term $f_{s1} \left(\frac{\Delta s}{R} \right)$ is exactly Oswatitsch entropy drag defined in equation (2.13). Entropy drag can be so generalized as

$$D_{\Delta s} = u_\infty \int_{\mathcal{V}} \boldsymbol{\nabla} \cdot (\rho g \boldsymbol{V}) \, \mathrm{d}\mathcal{V} \,, \tag{2.13}$$

where

$$g = g(\frac{\Delta s}{R}) = -f_{s1} \frac{\Delta s}{R} - f_{s2} \left(\frac{\Delta s}{R} \right)^2, \quad f_{s1} = -\frac{1}{\gamma_{pv} M_\infty^2}, \quad f_{s2} = -\frac{1 + (\gamma_{pv} - 1)\, M_\infty^2}{2\gamma_{pv}^2 M_\infty^2} \,. \tag{2.14}$$

Oswatitsch formula, even though could be transformed in a volume integral and so could be used to perform a breakdown in viscous and wave contributions, could not correctly take into account for viscous effects.

Paparone and Tognaccini showed that first order Oswatitsch's formula can correctly compute wave drag in transonic flows, but not the viscous contribution. Indeed a correct

computation of the viscous drag requires the contribution of at least the second order terms

Paparone and Tognaccini showed that the integrand of equation (2.13) is theoretically non-zero only where there is an entropy production, i.e. viscous and wave regions. Possible additional contributions outside of these regions are due only to numerical errors.

Introducing the viscous volume $\mathcal{V}_v$ and the shock wave volume $\mathcal{V}_w$, viscous and wave contribution can consequently be introduced as

$$D_v = u_\infty \int_{\mathcal{V}_v} \boldsymbol{\nabla} \cdot (\rho g \boldsymbol{V}) \, \mathrm{d}\mathcal{V} \, , \qquad D_w = u_\infty \int_{\mathcal{V}_w} \boldsymbol{\nabla} \cdot (\rho g \boldsymbol{V}) \, \mathrm{d}\mathcal{V} \, . \tag{2.15}$$

This method avoids the ill-definition of u_{irr} in some regions of the flow. A spurious drag contribution can also be defined, considering the volume $\mathcal{V}_{sp} = \mathcal{V} \setminus (\mathcal{V}_v \bigcup \mathcal{V}_w)$

$$D_{sp} = u_\infty \int_{\mathcal{V}_{sp}} \boldsymbol{\nabla} \cdot (\rho g \boldsymbol{V}) \, \mathrm{d}\mathcal{V} \, . \tag{2.16}$$

Again, as in Van der Vooren and Destarac method, while theoretically D_{sp} should be 0, numerically it could be significative. As shown, for example, by Tognaccini [44] (see figure 2.4), considering RANS simulations around a NACA 0012 airfoil, at 0 incidence in transonic flow conditions, is independent on mesh refinement, the computed drag can experience variation of up to 30%.

Drag breakdown has been applied on the same wing body configuration proposed by Van Der Vooren and Destarac [7]. In figure 2.5 computed drag polars are shown together with experimental results obtained by ONERA.

Application of present profile drag breakdown method has been performed on the NASA CRM [45], using an ad-hoc multiblock structured grid. Lift-induced drag has been computed by means of Maskell's formula. Farfield drag $D = D_i + D_w + D_v$ has been computed without the spurious contribution. A comparison between near field and farfield drag against the mesh refinement is proposed in figure 2.6, at $M_\infty = 0.85$, $Re_\infty = 5 \cdot 10^6$ and $C_L = 0.5$. Farfield drag does not change with the mesh size unlike near field results. It implies that the same accuracy in drag calculations could be obtained by a grid 64 times

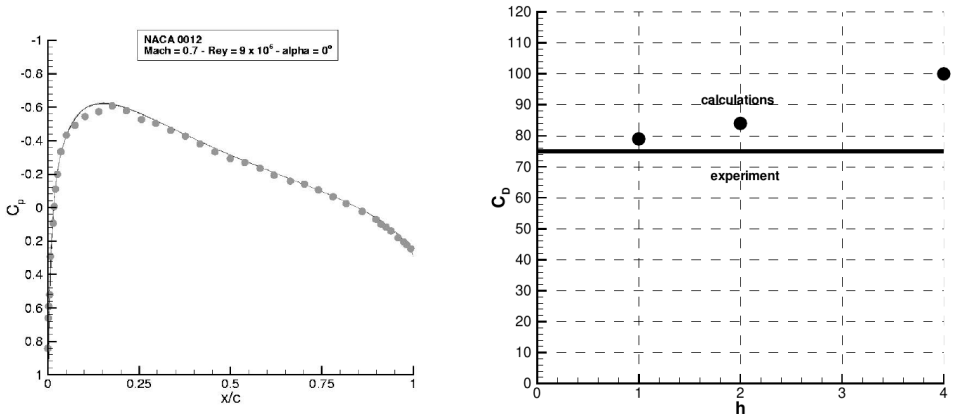

Figure 2.4 NACA 0012, $M_\infty = 0.7$, $Re_\infty = 9 \cdot 10^6$, $\alpha = 0°$; left figure: computed pressure coefficient on 3 grid levels vs experiments; right figure: computed near field drag vs experiments, h mesh average parameter, where $h = 1$ indicates the grid finest level. Extracted from [44].

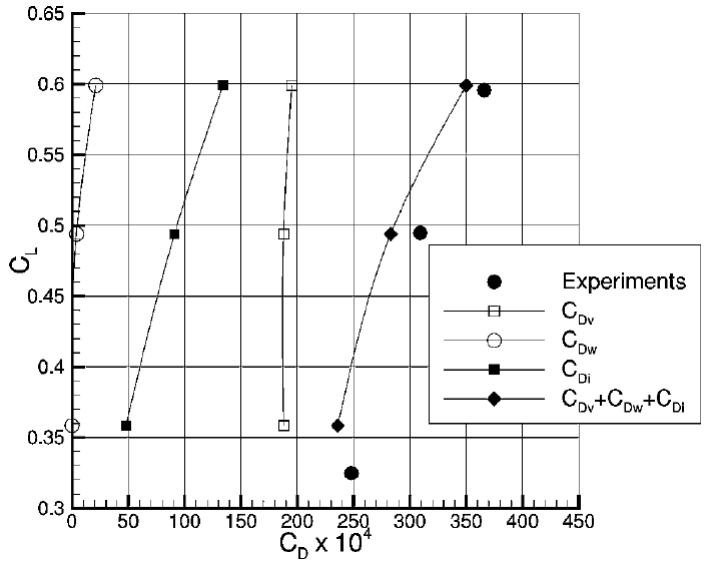

Figure 2.5 Computed drag polars and drag components on the DLR-ALVAST wing body transport aircraft configuration. $M_\infty = 0.75$, $Re_\infty = 4.3 \cdot 10^6$. Extracted from [6]

.

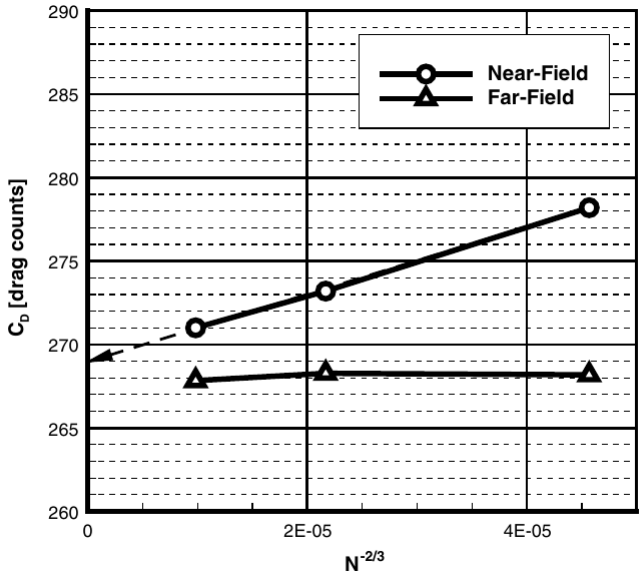

Figure 2.6 NASA CRM, $M_\infty = 0.85$, $Re_\infty = 5 \cdot 10^6$, $C_L = 0.5$. Grid convergence study on 3 multiblock structured grid levels. Near field drag against farfield drag. Extracted from [45].

coarser! The lift-drag polar and its breakdown are shown in figure 2.7 for the medium grid level.

An extension to powered aircraft configuration of present method has also been proposed by Tognaccini [46].

2.2.4 Gariepy et al. (2013)

Gariepy et al. proposed an extension of Van der Vooren and Destarac theory to obtain a breakdown method for unsteady drag [47].

They choose to work in the body reference frame. Integration domain is shown in figure 2.8, as defined in [47] Exploiting a definition of reversible velocity u_{rev}, that is

$$u_{rev} = u_\infty \sqrt{1 + \frac{2\Delta H}{u_\infty^2} - \frac{2}{(\gamma_{pv} - 1)\, M_\infty^2} \left(\left(\frac{p}{p_\infty} \right)^{\frac{\gamma_{pv}}{\gamma_{pv} - 1}} - 1 \right) - \frac{v^2 + w^2}{u_\infty^2}} \,, \qquad (2.17)$$

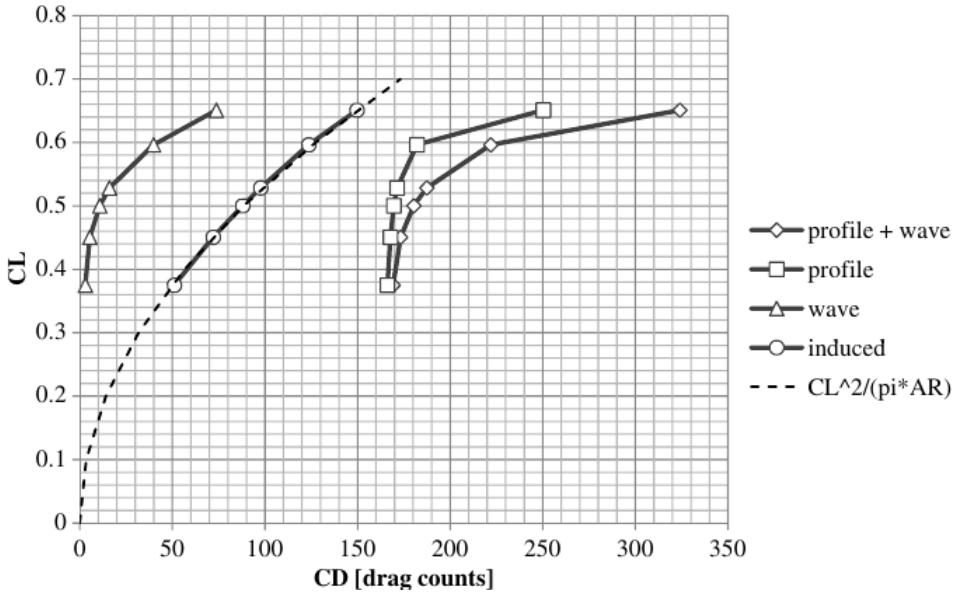

Figure 2.7 NASA CRM, $M_\infty = 0.85$, $Re_\infty = 5 \cdot 10^6$, medium grid level. Computed lift-drag polar. Extracted from [45].

where v and w are the y and z velocity components, they proposed

$$D_v = \int_{\mathcal{V}_v} \boldsymbol{\nabla} \cdot \left[\rho \left(u - u_{rev}\right) \boldsymbol{V}'\right] \mathrm{d}\mathcal{V}, \qquad D_w = \int_{\mathcal{V}_w} \boldsymbol{\nabla} \cdot \left[\rho \left(u - u_{rev}\right) \boldsymbol{V}'\right] \mathrm{d}\mathcal{V} \ , \tag{2.18}$$

where $\boldsymbol{V}'$ is the velocity in the relative reference frame. At the same way, spurious drag

$$D_{sp} = \int_{\mathcal{V}_{sp}} \boldsymbol{\nabla} \cdot \left[\rho \left(u - u_{rev}\right) \boldsymbol{V}'\right] \mathrm{d}\mathcal{V} \ . \tag{2.19}$$

Furthermore, they introduced an *unsteady drag* component. They first introduced a reversible axial velocity assuming a steady flow

$$u_{rev,s} = u_\infty \sqrt{1 - \frac{2}{\left(\gamma_{pv} - 1\right) M_\infty^2} \left(\left(\frac{p}{p_\infty} \right)^{\frac{\gamma_{pv}}{\gamma_{pv} - 1}} - 1 \right) - \frac{v^2 + w^2}{u_\infty^2}} \ . \tag{2.20}$$

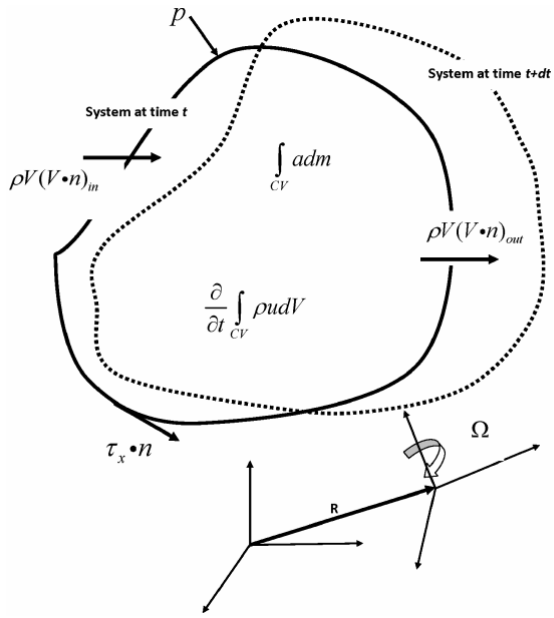

Figure 2.8 Integration domain definition for the application of the unsteady drag breakdown method proposed by Gariepy et al. Extracted from [47].

and then a reversible velocity due to unsteady fluctuations, $u_{rev,u} = u_{rev} - u_{rev,s}$. Finally

$$D_{uns} = -\int_{\mathcal{V}} \boldsymbol{\nabla} \cdot [\rho u_{rev,u} \boldsymbol{V}'] \, \mathrm{d}\mathcal{V} - \frac{\partial}{\partial t} \int_{\mathcal{V}} \rho \, (u - u_\infty) \, \mathrm{d}\mathcal{V} - \int_{\mathcal{V}} \boldsymbol{a} \cdot \boldsymbol{i}_x \mathrm{d}m \ , \tag{2.21}$$

where dm is the mass differential increment.

Again, induced drag is defined as the complementary part of D_v, D_w, D_{uns} with respect to the near field drag.

$$D_i = -\int_{\mathcal{V}_v} \boldsymbol{\nabla} \cdot [\rho u_{rev,s} \boldsymbol{V}' + (p - p_\infty) \, \boldsymbol{i}_x - \boldsymbol{\tau}_v \cdot \boldsymbol{i}_x] \, \mathrm{d}\mathcal{V} - D_p - D_f \ . \tag{2.22}$$

Application on pitching airfoil numerical test have been performed, both in an inertial and in a non-inertial frame. Here, in figures 2.9-2.10 is reported their application to a pitching NACA 0012 in subsonic flow, in the body reference of frame. The same test will be examined in chapter 5.

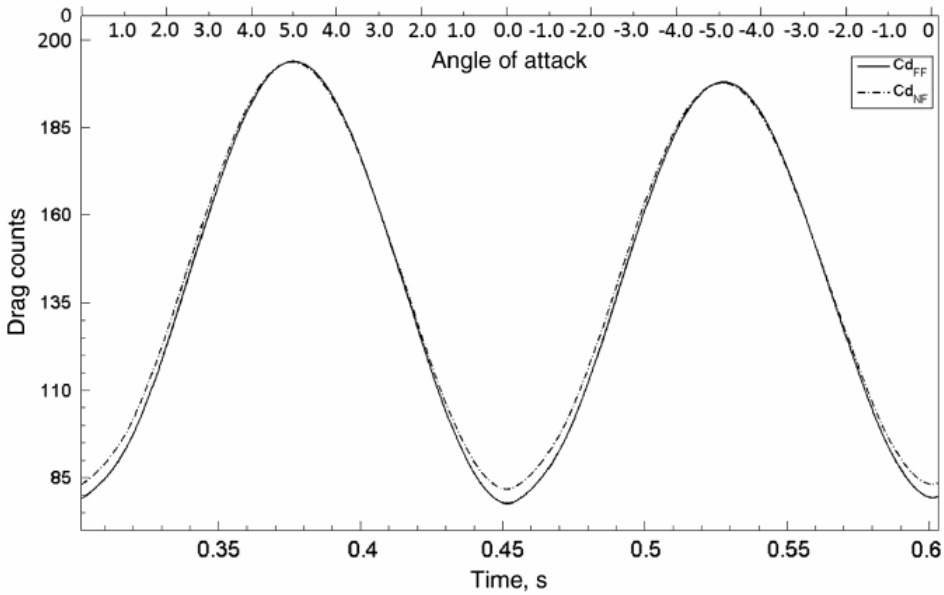

Figure 2.9 Pitching NACA 0012, $M_\infty = 0.3$, $Re_\infty = 6.6 \cdot 10^6$, sinusoidal pitching law, $\bar{\alpha} = 5°$, $k = 0.1$ Total drag versus farfield drag. Extracted from [47].

2.2.5 Toubin et al. (2015-16)

Toubin and Bailly [48] proposed an alternative unsteady drag breakdown. Differently from Gariépy et al., they choose to work in the inertial reference frame. They adopted surface integrals for the terms representing the steady drag breakdown, while they split the time derivative term so that single terms could be associated to each steady drag component, obtaining a new definition of wave, viscous and (unsteady) lift-induced drag. They proposed

$$D = D_v + D_w + D_{ui} + D_m \tag{2.23}$$

$$D_v = \int_{S_v} \left[-\rho \left(u_{irr} - u_\infty\right) \boldsymbol{V} + \boldsymbol{\tau}_v\right] \cdot \boldsymbol{n} \, \mathrm{d}S - \int_{\mathcal{V}_v} \frac{\partial \rho \left(u - u_\infty\right)}{\partial t} \, \mathrm{d}\mathcal{V} \ , \tag{2.24}$$

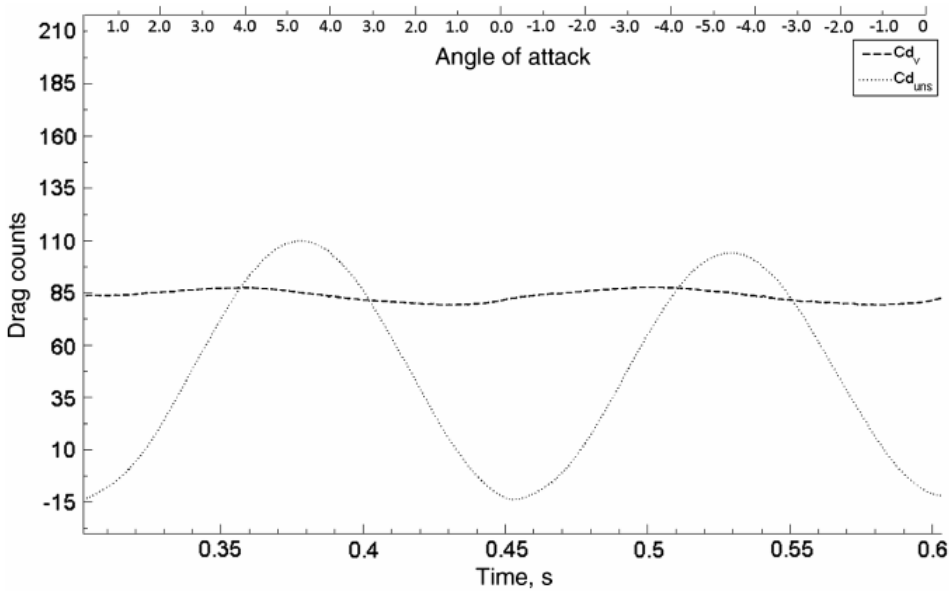

Figure 2.10 Pitching NACA 0012, $M_\infty = 0.3$, $Re_\infty = 6.6 \cdot 10^6$, sinusoidal pitching law, $\bar{\alpha} = 5°$, $k = 0.1$. Drag breakdown in viscous and unsteady components. Extracted from [47].

$$D_w = \int_{S_w} \left[-\rho\left(u_{irr} - u_\infty\right)\boldsymbol{V} + \boldsymbol{\tau}_v\right] \cdot \boldsymbol{n}\, \mathrm{d}S - \int_{\mathcal{V}_w} \frac{\partial \rho\left(u - u_\infty\right)}{\partial t}\, \mathrm{d}\mathcal{V} + \\ - \int_{\mathcal{V}_{wd}} \left[\frac{\partial \rho\left(u - u_{irr}\right)}{\partial t} + \frac{1}{u_{irr}}\frac{\partial p}{\partial t}\right]\, \mathrm{d}\mathcal{V} \tag{2.25}$$

$$D_{ui} = \int_{S_{far}} \left[-\rho\left(u - u_{irr}\right)\boldsymbol{V} - \left(p - p_\infty\right)\boldsymbol{i}_x\right] \cdot \boldsymbol{n}\, \mathrm{d}S \\ - \int_{\mathcal{V}_c} \left[\frac{\partial \rho\left(u - u_{irr}\right)}{\partial t} + \frac{1}{u_{irr}}\frac{\partial p}{\partial t}\right]\, \mathrm{d}\mathcal{V}\ , \tag{2.26}$$

$$D_m = -\int_{S_b} \rho\left(u - u_\infty\right)\boldsymbol{V} \cdot \boldsymbol{n}\, \mathrm{d}S\ , \tag{2.27}$$

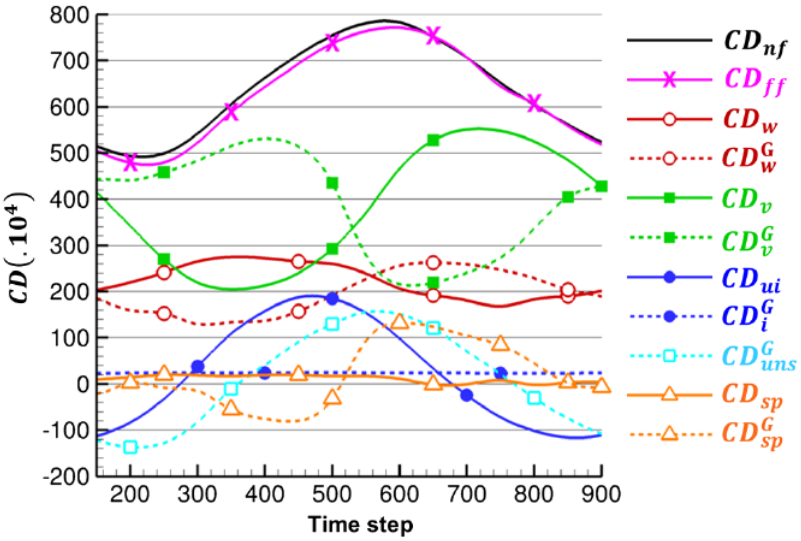

Figure 2.11 OAT15A Airfoil, $M_\infty = 0.73$, $Re_\infty = 3 \cdot 10^6$, $\alpha = 4.5°$ two-dimensional buffet simulation. Computed drag and drag decomposition. Extracted from [48].

where D_m is a *motion drag* term associated to the body velocity, negligible in aeronautical applications, D_{ui} is what they called unsteady induced drag, defined as the difference between near field formula (equation (1.7)) and wave, motion, viscous and unsteady induced drag.

The authors also defined a spurious drag contribution. Again, this is defined as the difference between near field and farfield drag.

This formula resulted very stable and accurate in numerical applications, concerning pitching airfoil and wing simulations, vortex shedding airfoil and airfoil buffet. They also achieved a synchronization in time property by which drag decomposition does not depend on the integration volume chosen.

Two results are shown n figures 2.11 and 2.12: a RANS airfoil buffet and a RANS pitching airfoil analyses, where the pitching airfoil test case is the same already proposed by Gariépy et al. [47]. Gariépy et al. drag breakdown is compared with present decomposition and near field results. For the buffet case an example of the selected viscous, wave and shock wake regions is reported in figure 2.13.

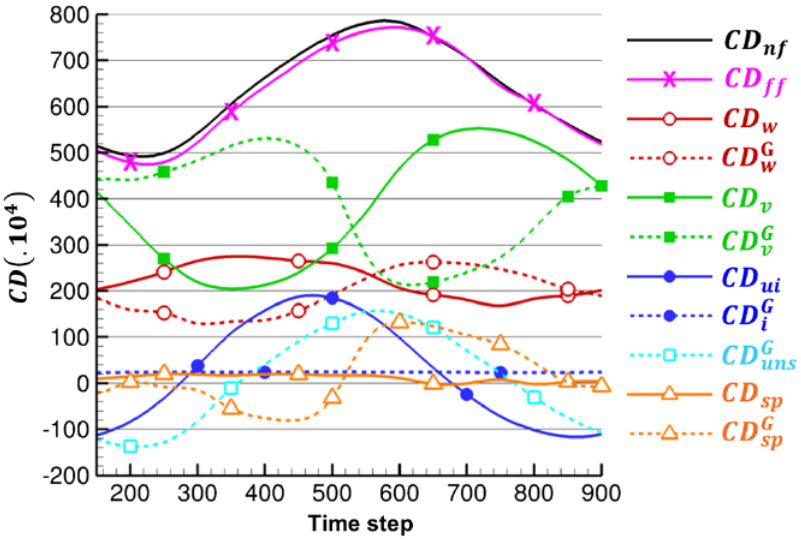

Figure 2.12 Pitching NACA 0012, $M_\infty = 0.3$, $Re_\infty = 6.6 \cdot 10^6$, sinusoidal pitching law, $\bar{\alpha} = 5°$, $k = 0.1$. Computed drag and drag breakdown. Extracted from [48].

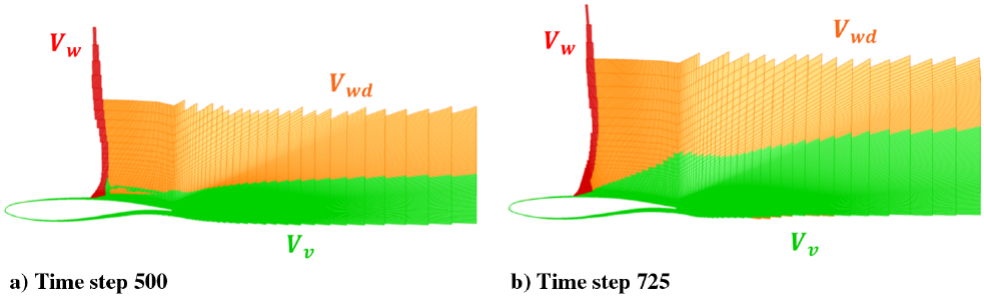

Figure 2.13 OAT15A Airfoil, $M_\infty = 0.73$, $Re_\infty = 3 \cdot 10^6$, $\alpha = 4.5°$ two-dimensional buffet simulation. Example of selected viscous, wave and shock wake volumes. Extracted from [48].

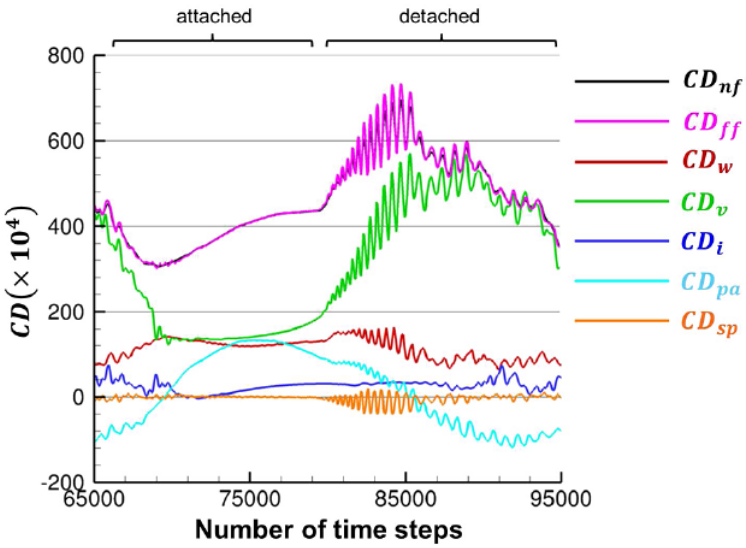

Figure 2.14 OAT15A Airfoil, $M_\infty = 0.73$, $Re_\infty = 3 \cdot 10^6$, $\alpha = 3.5°$, ZDES buffet simulation. Computed drag and drag decomposition. Extracted from [49].

Toubin et al. [49] also proposed a further decomposition. They split the unsteady induced drag contribution in an "induced" drag and a term associated to acoustic propagation effects:

$$\begin{aligned} D_i = &\int_{S_{far}} \left[-\rho\left(u - u_{irr}\right)\boldsymbol{V} - \left(p - p_\infty\right)\boldsymbol{i}_x\right] \cdot \boldsymbol{n}\, \mathrm{d}S + \\ &- \int_{\mathcal{V}_c} \left[\rho\left(u - u_{irr}\right)\left(\frac{1}{a} - \frac{1}{u_{irr}}\right)\frac{\partial u}{\partial t}\right] \mathrm{d}\mathcal{V}\ , \end{aligned} \tag{2.28}$$

$$D_{pa} = \int_{\mathcal{V}_c} \rho \frac{u - u_{irr}}{a} \frac{\partial R^+}{\partial t}\, \mathrm{d}\mathcal{V}\ . \tag{2.29}$$

where a is the local speed of sound and $R^+ = u + 2a/(\gamma_{pv} - 1)$ is the Riemann invariant. Successful application of the drag decomposition method was also proposed in a buffet Zonal Detached Eddy Simulation (ZDES), reported in figure 2.14.

2.3 Vortical methods

The force breakdown based on vorticity field computation and/or measurement is an innovative approach for the analysis of the aerodynamic force.

2.3.1 Noca et al. (1997-99)

Noca et al. [8, 9] proposed three exact expressions to compute aerodynamic force in unsteady incompressible flows. Here is reported the formula they call "flux form":

$$\boldsymbol{F} = \int\limits_{S_{far}(t)} \boldsymbol{n} \cdot \gamma_{flux} \, \mathrm{d}S - \int\limits_{S_b} \boldsymbol{n} \cdot (\boldsymbol{V} - \boldsymbol{V}_S) \, \boldsymbol{V} \, \mathrm{d}S - \frac{d}{dt} \int\limits_{S_b} \boldsymbol{n} \cdot (\boldsymbol{V}\boldsymbol{x}) \ , \tag{2.30}$$

where $\boldsymbol{V}_s$ is the body wall velocity, and γ_{flux}

$$\gamma_{flux} = \frac{1}{2} V^2 \boldsymbol{I} - \boldsymbol{V}\boldsymbol{V} - \boldsymbol{V}\boldsymbol{r} \times \boldsymbol{\omega} + \boldsymbol{\omega}\boldsymbol{r} \times \boldsymbol{V} - \left[\left(\boldsymbol{r} \cdot \frac{\partial \boldsymbol{V}}{\partial t} \right) \boldsymbol{I} - \boldsymbol{r} \frac{\partial \boldsymbol{V}}{\partial t} + \boldsymbol{x} \frac{\partial \boldsymbol{V}}{\partial t} \right] \ . \tag{2.31}$$

This formula has the particular advantage to be composed by surface integrals only, being ideal to compute aerodynamic force in experimental applications. This method is only applicable when the flow is unsteady.

Other formulae, here not reported, are the “impulsive form” and the “momentum” form. The first is called impulsive since, when S_{far} goes to infinity, in two-dimensional flows recovers the result by which total force is given by time derivative of the hydrodynamic impulse. The momentum form owes its name by the fact that it can be directly compared to the momentum equation, and does not present a pressure term. In any case, such as the flux form, these three formulae, even if present a breakdown, cannot allow for a physical one.

The application of the flux form formula, and the other formulations, is reported in figure 2.15. The test case is a numerical simulation of a two-dimensional heaving cylinder, impulsively started. In the upper figure the computed vorticity field is shown , while in the low figure application of force formulae on lift computations are reported.

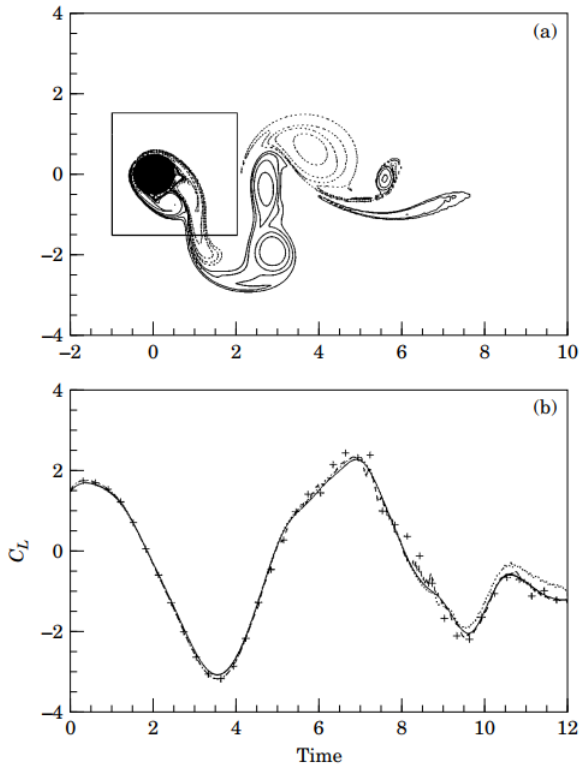

Figure 2.15 Two-dimensional heaving cylinder in incompressible flow. $Re = 392$. (a): Vorticity field at $V_\infty t/D = 12$ (D is the diameter). (b): computed lift. Extracted from [8].

2.3.2 Wu et al. (2007): incompressible flows

Wu et al. [50] proposed innovative unconventional exact formulae to compute aerodynamic force in incompressible viscous unsteady flows, based on the local vorticity field $\boldsymbol{\omega}$. Formulae have been found exploiting the so-called *Derivative Moment Transformations* (DMT) [51], reported in appendix A.

A first formula is what they call *diffusion form*, since it relies on a volume integral of local viscous stresses

$$\boldsymbol{F} = -\mu \int_{\mathcal{V}} \boldsymbol{r} \times \nabla^2 \boldsymbol{\omega} \, \mathrm{d}\mathcal{V} + \boldsymbol{F}_B + \boldsymbol{F}_\Sigma \tag{2.32}$$

where

$$\boldsymbol{F}_B = \int_{S_b} \rho \boldsymbol{r} \times \boldsymbol{n} \times \boldsymbol{a} \, \mathrm{d}S, \qquad \boldsymbol{F}_\Sigma = -\mu \int_{S_{far}} \boldsymbol{r} \times \boldsymbol{n} \times \boldsymbol{\nabla} \times \boldsymbol{\omega} \, \mathrm{d}S + \mu \int_{S_{far}} \boldsymbol{\omega} \times \boldsymbol{n} \, \mathrm{d}S \ . \tag{2.33}$$

$\boldsymbol{r}$ is defined as $\boldsymbol{x}/d - 1$, where $d = 2, 3$ is the space dimension and $\boldsymbol{x}$ is the position vector. Additional terms to the *diffusive* volume integral are $\boldsymbol{F}_B$, dependent on the body acceleration, which takes into account both body motion and potential body deformations, and a surface integral $\boldsymbol{F}_{\Sigma,,}$ over the external surface S_{far}, explicitly dependent on the local viscous stresses.

Second formula can be derived from the diffusive form by means of the DMT. It is called *advection form*, since it relies on local velocity derivatives

$$\boldsymbol{F} = -\rho \int_{\mathcal{V}} \left(\boldsymbol{r} \times \frac{\partial \boldsymbol{\omega}}{\partial t} + \boldsymbol{\ell} \right) \mathrm{d}\mathcal{V} - \rho \int_{\partial \mathcal{V}} \boldsymbol{r} \times \boldsymbol{n} \times \boldsymbol{\ell} \, \mathrm{d}S + \boldsymbol{F}_B + \boldsymbol{F}_\Sigma \ , \tag{2.34}$$

where $\boldsymbol{\ell} = \boldsymbol{\omega} \times \boldsymbol{V}$ is the Lamb vector, defined as the cross product of vorticity and velocity. As demonstrated in [51], this formula represents a different way to write the "momentum form" presented by Noca et al. It presents a first volume integral with the local moment of Lamb vector and vorticity Eulerian time derivative, and a surface integral over the surface S_{far} of the moment of the Lamb vector, other than the terms $\boldsymbol{F}_B$ and $\boldsymbol{F}_\Sigma$.

Finally, the third form presented is a particular case of equation (2.32), in which the

surface S_{far} shrinks to coincide S_b. The formula, valid in three-dimensional flows, is

$$\boldsymbol{F} = \int_{S_b} \rho \boldsymbol{x} \times \left(\frac{1}{2} \boldsymbol{n} \times \frac{\boldsymbol{\nabla} p}{\rho} + \nu \boldsymbol{n} \times \boldsymbol{\nabla} \times \boldsymbol{\omega} \right) \mathrm{d}S \ . \tag{2.35}$$

This final form is called *creation form*, since it relies on quantities characteristic of the body vorticity creation process.

Successful applications on the impulsively started unsteady separated flow around a two-dimensional circular cylinder, and on the three-dimensional unsteady flow over around a circular cylinder were presented. Figure 2.16 reports both aerodynamic lift and drag computed by equation (2.32) for the two-dimensional case, versus the near field force. As stated by the authors, application of equation (2.34) gave similar results.

Equations (2.32) and (2.34) are valid for integration domains $\mathcal{V}$ with no open surfaces at its boundary. Since the three-dimensional test case has been obtained adopting periodic conditions on S_{far}, diffusion form and advection form have been opportunely modified. Diffusion and advection form formulae become:

$$\boldsymbol{F} = -\mu \int_{\mathcal{V}} \boldsymbol{r} \times \nabla^2 \boldsymbol{\omega} \, \mathrm{d}\mathcal{V} + \boldsymbol{F}_B + \boldsymbol{F}_\Sigma + \boldsymbol{F}_{line} \ , \tag{2.36}$$

$$\boldsymbol{F} = -\rho \int_{\mathcal{V}} \left(\boldsymbol{r} \times \frac{\partial \boldsymbol{\omega}}{\partial t} + \boldsymbol{\ell} \right) \mathrm{d}\mathcal{V} - \rho \int_{\partial \mathcal{V}} \boldsymbol{r} \times \boldsymbol{n} \times \boldsymbol{\ell} \, \mathrm{d}S + \boldsymbol{F}_{B'} + \boldsymbol{F}_\Sigma + \boldsymbol{F}_{line} \ , \tag{2.37}$$

where

$$\boldsymbol{F}_{line} = \frac{1}{2} \oint_{\partial S_{far}} \boldsymbol{x} \times (-p \mathrm{d}\boldsymbol{x} + 2\mu \boldsymbol{\omega} \times \mathrm{d}\boldsymbol{x}) - 2\mu \oint_{\partial S_{far}} \boldsymbol{V} \times \mathrm{d}\boldsymbol{x} \ , \tag{2.38}$$

$$\boldsymbol{F}_{B'} = \int_{S_b} \boldsymbol{x} \times \left[\times \boldsymbol{n} \left(\frac{\partial \boldsymbol{V}}{\partial t} + \frac{1}{2} \boldsymbol{\nabla} \mid \boldsymbol{V} \mid^2 \right) \right] \mathrm{d}S \ . \tag{2.39}$$

A snapshot of the vorticity field for the three-dimensional test case is proposed in figure 2.17. Drag computation is shown in figure 2.18. D_{line} is $\boldsymbol{F}_{line}$ drag component, while D_{other} is the remaining contribution of equation (2.36). D_{line} contribution, that takes into account the open surface effects, gives a significative contribution, comparable to

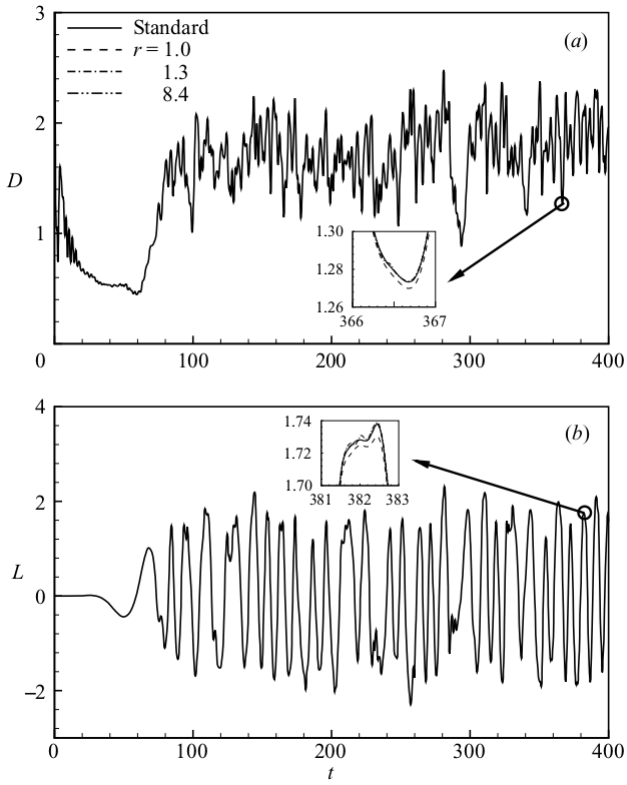

Figure 2.16 Two-dimensional impulsively started circular cylinder. $Re = 9500$. Computed lift and drag contributions by equation (2.32) vs near field force. Extracted from [50]

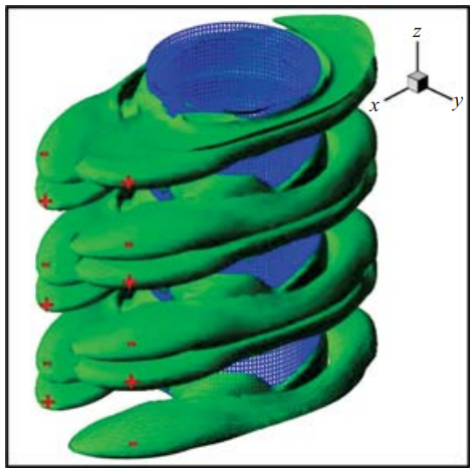

Figure 2.17 Three-dimensional oscyllating cylinder. $Re = 600$, $t = 24T$ (T is the period). Circumferential vorticity component. Extracted from [50]

.

D_{other}.

Yang et al. [52] already evidenced the possibility to obtain a physical force breakdown from advection form in the case of steady flows around aeronautical configurations. Following the arguments already proposed by Wu et al. [51], authors argued that the contribution $\boldsymbol{F}_\Sigma$ is negligible at high Reynolds number, and that $\boldsymbol{F}_B$ and $\dfrac{\partial \boldsymbol{\omega}}{\partial t}$ are 0 for steady flows.

Aerodynamic force in high Reynolds number flow is solely due to two contribution, a volume integral of the Lamb vector and a surface integral over the boundary domain of a moment of the Lamb vector. Aerodynamic force is thus only due to the Lamb vector. The force formula (2.34) becomes so a midfield formula (accordingly to the midfield concept already introduced in section 2.2.2), i.e. aerodynamic force is function of a flow variable, the $\boldsymbol{\ell}$ vector, non-negligible in a limited region of the flow, since vorticity is different than 0 only in the boundary layer and in the viscous wake. Furthermore, the contribution of the surface integral on the body surface is 0 in steady flows, since $\boldsymbol{V} = 0$. These two contributions can be interpreted to obtain a physical breakdown. Yang et al. argued that the volume integral accounts for the reversible part of the aerodynamic force, i.e.

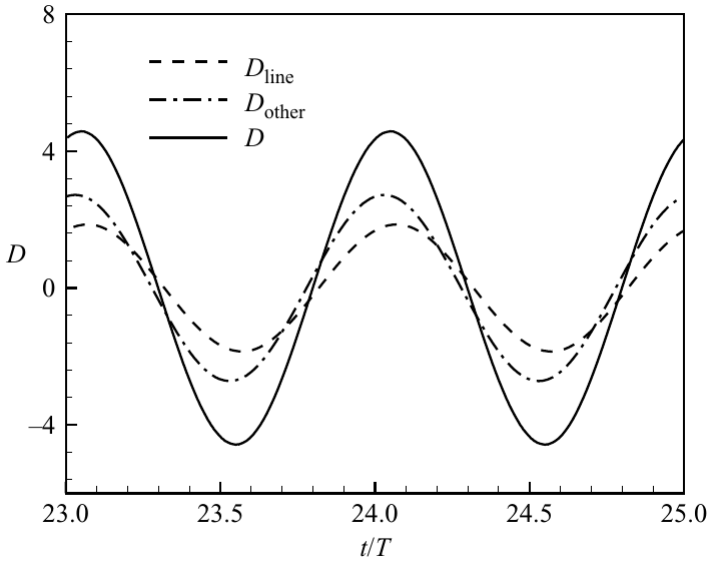

Figure 2.18 Three-dimensional oscyllating cylinder. $Re = 600$, $t = 24T$ (T is the period). Computed drag contributions. Extracted from [50]

.

the aerodynamic lift and the lift induced drag. The volume integral of the Lamb vector in the flow domain was not a new concept. Already introduced by Prandtl [10, 11] in his lifting line potential theory, Von Karman and Burgers [53], again, in potential form, discussed about of this integral in the flow domain as the responsible of the aerodynamic force in airfoil flows, basically giving the Kutta-Joukowskij theorem. Saffman [54] first related with a theoretical proof the aerodynamic force to this integral, calling it "vortex force", due its vortical nature. His arguments concerned about flow fields characterized by bounded vorticity field, where he demonstrated that the vortex force contributes to all the aerodynamic force. Wu [50] extended the vortex force concept to the aerodynamic force in a general incompressible flow, considering flows also with unbounded vorticity fields, the most common case when dealing with bodies with wakes convected infinitely downstream. The idea of relating vortex force to the reversible part of the aerodynamic force in steady flows, is given by the behaviour of the surface integral, which in high-Reynolds number flows, defined on the outer far surface S_{far}, becomes a wake integral

only. Wu et al. [51] found that this integral, considering a surface S_{far} far enough, results into the total pressure deficit on the wake plane, i.e. profile drag as already defined by classical farfield methods like Betz' or Jones' ones.

Applications to a slender delta wing at high angles of attack were performed, showing the highly localized Lamb vector field (figure 2.19). No data were available for comparison, so it is difficult to validate Yang et al. breakdown. Marongiu et al. [55] completed this theory, and further introduced with a numerical proof a rigorous definition of lift-induced drag in incompressible flows by means of the vortex force.

2.3.3 Marongiu and Tognaccini (2010)

Marongiu and Tognaccini [56] successfully extended the application of this method to turbulent flows, proving that the same formulae can compute the aerodynamic force by numerical RANS simulations, with an ad hoc substitution of the flow variables with averaged ones. The proof is reported in section 3.2, generalized to the compressible unsteady case. Furthermore, a discussion about the contribution $\boldsymbol{F}_\Sigma$ of equation (2.34) (explicitly dependent on the molecular viscosity) is proposed. They proved that this term is negligible in flows where the boundary layer hypothesis can be applied. The proof is reported in section B. Marongiu and Tognaccini [56] computed with equation (2.34) the aerodynamic force of numerical RANS solutions around a NACA 0012 airfoil, at different freestream Reynolds number and angles of attack, both in steady and unsteady regimes.

2.3.4 Marongiu et al. (2013), a definition of lift-induced in incompressible flow

Marongiu et al. [55] analyzed three-dimensional incompressible steady flows. Redefining equation (2.34), under the steady flow hypothesis, as

$$\boldsymbol{F} = \boldsymbol{F}_\ell + \boldsymbol{F}_{S_{far}} + \boldsymbol{\Delta}_\mu \ , \tag{2.40}$$

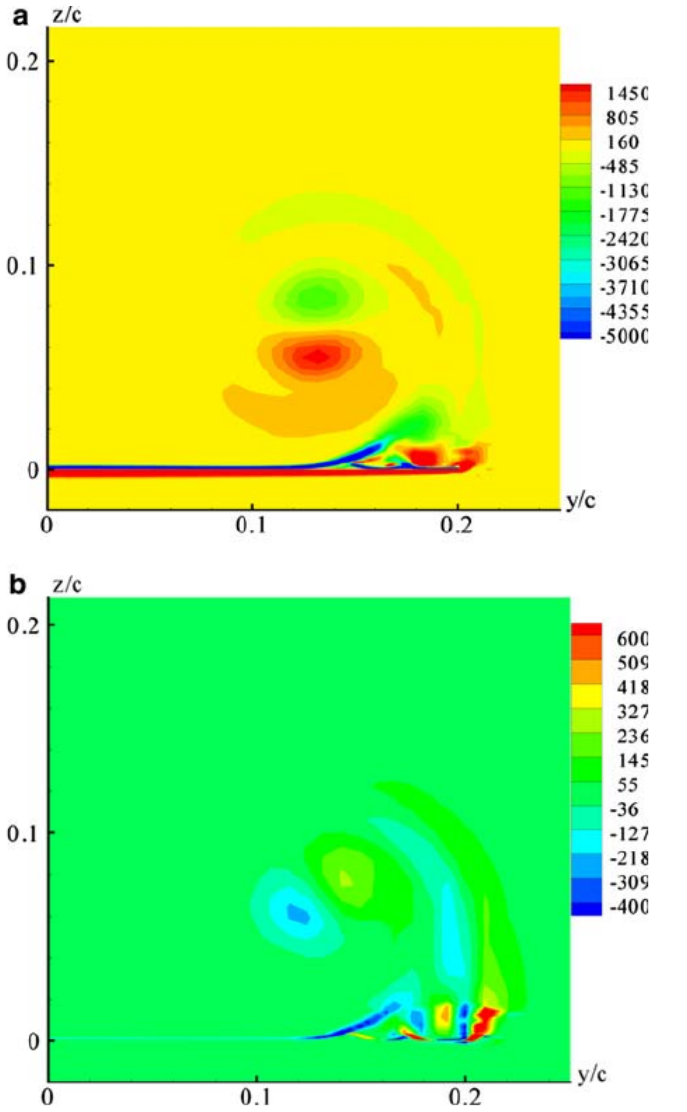

Figure 2.19 Computed z (upper figure) and x (lower figure) Lamb vector components contour for an incompressible flow around a slender wing. $x/c = 0.8$ (x is the axial direction). $\alpha = 20°$, $\chi = 76°$ (χ is the sweep angle). $Re = 5 \cdot 10^5$. Extracted from [52].

where

$$\begin{aligned} \boldsymbol{F}_\ell = & \quad -\rho \int_{\mathcal{V}} \boldsymbol{\ell}\, \mathrm{d}\mathcal{V}, & \boldsymbol{F}_{S_{far}} = -\rho \int\limits_{S_{far}} \boldsymbol{r} \times \boldsymbol{n} \times \boldsymbol{\ell}\, \mathrm{d}S, \\ \boldsymbol{\Delta}_\mu = & \int_{S_{far}} \boldsymbol{r} \times \boldsymbol{n} \times \boldsymbol{\nabla} \cdot \boldsymbol{\tau}_v\, \mathrm{d}S & + \int\limits_{S_{far}} \boldsymbol{n} \times \boldsymbol{\tau}_v\, \mathrm{d}S\ . \end{aligned}$$

they successfully demonstrated a rigorous physical force breakdown. First of all, as already demonstrated by Marongiu and Tognaccini [56], $\boldsymbol{\Delta}_\mu$ is negligible in high-Reynolds number flows. As argued by Wu [51], $\boldsymbol{F}_{S_{far}}$ is a wake integral only, and it only provides a drag contribution, the viscous profile drag indeed. A direct proof in 2-D flows has been proposed by Wu [57]. The general proof, valid also in compressible flows, will be discussed in section 3.3. Marongiu et al. proved that the vortex force is the reversible part of the aerodynamic force in incompressible flows. Taking into account for the vector identity $\boldsymbol{\ell} = \boldsymbol{V} \cdot \boldsymbol{\nabla}\boldsymbol{V} - \boldsymbol{\nabla}\dfrac{V^2}{2}$, and considering that $\boldsymbol{\nabla} \cdot \boldsymbol{V} = 0$ in incompressible flows (therefore, $\boldsymbol{V} \cdot \boldsymbol{\nabla}\boldsymbol{V} = \boldsymbol{\nabla} \cdot (\boldsymbol{V}\boldsymbol{V})$), the vortex force is

$$\boldsymbol{F}_\ell = -\rho \int\limits_{\mathcal{V}} \boldsymbol{\ell}\, \mathrm{d}\mathcal{V} = \rho \int\limits_{S_{far}} \left[\frac{V^2}{2} \boldsymbol{n} - \boldsymbol{V}\, (\boldsymbol{V} \cdot \boldsymbol{n}) \right] \mathrm{d}S\ , \tag{2.41}$$

where the last equality is obtained taking into account the Gauss's theorem and the fact that $\boldsymbol{V} = 0$ on S_b The RHS of Eq. (2.41) the far-field expression of the aerodynamic force (1.8) in the limit of inviscid flows (taking into account for Bernoulli's theorem). The vortex force gives therefore the reversible part of the aerodynamic force, its drag component is the lift-induced drag, while viscous profile drag is given by $\boldsymbol{F}_{S_{far}}$ and $\boldsymbol{\Delta}_\mu$. Replacing $\boldsymbol{V}$ with $\boldsymbol{V} = \boldsymbol{V}_\infty + \Delta\boldsymbol{V}$ in Eq. (2.41) and taking into account the continuity equation, we have

$$\begin{aligned} \boldsymbol{F}_\ell = & -\rho \Big[\int\limits_{S_{far}} (\Delta\boldsymbol{V}\boldsymbol{V}_\infty \cdot \boldsymbol{n} - \boldsymbol{V}_\infty \cdot \delta\boldsymbol{V}\boldsymbol{n})\, \mathrm{d}S + \\ & - \int\limits_{S_{far}} \left(\Delta\boldsymbol{V}\Delta\boldsymbol{V} \cdot \boldsymbol{n} - \frac{\Delta V^2}{2}\boldsymbol{n} \right) \mathrm{d}S \Big]\ . \end{aligned} \tag{2.42}$$

The first integral only contains first-order terms in ΔV, whereas quadratic terms are only present in the second one. Taking into account the expression of the double-cross vector product, the first integral becomes

$$\boldsymbol{F}_{\ell 1} = \rho \boldsymbol{V}_\infty \times \int\limits_{S_{far}} \boldsymbol{n} \times \boldsymbol{V} \, \mathrm{d}S \ , \tag{2.43}$$

which clearly only gives a lift contribution (in 2-D flows it is the Kutta-Joukowskij theorem). Considering the asymptotic behavior of the velocity perturbation, the quadratic terms vanish, except in the wake. Therefore, if S_{far} is built-up by Cartesian planes, the second integral of equation (2.42) has a nonzero contribution only on the face S_W, parallel to the (y, z) plane, behind the wing, with x parallel to the freestream (the Trefftz plane). The projection of this integral on x gives the lift-induced drag:

$$D_i = \frac{\rho}{2} \int\limits_{S_W} \left(v^2 + w^2 - u^2 \right) \, \mathrm{d}S \ , \tag{2.44}$$

that, as discussed for instanceby Kusunose [24], can also be computed by Maskell's formula eq. (2.3).

Summarizing, the proposed aerodynamic force breakdown is the following

$$L = \boldsymbol{F}_\ell \cdot \boldsymbol{i}_z \ , \tag{2.45}$$

$$D_i = \boldsymbol{F}_\ell \cdot \boldsymbol{i}_x \ , \tag{2.46}$$

$$D_{pr} = \boldsymbol{F}_{S_{far}} \cdot \boldsymbol{i}_x \ . \tag{2.47}$$

where L is the aerodynamif lift, D_i is the lift-induced drag, and D_{pr} is the profile viscous drag. This definition holds with the hypothesis that the integral of D_i converges as S_{far} extents toward infinity.

Marongiu et al. numerically proved their breakdown analyzing numerical simulations of the flow around incompressible an elliptic wing, showing a perfect agreement of the present lift-induced drag definition with celebrated Prandtl's formula ($C_{D_i} = C_L^2/(\pi \mathcal{AR})$) and Maskell's formula. These results will be extensively discussed in chapter 4.

2.3.5 A first extension to compressible flows (2006-14)

Wu et al. in [51] already proposed a first extension of equation (2.34) to compressible flows:

$$\begin{aligned}\boldsymbol{F}_a = &-\int_{\mathcal{V}} \boldsymbol{r}\times\boldsymbol{\nabla}\times\frac{\partial\rho\boldsymbol{V}}{\partial t} - \int_{\mathcal{V}}\left(\rho\boldsymbol{\ell} - \frac{1}{2}V^2\boldsymbol{\nabla}\rho\right)\mathrm{d}\mathcal{V} \\ &-\int_{S_{far}} \boldsymbol{r}\times\boldsymbol{n}\times\left(\rho\boldsymbol{\ell} - \frac{1}{2}V^2\boldsymbol{\nabla}\rho\right)\mathrm{d}S + \boldsymbol{F}_B + \boldsymbol{F}_\Sigma\ ,\end{aligned} \tag{2.48}$$

where $\boldsymbol{F}_B$ and $\boldsymbol{F}_\Sigma$, very similar to the incompressible case, are:

$$\boldsymbol{F}_B = \int_{S_b} \boldsymbol{r}\times\boldsymbol{n}\times\rho\boldsymbol{a}\,\mathrm{d}S, \quad \boldsymbol{F}_\Sigma = -\int_{S_{far}} \boldsymbol{r}\times\boldsymbol{n}\times\boldsymbol{\nabla}\cdot\boldsymbol{\tau}_v\,\mathrm{d}S + \int_{S_{far}} \boldsymbol{n}\cdot\boldsymbol{\tau}_v\,\mathrm{d}S\ . \tag{2.49}$$

Differently from the incompressible case, we have these changes:

$$\rho\boldsymbol{\ell} \to \rho\boldsymbol{\ell} - \frac{1}{2}V^2\boldsymbol{\nabla}\rho, \quad \rho\frac{\partial\boldsymbol{\omega}}{\partial t} \to \boldsymbol{\nabla}\times\frac{\partial\rho\boldsymbol{V}}{\partial t}\ .$$

At high Reynolds numbers, again $\boldsymbol{F}_\Sigma$ is negligible. In steady flow both $\boldsymbol{F}_B$ and $\dfrac{\partial\rho\boldsymbol{V}}{\partial t}$ are null. Equation 2.48 is not a midfield formula. Indeed, while in the incompressible case the aerodynamic force is only function of the Lamb vector field, non-negligible in the rotational region only, equation (2.48) is dependent on the local density gradient $\boldsymbol{\nabla}\rho$, which is non-negligible in the whole integration domain. This property, strongly useful in numerical applications, as already pointed out by Van Der Vooren and Destarac [7] and Paparone and Tognaccini [6], has been recovered by Mele and Tognaccini [58] with an equivalent aerodynamic force exact expression (see section 2.3.6). Xu et al. [59] analyzed by equation (2.48) a large eddy simulation around a wavy cylinder, at $M_\infty = 0.75$ and

$Re = 2 \cdot 10^5$. They arranged the terms as

$$\boldsymbol{F}_\ell = -\int_{\mathcal{V}} \rho\boldsymbol{\ell}\,\mathrm{d}\mathcal{V} - \int_{S_{far}} \boldsymbol{r}\times\boldsymbol{n}\times\rho\boldsymbol{\ell}\,\mathrm{d}S \tag{2.50}$$

$$\boldsymbol{F}_\rho = \int_{\mathcal{V}} \frac{1}{2}V^2\boldsymbol{\nabla}\rho\,\mathrm{d}\mathcal{V} + \int_{S_{far}} \boldsymbol{r}\times\boldsymbol{n}\times\frac{1}{2}V^2\boldsymbol{\nabla}\rho\,\mathrm{d}S \tag{2.51}$$

$$\boldsymbol{F}_{uns} = -\int_{\mathcal{V}} \boldsymbol{r}\times\boldsymbol{\nabla}\times\frac{\partial\rho\boldsymbol{V}}{\partial t}\,\mathrm{d}\mathcal{V}\ . \tag{2.52}$$

Computed force was in good agreement with the near contribution. $\boldsymbol{F}_\Sigma$ gave a negligible contribution, while $\boldsymbol{F}_B$ gave about half the total drag. $\boldsymbol{F}_\ell$ and $\boldsymbol{F}_\rho$ presented similar contributions to drag, with $\boldsymbol{F}_\rho$ being larger than $\boldsymbol{F}_\ell$, showing the growing importance of the compressible effects. No estimation of the unsteady term was given.

Liu et al. [60, 61] further developed Wu et al. compressible theory, analyzing the behavior of each component with the Mach number. In particular, they defined the vector $\rho\boldsymbol{j} = \dfrac{\partial\rho\boldsymbol{V}}{\partial t} + \boldsymbol{\nabla}\cdot\rho\boldsymbol{V}\boldsymbol{V} - \dfrac{1}{2}\boldsymbol{\nabla}\left(\rho V^2\right)$. Equation (2.48) can be rewritten as:

$$\boldsymbol{F} = -\int_{\mathcal{V}} \rho\boldsymbol{j}\,\mathrm{d}\mathcal{V} - \int_{S_{far}} \boldsymbol{r}\times\boldsymbol{n}\times\rho\boldsymbol{j}\,\mathrm{d}S + \boldsymbol{F}_B + \boldsymbol{F}_\Sigma\ . \tag{2.53}$$

A theoretical analysis by thermodynamic assumptions, on the behavior of $\boldsymbol{j}$ decomposition with the Mach number, lead to

$$\boldsymbol{j} = \alpha(M)\left(\frac{\partial\boldsymbol{V}}{\partial t} + \boldsymbol{\ell}\right) + \beta(M)\left(R\boldsymbol{\nabla}\alpha(M)T - \eta\right)\ . \tag{2.54}$$

where $\alpha = 1 + \dfrac{\gamma_{pv}}{2}M^2$, $\beta = \alpha - 1$ and $\eta = \dfrac{1}{\rho}\left(\mu_2\boldsymbol{\nabla}\cdot\boldsymbol{V} - \boldsymbol{\nabla}\times(\mu\boldsymbol{V})\right)$. η is the viscous force per unit mass. β is associated to the compressible effects. Finally, splitting velocity in a transverse component and a longitudinal component, that is $\boldsymbol{V} = \boldsymbol{\nabla}\phi + \boldsymbol{\nabla}\times\boldsymbol{\psi}$, $\boldsymbol{\nabla}\cdot\boldsymbol{\psi} = 0$, they split $\boldsymbol{j} = \boldsymbol{j}_L + \boldsymbol{j}_T$, having $\boldsymbol{F} = \boldsymbol{F}_L + \boldsymbol{F}_T + \boldsymbol{F}_B$. The transverse contribution, as $M \to 0$ becomes the incompressible vortex force. Compressible effects on this component are due to the shearing process by compressibility. The longidutinal contribution resembles a competition between total enthalpy and internal energy gradients, since these gradients

are often in opposite sign. Further theoretical details can be found in [60, 61]. Analyses of numerical two-dimensional steady flows around a cylinder, at various freestream Mach number, from subsonic to supersonic flow regime have been reported.

In figure 2.21 the x component of the vortex force distribution $\boldsymbol{F}_\ell$ is presented for serveral freestream Mach numbers. A comparison of the longitudinal and transverse drag components behavior for various values of the freestream Mach number is also reported.

2.3.6 Mele and Tognaccini (2014)

Mele and Tognaccini [58] proposed another extension of Wu's formula in compressible flows

$$\boldsymbol{F} = \boldsymbol{F}_\ell + \boldsymbol{F}_{m_\rho} + \boldsymbol{F}_{S_{far}} + \boldsymbol{F}_t + \boldsymbol{F}_{S_b} + \boldsymbol{F}_{tb} + \boldsymbol{\Delta}_\mu \tag{2.55}$$

where

$$\boldsymbol{F}_\ell = -\int_{\mathcal{V}} \rho\boldsymbol{\ell}\,\mathrm{d}\mathcal{V}\ , \qquad \boldsymbol{F}_{m_\rho} = -\int_{\mathcal{V}} \boldsymbol{r}\times\boldsymbol{\nabla}\rho\times\boldsymbol{\nabla}\frac{V^2}{2}\,\mathrm{d}\mathcal{V}\ , \tag{2.56}$$

$$\boldsymbol{F}_{S_{far}} = -\int_{S_{far}} \boldsymbol{r}\times\boldsymbol{n}\times\rho\boldsymbol{\ell}\,\mathrm{d}S, \qquad \boldsymbol{F}_t - = \int_{\mathcal{V}} \boldsymbol{r}\times\boldsymbol{\nabla}\times\rho\frac{\partial\boldsymbol{V}}{\partial t}\,\mathrm{d}\mathcal{V}\ , \tag{2.57}$$

$$\boldsymbol{F}_{S_b} = -\int_{S_b} \boldsymbol{r}\times\boldsymbol{n}\times\rho\boldsymbol{\ell}\,\mathrm{d}S\ , \qquad \boldsymbol{F}tb = \int_{S_b} \boldsymbol{r}\times\boldsymbol{n}\times\rho\boldsymbol{a}\,\mathrm{d}S\ , \tag{2.58}$$

$$\boldsymbol{\Delta}_\mu = \int_{S_{far}} \boldsymbol{r}\times\boldsymbol{n}\times\boldsymbol{\nabla}\cdot\boldsymbol{\tau}_v\,\mathrm{d}S \quad + \int_{S_{far}} \boldsymbol{n}\cdot\boldsymbol{\tau}_v\,\mathrm{d}S\ . \tag{2.59}$$

where $\boldsymbol{F}_{m_\rho}$ is a compressibility correction to the vortex force. Indeed, in the case of two-dimensional flows, they proved that $\boldsymbol{F}_{m_\rho}$ is non-negligible only in the rotational region of the fluid flow. Indeed, outside those regions, a real high Reynolds number flow is in practice homoenthalpic, i.e. with constant total enthalpy $H = h + V^2/2$, where h is the specific enthalpy and also homentropic, i.e. with constant entropy. Crocco's relation gives $\boldsymbol{\omega} = 0$; in addition, applying Gibbs' equation, it is $\boldsymbol{\nabla}h = \boldsymbol{\nabla}p/\rho$, whence $\rho\boldsymbol{\nabla}(V^2/2) = -\boldsymbol{\nabla}p$ with the result that both $\boldsymbol{\ell} = 0$ and $\boldsymbol{r}\times\boldsymbol{\nabla}\times\rho\boldsymbol{\nabla}(V^2/2) = 0$. The midfield property of the Wu's advection form is so recovered. Mele and Tognaccini extended present formula

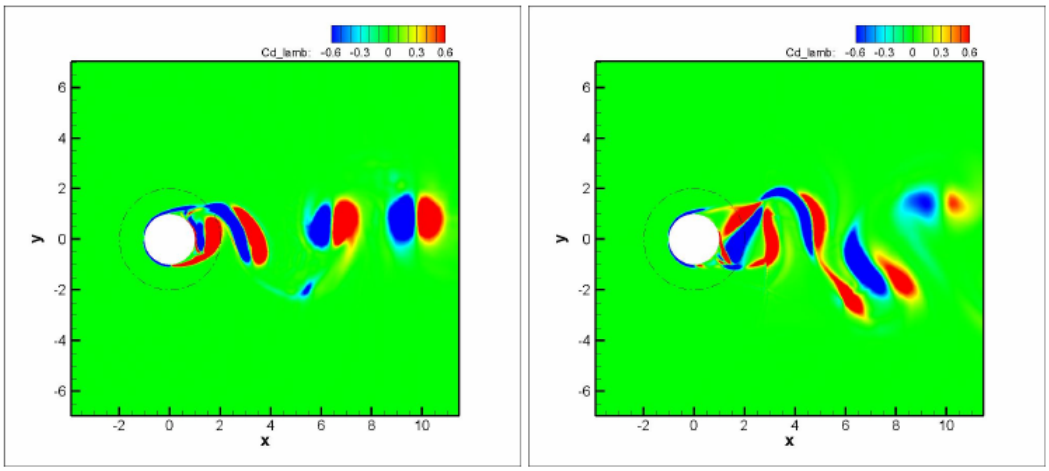

(a) $M_\infty = 0.2$ (b) $M_\infty = 0.8$

(c) $M_\infty = 0.9$ (d) $M_\infty = 2.0$

Figure 2.20 Two-dimensional cylinder, $Re = 1000$, $\alpha = 0°$. $\boldsymbol{F}_\ell$ x component distribution at various freestream Mach numbers. Extracted from [61].

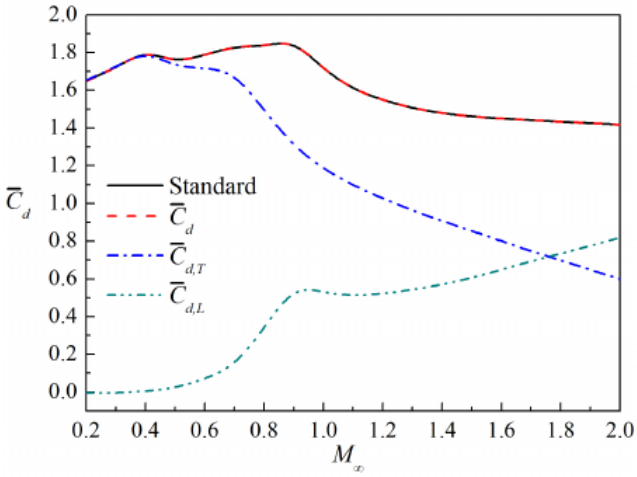

Figure 2.21 Two-dimensional cylinder, $Re = 1000$, $\alpha = 0°$. Longitudinal and transverse drag contributions vs freestream Mach number. Extracted from [61].

to turbulent flows; the proof is reported in section 3.2. Furthermore, they also found for compressible flows that $\boldsymbol{F}_{S_{far}}$ gives only a drag contribution, i.e. the profile drag. Again, a proof is reported in section 3.3. Numerical analyses of the flow around an airfoil at $Re_\infty = 9 \cdot 10^6$, were proposed. Simulations were performed at constant $C_l = 0.5$, varying the freestream Mach number. The analysis of the computed forces and decomposition are shown in figures 2.22a and 2.22b respectively for the lift and drag coefficient; The agreement with the near field results of both lift and drag is excellent in subsonic and low transonic conditions, some discrepancies appear in the high transonic regime when the freestream Mach number is approaching one. Increasing M_∞ the vortex force contribution C_{l_ℓ} decreases: it is compensated by the compressibility correction. Fig. 2.22b shows that the total drag coefficient is obtained for all M_∞ by the wake integral $C_{d_{\Sigma_I}}$. The vortex force contribution to drag, zero in incompressible condition is positive and increases for higher M_∞, it is therefore compensated by a thrust force associated with the compressibility correction. This is numerically confirmed in the tests by Mele and Tognaccini [58] up to $M_\infty = 0.7$. In the test performed at $M_\infty = 0.9$ and $M_\infty = 0.95$ the computation of the compressibility correction was probably not

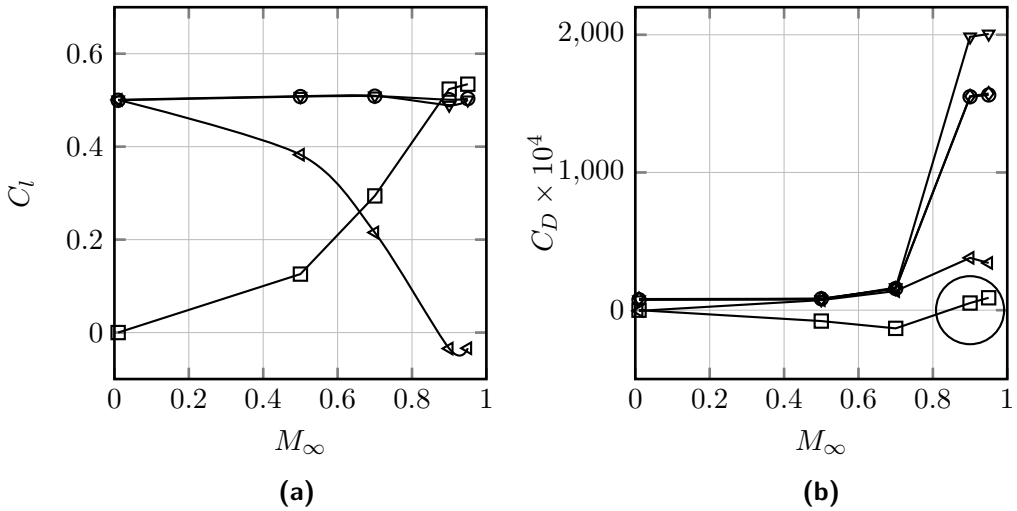

Figure 2.22 NACA 0012 airfoil. $C_l \approx 0.5$, $Re_\infty = 9 \times 10^6$. C_l (a) and C_d (b) contributions vs. Mach number such as reported in . $-\circ-$: near field. $-\triangledown-$: $\boldsymbol{F}_b$. $-\triangleleft-$: $\boldsymbol{F}_\ell$. $-\square-$: $\boldsymbol{F}_{m_\rho}$. $-\diamond-$: $\boldsymbol{F}_{S_{far}}$. Data extracted from [58]

sufficiently accurate, since accuracy becomes poorer in the shock regions, to be included in force computation. Indeed, compressibility correction is defined by the product of two gradients, being more sensitive to flow simulation accuracy. This problem requires a solution and will be extensively discussed in chapter 4.

2.3.7 A generalized Kutta-Joukowskij-Filon theorem in two-dimensional compressible flows (2015)

Liu et al. [62] proposed an extension of the Kutta-Joukowskij theorem [4, 5], concerning the lift force, and of the Filon theorem [63], concerning the drag force, in steady two-dimensional compressible viscous flows.

Considering the perturbed Navier Stokes equations, in the hypothesis by which the farfield boundary is sufficiently far from the body so that Navier Stokes can be linearized, the perturbed velocity $\boldsymbol{V}'$ is subdivided by an Helmoltz decomposition [64] in a longitudinal component $\boldsymbol{V}_\phi = \boldsymbol{\nabla}\phi$, where ϕ is an ad-hoc potential function, and a transverse component $\boldsymbol{V}_\psi$.

Thanks to this decomposition, they found the following exact decomposition of the aerodynamic force:

$$\boldsymbol{F} = \rho_\infty \boldsymbol{V}_\infty \times \boldsymbol{i}_z \Gamma_\phi + \rho_\infty \boldsymbol{V}_\infty \mathcal{Q}_\psi \boldsymbol{i}_x \ , \tag{2.60}$$

where

$$\Gamma_\phi = [[\phi]], \qquad \mathcal{Q}_\psi = [[\psi]] \ , \tag{2.61}$$

and with $[[\cdot]]$ is indicated the jump across C, that is an arbitrarily chosen contour surrounding the airfoil.

The first term of equation (2.60) is the generalization of the Kutta-Joukowskij theorem, while the second term is the generalization of the Filon theorem.

A discussion on the farfield linear behavior hypothesis, (the validity of this hypotheis has been demonstrated by Lagerstrom et al. [64]), is performed, with a quantitative definition of the farfield limit. Furthermore, solution of the linearized Navier-Stokes equation is discussed by means of the fundamental Green solution¸ found by Lagerstrom et al. [64], for a different purpose, without heat conduction, and extended to the heat conduction case when viscosities and heat conductivity are assumed to be small [65].

Since the potential function ϕ and the stream function ψ can not be found numerically or experimentally, a *testable* version of equation (2.60) is also provided, which is valid for small values of $\Gamma_\psi = \Gamma_C - \Gamma_\phi$, proportional to the vorticity integral along the wake plane, and for integrations performed on a farfield boundary that has reached the farfield limit.

2.4 Summary, research needs and future directions

During last decades many aerodynamic force analysis and breakdown methods have been proposed. In steady flows theories have been extensively developed, obtaining drag breakdown methods which are currently used for the aerodynamic design of an aircraft. The major developments regarded the analysis of the aerodynamic force from numerical flow solutions. In particular thermodynamic methods are highly accurate and reliable. They introduce a rigorous definition of viscous and wave drag components, but lift-induced drag is defined as the complementary part with respect to the total farfield drag, so that there

is a lack of physical insight in the lift-induced drag generation. Some recent extensions of these theories to unsteady regimes have the same drawback. Finally, these theories don't allow for the analysis of the aerodynamic lift. Vortical methods allow for the analysis of the whole aerodynamic force. They are directly linkable to the aerodynamic force generation and the local structures of the flow. These theories cover all the flow regimes, both incompressible and compressible, steady and unsteady. Furthermore they allow to find a direct link with inviscid theories. Differently from thermodynamic methods, vortical methods are affected by numerical issues, above all in compressible flows.

This thesis is developed in order to solve some open problems of the previous aerodynamic force vortical theories. There's a lack of a rigorous definition of the lift-induced drag in compressible flows. For this aim, the aerodynamic force formula introduced by Mele and Tognaccini [58] will be developed in order to introduce a rigorous lift-induced drag definition in steady compressible flows. A new equivalent aerodynamic force theory is then derived to overcome the numerical issues that occurs in transonic regime, with a first application on a transonic aircraft configuration. Finally, the full aerodynamic drag breakdown in viscous, wave and lift-induced drag components has to be defined in terms of vorticity integrals. In particular, a vortical definition of wave drag will be discussed. In unsteady flows there's a lack of a theory for the aerodynamic force analysis and breakdown, in particular a rigorous definition of dynamic force derivatives. Present aerodynamic force theory is thus focused on the incompressible unsteady regime. Flat plate flows have been analyzed, with the introduction of another equivalent aerodynamic force expression to overcome numerical issues to the adoption of moving grids. In particular, a direct link with classical inviscid theories is discussed. This link allows for the introduction of a rigorous definition of dynamic force derivatives in nonlinear flows. Finally, the problem of the aerodynamic drag decomposition in unsteady flows is analyzed, with the proposal of an aerodynamic force decomposition in reversible and irreversible parts.

Present vorticity theory, thanks to its direct link with local vorticity, could be a valid tool in order to solve other issues concerning the aerodynamic force analysis. Very recently, an application to the problem of the drag-thrust bookkeping in steady and unsteady flows has been proposed [66]. In particular, in steady flows it has been introduced

a rigorous definition of the thrust due to an actuator disk. In unsteady flows, the proposed breakdown of the aerodynamic force in reversible and irreversible parts allowed for the definition and computation of the thrust produced by a plunging plate in viscous flows.

3

A LAMB-VECTOR BASED THEORY

Contents

In this chapter the general exact formula derived by Mele ant Tognaccini [58] for the analysis and decomposition of the aerodynamic force by means of Lamb vector integrals is discussed. In particular theoretical proofs are proposed. The contribution of the author to this research will be addressed in the following chapters.

3.1 An exact unconventional formula of the aerodynamic force

The exact formula to compute, decompose and analyze the aerodynamic force is

$$\boldsymbol{F} = \boldsymbol{F}_\ell + \boldsymbol{F}_{m_\rho} + \boldsymbol{F}_{S_{far}} + \boldsymbol{F}_t + \boldsymbol{F}_{S_b} + \boldsymbol{F}_{tb} + \boldsymbol{\Delta}_\mu \ , \tag{3.1}$$

where

$$\boldsymbol{F}_\ell = -\int_{\mathcal{V}} \rho\boldsymbol{\ell}\,\mathrm{d}\mathcal{V} \ , \qquad \boldsymbol{F}_{m_\rho} = -\int_{\mathcal{V}} \boldsymbol{r}\times\boldsymbol{\nabla}\rho\times\boldsymbol{\nabla}\frac{V^2}{2}\,\mathrm{d}\mathcal{V} \ , \tag{3.2}$$

$$\boldsymbol{F}_{S_{far}} = -\int_{S_{far}} \boldsymbol{r}\times\boldsymbol{n}\times\rho\boldsymbol{\ell}\,\mathrm{d}S, \qquad \boldsymbol{F}_t - = \int_{\mathcal{V}} \boldsymbol{r}\times\boldsymbol{\nabla}\times\rho\frac{\partial\boldsymbol{V}}{\partial t}\,\mathrm{d}\mathcal{V} \ , \tag{3.3}$$

$$\boldsymbol{F}_{S_b} = -\int_{S_b} \boldsymbol{r}\times\boldsymbol{n}\times\rho\boldsymbol{\ell}\,\mathrm{d}S, \qquad \boldsymbol{F}t_b = \int_{S_b} \boldsymbol{r}\times\boldsymbol{n}\times\rho\boldsymbol{a}\,\mathrm{d}S \ , \tag{3.4}$$

$$\boldsymbol{\Delta}_\mu = \int_{S_{far}} \boldsymbol{r}\times\boldsymbol{n}\times\boldsymbol{\nabla}\cdot\boldsymbol{\tau}_v\,\mathrm{d}S \quad + \int_{S_{far}} \boldsymbol{n}\cdot\boldsymbol{\tau}_v\,\mathrm{d}S \ . \tag{3.5}$$

where $\mathcal{V}$ is the integration domain, ρ is the density, $\boldsymbol{n}$ the local normal versor, $\boldsymbol{\ell} = \boldsymbol{\omega}\times\boldsymbol{V}$ is the Lamb vector and $\boldsymbol{\omega}$ is the flow vorticity. $\boldsymbol{a}$ is the local acceleration and $\boldsymbol{\tau}_v = 2\mu[\boldsymbol{\nabla V} + \boldsymbol{\nabla V}^T]$ is the viscous stress tensor (μ is the kinematic viscosity).

This formula is valid for a compressible, viscous unsteady flow. It can be applied to any integration volume $\mathcal{V}$, provided it contains the whole body boundary layer [56].

The first term, $\boldsymbol{F}_\ell$, is the so-called vortex force. Already dealt by Prandtl in its potential lifting line theory [10, 11], this name was introduced by Von Karman and Burgers [53].

Saffman extensively discussed the link between vortex force and aerodynamic force in incompressible flows [54]. Considering a flow with a bounded vorticity field, he found

that the vortex force gives the entire aerodynamic force.

As already evidenced in section 2.3.2, Wu et al. [50] extended the link between the vortex force and aerodynamic force in incompressible flows, characterized by an unbounded vorticity field, like happens in the body wake.

$\boldsymbol{F}_{m_\rho}$ is a term only present in compressible flows, since it relies on the density gradient.

$\boldsymbol{F}_{S_{far}}$ is a moment of the Lamb vector integrated on the external surface. It takes into account for the vortex force, and, more generally, for the vorticity of the "outer" domain, where with outer domain we call the part of the fluid volume not included in the chosen integration domain (see appendix C). In steady flows it represents the profile drag (proof is provided in section 3.3, while a discussion on the drag breakdown will be proposed in the next chapter).

$\boldsymbol{F}_t$ is a term that arises in unsteady flows. In incompressible flows assumes an easier form, directly linked with local vorticity. $\boldsymbol{F}_{S_b}$ is also an unsteady term, since Lamb vector is 0 on the body surface in steady flows.

$\boldsymbol{F}_{tb}$ is directly linked to the body acceleration, different from 0 only in unsteady regime. Finally, $\boldsymbol{\Delta}_\mu$ is a term that explicitly depends on viscosity. Its contribution is discussed in appendix B.

Proof of equation (3.1) is reported in the following. The analysis of this force formula will be proposed in the next two chapters.

Proof of the Lamb vector based aerodynamic force formula Let us begin from the farfield formula,equation (1.8), applied to the volume defined in figure 3.1

$$\boldsymbol{F} = -\int_{\mathcal{V}} \rho \boldsymbol{a}\, \mathrm{d}\mathcal{V} - \int_{S_{far}} \left(p\boldsymbol{n} - \boldsymbol{n}\cdot\boldsymbol{\tau}_v\right)\, \mathrm{d}S\ . \tag{3.6}$$

The volume integral of the acceleration can be transformed by identity (D.5). We obtain

$$-\int_{\mathcal{V}} \rho \boldsymbol{a}\, \mathrm{d}\mathcal{V} = \underbrace{-\int_{\mathcal{V}} \boldsymbol{r}\times\boldsymbol{\nabla}\times(\rho\boldsymbol{a})\, \mathrm{d}\mathcal{V}}_{A} + \int_{\partial\mathcal{V}} \boldsymbol{r}\times\boldsymbol{n}\times\rho\boldsymbol{a}\, \mathrm{d}S\ . \tag{3.7}$$

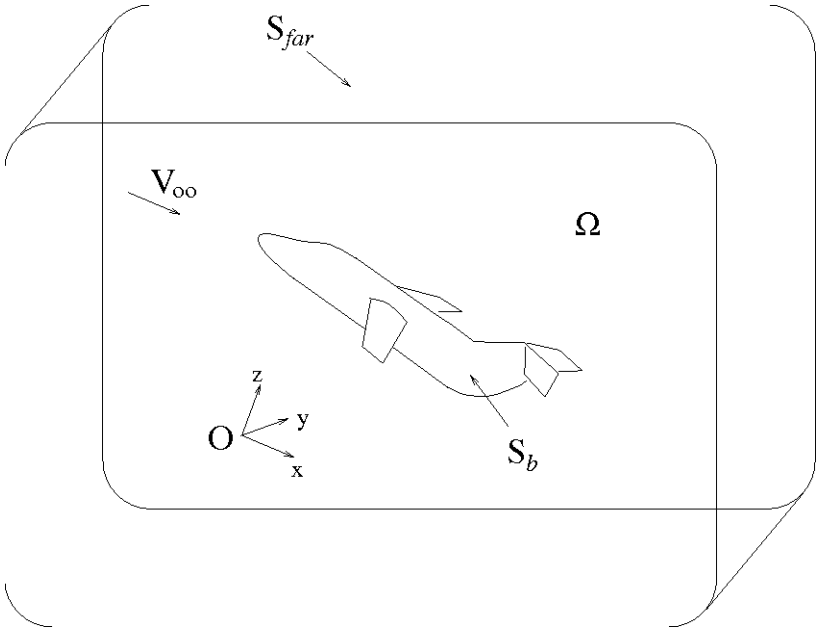

Figure 3.1 Definition of the integration domain.

Examining the RHS of equation (5.40), acceleration can be split as $\rho\boldsymbol{a} = \rho\boldsymbol{\ell} + \rho\boldsymbol{\nabla}\left(\frac{V^2}{2}\right) + \rho\frac{\partial \boldsymbol{V}}{\partial t}$. This splitting can be substituted to the volume integral A of equation (5.40):

$$-\int_{\mathcal{V}} \rho\boldsymbol{a}\,\mathrm{d}\mathcal{V} = -\int_{\mathcal{V}} \boldsymbol{r}\times\boldsymbol{\nabla}\times\left[\rho\boldsymbol{\ell} + \rho\boldsymbol{\nabla}\left(\frac{V^2}{2}\right) + \rho\frac{\partial \boldsymbol{V}}{\partial t}\right]\mathrm{d}\mathcal{V} + \underbrace{+\int_{\partial\mathcal{V}} \boldsymbol{r}\times\boldsymbol{n}\times\rho\boldsymbol{a}\,\mathrm{d}S}_{B} \ . \tag{3.8}$$

The boundary domain $\partial\mathcal{V} = S_{far}\bigcup S_b$ can be split. So the surface integral B becomes

$$\int_{\partial\mathcal{V}} \boldsymbol{r}\times\boldsymbol{n}\times\rho\boldsymbol{a}\,\mathrm{d}S = \int_{S_b} \boldsymbol{r}\times\boldsymbol{n}\times\rho\boldsymbol{a}\,\mathrm{d}S + \underbrace{\int_{S_{far}} \boldsymbol{r}\times\boldsymbol{n}\times\rho\boldsymbol{a}\ \mathrm{d}S}_{C} \ . \tag{3.9}$$

Using the momentum balance $\rho\boldsymbol{a} = -\boldsymbol{\nabla}p + \boldsymbol{\nabla}\cdot\boldsymbol{\tau}_v$, the integral C can be rewritten as

$$\int\limits_{S_{far}} \boldsymbol{r}\times\boldsymbol{n}\times\rho\boldsymbol{a} = -\int\limits_{S_{far}} \boldsymbol{r}\times\boldsymbol{n}\times\boldsymbol{\nabla}p\,\mathrm{d}S + \int\limits_{S_{far}} \boldsymbol{r}\times\boldsymbol{n}\times\boldsymbol{\nabla}\cdot\boldsymbol{\tau}_v\,\mathrm{d}S\ . \tag{3.10}$$

Substituting equation (3.10) in equation (5.40) we have

$$\begin{aligned}\boldsymbol{F} = &-\int\limits_{\mathcal{V}} \boldsymbol{r}\times\boldsymbol{\nabla}\times\left[\rho\boldsymbol{\ell} + \rho\boldsymbol{\nabla}\left(\frac{V^2}{2}\right) + \rho\frac{\partial\boldsymbol{V}}{\partial t}\right]\mathrm{d}\mathcal{V} + \int\limits_{S_b} \boldsymbol{r}\times\boldsymbol{n}\times\rho\boldsymbol{a}\,\mathrm{d}S + \\ &\underbrace{-\int\limits_{S_{far}} \boldsymbol{r}\times\boldsymbol{n}\times\boldsymbol{\nabla}p\,\mathrm{d}S}_{D} \underbrace{-\int\limits_{S_{far}} p\boldsymbol{n}\,\mathrm{d}S}_{E} + \int\limits_{S_{far}} \boldsymbol{n}\cdot\boldsymbol{\tau}_v\,\mathrm{d}S + \int\limits_{S_{far}} \boldsymbol{r}\times\boldsymbol{n}\times\boldsymbol{\nabla}\cdot\boldsymbol{\tau}_v\,\mathrm{d}S\ .\end{aligned} \tag{3.11}$$

To cancel the pressure term, the pressure distribution has to be continued in the body. The body is so replaced with a fictitious fluid volume B, with a proper pressure (and velocity) distribution. Thanks to this assumption, the boundary domain of $\mathcal{V}\bigcup B$ is exactly S_{far}. Finally, we introduce a potential function ϕ, defined in the volume $\mathcal{V}\bigcup B$, which has to be equal to p on S_{far}. Considering the integral E in equation (3.11), and applying identity (A.2) to ϕ in the whole domain, we have

$$\begin{aligned}E = -\int\limits_{S_{far}} p\boldsymbol{n}\,\mathrm{d}S = -\int\limits_{S_{far}} \phi\boldsymbol{n}\,\mathrm{d}S = \int\limits_{S_{far}} \boldsymbol{r}\times\boldsymbol{n}\times\boldsymbol{\nabla}\phi\,\mathrm{d}S = \\ = \int\limits_{S_{far}} \boldsymbol{r}\times\boldsymbol{n}\times\boldsymbol{\nabla}p\,\mathrm{d}S = -D\ ,\end{aligned} \tag{3.12}$$

since ϕ is equal to p on S_{far}. The terms D and E of equation (3.11) cancel each other. Equation (3.6) reduces to

$$\begin{aligned}\boldsymbol{F} = &-\int\limits_{\mathcal{V}} \boldsymbol{r}\times\boldsymbol{\nabla}\times\left[\rho\boldsymbol{\ell} + \rho\boldsymbol{\nabla}\left(\frac{V^2}{2}\right) + \rho\frac{\partial\boldsymbol{V}}{\partial t}\right]\mathrm{d}\mathcal{V} + \int\limits_{S_b} \boldsymbol{r}\times\boldsymbol{n}\times\rho\boldsymbol{a}\,\mathrm{d}S + \\ &+\int\limits_{S_{far}} \boldsymbol{n}\cdot\boldsymbol{\tau}_v\,\mathrm{d}S + \int\limits_{S_{far}} \boldsymbol{r}\times\boldsymbol{n}\times\boldsymbol{\nabla}\cdot\boldsymbol{\tau}_v\,\mathrm{d}S\ .\end{aligned} \tag{3.13}$$

Finally, applying (D.5) to the vector $\rho\boldsymbol{\ell}$, we have

$$\begin{aligned}\boldsymbol{F} = &-\int_{\mathcal{V}} \rho\boldsymbol{\ell}\,\mathrm{d}\mathcal{V} - \int_{S_{far}} \boldsymbol{r}\times\boldsymbol{n}\times\rho\boldsymbol{\ell}\,\mathrm{d}S - \int_{S_b} \boldsymbol{r}\times\boldsymbol{n}\times\rho\boldsymbol{\ell}\,\mathrm{d}S + \\ &- \int_{\mathcal{V}} \boldsymbol{r}\times\boldsymbol{\nabla}\times\rho\boldsymbol{\nabla}\left(\frac{V^2}{2}\right)\mathrm{d}\mathcal{V} + \int_{\mathcal{V}} \boldsymbol{r}\times\boldsymbol{\nabla}\times\left(\rho\frac{\partial\boldsymbol{V}}{\partial t}\right)\mathrm{d}\mathcal{V} + \\ &+ \int_{S_b} \boldsymbol{r}\times\boldsymbol{n}\times\rho\boldsymbol{a}\,\mathrm{d}S + + \int_{S_{far}} \boldsymbol{n}\cdot\boldsymbol{\tau}_v\,\mathrm{d}S + \int_{S_{far}} \boldsymbol{r}\times\boldsymbol{n}\times\boldsymbol{\nabla}\cdot\boldsymbol{\tau}_v\,\mathrm{d}S\ .\end{aligned} \tag{3.14}$$

which is exactly equation (3.1).

3.2 Extension to turbulent flows

Mele and Tognaccini [58] successfully extended in steady flows the application of formula (3.1) to turbulent flows, by means of Favre averaging of the flow variables. Here is proposed a similar discussion, for the unsteady case.

We assume a flow governed by the URANS equations [67]. Particular care has to be taken for the averaging of the Lamb vector, which is non linear.

A property f is expressed as $f = \overline{f} + f'$ or $f = \tilde{f} + f''$, where $\overline{f}$ and $\tilde{f}$ are ensembled and Favre averaged variables, while f' and f'' are the respective fluctuation. Favre average is defined as $\tilde{f} = \overline{\rho f}/\overline{f}$. We have, averaging the Lamb vector

$$\tilde{\boldsymbol{\ell}} = \tilde{\boldsymbol{\omega}}\times\tilde{\boldsymbol{V}} + \widetilde{\boldsymbol{\omega}''\times\boldsymbol{V}''}\ , \tag{3.15}$$

$$\bar{\rho}\widetilde{\boldsymbol{\omega}''\times\boldsymbol{V}''} = -\boldsymbol{\nabla}\cdot\boldsymbol{\tau}_R - \bar{\rho}\boldsymbol{\nabla}\kappa - \boldsymbol{\delta}_{\rho V}\ , \tag{3.16}$$

where $\boldsymbol{\tau}_R = -\overline{\rho\boldsymbol{V}''\boldsymbol{V}''}$ is the Reynolds stress tensor, κ is the turbulent kinetic energy and $\boldsymbol{\delta}_{\rho V} = \overline{\boldsymbol{V}''\boldsymbol{\nabla}\cdot(\rho\boldsymbol{V}'')}$.

Averaging $\boldsymbol{F}_\ell$, we have

$$-\overline{\int_{\mathcal{V}} \rho\boldsymbol{\ell}\,\mathrm{d}\mathcal{V}} = -\int_{\mathcal{V}} \bar{\rho}(\tilde{\boldsymbol{\omega}}\times\tilde{\boldsymbol{V}})\,\mathrm{d}\mathcal{V} + \int_{\mathcal{V}} \boldsymbol{\nabla}\cdot\boldsymbol{\tau}_R\,\mathrm{d}\mathcal{V} + \int_{\mathcal{V}} \bar{\rho}\boldsymbol{\nabla}\kappa\,\mathrm{d}\mathcal{V} + \int_{\mathcal{V}} \boldsymbol{\delta}_{\rho V}\,\mathrm{d}\mathcal{V}\ . \tag{3.17}$$

As concerning $\boldsymbol{F}_{m_\rho}$ and $\boldsymbol{F}_t$

$$-\overline{\int_{\mathcal{V}} \boldsymbol{m}_\rho \,\mathrm{d}\mathcal{V}} = -\int_{\mathcal{V}} \widetilde{\boldsymbol{m}_\rho}\,\mathrm{d}\mathcal{V} - \int_{\mathcal{V}} \boldsymbol{r}\times\left[\boldsymbol{\nabla}\times(\bar{\rho}\boldsymbol{\nabla}\kappa)\right]\,\mathrm{d}\mathcal{V}\ , \tag{3.18}$$

$$-\overline{\int_{\mathcal{V}} \boldsymbol{r}\times\boldsymbol{\nabla}\times\left(\rho\frac{\partial \boldsymbol{V}}{\partial t}\right)\,\mathrm{d}\mathcal{V}} = -\int_{\mathcal{V}} \boldsymbol{r}\times\boldsymbol{\nabla}\times\overline{\rho}\frac{\partial\tilde{\boldsymbol{V}}}{\partial t}\,\mathrm{d}\mathcal{V}\ , \tag{3.19}$$

where $\widetilde{\boldsymbol{m}_\rho} = \boldsymbol{r}\times\boldsymbol{\nabla}\times\left[\bar{\rho}\boldsymbol{\nabla}\left(\frac{\tilde{V}^2}{2}\right)\right]$. Averaging the surface integrals $\boldsymbol{F}_{S_{far}} + \boldsymbol{F}_{S_b}$

$$\begin{aligned}-\overline{\int_{\partial\mathcal{V}} \boldsymbol{r}\times\boldsymbol{n}\times\rho\boldsymbol{\ell}\,\mathrm{d}S} = &-\int_{\partial\mathcal{V}} \boldsymbol{r}\times\boldsymbol{n}\times\left(\bar{\rho}\tilde{\boldsymbol{\omega}}\times\tilde{\boldsymbol{V}}\right)\,\mathrm{d}S + \int_{\partial\mathcal{V}} \boldsymbol{r}\times\boldsymbol{n}\times(\boldsymbol{\nabla}\cdot\boldsymbol{\tau}_R)\,\mathrm{d}S\\ &+\int_{\partial\mathcal{V}} \boldsymbol{r}\times\boldsymbol{n}\times(\bar{\rho}\boldsymbol{\nabla}\kappa)\,\mathrm{d}S + \int_{\partial\mathcal{V}} \boldsymbol{r}\times\boldsymbol{n}\times\boldsymbol{\delta}_{\rho V}\,\mathrm{d}S\ .\end{aligned} \tag{3.20}$$

Finally, for $\boldsymbol{\Delta}_\mu$

$$\overline{\int_{S_{far}} \boldsymbol{r}\times\boldsymbol{n}\times\boldsymbol{\nabla}\cdot\boldsymbol{\tau}_v\,\mathrm{d}S} + \overline{\int_{S_{far}} \boldsymbol{\tau}_v\cdot\boldsymbol{n}\,\mathrm{dS}} = \int_{S_{far}} \boldsymbol{r}\times\boldsymbol{n}\times\boldsymbol{\nabla}\cdot\boldsymbol{\tau}_{vt}\,\mathrm{d}S + \int_{S_{far}} \boldsymbol{n}\cdot\boldsymbol{\tau}_{vt}\,\mathrm{d}S\ , \tag{3.21}$$

where $\boldsymbol{\tau}_{vt} = \mu(\boldsymbol{\nabla}\tilde{\boldsymbol{V}} + \boldsymbol{\nabla}\tilde{\boldsymbol{V}}^T)$. Applying (D.5) to the vector $\overline{\rho}\boldsymbol{\nabla}\kappa$ in equation (3.17)

$$\int_{\mathcal{V}} \overline{\rho}\boldsymbol{\nabla}\kappa\,\mathrm{d}\mathcal{V} = \int_{\mathcal{V}} \boldsymbol{r}\times\boldsymbol{\nabla}\times\overline{\rho}\boldsymbol{\nabla}\kappa\,\mathrm{d}\mathcal{V} - \int_{\partial\mathcal{V}} \boldsymbol{r}\times\boldsymbol{n}\times\overline{\rho}\boldsymbol{\nabla}\kappa\,\mathrm{d}S\ , \tag{3.22}$$

the RHS cancels with the same terms in equations (3.18) and (3.21). Applying (D.5) to the vector $\boldsymbol{\delta}_{\rho V}$ in equation (3.17)

$$\int_{\mathcal{V}} \boldsymbol{\delta}_{\rho V}\,\mathrm{d}\mathcal{V} = \int_{\mathcal{V}} \boldsymbol{r}\times\boldsymbol{\nabla}\times\boldsymbol{\delta}_{\rho V}\,\mathrm{d}\mathcal{V} - \int_{\partial\mathcal{V}} \boldsymbol{r}\times\boldsymbol{n}\times\boldsymbol{\delta}_{\rho V}\,\mathrm{d}S\ , \tag{3.23}$$

where the surface integral at RHS cancels with the same term in equation (3.20). Finally,

applying Gauss' theorem

$$\int_{\mathcal{V}} \boldsymbol{\nabla} \cdot \boldsymbol{\tau}_R \, \mathrm{d}\mathcal{V} = \int_{\partial\mathcal{V}} \boldsymbol{n} \cdot \boldsymbol{\tau}_R \, \mathrm{d}S = \int_{S_{far}} \boldsymbol{n} \cdot \boldsymbol{\tau}_R \, \mathrm{d}S \ , \tag{3.24}$$

since $\boldsymbol{\tau}_R = 0$ on S_b. Finally

$$\boldsymbol{F} = \boldsymbol{F}_\ell + \boldsymbol{F}_{S_{far}} + \boldsymbol{F}_{S_b} + \boldsymbol{F}_{m_\rho} + \boldsymbol{F}_t + \boldsymbol{\Delta}_\mu \ , \tag{3.25}$$

$$\boldsymbol{F}_\ell = -\int_{\mathcal{V}} \overline{\rho}\tilde{\boldsymbol{\omega}} \times \tilde{\boldsymbol{V}} \, \mathrm{d}\mathcal{V} \ , \tag{3.26}$$

$$\boldsymbol{F}_{S_{far}} = -\int_{S_{far}} \boldsymbol{r} \times \boldsymbol{n} \times \overline{\rho}\tilde{\boldsymbol{\omega}} \times \tilde{\boldsymbol{V}} \, \mathrm{d}S \ , \tag{3.27}$$

$$\boldsymbol{F}_{S_b} = -\int_{S_b} \boldsymbol{r} \times \boldsymbol{n} \times \overline{\rho}\tilde{\boldsymbol{\omega}} \times \tilde{\boldsymbol{V}} \, \mathrm{d}S \ , \tag{3.28}$$

$$\boldsymbol{F}_{m_\rho} = -\int_{\mathcal{V}} \widetilde{\boldsymbol{m}_\rho} \, \mathrm{d}\mathcal{V} \ , \tag{3.29}$$

$$\boldsymbol{F}_t = -\int_{\mathcal{V}} \boldsymbol{r} \times \boldsymbol{\nabla} \times \overline{\rho} \frac{\partial \tilde{\boldsymbol{V}}}{\partial t} \, \mathrm{d}\mathcal{V} \ , \tag{3.30}$$

$$\boldsymbol{\Delta}_{\mu t} = \int_{S_{far}} \boldsymbol{r} \times \boldsymbol{n} \times \boldsymbol{\nabla} \cdot (\boldsymbol{\tau}_{vt} + \boldsymbol{\tau}_R) \, \mathrm{d}S + \int_{S_{far}} \boldsymbol{n} \cdot (\boldsymbol{\tau}_{vt} + \boldsymbol{\tau}_R) \, \mathrm{d}S + \int_{\mathcal{V}} \boldsymbol{r} \times \boldsymbol{\nabla} \times \boldsymbol{\delta}_{\rho V} \, \mathrm{d}\mathcal{V} \ . \tag{3.31}$$

The last term in equation (3.31) can be assumed negligible, considering the Morkovin hypothesis ([67], page 228). Throughout the dissertation the quantity $\tilde{\boldsymbol{\omega}} \times \tilde{\boldsymbol{V}}$ will be denoted as $\boldsymbol{\ell}^*$.

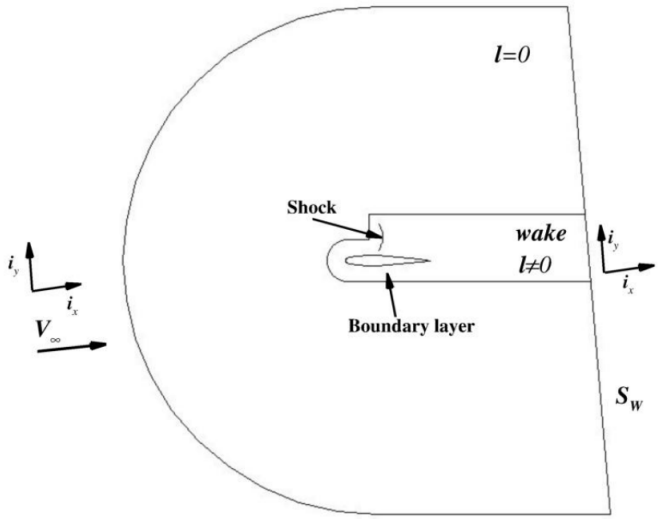

Figure 3.2 Integration domain: S_w definition.

3.3 Analysis of the $\boldsymbol{F}_{S_{far}}$ term

Let us consider the term $\boldsymbol{F}_{S_{far}}$ defined in section 3.1

$$\boldsymbol{F}_{S_{far}} = -\int_{S_{far}} \boldsymbol{r} \times \boldsymbol{n} \times \rho \boldsymbol{\ell} \, \mathrm{d}S \ . \tag{3.32}$$

When boundary layer hypothesis can be applied, $\boldsymbol{F}_{S_{far}}$ is a wake integral, since the Lamb vector is 0 on the lateral surface of the volume $\mathcal{V}$. Integration can be thus limited to the surface S_w, defined in figure 3.2, orthogonal to the freestream direction.

The x-component and y-component of $\boldsymbol{F}_{S_{far}}$ are

$$\boldsymbol{F}_{S_{far}} \cdot \boldsymbol{i}_x = \int_{S_w} (\rho y \ell_y + \rho z \ell_z) \, \mathrm{d}S \ , \tag{3.33}$$

$$\boldsymbol{F}_{S_{far}} \cdot \boldsymbol{i}_y = -\int_{S_w} \rho x \ell_y \, \mathrm{d}S \ . \tag{3.34}$$

The origin of the reference system in these equations is arbitrary. If we move on the wake plane S_w, $\boldsymbol{F}_{S_{far}} \cdot \boldsymbol{i}_y = 0$, i.e. $\boldsymbol{F}_{S_{far}}$ gives no lift contribution, and it is only a drag contribution. This result is valid for an arbitrary choice of the origin of the frame.

Total aerodynamic force formula (3.1) is not dependent on the choice of the origin of the reference frame. On the contrary of his components can be dependent on the origin position. When dealing with steady, incompressible flows, $\boldsymbol{F}_{S_{far}}$ and $\boldsymbol{\Delta}_\mu$ are the only force components depending on $\boldsymbol{r}$; however $\boldsymbol{\Delta}_\mu$ is negligible in moderately high Reynolds number flows (see appendix D). Consequently, $\boldsymbol{F}_{S_{far}}$ also does not depend on the choice of the origin of the frame and the result by which $\boldsymbol{F}_{S_{far}}$ is only a drag contribution is valid for any origin of the frame we choose.

When dealing with compressible flows, the terms depending on $\boldsymbol{r}$ are $\boldsymbol{F}_{S_{far}}$ and $\boldsymbol{F}_{m_\rho}$. If we prove $\boldsymbol{F}_{m_\rho}$ does not depend on the choice of the origin of the frame, the same should hold for $\boldsymbol{F}_{S_{far}}$, since total force is not dependent on it.

Wu et al. proposed a theorem that states a condition by which an integral does not depend on the choosen origin of the frame [51]. Let us call $\mathcal{I}$ a generic integral and $\mathcal{F}$ part of his integrand, multiplied to the position vector by a generic product operation $\circ$. The integral $\mathcal{I}$ is not dependent on the origin of the frame if

$$\mathcal{I}\{(\boldsymbol{x} - \boldsymbol{x}_0) \circ \mathcal{F}\} = \mathcal{I}\{\boldsymbol{x} \circ \mathcal{F}\} \ . \tag{3.35}$$

To be valid identity (3.35), it must be $\mathcal{I}\{\mathcal{F}\} = 0$.

Considering $\mathcal{I} = \boldsymbol{F}_{m_\rho}$, $\mathcal{F}$ is $\boldsymbol{\nabla} \times \rho \boldsymbol{\nabla} \dfrac{V^2}{2}$. Let us focus on $\mathcal{I}\{\mathcal{F}\}$. Applying Gauss' theorem

$$\int_{\mathcal{V}} \boldsymbol{\nabla} \times \left(\rho \boldsymbol{\nabla} \frac{V^2}{2} \right) \mathrm{d}\mathcal{V} = \int_{\partial\mathcal{V}} \boldsymbol{n} \times \left(\rho \boldsymbol{\nabla} \frac{V^2}{2} \right) \mathrm{d}S \ . \tag{3.36}$$

The RHS of equation (3.36) can be decomposed in two contributions A and B on the body surface S_b and on the farfield surface S_{far}:

$$\int_{\partial\mathcal{V}} \boldsymbol{n} \times \left(\rho \boldsymbol{\nabla} \frac{V^2}{2} \right) \mathrm{d}S = \underbrace{\int_{S_{far}} \boldsymbol{n} \times \left(\rho \boldsymbol{\nabla} \frac{V^2}{2} \right) \mathrm{d}S}_{A} + \underbrace{\int_{S_b} \boldsymbol{n} \times \left(\rho \boldsymbol{\nabla} \frac{V^2}{2} \right) \mathrm{d}S}_{B} \ . \tag{3.37}$$

If we consider the identity $\boldsymbol{\nabla}\dfrac{V^2}{2} = \boldsymbol{a} - \boldsymbol{\ell}$, and the hypothesis of steady flow ($\boldsymbol{V}$ is 0 on the body), the integral B is exactly 0.

As concerning A, let us move $S_{far} \to S_\infty$ far infinitely from the body. In these hypothesis the density can be written as the sum of the freestream density ρ_∞ and a perturbation $\Delta\rho$, $\rho = \rho_\infty + \Delta\rho$. Substituting in A

$$\int_{S_{far}} \boldsymbol{n} \times \left(\rho\boldsymbol{\nabla}\frac{V^2}{2}\right) \mathrm{d}S = \rho_\infty \int_{S_{far}} \boldsymbol{n} \times \left(\boldsymbol{\nabla}\frac{V^2}{2}\right) \mathrm{d}S + \int_{S_{far}} \boldsymbol{n} \times \left(\Delta\rho\boldsymbol{\nabla}\frac{V^2}{2}\right) \mathrm{d}S \ . \quad (3.38)$$

Examining the RHS of equation (3.38), the first integral is 0 by applying Gauss' theorem, since it appears the curl of a gradient. The second integral is also 0 provided that $\Delta\rho\boldsymbol{\nabla}\dfrac{V^2}{2} \approx \mathcal{O}\left(\dfrac{1}{r^{2+\epsilon}}\right)$, with $\epsilon > 0$.

Summing up all these results, equation (3.36) is 0 in the hypothesis we move $S_{far} \to S_\infty$ infinitely far from the body. As a consequence, $\boldsymbol{F}_{m_\rho}$ is not dependent on the origin of the frame we choose. Finally, $\boldsymbol{F}_{S_{far}}$ also does not depend on the origin, being only a drag contribution in steady flows.

4

AERODYNAMIC FORCE IN STEADY FLOWS

Contents

The subject of this chapter is the analysis of the aerodynamic force, by means of equation (3.1) in steady flows. In the first part the analysis is focused on the concept of lift-induced drag in compressible flow. Indeed, a rigorous lift-induced drag definition lacks for a real viscous flow. This is an open issue in modern aerodynamics, as stated by Spalart [15]. This dissertation provides an attempt to solve this issue. A new definition of lift-induced drag is here derived and proposed. Application on elliptic wing flows have been performed to validate present lift-induced drag definition, and more generally, to validate the drag breakdown in profile and lift-induced drag component.

The second part of the chapter is dedicated to the resolution of the numerical problems already encountered by Mele and Tognaccini [58] in high transonic flows, discussed in section 2.3.6. A new exact aerodynamic force formula is derived. Furthermore, a first viscous-wave profile drag breakdown by means of Lamb vector surface integrals is proposed. Applications to flows around a NACA 0012 airfoil and around an elliptic wing have been performed in order to validate the new theory. Finally, a first application of present Lamb vector based theory to a transonic aircraft wing-body configuration is discussed.

Finally, a new wave drag definition by volume Lamb vector integrals is proposed and validated through the analysis of the flow around a NACA 0012 airfoil.

4.1 The analysis of three-dimensional compressible steady flows

We assume a compressible and steady high-Reynolds-number flow around a lifting rigid impermeable body in motion at constant speed and symmetric flow. Considering an orthogonal reference system $O(xyz)$ fixed to the body, and with the x axis parallel to the free stream velocity V_∞ (xz is the symmetry plane), $\boldsymbol{V} = [V_\infty + u, v, w]^T$ specifies the local velocity, p is the pressure, and $\boldsymbol{\tau}_v = 2\mu(\boldsymbol{\nabla V})_0^{(s)}$ is the viscous stress tensor ($(\boldsymbol{\nabla V})_0^{(s)}$ is the symmetric deviatoric part of the velocity gradient tensor).

Aerodynamic force exact expression (3.1) in the case of laminar steady flows becomes

$$\boldsymbol{F}_b = -\int_{\mathcal{V}} \left(\rho\boldsymbol{\ell} + \boldsymbol{m}_\rho\right) \mathrm{d}\mathcal{V} - \int_{S_{far}} \boldsymbol{r} \times (\boldsymbol{n} \times \rho\boldsymbol{\ell}) \, \mathrm{dS} + \boldsymbol{\Delta}_\mu \ , \tag{4.1}$$

where

$$\begin{aligned} \boldsymbol{m}_\rho = \boldsymbol{r} \times \left\{ \nabla \times \left[\rho \boldsymbol{\nabla} \left(\frac{V^2}{2} \right) \right] \right\} &= -\boldsymbol{r} \times \left[\nabla \times \left(\frac{V^2}{2} \boldsymbol{\nabla} \rho \right) \right] \\ &= \boldsymbol{r} \times \left[\boldsymbol{\nabla} \rho \times \boldsymbol{\nabla} \left(\frac{V^2}{2} \right) \right] \ . \end{aligned} \tag{4.2}$$

Three equivalent expressions are reported in Eq. (4.2); the first expression is the one already proposed in section 3.1; the last one is more suitable in numerical applications because of the lower order derivatives.

The role of the compressibility correction is better understood in two-dimensional flow taking into account that lift force is also given by [58] $\boldsymbol{F} = \rho_\infty \boldsymbol{V}_\infty \times \int_{\mathcal{V}} \boldsymbol{\omega} \, \mathrm{d}\mathcal{V}$. Therefore, due to vectorial form of Eq. (4.4), $-\int_{\mathcal{V}} \boldsymbol{m}_\rho \, \mathrm{d}\mathcal{V} = \int_{\mathcal{V}} (\rho_\infty \boldsymbol{V}_\infty - \rho \boldsymbol{V}) \times \boldsymbol{\omega} \, \mathrm{d}\mathcal{V}$. Lamb vector describes an interaction between vorticity and momentum: it is the latter which requires a correction to obtain the whole lift in compressible flows.

As already shown in section 2.3.6, equation (4.1) is a midfield formula.

4.1.1 Force breakdown

As in the incompressible case $\boldsymbol{\Delta}_\mu$ can be neglected in high Reynolds number flows, therefore profile drag (as shown in section 3.3, and also including the wave contribution), lift and induced drag are given by:

$$D_{pr} = -\boldsymbol{i}_x \cdot \int_{S_{far}} \boldsymbol{r} \times (\boldsymbol{n} \times \rho \boldsymbol{\ell}) \, \mathrm{dS} \ , \tag{4.3}$$

$$L = -\boldsymbol{i}_z \cdot \int_{\mathcal{V}} \Big(\rho \boldsymbol{\ell} + \boldsymbol{m}_\rho \Big) \, \mathrm{d}\mathcal{V} \ , \tag{4.4}$$

$$D_i = -\boldsymbol{i}_x \cdot \int_{\mathcal{V}} \Big(\rho \boldsymbol{\ell} + \boldsymbol{m}_\rho \Big) \, \mathrm{d}\mathcal{V} \ . \tag{4.5}$$

These equations imply a proposal of breakdown for the aerodynamic force that will be verified in the subsequent sections.

4.1.2 Numerical method

4.1.2.1 Aerodynamic force computation

Aerodynamic force has been computed by the turbulent extension of equation (3.1) proposed in section 3.2, that in steady flows becomes

$$\boldsymbol{F}_b = \boldsymbol{F}_\ell + \boldsymbol{F}_{m_\rho} + \boldsymbol{F}_{S_{far}} \ , \tag{4.6}$$

where

$$\boldsymbol{F}_\ell = -\int_{\mathcal{V}} \overline{\rho}\boldsymbol{\ell}^* \mathrm{d}\mathcal{V} \ , \tag{4.7}$$

$$\boldsymbol{F}_{m_\rho} = -\int_{\mathcal{V}} \widetilde{\boldsymbol{m}}_\rho \, \mathrm{d}\mathcal{V} \ , \tag{4.8}$$

$$\boldsymbol{F}_{S_{far}} = -\int_{S_{far}} \boldsymbol{r} \times \left[\boldsymbol{n} \times \left(\overline{\rho}\tilde{\boldsymbol{\ell}}\right)\right] \, \mathrm{dS} \ . \tag{4.9}$$

where $\boldsymbol{\ell}^* = \tilde{\boldsymbol{\omega}} \times \tilde{\boldsymbol{V}}$, as already discussed in section 3.2. The force coefficients are referenced, as usual, to $\rho_\infty V_\infty^2 S_W/2$, where S_W is the wing area.

$$C_{L_b} = C_{L_\ell} + C_{L_{m_\rho}} \ , \tag{4.10}$$

where C_{L_ℓ}, $C_{L_{m_\rho}}$, are respectively the lift contributions of $\boldsymbol{F}_\ell$ and $\boldsymbol{F}_{m_\rho}$.

The drag coefficient has been computed by

$$C_{D_b} = C_{D_{pr}} + C_{D_i} \ , \tag{4.11}$$

where $C_{D_{pr}}$ is the drag contribution of $\boldsymbol{F}_S$ (the viscous and wave drag) and the here defined lift induced drag coefficient is

$$C_{D_i} = C_{D_\ell} + C_{D_{m_\rho}} \ , \tag{4.12}$$

where C_{D_ℓ} and $C_{D_{m_\rho}}$ are respectively the drag contributions of $\boldsymbol{F}_\ell$ and $\boldsymbol{F}_{m_\rho}$. The near field lift and drag coefficients will be denoted respectively with $C_{L_{nf}}$ and $C_{D_{nf}}$.

The volume integrals in equation (4.6) when dealing with numerical simulations can be computed as

$$\boldsymbol{F}_\ell = -\sum_{i=1}^{N} \left(\overline{\rho}\boldsymbol{\ell}^*\right)_i \Delta\Omega_i; \qquad \boldsymbol{F}_{m_\rho} = -\sum_{i=1}^{N} \left(\widetilde{\boldsymbol{m}}_\rho\right)_i \Delta\Omega_i \ , \tag{4.13}$$

where N is the number of grid cells in the integration domain Ω, $\left(\overline{\rho}\boldsymbol{\ell}^*\right)_i$ and $\left(\widetilde{\boldsymbol{m}}_\rho\right)_i$ are the values in grid cell i of volume $\Delta\Omega_i$, and $\Omega = \Delta\Omega_1 \cup \cdots \cup \Delta\Omega_i \cup \cdots \cup \Delta\Omega_N$. Vorticity components are computed using Green-Gauss' formula, whereas the gradients required in the computation of $\left(\widetilde{\boldsymbol{m}}_\rho\right)_i$ are obtained applying Gauss' formula. The modified position vector $\boldsymbol{r}$ of the grid cell i is computed by

$$\boldsymbol{r}_i = \frac{1}{d-1} \frac{\sum_{k=1}^{24} \boldsymbol{x}_{tet_k} \quad \Delta\Omega_{tet_k}}{\Delta\Omega_i} \ , \tag{4.14}$$

where the subscript tet_k specifies one of the 24 tetrahedrons in which the hexahedron is partitioned, $\Delta\Omega_{tet_k}$ is the volume of the k-th tetrahedron and $\boldsymbol{x}_{tet_k}$ is the position vector of the center of the k-th tetrahedron, obtained averaging the position vectors of its vertices. The surface integral has been computed as

$$\boldsymbol{F}_{S_{far}} = -\sum_{j=1}^{M} \boldsymbol{r}_j \times \left[\boldsymbol{n}_j \times \left(\overline{\rho}\boldsymbol{\ell}^*\right)_j\right] \Delta S_j \ , \tag{4.15}$$

where M is the number of grid cell faces building-up S_{far}, $\left(\overline{\rho}\boldsymbol{\ell}^*\right)_j$ is the value on the grid cell face j of area ΔS_j computed averaging adjacent cell center values, $\boldsymbol{n}_j$ is the normal vector of the j-th face, and $\boldsymbol{r}_j$ has been computed by

$$\boldsymbol{r}_j = \frac{1}{d-1} \frac{\sum_{k=1}^{2} \boldsymbol{x}_{tri_k} \quad \Delta S_{tri_k}}{\Delta S_j} \ , \tag{4.16}$$

where the subscript tri_k points to the triangles in which the quadrilateral face is partitioned, ΔS_{tri_k} is the area of the k-th triangle and $\boldsymbol{x}_{tri_k}$ is the position vector of the center

of the k-th triangle, obtained averaging the position vector values of its vertices.

4.1.3 Application: elliptic wing flow

Three-dimensional steady RANS CFD simulations of a flow around an elliptic wing have been performed by the standard flow solver FLOWer developed at DLR (the German Aerospace Center) and widely used both in the industry and for applied research [68]. The FLOWer code solves the compressible three-dimensional steady and unsteady RANS equations on block-structured meshes. The spatial discretization adopted is a central or AUSM finite volume formulation with explicit blended 2nd and 4th order artificial dissipation. Time integration is carried out by an explicit hybrid multistage Runge-Kutta scheme. Very low Mach number calculations are possible via preconditioning. Turbulence is modeled by either algebraic or transport equation models. The $k-\omega$ SST (Shear Stress Transport) turbulence model assuming a completely turbulent flow has been here applied. Different turbulence models have been tested finding negligible effect on the accuracy of the proposed aerodynamic force formula.

Post-processing has been performed by an unstructured force decomposition software, BreakForce, currently in development at the Department of Industrial Engineering of University of Naples Federico II, by the research group in which the author is active, and with the contribution of the author himself. This code takes as input unstructured steady CFD solutions in the CFD General Notation System (CGNS, [69]), which is a standard format in the aeronautical industry, developed by a joint effort between Boeing and NASA. As output, the code returns the full force breakdown by present method, the viscous/wave profile drag breakdown by Paparone and Tognaccini method [6], and Maskell's lift-induced drag [23].

The flow solutions have been converted from structured data to unstructured data, with a FLOWer-CGNS converter, in order to obtain the input to BreakForce to compute the force breakdown.

The adopted geometry and grid are the same used by Marongiu et al. [55]. The wing aspect ratio is $\mathcal{AR} = 7$ and the wing section is the NACA 0012 airfoil. The elliptic wing

planform has been chosen in such a way to obtain a straight trailing edge, see Fig. 4.22. The grid topology is C-C type structured in two blocks. The far-field is located 30 root chords from the body. The grid is made of more than 3 million cells with 384×64 cells over the wing, 64 cells along the wake, 96 cells in the direction normal to the wing. Very strict convergence has been obtained in all CFD calculations, with the L_2-norm of the residual of the continuity equation reduced to 10^{-8} times the initial residual.

Calculations were performed at different angles of attack and free stream Mach numbers, with Reynolds number $Re_\infty = 3 \cdot 10^6$. Fig. 4.22 shows the pressure coefficient distribution on the upper surface of the wing and at four wing sections computed at $M_\infty = 0.75$ and $\alpha = 4°$, which is the transonic test which produced the strongest shock wave.

4.1.3.1 Influence of the integration domain

The integration domain is identified by two grid coordinates in the symmetry plane of the wing as shown in Fig. 4.2 (x_s and z_s are referenced to the root chord). S_{far} is given by $S_{far} = \Sigma_I \cup \Sigma_J$, where Σ_I and Σ_J are grid surfaces, defined respectively by a constant i and k values.

In Figs. 4.3 and 4.4 the results obtained by varying x_s and z_s are proposed for $M_\infty = 0.5$, $\alpha = 4°$. The figures show that Eq. (4.6) correctly computes both lift and drag coefficients with a weak sensitivity to the selected integration domain provided that the whole boundary layer is contained in Ω. In particular Figs. 4.3 (b) and 4.4 (b) also show that, as discussed by Marongiu and Tognaccini [56], the viscous term $\boldsymbol{\Delta}_\mu$ can not be neglected in Eq. (4.1) if Ω is smaller than the physical boundary layer.

Fig. 4.4(a) shows that in the near wake, a reduction of $C_{D_{pr}}$ is compensated by an increase of C_{D_ℓ}. In Eq. (4.1) the choice of Ω is arbitrary. However the correct breakdown is theoretically obtained with infinite Ω. Clearly this is not possible in practice, and so we expect a variation of the breakdown with the choice of Ω. The obtained maximum value of $C_{D_\ell} + C_{D_{m_\rho}}$ (with $x_s \approx 3$) is the lift-induced drag. $\boldsymbol{\ell}$ and $\boldsymbol{m}_\rho$ contribute to $\boldsymbol{F}_b$ in the near wake only, because ρ quickly becomes constant, and the contribution of the

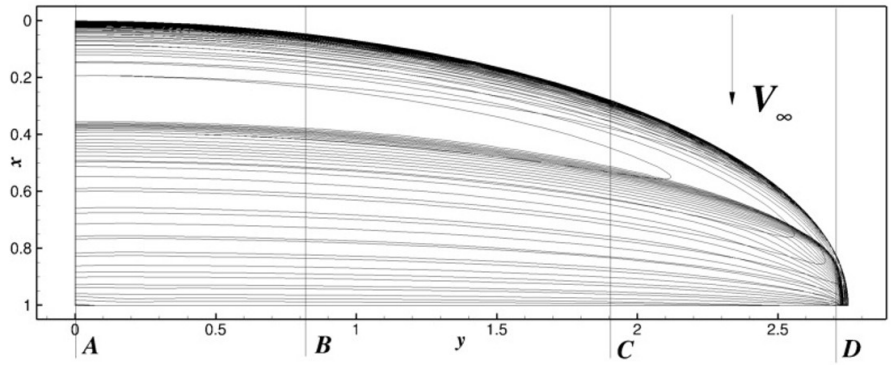

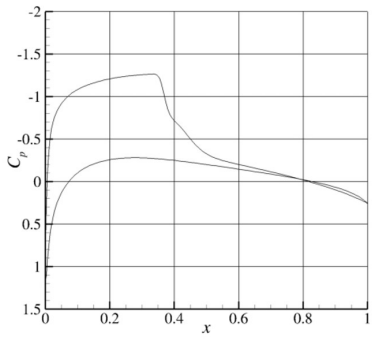

(a) Section A: $y/(b/2) = 0$

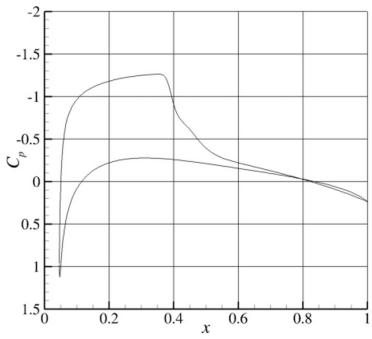

(b) Section B: $y/(b/2) = 0.3$

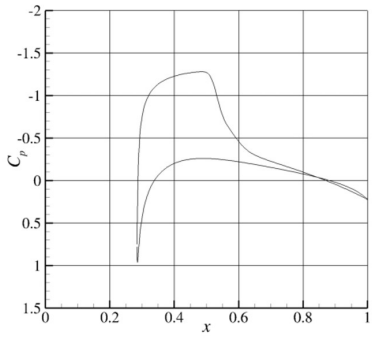

(c) Section C: $y/(b/2) = 0.7$

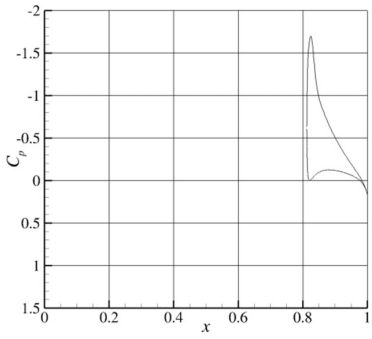

(d) Section D: $y/(b/2) = 0.98$

Figure 4.1 Elliptic wing. $M_\infty = 0.75$, $Re_\infty = 3 \cdot 10^6$, $\alpha = 4$. Iso-contours ($\Delta C_p = 0.05$) on the upper wing and pressure coefficient distributions at 4 wing stations.

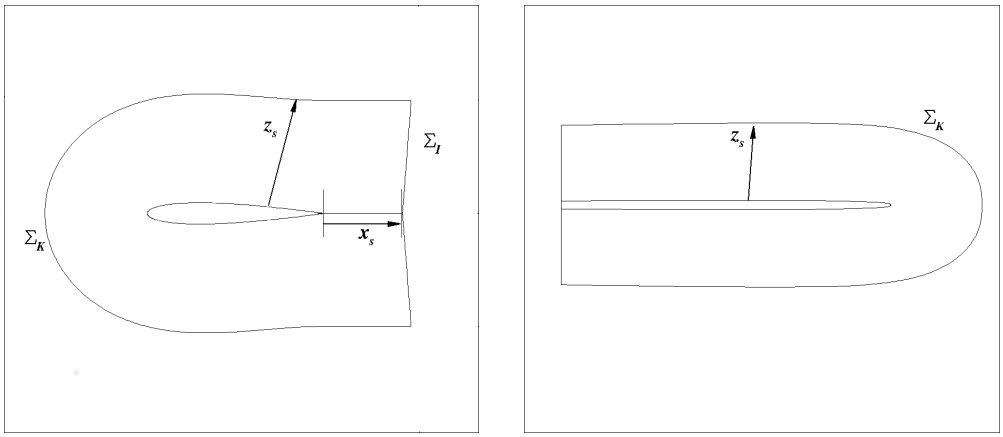

Figure 4.2 Elliptic wing. Definition of the integration domain.

vortex force in the far wake is negligible due to the symmetry of the boundary layer.

The variations of C_{D_ℓ}, that can be noted for larger values of x_s, are a numerical effect, the same behaviour observed in the incompressible case by Marongiu et al.[55], i.e. a conversion of lift induced drag in viscous drag due to the non physical *numerical* dissipation of the kinetic energy of the free vortices in internal energy.

The same analysis for a transonic test is proposed in Figs. 4.5 and 4.6. In this case also, both lift and drag are correctly computed. Again a weak sensitivity to the selected integration domain is achieved if the whole boundary layer and now also the wake of the shock wave are contained in Ω. In fact, a contribution to $\boldsymbol{F}_\ell$ in the shock wave wake should be taken in account, due to the curved shock-induced vorticity.

A grid sensitivity analysis is shown in Fig. 4.7. RANS calculations were performed on three successively refined grids (h = 1 specifies the finest level used). The computed force coefficients are plotted against mesh average size, showing that they converge while reducing the mesh size, with larger variations obtained for the drag coefficient.

The volume integrals in Eq. (4.6)allow to identify in which regions of the flow the aerodynamic force is generated.

In Fig. 4.8 the results for a subsonic test are shown ($x_s = -1$ specifies empty integration domain). The whole lift is obtained in practice with $x_s = 0$, implying that the contribution of the wake to the volume integrals is negligible. With $x_s = 0$, the total

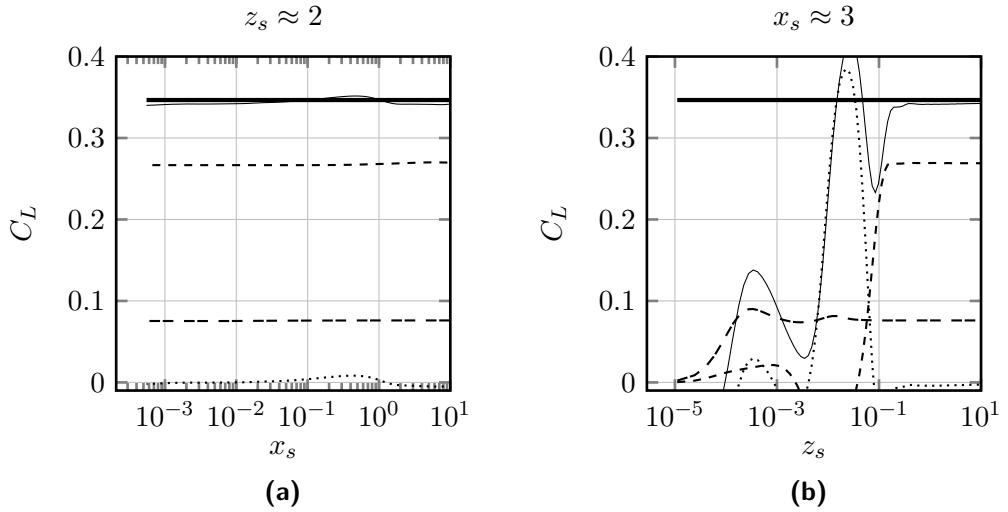

Figure 4.3 Elliptic wing, $M_\infty = 0.5$, $Re_\infty = 3 \cdot 10^6$, $\alpha = 4°$. Influence of domain of integration on lift coefficient. ▬: $C_{L_{nf}}$. —: C_{L_b}. − − −: C_{L_ℓ}. − − ——: $C_{L_{m_\rho}}$. ⋯: $C_{L_{S_{far}}}$.

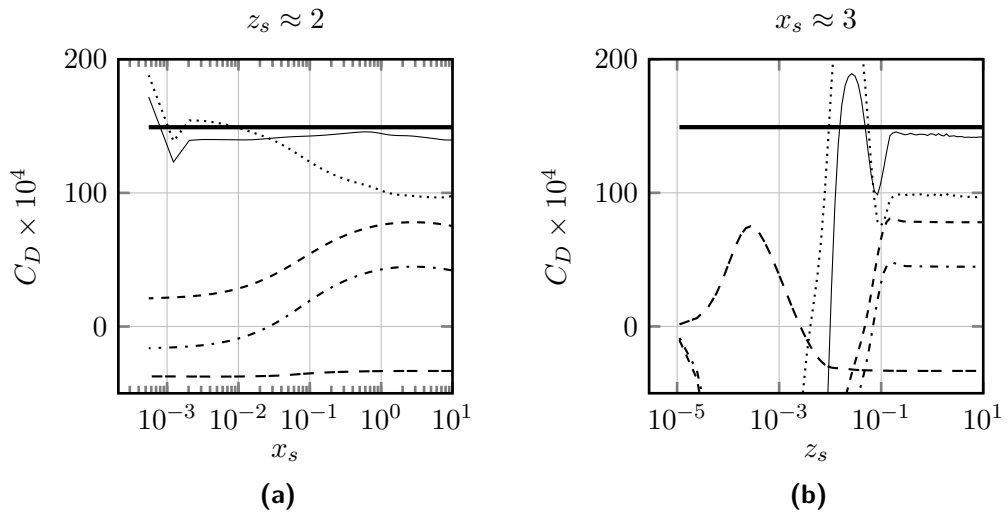

Figure 4.4 Elliptic wing, $M_\infty = 0.5$, $Re_\infty = 3 \cdot 10^6$, $\alpha = 4°$. Influence of domain of integration on drag coefficient. ▬: $C_{D_{nf}}$. —: C_{D_b}. − − −: C_{D_ℓ}. − − ——: $C_{D_{m_\rho}}$. ⋯: $C_{D_{pr}}$. − · −: C_{D_i}.

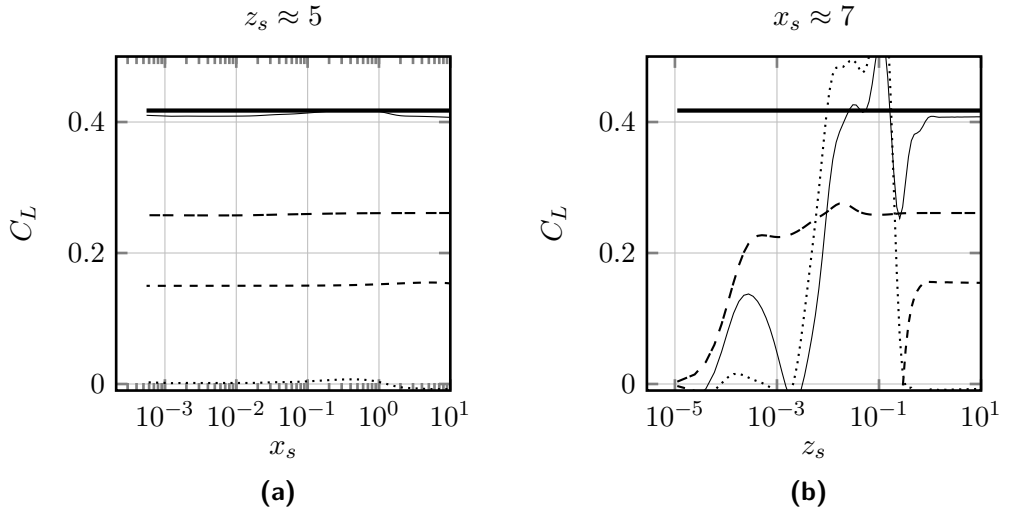

Figure 4.5 Elliptic wing, $M_\infty = 0.75$, $Re_\infty = 3 \cdot 10^6$, $\alpha = 4°$. Influence of domain of integration on lift coefficient. ▬: $C_{L_{nf}}$. —: C_{L_b}. − − −: C_{L_ℓ}. − − ——: $C_{L_{m_\rho}}$. ⋯: $C_{L_{S_{far}}}$.

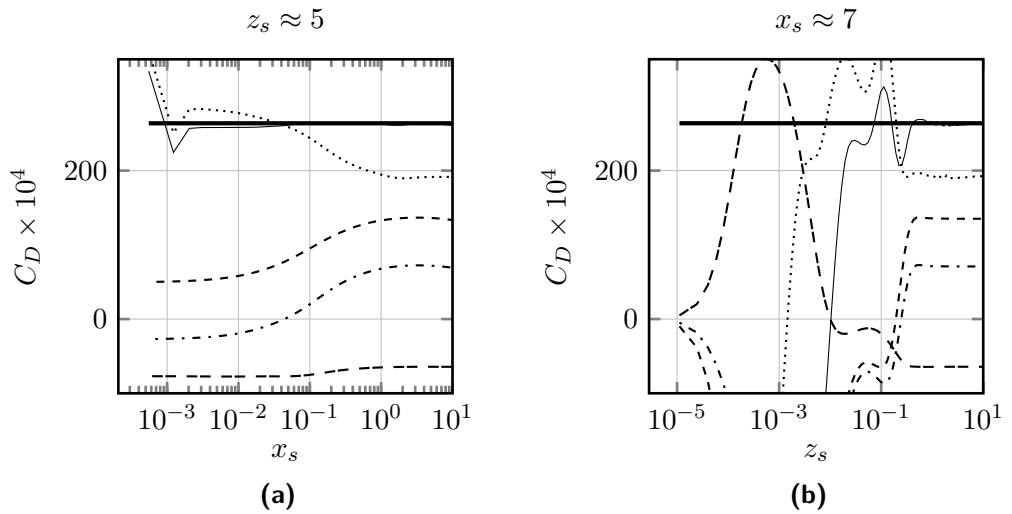

Figure 4.6 Elliptic wing, $M_\infty = 0.75$, $Re_\infty = 3 \cdot 10^6$, $\alpha = 4°$. Influence of domain of integration on drag coefficient. ▬: $C_{D_{nf}}$. —: C_{D_b}. − − −: C_{D_ℓ}. − − ——: $C_{D_{m_\rho}}$. ⋯: $C_{D_{pr}}$. − · −: C_{D_i}.

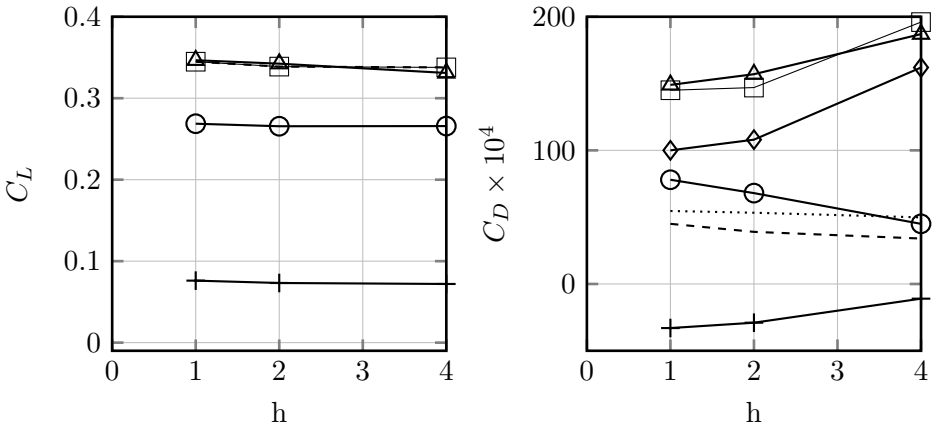

Figure 4.7 Elliptic wing, $M_\infty = 0.5$, $Re_\infty = 3 \cdot 10^6$, $\alpha = 4°$. Grid convergence analysis. ━△━: $\boldsymbol{F}_{nf}$. —□—: $\boldsymbol{F}_b$. — ∘ —: $\boldsymbol{F}_\ell$. — + —: $\boldsymbol{F}_{m_\rho}$. — ⋄ —: $\boldsymbol{F}_S$, — — —: $\boldsymbol{F}_\ell + \boldsymbol{F}_{m_\rho}$, ⋯: $C_L^2/(\pi \mathcal{AR})$.

drag is also correctly computed, but it is obtained by $C_{D_{pr}}$ only, whereas C_{D_ℓ} and $C_{D_{m_\rho}}$ cancel each other. However Fig. 4.8(b) shows that for $x_s > 0$ $C_{D_i} = C_{D_\ell} + C_{D_{m_\rho}}$ approaches $C_L^2/(\pi \mathcal{AR})$, the lift-induced drag coefficient of classical elliptic wing theory; $C_{D_{pr}}$ decreases, but C_{D_i} increases, then the sum $C_{D_{pr}} + C_{D_i}$ still gives the reference total near field drag. This result suggests that the lift-induced drag is essentially generated by the Lamb vector field in the boundary layer of the very near wake.

The analysis has been completed by limiting the integration just to the boundary layer and near wake, selecting the domain of integration by an appropriate *boundary layer numerical sensor*, as discussed by Lanzetta et al.[29]. In this way the sensitivity to the x_s position is further reduced. Table 4.1 presents the computed force coefficients for the subsonic test, limiting the integration to the wing boundary layer (Ω_{bl}), visualized in the wing symmetry plane in Fig. 4.9. As anticipated, total lift is almost completely captured in Ω_{bl}, whereas total drag is given by the surface integral ($C_{D_{pr}}$). Fig. 4.10 shows the computed drag coefficients C_{D_ℓ}, $C_{D_{m_\rho}}$ and $C_{D_i} = C_{D_\ell} + C_{D_{m_\rho}}$ limiting the integration to the wake ($0 < x < x_s$). The figure confirms that the lift-induced drag can

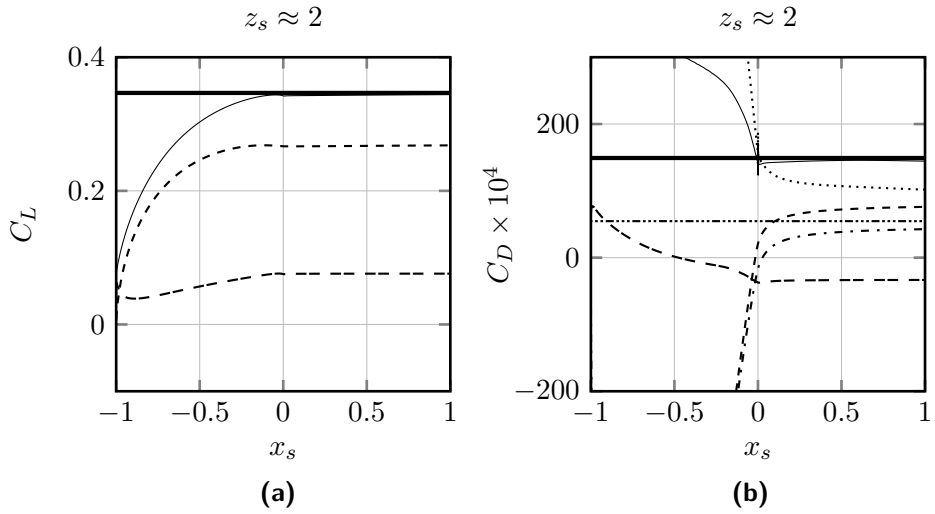

Figure 4.8 Elliptic wing, $M_\infty = 0.5$, $Re_\infty = 3{\cdot}10^6$, $\alpha = 4°$. Analysis of force contributions generation. $x_s = -1$: position of wing leading edge, $x_s = 0$: position of the wing trailing edge. ▬: $\boldsymbol{F}_{nf}$. —: $\boldsymbol{F}_b$. − − −: $\boldsymbol{F}_\ell$. − − ——: $\boldsymbol{F}_{m_\rho}$. ⋯: $\boldsymbol{F}_{S_{far}}$. − · −: C_{D_i} − ⋯ −: $C_L^2/(\pi \mathcal{AR})$.

C_{L_ℓ}	$C_{L_{m_\rho}}$	C_{L_b}	$C_{L_{nf}}$	C_{D_ℓ}	$C_{D_{m_\rho}}$	$C_{D_{pr}}$	C_{D_b}	$C_{D_{nf}}$
0.2638	0.0755	0.3393	0.3466	0.0038	-0.0038	0.0149	0.0149	0.0149

Table 4.1 Elliptic wing, $M_\infty = 0.5$, $Re_\infty = 3 \cdot 10^6$, $\alpha = 4$. Force coefficients contributions computed in Ω_{bl} (see Fig. 4.9).

also be obtained by

$$D_i = -\boldsymbol{i}_x \cdot \int_{\Omega_\mathrm{w}} (\overline{\rho}\boldsymbol{\ell}^* + \widetilde{\boldsymbol{m}}_\rho)\, \mathrm{d}\Omega \ , \tag{4.17}$$

where Ω_w is the near wake of the wing. The main part of induced drag is given by the Lamb vector, however $\boldsymbol{m}_\rho$ contribution still produces a few drag counts.

4.1.4 Lift-drag polar curves

The polar curves computed at different Mach numbers are shown in Fig. 4.11. Higher transonic regimes have not been shown here. They presented the same numerical issues found by Mele and Tognaccini [58], shown in section 2.3.6. The solution to these issues,

Figure 4.9 Elliptic wing, $M_\infty = 0.5$, $Re_\infty = 3 \cdot 10^6$, $\alpha = 4$. Symmetry plane. Selected boundary layer region.

and the relative high transonic lift-drag polars will be discussed in section 4.2 The integration domain has been limited to the boundary layer and shock wave wake with the boundary layer automatically selected. The nearly incompressible case ($M_\infty = 0.01$), already presented[55], is also proposed for comparison. At all Mach numbers Eq. (4.6) is in very good agreement with the near field result. The transonic tests were limited to $\alpha \leq 4°$ due to the appearance of unsteady phenomena (buffet).

It is interesting to note the agreement of present definition of lift-induced drag Eq. (4.12) with the reference analytical expression ($C_{D_i} = C_L^2/(\pi \mathcal{AR})$), which is not obvious even in transonic flow. As expected, $C_{D_{pr}}$ is weakly influenced by the angle of attack in the subsonic tests, but it significantly increases with the onset of strong shocks, because of the appearance of the wave drag. C_{D_0} (zero-lift drag coefficient) is almost constant if the flow remains subsonic. In Fig. 4.12 the polar curves for $M_\infty = 0.5$ and $M_\infty = 0.75$ are reported in the plane C_D vs C_L^2. Considering [70] $C_D = C_{D_0} + \Delta C_D(C_L) + C_L^2/(\pi e \mathcal{AR})$,

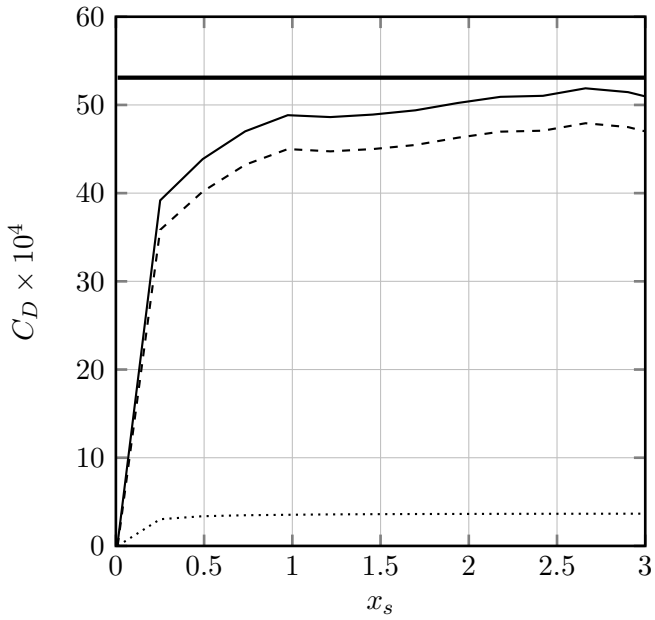

Figure 4.10 Elliptic wing, $M_\infty = 0.5$, $\alpha = 4$, $Re_\infty = 3 \cdot 10^6$. Lift-induced drag coefficient contributions computed in Ω_W. — — —: C_{D_ℓ}. $\cdots$: $C_{D_{m_\rho}}$. —: C_{D_i}. ▬: $C_L^2/(\pi \mathcal{AR})$.

with e being the span efficiency, Fig. 4.12 highlights the quadratic behavior of the profile drag ($C_{D_{pr}} = C_{D_0} + \Delta C_D(C_L)$) in the subsonic test. Lifting line theory results for $e = 1$ still hold for both high subsonic and transonic regime.

4.1.4.1 Effect of the free stream Mach number

The effect of the free stream Mach number on the computed force breakdown is proposed in Fig. 4.13 at $\alpha = 4°$ respectively for lift (a) and drag (b). Increasing M_∞, the vortex force contribution to lift decreases but it is compensated by the compressibility correction. $\boldsymbol{F}_{m_\rho}$ provides a thrust term increasing as M_∞ increases which is balanced by the drag due to the vortex force, in agreement with the 2-D computations by Mele and Tognaccini [58]. These opposite forces arise in the wing boundary layer.

The lift behavior in a subsonic flow is ruled by well known similitudes, for instance by the simple Prandtl-Glauert correction $C_L = C_{L_0}/\beta$, where C_{L_0} is the lift coefficient

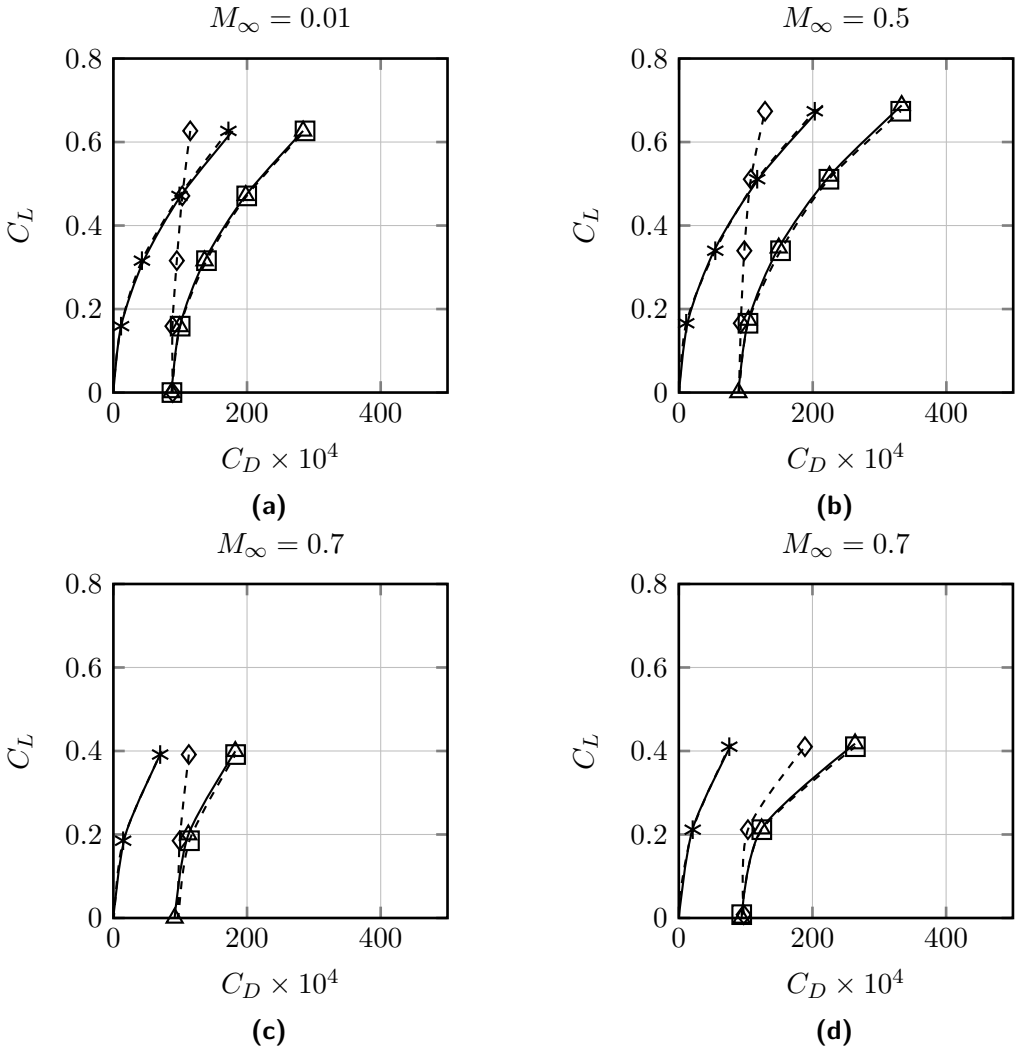

Figure 4.11 Elliptic wing, $Re_\infty = 3 \cdot 10^6$. Computed lift-drag polars. $-\triangle-$: reference near field. $--\square--$: $C_{L_b} = C_{L_b}(C_{D_b})$. $-- * --$: $C_{L_b} = C_{L_b}(C_{D_i})$. $-- \diamond --$: $C_{L_b} = C_{L_b}(C_{D_{pr}})$. $---$: $C_L^2/(\pi \mathcal{AR})$.

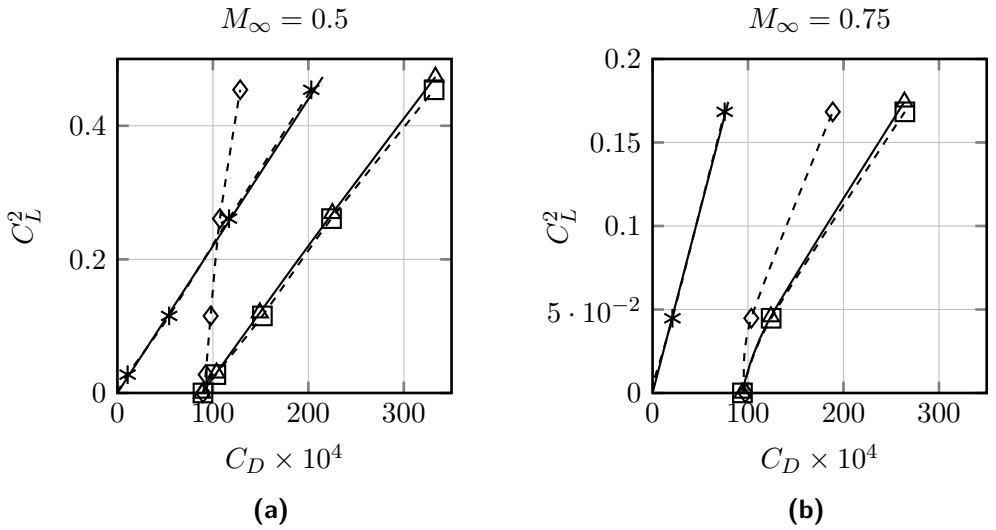

Figure 4.12 Elliptic wing, $Re_\infty = 3 \cdot 10^6$. Computed C_D vs C_L^2 polars. $-\triangle-$: reference near field. $--\square--$: $C_{L_b} = C_{L_b}(C_{D_b})$. $-- * --$: $C_{L_b} = C_{L_b}(C_{D_i})$. $-- \diamond --$: $C_{L_b} = C_{L_b}(C_{D_{pr}})$. ——: $C_L^2/(\pi \mathcal{AR})$.

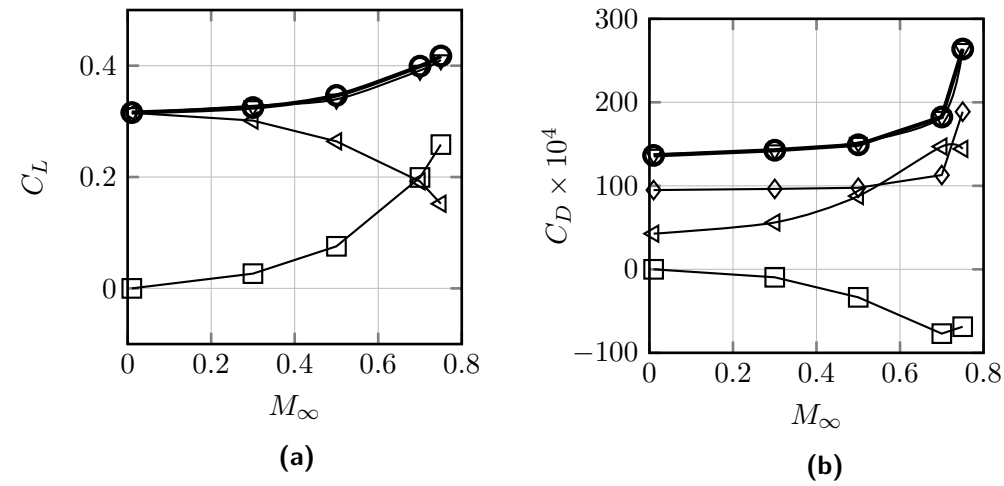

Figure 4.13 Elliptic wing, $Re_\infty = 3 \cdot 10^6$, $\alpha = 4°$. Computed lift (a) and drag (b) coefficient versus Mach number. ━○━: $\boldsymbol{F}_{nf}$. $-\triangledown-$: $\boldsymbol{F}_{bc}$. $-\triangleleft-$: $\boldsymbol{F}_{\ell}$. $-\square-$: $\boldsymbol{F}_{m_{\rho c}}$. $-\diamond-$: $\boldsymbol{F}_S$.

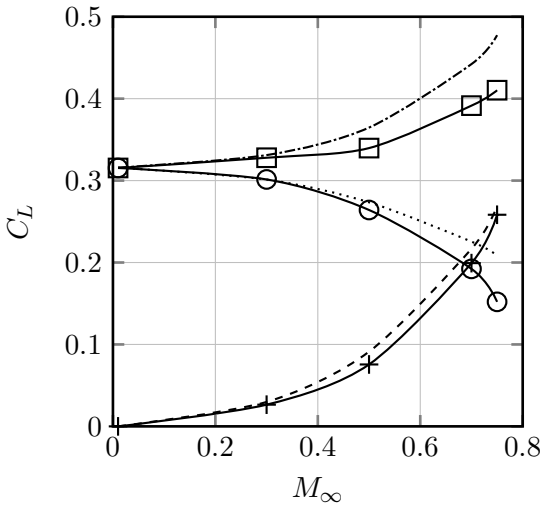

Figure 4.14 Elliptic wing, $Re_\infty = 3 \cdot 10^6$, $\alpha = 4°$. Scaling laws. Comparison with numerical results. . $-\square-$: $C_{L_\ell} + C_{L_{m_\rho}}$. $-\circ-$: C_{L_ℓ}, $-+-$: $C_{L_{m_\rho}}$, $\cdots$: C_{L_ℓ} scale law, $---$: $C_{L_{m_\rho}}$ scale law, $-\cdot-$: $C_{L_\ell} + C_{L_{m_\rho}}$ scale laws.

at $M_\infty = 0$, and $\beta = \sqrt{1 - M_\infty^2}$. Fig. 4.13 (a) suggests

$$C_{L_\ell} = C_{L_0}\beta \ . \tag{4.18}$$

Therefore, since $C_{L_\ell} + C_{L_{m_\rho}} = C_{L_0}/\beta$:

$$C_{L_{m_\rho}} = C_{L_0}\frac{(1-\beta^2)}{\beta} \ . \tag{4.19}$$

These equations are plotted in Fig. 4.14 showing a good agreement of the computed C_{L_ℓ} and $C_{L_{m_\rho}}$ with the suggested Mach number scaling as far as the Prandtl-Glauert rule is correct.

The breakdown of the lift induced drag is detailed in Fig. 4.15 for different Mach numbers.

The curves $C_L = C_L(\alpha)$ at $M_\infty = 0.5$ and $M_\infty = 0.75$ are proposed in Fig. 4.16. $C_{L_{m_\rho}}$ is greater than C_{L_ℓ} at the higher Mach number test.

In addition, despite of the linear behavior of the total lift, both the vortex force and

the compressibility correction have a non linear trend.

4.2 A new robust formula for compressible flows

Eq. (4.6) revealed not accurate when applied to high transonic and supersonic flows, as already shown in section 2.3.6 in case of two-dimensional flow.

Such numerical difficulties can be ascribed to the loss of accuracy of the flow solution in the shock wave region increasing with the Mach number approaching one. In what follows an alternative formula is proposed to overcome this problem. Let us begin from the compressible aerodynamic force formula derived by Wu et al. [51], already proposed in section 2.3.5 and here rewritten in the steady case as

$$\boldsymbol{F} = \boldsymbol{F}_{\ell} + \boldsymbol{F}_{m_\rho} + \boldsymbol{F}_{S_{far}} + \boldsymbol{\Delta}_{\mu} \tag{4.20}$$

where $\boldsymbol{F}_{m_\rho}$ is here defined as

$$\boldsymbol{F}_{m_\rho} = \int_{\mathcal{V}} \frac{V^2}{2} \boldsymbol{\nabla}\rho \, \mathrm{d}\mathcal{V} \tag{4.21}$$

The application of identities $V^2/2\boldsymbol{\nabla}\rho = \boldsymbol{\nabla}(\rho V^2/2) - \rho\boldsymbol{\nabla}\left(V^2/2\right)$ and $\rho\boldsymbol{\ell} + \rho\boldsymbol{\nabla}(V^2/2) = \rho\boldsymbol{V}\cdot\boldsymbol{\nabla}\boldsymbol{V}$, to equation (4.20), leads to:

$$\begin{aligned} \boldsymbol{F} = -\int_{\mathcal{V}} \rho\boldsymbol{V}\cdot\boldsymbol{\nabla}\boldsymbol{V}\,\partial\mathcal{V} + \int_{\mathcal{V}} \boldsymbol{\nabla}\left(\rho\frac{V^2}{2}\right)\partial\mathcal{V} + \\ + \int_{S_{far}} \boldsymbol{r}\times\boldsymbol{n}\times\left(\frac{V^2}{2}\boldsymbol{\nabla}\rho\right)\,\mathrm{dS} - \int_{S_{far}} \boldsymbol{r}\times\boldsymbol{n}\times\rho\boldsymbol{\ell}\,\mathrm{dS}\;, \end{aligned} \tag{4.22}$$

then, from the continuity equation, and applying the Gauss theorem to the volume integrals of Eq. (4.22), the following *far-field* formula is obtained:

$$\boldsymbol{F}_c = -\int_{S_{far}} \rho\boldsymbol{V}\boldsymbol{V}\cdot\boldsymbol{n}\,\mathrm{dS} + \int_{S_{far}} \rho\frac{V^2}{2}\boldsymbol{n}\,\mathrm{dS} + \int_{S_{far}} \boldsymbol{r}\times\boldsymbol{n}\times\left(\frac{V^2}{2}\boldsymbol{\nabla}\rho\right)\,\mathrm{dS} - \int_{S_{far}} \boldsymbol{r}\times\boldsymbol{n}\times\rho\boldsymbol{\ell}\,\mathrm{dS}\;. \tag{4.23}$$

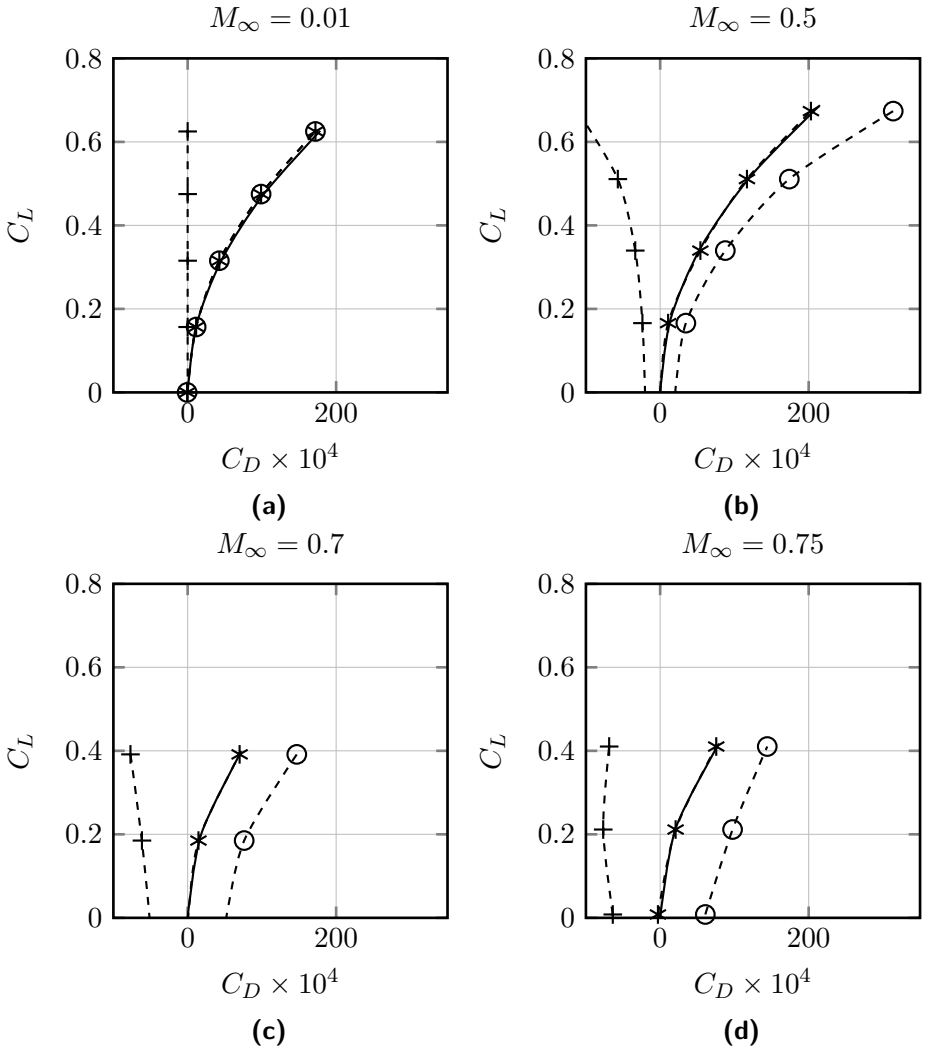

Figure 4.15 Elliptic wing, $Re_\infty = 3 \cdot 10^6$. Breakdown of the lift induced drag. $--*--$: $C_{L_{bc}} = C_{L_{bc}}(C_{D_{i\ell}})$. $--\circ--$: $C_{L_{bc}} = C_{L_{bc}}(C_{D_\ell})$. $--+--$: $C_{L_{bc}} = C_{L_{bc}}(C_{D_{m_{\rho c}}})$. ——: $C_L^2/(\pi \mathcal{AR})$.

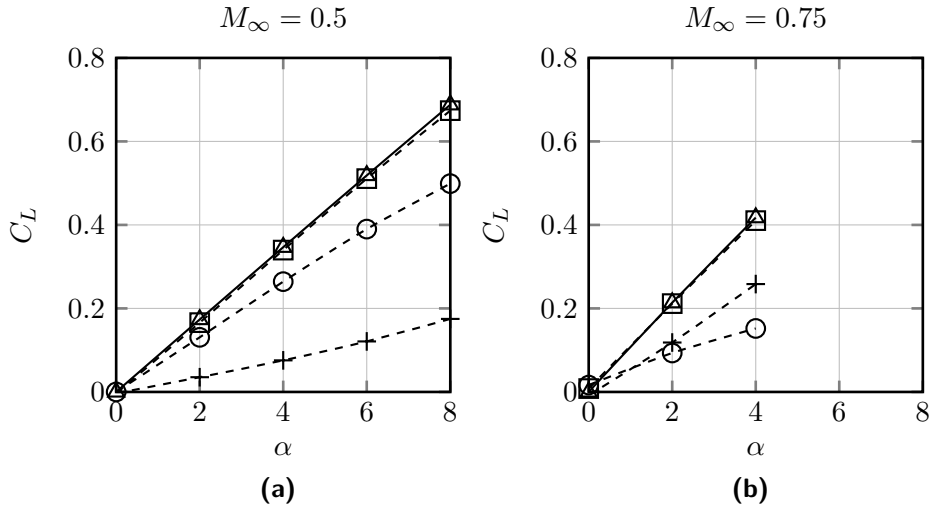

Figure 4.16 Elliptic wing, $Re_\infty = 3 \cdot 10^6$. Breakdown of the lift coefficient. $-\triangle-$: $C_{L_{nf}} = C_{L_{nf}}(\alpha)$. $--\square--$: $C_{L_{bc}} = C_{L_{bc}}(\alpha)$. $-- \circ --$: $C_{L_\ell} = C_{L_\ell}(\alpha)$. $-- + --$: $C_{L_{m_{\rho c}}} = C_{L_{m_{\rho c}}}(\alpha)$.

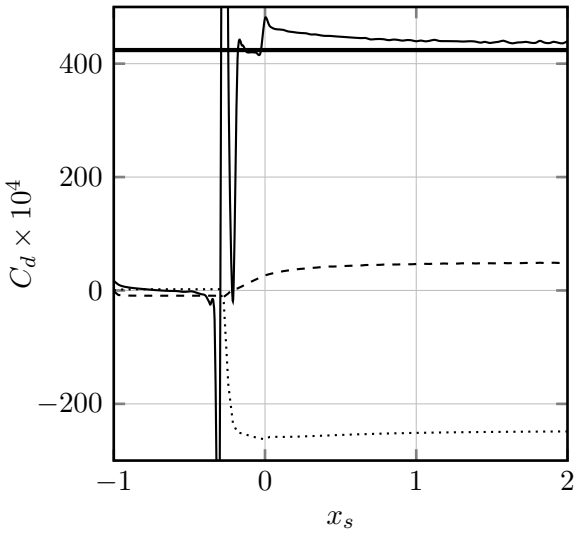

Figure 4.17 NACA 0012, $M_\infty = 0.8$, $\alpha = 2$, Euler flow. Drag coefficient contributions vs x_s. $- - -$: C_{d_ℓ}. $\cdots$: $C_{d_{m_\rho}}$. —: $C_{d_{pr}}$.━: reference near field value.

Eq. (4.23) loses the notable mid-field property (bounded integration domain).

However, if the shock wave region is identified (here denoted as $\mathcal{V}_{sw}$), for instance adopting an appropriate shock sensor [6, 29], then, Eq. (4.1) can be rearranged into:

$$\boldsymbol{F} = -\int\limits_{\mathcal{V}-\mathcal{V}_{sw}} \Big(\rho\boldsymbol{\ell} + \boldsymbol{m}_\rho\Big)\,\mathrm{d}\mathcal{V} - \int\limits_{\mathcal{V}_{sw}} \Big(\rho\boldsymbol{\ell} + \boldsymbol{m}_\rho\Big)\,\mathrm{d}\mathcal{V} - \int\limits_{S_{far}} \boldsymbol{r}\times(\boldsymbol{n}\times\rho\boldsymbol{\ell})\,\mathrm{dS} + \boldsymbol{\Delta}_\mu\ . \quad (4.24)$$

Applying to $\int_{\mathcal{V}_{sw}} \Big(\rho\boldsymbol{\ell} + \boldsymbol{m}_\rho\Big)\,\mathrm{d}\mathcal{V}$ the same steps followed for the derivation of Eq. (4.23), we finally obtain the following *mid-field* formula:

$$\begin{aligned}\boldsymbol{F}_{bc} = &-\int\limits_{\mathcal{V}-\mathcal{V}_{sw}} \Big(\rho\boldsymbol{\ell} + \boldsymbol{m}_\rho\Big)\,\mathrm{d}\mathcal{V} - \int\limits_{S_{far}} \boldsymbol{r}\times(\boldsymbol{n}\times\rho\boldsymbol{\ell})\,\mathrm{dS} + \boldsymbol{\Delta}_\mu \\ &- \int\limits_{\partial\mathcal{V}_{sw}} \rho\boldsymbol{V}\boldsymbol{V}\cdot\boldsymbol{n}\,\mathrm{dS} + \int\limits_{\partial\mathcal{V}_{sw}} \rho\frac{V^2}{2}\boldsymbol{n}\,\mathrm{dS} + \int\limits_{\partial\mathcal{V}_{sw}} \boldsymbol{r}\times\boldsymbol{n}\times\left(\frac{V^2}{2}\boldsymbol{\nabla}\rho\right)\,\mathrm{dS}.\end{aligned} \quad (4.25)$$

This equation can be rearranged as

$$\boldsymbol{F}_{bc} = \boldsymbol{F}_\ell + \boldsymbol{F}_{m_{\rho c}} + \boldsymbol{F}_{S_{far}}\ , \quad (4.26)$$

where $\boldsymbol{F}_\ell$ and $\boldsymbol{F}_{S_{far}}$ are defined as before and

$$\begin{aligned}\boldsymbol{F}_{m_{\rho c}} = &-\int\limits_{\mathcal{V}-\mathcal{V}_{sw}} \boldsymbol{m}_\rho\,\mathrm{d}\mathcal{V} - \int\limits_{\partial\mathcal{V}_{sw}} \rho\boldsymbol{V}\boldsymbol{V}\cdot\boldsymbol{n}\,\mathrm{dS} + \\ &+ \int\limits_{\partial\mathcal{V}_{sw}} \rho\frac{V^2}{2}\boldsymbol{n}\,\mathrm{dS} + \int\limits_{\partial\mathcal{V}_{sw}} \boldsymbol{r}\times\boldsymbol{n}\times\left(\frac{V^2}{2}\boldsymbol{\nabla}\rho\right)\,\mathrm{dS} + \int\limits_{\mathcal{V}_{sw}} \rho\boldsymbol{\ell}\,\mathrm{d}\mathcal{V}.\end{aligned} \quad (4.27)$$

Equation (4.25) preserves the property of bounded integration domain of the original formula (4.23) and it avoids integration of $\boldsymbol{m}_\rho$ inside the shock wave region where numerical accuracy is first order at most. Equations (4.23) and (4.25) can be extended to turbulent flows similarly to the original formulation such as described in the previous section; Eq. (4.27) still holds, if the instantaneous velocity is replaced by its Favre average.

4.3 Viscous-wave drag breakdown

$\boldsymbol{F}_{S_{far}}$ provides the whole profile drag, but, in case of transonic flow, its breakdown in viscous and wave components is not trivial. The contribution to $\boldsymbol{F}_{S_{far}}$ is only obtained in the wake (the region where $\boldsymbol{\ell} \neq 0$) and a straightforward choice could consist in separating the integration in the contribution due to the intersection of the S_{far} with the boundary layer and with the shockwave wakes.

However this breakdown depends on the position of the chosen integration surface. Indeed, as the integration surface is moved downstream, while preserving the total drag value, higher viscous and lower wave drag are obtained, due to the flow entrainment of the boundary layer. In particular, sufficiently downstream only viscous drag would be obtained due to the theoretically infinite thickening of the boundary layer wake.

Therefore, here it is proposed to *define* the wave drag in a real flow as:

$$D_w = -\boldsymbol{i}_x \cdot \int_{W_{sw}} \boldsymbol{r} \times [\boldsymbol{n} \times (\overline{\rho}\boldsymbol{\ell}^*)] \, \mathrm{dS} \ , \tag{4.28}$$

where W_{sw} specifies a surface of general shape intersecting the shock wave wake and positioned just downstream of the shock (see Fig. 4.18). The *indirect* definition of viscous drag follows:

$$D_v = -\boldsymbol{i}_x \cdot \boldsymbol{F}_{S_{far}} - D_w \ , \tag{4.29}$$

It is worth to remark that the present viscous-wave breakdown, whose application will be discussed in the next sections, could lead to some discrepancies in wave drag estimation with respect to the previous definitions of wave drag.

Completing the force breakdown defined by Eq. (4.26), lift and lift induced drag are:

$$L = \boldsymbol{i}_z \cdot \left(\boldsymbol{F}_\ell + \boldsymbol{F}_{m_{\rho c}}\right) \ , \tag{4.30}$$

$$D_i = \boldsymbol{i}_x \cdot \left(\boldsymbol{F}_\ell + \boldsymbol{F}_{m_{\rho c}}\right) \ . \tag{4.31}$$

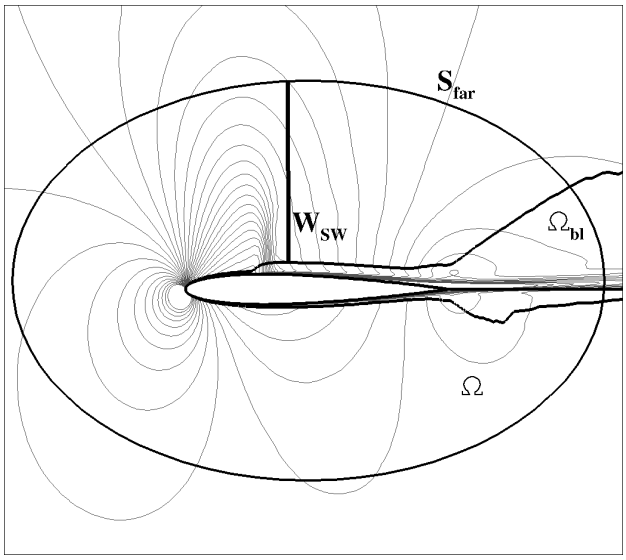

Figure 4.18 Sketch of the domain adopted for performing viscous wave drag breakdown. $\mathcal{V}_{bl}$ is the boundary layer region.

4.4 Application of $\boldsymbol{F}_{bc}$ and viscous wave drag breakdown

All CFD RANS simulations have been performed by the flow solver FLOWer [68], already introduced in section 4.1.3, with the same schemes, time integration and turbulence models. Post-processing has been performed with the BreakForce code, already described in section 4.1.3.

4.4.1 NACA 0012 airfoil

Calculations are the same reported in section 2.3.6.

Force coefficients are now computed by Eq. (4.26) with a proper selection of the boundary layer and shock wave regions [6, 29].

In Fig. 4.19 the effect of free stream Mach number on the computed aerodynamic force is shown. At $M_\infty = 0.9$ and $M_\infty = 0.95$, both lift and drag coefficients are now in perfect agreement with the reference near field values. It is worth comparing Fig. 4.19 (b) with Fig. 2.22 (b) for a better evaluation of the improvements provided by the new equation:

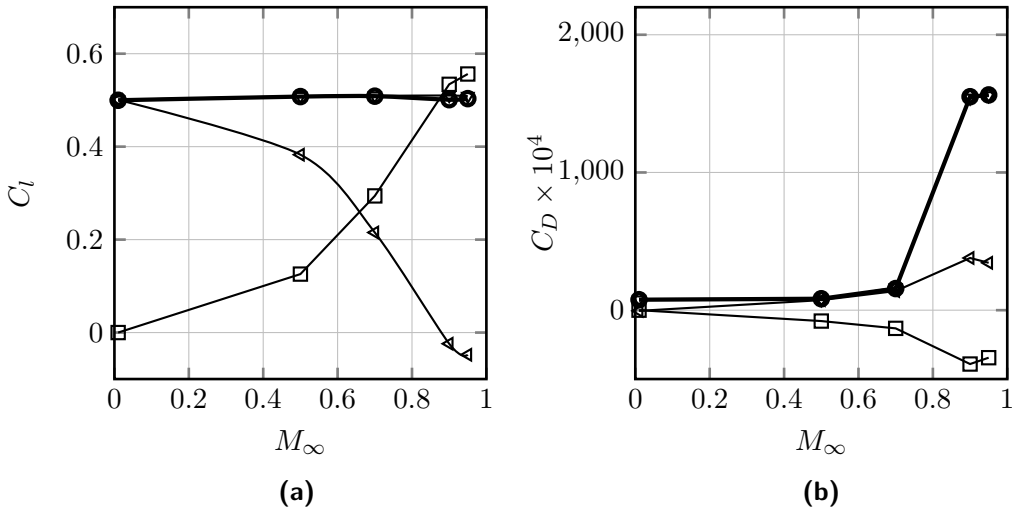

Figure 4.19 NACA 0012, $Re_\infty = 9 \cdot 10^6$, $C_l \approx 0.5$. Computed lift (a) and drag (b) coefficient versus Mach number. —○—: $\boldsymbol{F}_{nf}$. —▽—: $\boldsymbol{F}_{bc}$. — ◁ —: $\boldsymbol{F}_{\ell}$. —□—: $\boldsymbol{F}_{m_{\rho c}}$. — ◇ —: $\boldsymbol{F}_S$.

the thrust force contribution due to compressibility correction term is now retained also at $M_\infty = 0.9$ and $M_\infty = 0.95$ and compensates the vortex force drag contribution.

The same numerical solutions around the NACA 0012 airfoil have been post processed to obtain the viscous-wave drag breakdown as defined by equations (4.28) and (4.29). The obtained results have been compared in Fig. 4.20 with the breakdown obtained by adopting the entropy drag concept as proposed by Paparone & Tognaccini [6]. The results, obtained adopting the same integration domains, are in excellent agreement. It is interesting to note that with the proposed choice of W_{sw} also the Lamb vector based breakdown allows to identify the spurious drag generated outside of the boundary layer and shock wave regions. The effect of grid size on the total drag is shown in figure 4.21. h specifies the average mesh size ($h = 4$ is the coarsest grid). In the picture the reference near field value, obtained on the grid $h = 0.5$ is also included, with a dot. In the figure $C_{d_{bc}}$, $C_{d_{\Delta s}}$ and near field drag are plotted, as obtained in each grid level. They all converge as the mesh size is reduced. $C_{d_{\Delta s}}$ and $C_{d_{bc}}$ are in good agreement and show a lower sensitivity to the adopted grid, due to the removal of at least part of the spurious drag.

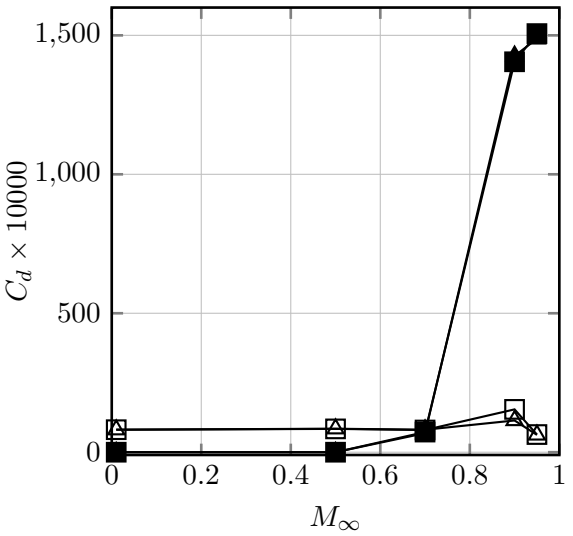

Figure 4.20 NACA 0012, $Re_\infty = 9 \cdot 10^6$, $C_l \approx 0.5$. Viscous and wave drag coefficients against freestream Mach number. $-\triangle-$: $C_{d_{v_{\Delta s}}}$. $-\blacktriangle-$: $C_{d_{w_{\Delta s}}}$. $-\square-$: $C_{d_{v\ell}}$. $-\blacksquare-$: $C_{d_{w\ell}}$.

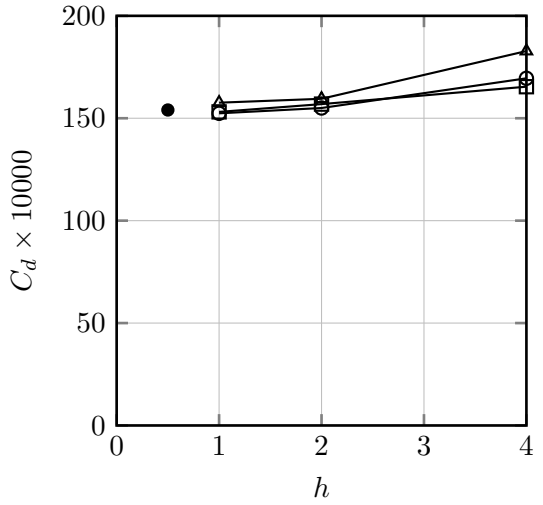

Figure 4.21 NACA 0012, $Re_\infty = 9 \cdot 10^6$, $M_\infty = 0.7$, $C_{l_{nf}} \approx 0.50 \pm 0.01$. Drag coefficient versus grid density. $-\triangle-$: $C_{d_{nf}}$. $-\square-$: $C_{d_{bc}}$. $-\circ-$: $C_{d_{\Delta s}}$. $\bullet$: 512 body points solution, reference value.

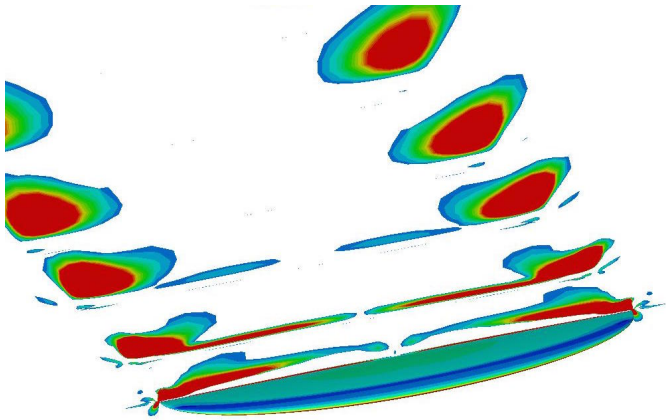

Figure 4.22 Elliptic wing. $Re_\infty = 3 \cdot 10^6$, $M_\infty = 0.9$, $\alpha = 6°$. Computed pressure coefficient contours on the wing and x-vorticity module in the wake.

4.4.2 Elliptic wing flow

With the application of equation (4.1) to elliptic wing flows shown in section 4.1.3 it was possible to obtain the profile-lift induced drag breakdown; however the already described numerical difficulties arose in the high transonic regime. The problem is even more relevant in three-dimensional flows, because while for an airfoil it is *a priori* known that at least total drag could be obtained by the wake surface contribution only [58], lift induced drag computation requires the knowledge of the volume integrals. Therefore, here we re-propose the same analysis performed in section 4.1.3 by new Eq. (4.26) and adding calculations at $M_\infty = 0.9$ and 0.95.

Figure 4.22 reports the pressure coefficient distribution on the upper surface computed at $M_\infty = 0.9$ and $\alpha = 6°$ together with x-vorticity module contours in the wake.

4.4.2.1 Lift-drag polar curves

The polar curves computed by Eq. (4.26) at Mach numbers 0.9 and 0.95 are shown in Fig. 4.23. Eq. (4.26) is in excellent agreement with the near field result. It is interesting to note the agreement of the definition of lift-induced drag by Eq. (4.31) with the reference analytical expression ($C_{D_i} = C_L^2/(\pi \mathcal{AR})$) and, not obvious, even in transonic flow at

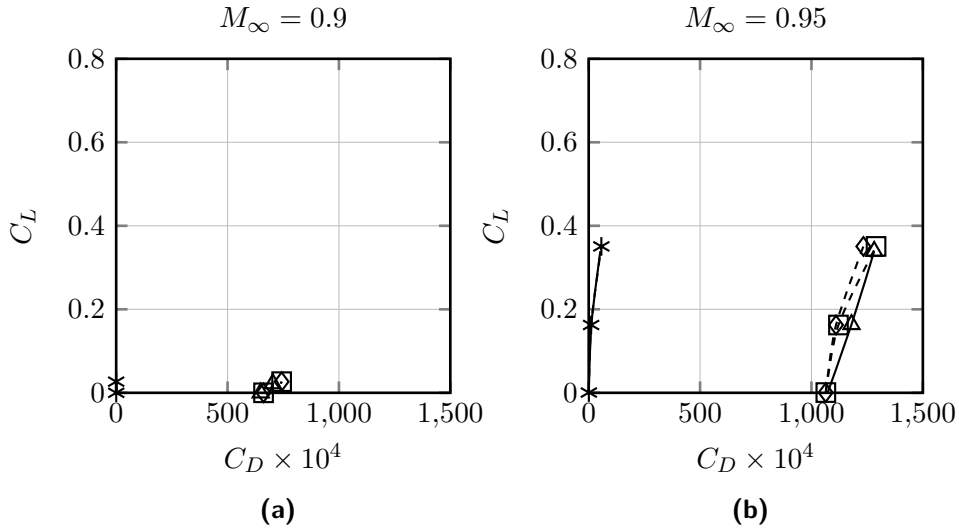

Figure 4.23 Elliptic wing, $Re_\infty = 3 \cdot 10^6$. Computed lift-drag polars. $-\triangle-$: reference near field. $--\square--$: $C_{L_{bc}} = C_{L_{bc}}(C_{D_{bc}})$. $-- * --$: $C_{L_{bc}} = C_{L_{bc}}(C_{D_{i\ell}})$. $-- \diamond --$: $C_{L_{bc}} = C_{L_{bc}}(C_{D_{pr}})$. $---$: $C_L^2/(\pi \mathcal{AR})$.

$M_\infty = 0.9$ and $M_\infty = 0.95$. As expected, $C_{D_{pr}}$, differently from the test-cases shown in figure 4.11, significantly increases at the appearance of strong shocks, because of the appearance of the wave drag.

4.4.2.2 Effect of free stream Mach number

The effect of the free stream Mach number on the computed force breakdown (previously shown in figure 4.13) is re-proposed in Fig. 4.24 at $\alpha = 4°$ respectively for lift (a) and drag (b). A shock stall is evident at $M_\infty = 0.9$. It is interesting to note that the lift loss is essentially due to a steep decrease of the compressibility correction lift ($C_{L_{m_{\rho c}}}$), while the vortex force contribution does not change its trend. $\boldsymbol{F}_{S_{far}}$ is fully responsible of the transonic drag rise, whereas the lift induced drag at constant C_L is independent of M_∞ and is given by the unbalance between the drag due to $\boldsymbol{F}_\ell$ and the thrust force due to $\boldsymbol{F}_{m_{\rho c}}$.

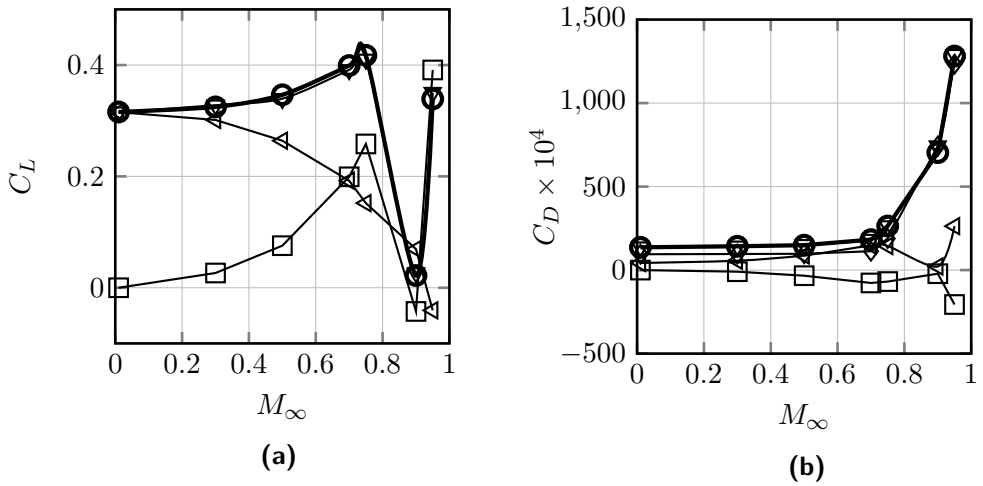

Figure 4.24 Elliptic wing, $Re_\infty = 3 \cdot 10^6$, $\alpha = 4°$. Computed lift (a) and drag (b) coefficient versus Mach number. ━○━: $\boldsymbol{F}_{nf}$. −▽−: $\boldsymbol{F}_{bc}$. − ◁ −: $\boldsymbol{F}_{\ell}$. −□−: $\boldsymbol{F}_{m_{\rho c}}$. − ◇ −: $\boldsymbol{F}_S$.

4.4.3 Wing body NASA Common Research Model

The analysis of the NASA Common Research Model (CRM) has been the subject of the 5^{th} AIAA CFD Drag Prediction Workshop (DPW5) [38]. The wing-body no-tail configuration is here studied. It consists of a supercritical transonic wing and fuselage, representative of a contemporary transonic commercial transport aircraft designed for a cruise Mach number of $M_\infty = 0.85$ and lift coefficient of $C_L = 0.5$. The aspect ratio is $\mathcal{AR} = 9.0$.

Transonic simulations at $M_\infty = 0.85$ and $Re_\infty = 5 \times 10^6$ have been performed adopting the DPW5 medium grid referred as "*L3*" grid [71]. It is a 5-block structured mesh that counts about 5 million of hexahedral cells; more details on the aircraft configuration and meshing can be obtained from the DPW5 web page [1]. An isometric view of the CRM is shown in Fig. 4.25 together with pressure coefficient distribution over the body and x-vorticity module in the wake computed at $C_L = 0.5$.

The computed lift-drag polar curves for three different grid levels of the $L3$ grid are

[1] http://aaac.larc.nasa.gov/tsab/cfdlarc/aiaa-dpw/

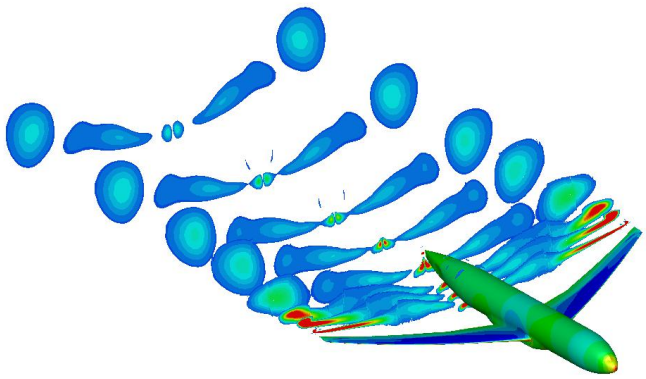

Figure 4.25 NASA CRM, $Re_\infty = 5 \cdot 10^6$, $M_\infty = 0.85$, $C_L = 0.5$. Computed pressure coefficient contours on the body and x-vorticty module in the wake.

shown in Fig. 4.26 and compared with the results of the experiments performed at Langley National Transonic Facility [72]. The computed polar curves converge while reducing the mesh size and the results obtained using the finest grid level are in satisfactory agreement with experimental data, despite of already evidenced effects not taken into account in the numerical simulations as the influence of the wind tunnel walls and of the support sting, the aeroelastic deformation of the model, and the laminar-turbulent transition [38] [73].

Figure 4.27 shows the computed and measured pressure coefficients at six different wing sections at $C_L = 0.5$. The results are comparable to the data of the DPW5 [38]. At the inboard sections, the computations are in good agreement with the experiments. Moving outboard, the shock is predicted downstream of the experimental data, and some discrepancies are noted for the load on the upper surface. In particular, the expansion levels on the upper surface of the wing tend to decrease in the wind tunnel data as the span station moves to the tip of the wing. This effect has been ascribed to the aeroelastic

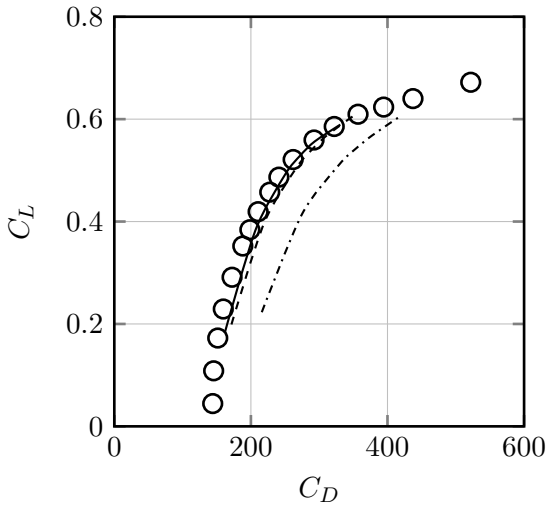

Figure 4.26 NASA CRM, $Re_\infty = 5 \cdot 10^6$, $M_\infty = 0.85$. Computed ($L3$ grid) and experimental lift drag polar curves. $-\cdot-$: computed coarse grid. $--$: computed medium grid. $-$: computed fine grid. $\boldsymbol{o}$: experiment [72].

deformation of the experimental model that lowers the local incidence at the outboard stations [73, 42].

The vorticity based breakdown of the lift polar curve is proposed in Fig. 4.28. Both lift and drag coefficients have been computed by Eq. (4.26) with the wave and viscous drag definitions given in Eqs. (4.28) and (4.29). The computed values are also reported in table 4.2. Eq. (4.26) has been applied to a domain limited to the selected boundary layer and

α	$C_{D_{v\ell}}$	$C_{D_{w\ell}}$	$C_{D_{i\ell}}$	$C_{L_{bc}}$	$C_{D_{v\Delta s}}$	$C_{D_{w\Delta s}}$	$C_{D_{i_{msk}}}$	$C_{L_{nf}}$
0.000	137.5	1.6	13.8	0.181	140.7	0.9	14.2	0.185
1.500	142.0	4.3	54.2	0.381	149.3	3.4	49.5	0.384
2.200	143.4	8.8	89.0	0.490	154.6	9.2	75.5	0.484
2.250	145.1	9.1	93.5	0.497	155.2	10.0	78.7	0.492
2.400	145.8	14.4	94.8	0.506	156.5	13.6	86.1	0.514
2.700	148.7	25.8	111.3	0.547	162.6	23.2	100.4	0.557

Table 4.2 NASA CRM, $Re_\infty = 5 \cdot 10^6$, $M_\infty = 0.85$. Computed entropy breakdown and $\boldsymbol{F}_{bc}$ breakdown.

shock wave regions and evidences a lower total drag when compared with the near field

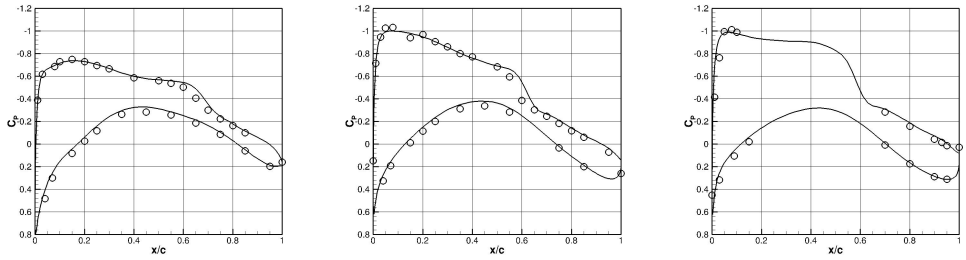

(a) $\eta = 0.131$ **(b)** $\eta = 0.283$ **(c)** $\eta = 0.397$

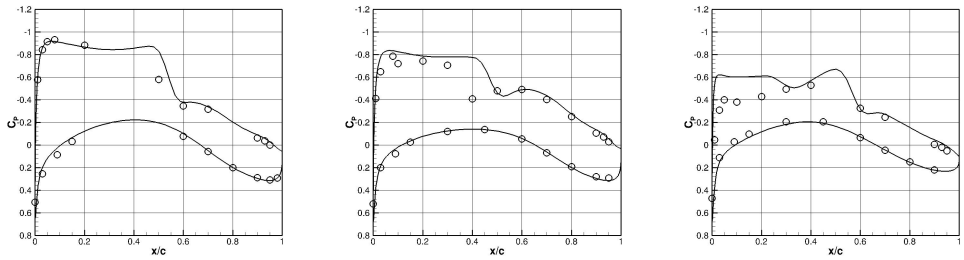

(d) $\eta = 0.502$ **(e)** $\eta = 0.727$ **(f)** $\eta = 0.95$

Figure 4.27 NASA CRM, $Re_\infty = 5 \cdot 10^6$, $M_\infty = 0.85$, $C_L = 0.5$. Computed and experimental pressure coefficients. $---$: present computation, $\circ$: experiment [72].

value showing the presence in the near field values of a notable spurious drag associated with the artificial dissipation introduced by the numerical discretization, still present on the relatively "coarse" grid adopted. The computed lift induced drag is compared with the analytic expression $C_L^2/(\pi e \mathcal{AR})$, with $e = 1$. The best fitting with a parabola of the computed C_{d_i} provided $e = 0.96$. The computed viscous drag is almost constant with lift, whereas the wave drag increases, as it should be expected.

The selected boundary layer and shock wave regions at design lift coefficient are shown in Fig. 4.29. The presence of a shock near the cockpit is evidenced.

The breakdown of the lift induced drag in vortex force and compressibility contributions is shown in Fig. 4.30 and is in substantial agreement with what obtained for the elliptic wing, such as for the breakdown of the lift coefficient (Fig. 4.31).

A quantitative analysis of the breakdown has been obtained by comparing present results with the ones obtained by the entropy based drag method proposed by Paparone

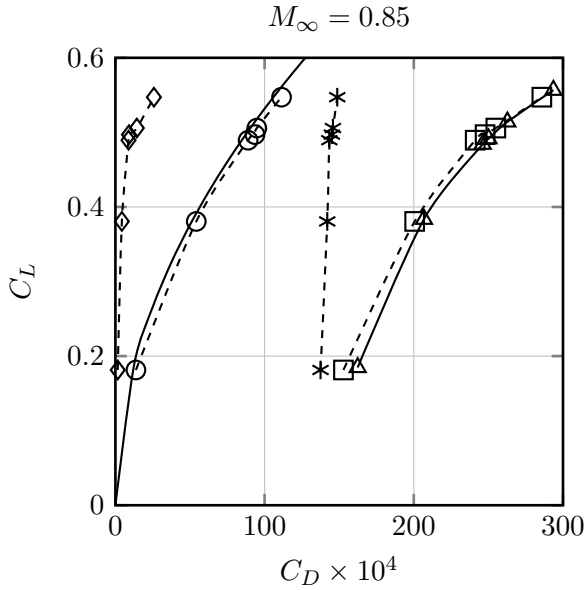

Figure 4.28 NASA CRM, $Re_\infty = 5 \cdot 10^6$. Computed lift-drag polars. $-\triangle-$: reference near field. $--\square--$: $C_{L_{bc}} = C_{L_{bc}}(C_{D_{bc}})$. $--\circ--$: $C_{L_{bc}} = C_{L_{bc}}(C_{D_{i\ell}})$. $--\diamond--$: $C_{L_{bc}} = C_{L_{bc}}(C_{D_{w\ell}})$. $--*--$: $C_{L_{bc}} = C_{L_{bc}}(C_{D_{v\ell}})$. $—$: $C_L^2/(\pi \mathcal{A}R)$.

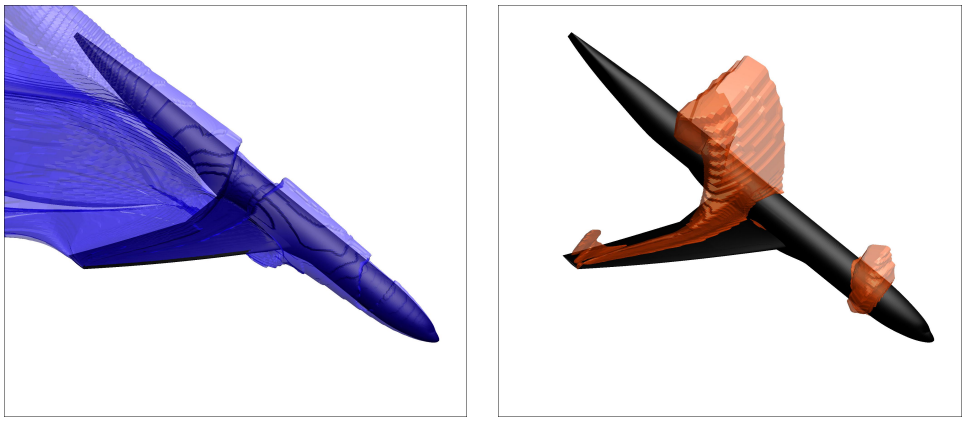

(a) **(b)**

Figure 4.29 NASA CRM, $Re_\infty = 5 \cdot 10^6$, $M_\infty = 0.85$, $C_L = 0.5$. Selected boundary layer and shock wave regions.

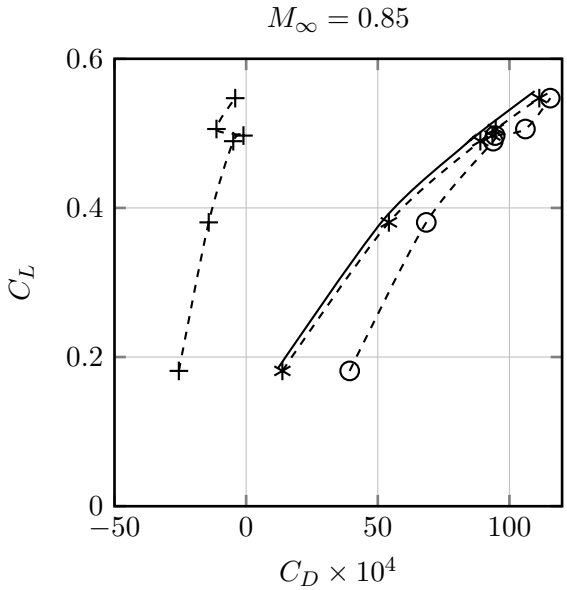

Figure 4.30 NASA CRM, $Re_\infty = 5 \cdot 10^6$. Breakdown of the lift induced drag. $--*--$: $C_{L_{bc}} = C_{L_{bc}}(C_{D_{i\ell}})$. $--\circ--$: $C_{L_{bc}} = C_{L_{bc}}(C_{D_\ell})$. $--+--$: $C_{L_{bc}} = C_{L_{bc}}(C_{D_{m_{\rho c}}})$. ——: $C_L^2/(\pi \mathcal{AR})$.

& Tognaccini [6]. In this case the *reversible* lift induced drag has been computed by Maskell's formula [23], placing the *numerical* Trefftz plane just aft the end of the fuselage. The entropy based lift-drag polar curve is proposed in Fig. 4.32 (to be compared to Fig. 4.28), with lift coefficient computed with the near field formula; table 4.2 also reports this breakdown. The agreement with present results is very satisfactory. At the highest incidences Maskell's formula underpredicts the lift induced drag by 6 drag counts. It can be ascribed to the necessity to place the numerical Trefftz plane at a certain distance from the wing because of the fuselage. As evidenced by Fig. 4.25, the numerical dissipation, especially introduced by the grid coarsening, significantly reduces the intensity of the trailing vortices and of the associated kinetic energy. This artificial *irreversible* mechanism implies an increase of the viscous drag and a reduction of the computed lift induced drag when the Trefftz plane cannot be placed just aft the wing trailing edge as in the case of the elliptic wing. This is a widely discussed drawback of the numerical application of Maskell's formula [7], [45], that is at least partially overcome by Lamb vector based

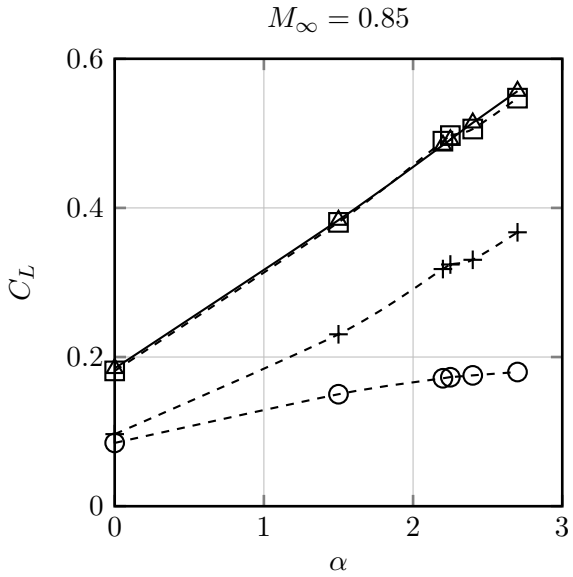

Figure 4.31 NASA CRM, $Re_\infty = 5 \cdot 10^6$. Breakdown of the lift coefficient. $-\triangle-$: $C_{L_{nf}} = C_{L_{nf}}(\alpha)$. $--\square--$: $C_{L_{bc}} = C_{L_{bc}}(\alpha)$. $--\circ--$: $C_{L_\ell} = C_{L_\ell}(\alpha)$. $--+--$: $C_{L_{m_{\rho c}}} = C_{L_{m_{\rho c}}}(\alpha)$.

method.

An entropy based far-field drag analysis and decomposition over the NASA CRM tail-off configuration has already been performed by Gariépy et al. [47] adopting a set of grids generated by the IDEA Research Chair at Polytechnique Montréal denoted as IDEA grids. The grids are four structured meshes with increasing refinement, in particular we discuss here the medium grid results (counting about 5.9 millions cells, the medium grid size is comparable with the one we adopted). Hue and Esquieu [41] also performed a far-field analysis of the NASA CRM focusing in particular on the wing body tail-on configuration. However they reported some results for the tail-off configuration obtained using a structured mesh that counts about 11 millions of grid nodes.

The drag breakdown performed at design conditions is reported in table 4.3. It is in substantial agreement with the above discussed results. The spurious drag contribution is computed as the difference between the near field drag and the drag computed in boundary layer and shock wave regions. The very low spurious drag computed by Hue and Esquieu

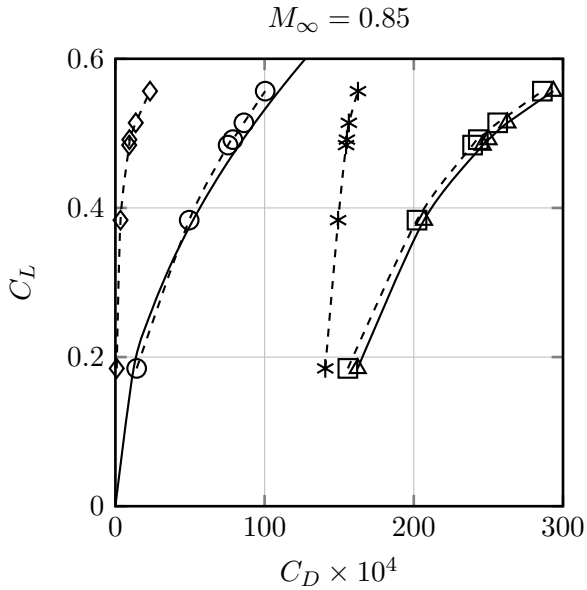

Figure 4.32 NASA CRM, $Re_\infty = 5 \cdot 10^6$. Computed lift-drag polars, entropy method. $-\triangle-$: reference near field. $--\square--$: $C_{L_{nf}} = C_{L_{nf}}(C_{D_{v\Delta s}} + C_{D_{w\Delta s}} + C_{D_{i_{msk}}})$. $--*--$: $C_{L_{nf}} = C_{L_{nf}}(C_{D_{v\Delta s}})$. $--\diamond--$: $C_{L_{nf}} = C_{L_{nf}}(C_{D_{w\Delta s}})$. $--\circ--$: $C_{L_{nf}} = C_{L_{nf}}(C_{D_{i_{msk}}})$. ——: $C_L^2/(\pi \mathcal{AR})$.

is easily explained because of the greater refinement of the grid. The discrepancies in the computed wave drag is probably due to the different definitions adopted for viscous-wave drag breakdown and also to some details on their implementation. Indeed, it depends on the assumed shock wave and boundary layer regions. Clearly their distinction is ambiguous in the zone of the shock wave-boundary layer interaction. In present algorithm it was first checked if a grid cell belongs to a shock wave and then if it is part of the boundary layer, therefore we assume that the shock-boundary layer interaction region is producing wave drag. This effect is quite clear from the analysis of Fig. 4.29 (a), when looking at the two "holes" in the selected boundary layer region on the fuselage in correspondence of the cockpit and wing shock waves.

	C_L	C_{D_i}	C_{D_v}	C_{D_w}	Spurious	Total
Gariépy et al. [74]	0.50	87.7	156.0	5.5	7.3	256.5
Hue and Esquieu [41]	0.50	92.0	158.0	3.90	1.0	254.9
Present study	0.50	93.5	145.1	9.10	2.3	250.0

Table 4.3 NASA CRM, $Re_\infty = 5 \cdot 10^6$, $M_\infty = 0.85$. Comparison of present vorticity based drag breakdown with literature.

4.5 A vorticity based definition of wave drag

A nice feature of methods [6] and [7] is that profile drag is defined as a volume integral in the flow; the integrand essentially depends on the local production of entropy, therefore it can be interpreted as a local source of *irreversible* drag. A straightforward definition of viscous and wave drag could be obtained by limiting the integration domain to the boundary layer and shock wave regions only, procedure correctly computing the wave drag of an inviscid transonic flow. As already discussed in section 4.3, the proposed viscous-wave profile drag breakdown by Lamb vector surface integrals could be inconsistent with previous wave drag definition, since it doesn't account for the boundary layer entrainment after the shock waves.

An equivalent breakdown in volume contributions of the profile drag computed could be obtained if the surface integral $\boldsymbol{F}_{S_{far}}$ in equation (4.1) is transformed in a volume integral. The well known identity of the double vector cross product gives

$$\boldsymbol{r} \times (\boldsymbol{n} \times \rho\boldsymbol{\ell}) = (\boldsymbol{r} \cdot \rho\boldsymbol{\ell})\boldsymbol{n} - (\boldsymbol{r} \cdot \boldsymbol{n})\rho\boldsymbol{\ell} \ , \tag{4.32}$$

therefore

$$\boldsymbol{F}_{S_{far}} = -\int\limits_{S_{far}} (\boldsymbol{r} \cdot \rho\boldsymbol{\ell})\boldsymbol{n}\mathrm{d}S + \int\limits_{S_{far}} (\boldsymbol{r} \cdot \boldsymbol{n})\rho\boldsymbol{\ell}\mathrm{d}S \ . \tag{4.33}$$

Gauss theorem can be applied to both integrals of this equation and, since $\boldsymbol{D}_{pr} = \boldsymbol{F}_{S_{far}}$, we have

$$\boldsymbol{D}_{pr} = \boldsymbol{F}_{S_\Omega} = -\int\limits_{\mathcal{V}} \boldsymbol{\nabla}(\boldsymbol{r} \cdot \rho\boldsymbol{\ell})\mathrm{d}\mathcal{V} + \int\limits_{\mathcal{V}} \boldsymbol{\nabla} \cdot (\boldsymbol{r}\rho\boldsymbol{\ell})\mathrm{d}\mathcal{V} \ , \tag{4.34}$$

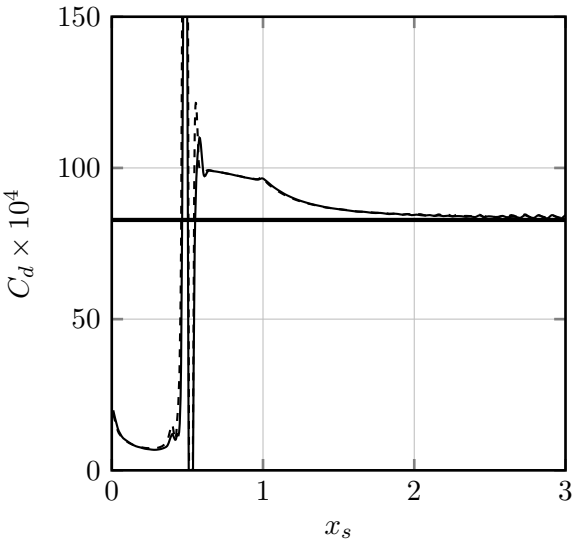

Figure 4.33 NACA 0012, $M_\infty = 0.8$, $\alpha = 0°$, Euler flow. Comparison of drag coefficients as obtained by equation (4.34) and equation (4.28) vs x_s. —: equation (4.34). - - -: equation (4.28) ▬: reference near field value.

where the subscript Ω in $\boldsymbol{F}_{S_\Omega}$, specifies volume integral expression of $\boldsymbol{F}_{S_{far}}$. Choosing $\mathcal{V} = \mathcal{V}_{bl}$, where $\mathcal{V}_{bl}$ is the boundary layer region and part of its wake, the viscous drag can now be obtained and, as consequence, the wave drag is defined by the complementary part which can also be obtained adopting $\mathcal{V} = \mathcal{V}_{sw}$, where $\mathcal{V}_{sw}$ is the shock region including a significant part of its wake. The application of equation (4.34) to the inviscid Euler flow test is presented in figure 4.33. The integration volume $\mathcal{V}$ is limited by the wake surface W_{sw} adopted for the computation of $\boldsymbol{F}_S$. Varying its position x_s, there is a perfect agreement with equation (4.28).

The aerodynamic force is independent of the choice of $\mathcal{V}$. Therefore, with reference to figure 4.34, comparing equation (4.1) as obtained choosing $\mathcal{V} = \mathcal{V}_1 \bigcup \mathcal{V}_2 \bigcup \mathcal{V}_{bl}$ and $\mathcal{V} = \mathcal{V}_1 \bigcup \mathcal{V}_{bl}$ we have

$$\boldsymbol{F}_{S_{\Omega_2}} = -\boldsymbol{F}_{\ell_{\Omega_2}} - \boldsymbol{F}_{m_{\rho\,\Omega_2}} \,, \tag{4.35}$$

where the subscripts clearly identify the domain of integration. $\boldsymbol{F}_{S_{\Omega_2}}$ is exactly the difference between equation (4.28) applied choosing W_{sw} just downstream of the shock

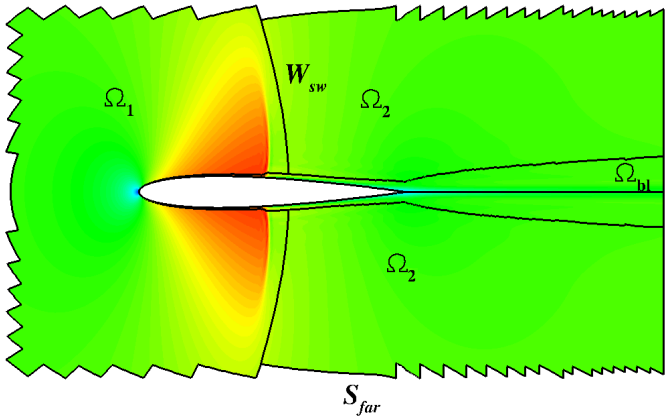

Figure 4.34 Sketch of the domain adopted for performing viscous wave drag breakdown. $\mathcal{V}_{bl}$ is the boundary layer region. $\mathcal{V} = \mathcal{V}_{bl} \bigcup \mathcal{V}_1 \bigcup \mathcal{V}_2$.

and in the far wake. $\boldsymbol{F}_{\ell_{\Omega_2}}$ and $\boldsymbol{F}_{m_{\rho\,\Omega_2}}$ are in general different than zero downstream of a shock of variable intensity along its shape. They can be expected to be small in the case of transonic flows characterized by normal shocks of small intensity, but these contributions can explain the small differences between the application of equation (4.28) as proposed in section 4.4.3 and in reference methods [6, 7]. The contribution of $\boldsymbol{F}_{\ell_{\Omega_2}}$ is already evidenced in figure 4.33; indeed it is responsible of the slight, but significant, decrease of the computed drag between the shock foot $x_s \approx 0.55$ and the trailing edge $x_s = 1$.

Equation (4.34) gives a simple new definition of the wave drag consistent with methods [6, 7] when the domain of integration excludes $\mathcal{V}_{bl}$. In order to verify this result in the case of a viscous flow, a RANS solution around the NACA0012 airfoil at the same freestream conditions $M_\infty = 0.8$, $\alpha = 0°$ and Reynolds number $Re_\infty = 9 \cdot 10^6$ has been analysed (Spalart-Allmaras turbulence model). This solution, obtained by ONERA elsA RANS solver [75], has been kindly provided by Daniel Destarac and Didier Bailly, researchers at ONERA. The structured grid is built up by 768×192 cells with a far field 500 airfoil chords distant from the body. Method [6] returned a total drag $C_{d_v} = 0.0157$ (equal to the near field value), with a breakdown in viscous drag $C_{d_v} = 0.0092$, and wave drag

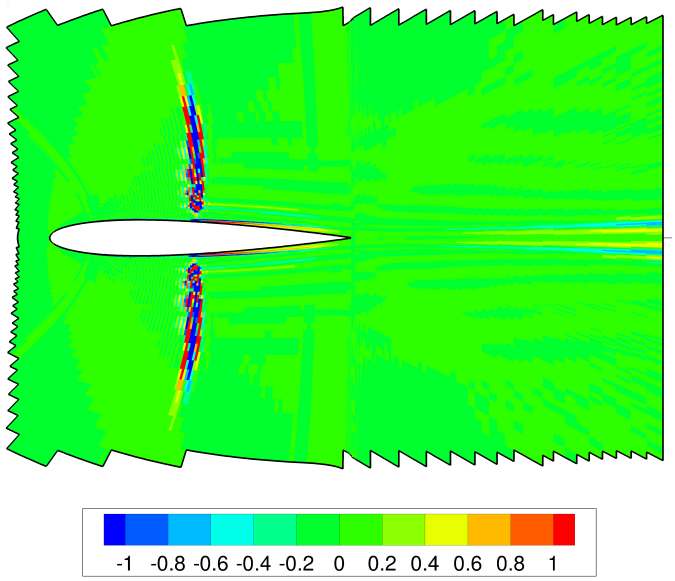

Figure 4.35 NACA0012 airfoil. RANS solution, $M_\infty = 0.8$, $\alpha = 0°$, $Re_\infty = 9 \cdot 10^6$. Adopted volume for the computation of wave drag by equation (4.34). The color scale represents the local production of drag (in counts) by equation (4.34).

$C_{d_w} = 0.0062$.

Figure 4.35 shows the integration domain used in the calculation of the total drag. In addition, the adopted color scale represents the integrand of equation (4.34) times the cell volume, therefore it provides the drag (in counts) produced in each grid cell. The drag coefficient obtained by equation (4.1) is $C_d = 0.0157$ in perfect agreement with both near field and method [6]. In particular, the surface integral returned $C_{d_{S_{far}}} = 0.0161$ whereas $C_{d_\ell} + C_{d_{m_\rho}} = -0.0004$ was not exactly zero. This error is introduced, as already shown [16], by a numerical spurious exchange between the reversible and irreversible components of the aerodynamic force. It can be reduced if the integration is strictly limited to the theoretically rotational regions of the flow (boundary layer and shock wave including its wake).

The figures evidence that drag is essentially produced in the shock and in the boundary layer regions and that they are quite clearly separated, as evidenced by the adopted color scale. The calculation was repeated by means of equation (4.34) adopting the domain

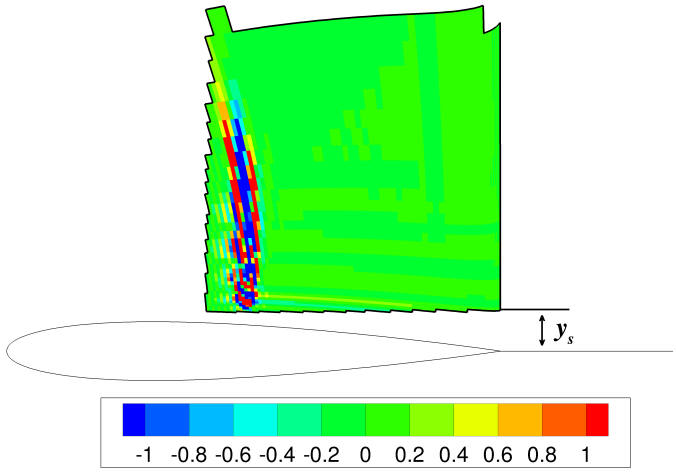

Figure 4.36 NACA0012 airfoil. RANS solution, $M_\infty = 0.8$, $\alpha = 0°$, $Re_\infty = 9 \cdot 10^6$. The color scale represents the local production of drag (in counts) by equation (4.34).

of integration proposed in figure 4.36 only containing the shock region and part of its wake. The computed drag coefficient (also including in the integration the lower shock) is $C_d = 0.0060$, this time in good agreement with the wave drag prediction by method [6]. In addition, figure 4.37 shows the sensitivity of the computed wave drag to the choice of the adopted shock wave domain $\mathcal{V}_{sw}$. The figure proposes the calculated drag coefficient while varying the lower border of the shock domain (see figure 4.36 for the definition of y_s). The sensitivity is quite low, the correct wave drag value is obtained in a wide range of y_s values.

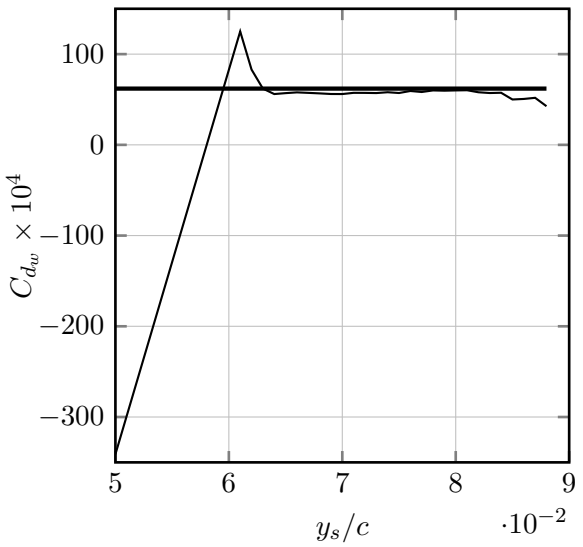

Figure 4.37 NACA 0012 airfoil. RANS solution, $M_\infty = 0.8$, $\alpha = 0°$, $Re_\infty = 9 \cdot 10^6$. Computed wave drag against position of shock region lower surface (y_s). ▬: reference calculation by method [6].

5

AERODYNAMIC FORCE IN UNSTEADY FLOWS

Contents

The subject of this chapter is the analysis of the aerodynamic force in unsteady flows. The first part of the chapter is dedicated to the analysis of incompressible two-dimensional flows. After a discussion on present aerodynamic force theory applied in inertial or non-inertial reference frames, a new mixed inertial-non inertial exact formula is derived, which was shown to be more accurate than Wu et al. formula [50] when dealing with moving rigid grid simulations. Application of present formulae is validated on low-Reynolds number and high-Reynolds number pitching and plunging flat plate flows. A theoretical analysis is then carried out, with a link between inviscid oscillating flat plate flows and present method. Thanks to this link, a new definition of dynamic force derivatives is derived and discussed, with numerical applications to low and high Reynolds numbers flows.

The second part concerns about unsteady compressible flows. A new definition of irreversible and reversible part of the aerodynamic force in unsteady incompressible flows is derived, and extended to compressible flows. An application to a pitching airfoil flow already proposed by Toubin et al. [48], is performed and compared with Toubin et al. results. This work is the result of a stage performed by the author at ONERA, the french aerospace center, in Meudon, in the context of a collaboration between the department of Industrial Engineering of University of Naples Federico II and the department of Aerodynamics, Aerolasticity and Acoustics of ONERA.

5.1 The analysis of two-dimensional incompressible flows

5.1.1 Inertial reference frame

Let us consider an incompressible unsteady two-dimensional flow characterized by a time varying asymptotic velocity $\boldsymbol{V}_\infty(t)$ around an oscillating and impermeable body. Assuming an inertial reference system $O(xz)$, aerodynamic force formula derived by Wu et al. [50], already discussed in section 2.3.2, here referred as $\boldsymbol{F}_{au}$, with present nomenclature can be written as:

$$\boldsymbol{F}_{au} = \boldsymbol{F}_\ell + \boldsymbol{F}_t + \boldsymbol{F}_{S_{far}} + \boldsymbol{F}_{S_b} + \boldsymbol{F}_{t_b} + \boldsymbol{\Delta}_\mu \ . \tag{5.1}$$

where:

$$\boldsymbol{F}_t = -\rho \int_{\mathcal{V}} \boldsymbol{r} \times \frac{\partial \boldsymbol{\omega}}{\partial t} \mathrm{d}\mathcal{V} \ , \qquad \boldsymbol{F}_{S_{far}} = -\rho \int_{S_{far}} \boldsymbol{r} \times (\boldsymbol{n} \times \boldsymbol{\ell}) \mathrm{d}S \ ,$$

$$\boldsymbol{F}_{S_b} = -\rho \int_{S_b} \boldsymbol{r} \times (\boldsymbol{n} \times \boldsymbol{\ell}) \mathrm{d}S \ , \qquad \boldsymbol{F}_{t_b} = \rho \int_{S_b} \boldsymbol{r} \times (\boldsymbol{n} \times \boldsymbol{a}) \mathrm{d}S \ ,$$

$$\boldsymbol{\Delta}_\mu = \int_{S_{far}} \boldsymbol{r} \times (\boldsymbol{n} \times \boldsymbol{\nabla} \cdot \boldsymbol{\tau}_v) \, \mathrm{d}S + \int_{S_{far}} \boldsymbol{\tau}_v \cdot \boldsymbol{n} \, \mathrm{d}S \ ,$$

where $\boldsymbol{r}$ is the position vector with respect to an arbitrary pole. $\boldsymbol{F}_t$ and $\boldsymbol{F}_{S_b}$ are related with the hydrodynamic impulse in $\mathcal{V}$: $\boldsymbol{I} = \rho \int_{\mathcal{V}} \boldsymbol{r} \times \boldsymbol{\omega} \mathrm{d}\mathcal{V}$. Indeed, taking into account for Reynolds transport theorem with S_{far} fixed in time, we have:

$$\boldsymbol{F}_t + \boldsymbol{F}_{S_b} = -\frac{d\boldsymbol{I}}{dt} \equiv \boldsymbol{F}_\tau \ . \tag{5.2}$$

Equation (5.1) also holds for three-dimensional flows, provided $\boldsymbol{r}$ is replaced by $\tilde{\boldsymbol{r}} = \boldsymbol{r}/2$.

Pressure does not explicitly appear in equation (5.1). An extension and verification of this formula in high Reynolds number and turbulent flows based on averaged quantities has been proposed by Marongiu and Tognaccini [56]. Wu et al. [50] considering the flow around a cylinder, found that the $\boldsymbol{\Delta}_\mu$ contribution was about the 10% of the total drag at a Reynolds number of 10^4. In the case of boundary layer flows, Marongiu and Tognaccini [55] found that lift and drag contribution of $\boldsymbol{\Delta}_\mu$ are, respectively, of order $\mathcal{O}(1/\sqrt{Re})$ and $\mathcal{O}(1/Re)$. Numerical applications of equation (5.1) in low-Reynolds number flows are given by Liu et al. [76] and Wang et al. [77]. When the vorticity is non-negligible only inside the boundary layer and wake, as for example in the case of airfoil flow at high Reynolds numbers, numerical integration can be limited to these regions, evidencing the boundary layer as the region where the aerodynamic force is generated.

It is interesting to note that in the case of steady flow $\boldsymbol{F}_{au}$ only depends on the Lamb vector field if $\mathcal{V}$ contains the whole vortical region. In particular, as demonstrated by Marongiu and Tognaccini [55] the vortex force is the reversible part of the aerodynamic force, $\boldsymbol{F}_{S_{far}}$ is the profile drag, and $\boldsymbol{\Delta}_\mu$ is negligible ($\boldsymbol{F}_{tb} = 0$ and $\boldsymbol{F}_{S_b} = 0$ due to the

no-slip boundary condition on the wall).

5.1.2 Non inertial reference frame

Let us consider a non-inertial reference frame $O'(x'z')$ fixed with respect to a moving body with the same clock of $O(xz)$ ($t' = t$) and let us specify with superscript $'$ the variables in this reference frame. The motion of $O'(x'z')$ is described by the translational velocity of its origin $\boldsymbol{U}(t)$ and by its angular velocity $\boldsymbol{\Omega}(t)$. The relation between the fluid velocities in the non inertial (O') and an inertial (O) reference frame is

$$\boldsymbol{V} = \boldsymbol{V}' + \boldsymbol{V}_T \ , \qquad \boldsymbol{V}_T = \boldsymbol{U} + \boldsymbol{\Omega} \times \boldsymbol{r}' \ , \tag{5.3}$$

whereas, for an arbitrary vector $\boldsymbol{b}$, the relation between the Eulerian time derivatives is

$$\frac{\partial \boldsymbol{b}}{\partial t} = \frac{\partial \boldsymbol{b}}{\partial t'} - \boldsymbol{V}_T \cdot \boldsymbol{\nabla} \boldsymbol{b} + \boldsymbol{\Omega} \times \boldsymbol{b} \ . \tag{5.4}$$

Specifying with $\boldsymbol{\ell}'' = \boldsymbol{\omega}' \times \boldsymbol{V}'$ ($\boldsymbol{\omega}' = \boldsymbol{\omega} - 2\boldsymbol{\Omega}$), equation (5.1) can be expressed in another form. We name here $\boldsymbol{F}_{bu}$:

$$\boldsymbol{F}_{bu} = \boldsymbol{F}_{\ell''} + \boldsymbol{F}_{t''} + \boldsymbol{F}_{S''_{far}} + \boldsymbol{F}_m \ + \boldsymbol{\Delta}'_\mu, \tag{5.5}$$

where

$$\boldsymbol{F}_{\ell''} = -\rho \int_{\mathcal{V}} \boldsymbol{\ell}'' \mathrm{d}\mathcal{V} \ , \qquad \boldsymbol{F}_{t''} = -\rho \int_{\mathcal{V}} \boldsymbol{r}' \times \frac{\partial \boldsymbol{\omega}'}{\partial t'} \mathrm{d}\mathcal{V} \ ,$$

$$\boldsymbol{F}_{S''_{far}} = -\rho \int_{S_{far}} \boldsymbol{r}' \times (\boldsymbol{n} \times \boldsymbol{\ell}'') \mathrm{d}S \ , \qquad \boldsymbol{F}_m = \rho \int_{S_{far}} \boldsymbol{r}' \times (\boldsymbol{n} \times \boldsymbol{f}_m) \mathrm{d}S + \rho \int_{\mathcal{V}} \boldsymbol{f}_m \mathrm{d}\mathcal{V}$$

$$\boldsymbol{\Delta}'_\mu = \int_{S_{far}} \boldsymbol{r}' \times (\boldsymbol{n} \times \boldsymbol{\nabla} \cdot \boldsymbol{\tau}_v) \, \mathrm{d}S + \int_{S_{far}} \boldsymbol{\tau}_v \cdot \boldsymbol{n} \, \mathrm{d}S \ ,$$

and $\boldsymbol{f}_m = -\left[d\boldsymbol{U}/dt + d\boldsymbol{\Omega}/dt \times \boldsymbol{r}' + \boldsymbol{\Omega} \times \boldsymbol{V}_T + 2\boldsymbol{\Omega} \times \boldsymbol{V}'\right]$ is the the apparent force per unit mass[1].

Equation (5.5) has one term less than equation (5.1) because $\boldsymbol{\ell}'' = 0$ on the body; it is however less convenient and interesting since, even in high Reynolds number flows, integration cannot be limited to the boundary layer due to the presence of the body force $\boldsymbol{f}_m$ and because $\boldsymbol{\omega}' \neq 0$ everywhere due to the $-2\boldsymbol{\Omega}$ part.

5.1.3 Mixed inertial-non inertial formula

In order to overcome this latter drawback and recover the mid field property, we here introduce another equivalent formula based on a *mixed* inertial-non inertial definition of the Lamb vector field: $\boldsymbol{\ell}' = \boldsymbol{\omega} \times \boldsymbol{V}'$. This idea has been already used in CFD simulations of rotating and geophysical flows [78]; here it has been exploited to obtain another exact expression of the aerodynamic force.

By the introduction of $\boldsymbol{\ell}'$ equation (5.1) reduces, in two-dimensional flows, to the following expression. We name here $\boldsymbol{F}_{cu}$ (see appendix D for the proof)

$$\boldsymbol{F}_{cu} = \boldsymbol{F}_{\ell'} + \boldsymbol{F}_{t'} + \boldsymbol{F}_{S'_{far}} + \boldsymbol{F}_{t_b} + \boldsymbol{\Delta}_{\mu} \ , \tag{5.6}$$

where

$$\boldsymbol{F}_{\ell'} = -\rho \int_{\mathcal{V}} \boldsymbol{\ell}' \mathrm{d}\mathcal{V} \ , \qquad \boldsymbol{F}_{t'} = -\rho \int_{\mathcal{V}} \boldsymbol{r} \times \frac{\partial \boldsymbol{\omega}}{\partial t'} \mathrm{d}\mathcal{V} \ , \qquad \boldsymbol{F}_{S'_{far}} = -\rho \int_{S_{far}} \boldsymbol{r} \times (\boldsymbol{n} \times \boldsymbol{\ell}') \mathrm{d}S \ . \tag{5.7}$$

The mid field property is clearly recovered since $\boldsymbol{\ell}'$ depends on $\boldsymbol{\omega}$ and not on $\boldsymbol{\omega}'$.

5.2 Periodic small oscillations of the plate in inviscid flow

The classical solutions of Theodorsen and Mutchler [79] and Von Karman and Sears [80] describe the case of a plate in inviscid flow and small oscillations. The connections with

[1] Equation (5.5) can be derived as equation (5.1) [50] taking into account that in a non inertial frame the far field formula is $\boldsymbol{F} = -\rho \int_{\mathcal{V}} \boldsymbol{a}' \mathrm{d}\mathcal{V} - \int_{S_{far}} (p\boldsymbol{n} - \boldsymbol{\tau}_v \cdot \boldsymbol{n}) \, \mathrm{d}S + \rho \int_{\mathcal{V}} \boldsymbol{f}_m \mathrm{d}\mathcal{V}$.

the Lamb vector based formula can be obtained by performing a direct integration of the pressure load over the plate. As proved in appendix E, the obtained lift is

$$l = -\int_{-b}^{b} \Delta p(x,t)\mathrm{d}x = \rho V_\infty \Gamma - \rho \frac{d}{dt}\int_{-b}^{b} x\gamma_b(x,t)\mathrm{d}x - \rho V_\infty b\gamma_w(b,t) \ , \tag{5.8}$$

where Γ is the body circulation, γ_b and γ_w are respectively the bound and the free vorticity systems ($2b$ is the plate length). Taking into account for equation (5.2) and that, in case of flat plate flow, $\boldsymbol{F}_{tb} = 0$ and $\boldsymbol{\Delta}_\mu \to 0$ for $Re_\infty \to \infty$, equation (3.1) clearly reduces to equation (5.38) when considering an inviscid flow, and the integration domain $\mathcal{V}$ chosen excluding the airfoil wake, with vorticity replaced by the vorticity sheets γ_b and γ_w. The first term is the inviscid vortex force, the second is the hydrodynamic impulse variation and the third term is the inviscid wake integral. We can write

$$l = l_\ell + l_\tau + l_{S_{far}} \ , \tag{5.9}$$

where

$$l_\ell = \rho V_\infty \int_{-b}^{b} \gamma_b(\xi.t)\mathrm{d}x \tag{5.10}$$

is the vortex force of the bound vorticity,

$$l_\tau = -\rho \frac{d}{dt}\int_{-b}^{b} x\gamma_b(\xi,t)\mathrm{d}x \tag{5.11}$$

is the time derivative of the hydrodynamic impulse on the body and

$$l_{S_{far}} = -\rho V_\infty b\gamma_w(b,t) \tag{5.12}$$

is the wake integral.

Von Karman and Sears [80] derived a particular expression of the lift acting on a plate in inviscid unsteady incompressible flow by computing the time derivative of the

hydrodynamic impulse of the complete vortex system (bound and free vorticity):

$$l = \rho V_\infty \int_{-b}^{b} \gamma_0(\xi,t)\mathrm{d}x - \rho \frac{d}{dt}\int_{-b}^{b} x\gamma_0(\xi,t)\mathrm{d}x + \rho b V_\infty \int_{b}^{\infty} \frac{\gamma_w(\eta,t)}{\sqrt{\eta^2-b^2}}\mathrm{d}\eta \ , \tag{5.13}$$

where γ_0 is the so called quasi-steady vorticity. This equation can also be derived by direct integration of equation (5.38) as shown appendix E.

The first term in equation (5.13) is the *quasi-steady* lift:

$$l_{QS} = \rho V_\infty \int_{-b}^{b} \gamma_0(\xi,t)\mathrm{d}x \ , \tag{5.14}$$

i.e. the lift obtained when the wake effect is neglected. Due to equation (E.17) and taking into account for the first of equations (E.11), it is also given by:

$$l_{QS} = -\rho V_\infty \int_{b}^{\infty} \sqrt{\frac{\eta+b}{\eta-b}}\gamma_w(\eta,t)\mathrm{d}\eta \ . \tag{5.15}$$

5.2.1 Linear decomposition of the aerodynamic force

The analysis has been restricted to periodic pitching and plunging motion:

$$\alpha = \bar{\alpha}\mathrm{e}^{\mathrm{i}\bar{\omega}_\alpha t} \ , \qquad h = \bar{h}\mathrm{e}^{\mathrm{i}\bar{\omega}_h t} \ . \tag{5.16}$$

Due to the linearity of the problem, each generic angular frequency $\bar{\omega}$ can be separately studied. Free vorticity is also be periodic with the same angular frequency $\bar{\omega}$ and, due to Kelvin theorem, it is shed along the wake with velocity V_∞; therefore

$$\gamma_w(\eta,t) = \bar{\gamma}_w \mathrm{e}^{i\bar{\omega}(t-\eta/V_\infty)} = \bar{\gamma}_w \mathrm{e}^{\mathrm{i}(\bar{\omega}t - k\bar{\eta})} \ , \tag{5.17}$$

where $\bar{\eta} = \eta/b$ and $k = \bar{\omega}b/V_\infty$ is the reduced frequency.

In case of harmonic oscillations we can explicitly compute each term of equation

(5.9) in which lift is decomposed. Indeed, following the same procedure suggested by Theodorsen and Mutchler, we can relate each term to the quasi-steady lift l_{QS}. In particular, we have:

$$l_\ell = \frac{l_\ell}{l_{QS}} l_{QS} = \frac{\int_1^\infty e^{-\mathrm{i}k\bar{\eta}} \mathrm{d}\bar{\eta}}{\int_1^\infty \sqrt{\frac{\bar{\eta}+1}{\bar{\eta}-1}} e^{-\mathrm{i}k\bar{\eta}} \mathrm{d}\bar{\eta}} l_{QS} \ . \tag{5.18}$$

The integrals in this equation are not convergent. However, as discussed by Bisplinghoff [81, p. 272], we can solve them assuming k complex with a vanishing negative imaginary part obtaining:

$$l_\ell = D(k) l_{QS} \ , \tag{5.19}$$

with

$$D(k) = \frac{2\mathrm{i}}{\pi k} \frac{e^{-\mathrm{i}k}}{[H_1^{(2)}(k) + \mathrm{i}H_0^{(2)}(k)]} \ , \tag{5.20}$$

where $H_\nu^{(2)} = J_\nu - \mathrm{i}Y_\nu$ is one of the Hankel functions and J_ν, Y_ν are respectively Bessel functions of the first and second kind.

Similarly, we also have

$$l_{S_{far}} = \mathrm{i}kD(k) l_{QS} \ . \tag{5.21}$$

A slightly more complex analysis is necessary for l_τ given by:

$$l_\tau = -\rho \frac{d}{dt} \int_{-b}^{b} x\gamma_0(x,t) \mathrm{d}x - \rho \frac{d}{dt} \int_{-b}^{b} x\gamma_1(x,t) \mathrm{d}x \ . \tag{5.22}$$

The first term in this equation is the so called *non-circulatory* lift l_{NC}. Due to equation (E.19) we have

$$l_\tau = l_{NC} - \rho b^2 \frac{d}{dt} \int_1^\infty \bar{\gamma}_w \mathrm{e}^{\mathrm{i}(\bar{\omega}t - k\bar{\eta})} \left(\sqrt{\bar{\eta}^2 - 1} - \eta \right) \mathrm{d}\bar{\eta} \ . \tag{5.23}$$

Computing the time derivative, multiplying and dividing by l_{QS} and solving the integrals

we finally obtain

$$l_\tau = l_{NC} + \mathrm{i}kE(k)l_{QS} \ , \tag{5.24}$$

where

$$E(k) = -\frac{\mathrm{i}\pi k^2[H_0^{(2)}(k) + H_2^{(2)}(k)] + 4\mathrm{i}(k-\mathrm{i})\mathrm{e}^{-\mathrm{i}k}}{2\pi k^2[H_1^{(2)}(k) + \mathrm{i}H_0^{(2)}(k)]} \ . \tag{5.25}$$

Summing equations, (5.19), (5.21) and (5.24):

$$l = l_\ell + l_\tau + l_{S_{far}} = l_{NC} + C(k)l_{QS} \ , \tag{5.26}$$

where

$$C(k) = D(k) + \mathrm{i}kD(k) + \mathrm{i}kE(k) = \frac{H_1^{(2)}}{H_1^{(2)} + \mathrm{i}H_0^{(2)}} \tag{5.27}$$

is the Theodorsen's function.

Assuming $w_a = \sum_{n=0}^{\infty} w_n \cos(n\theta)$ with $x = b\cos\theta$, where w_a is velocity distribution on the plate, we have

$$w_0 = -V_\infty \alpha - \dot{h} + \dot{\alpha}ab \ , \qquad w_1 = -b\dot{\alpha} \ , \qquad w_n = 0 \quad \forall n \geq 2 \ . \tag{5.28}$$

It can be shown (see Bisplinghoff [81]) that quasi-steady and non circulatory lift for periodic flow, through the expression (E.15) of γ_0, become:

$$l_{QS} = \rho V_\infty \int_{-b}^{b} \gamma_0(x,t)\mathrm{d}x = 2\pi\rho V_\infty b \left[V_\infty \alpha + \dot{h} + b\left(\frac{1}{2} - a\right)\dot{\alpha}\right] \tag{5.29}$$

and

$$l_{NC} = -\rho\frac{d}{dt}\int_{-b}^{b} x\gamma_0(x,t)\mathrm{d}x = \pi\rho b^2\left(V_\infty\dot{\alpha} + \ddot{h} - ab\ddot{\alpha}\right) \ . \tag{5.30}$$

With these expressions of l_{NC} and l_{QS}, equation (5.26) exactly returns the lift formula of Theodorsen and Mutchler.

Summarizing the results of the Lamb vector based decomposition, we re-write each obtained contribution to the lift coefficient $C_l = C_{l_\ell} + C_{l_{S_{far}}} + C_{l_\tau}$, adopting as usual

$\rho V_\infty^2 b$ as reference force per unit length:

$$C_{l_\ell} = 2\pi D(k)\left[\alpha + \left(\frac{1}{2} - a\right)\frac{b\dot{\alpha}}{V_\infty} + \frac{\dot{h}}{V_\infty}\right] , \tag{5.31}$$

$$C_{l_{S_{far}}} = 2\pi \mathrm{i}kD(k)\left[\alpha + \left(\frac{1}{2} - a\right)\frac{b\dot{\alpha}}{V_\infty} + \frac{\dot{h}}{V_\infty}\right] \tag{5.32}$$

and

$$C_{l_\tau} = \pi\left(\frac{b\dot{\alpha}}{V_\infty} - a\frac{b^2\ddot{\alpha}}{V_\infty^2} + \frac{b\ddot{h}}{V_\infty^2}\right) + 2\pi \mathrm{i}kE(k)\left[\alpha + \left(\frac{1}{2} - a\right)\frac{b\dot{\alpha}}{V_\infty} + \frac{\dot{h}}{V_\infty}\right] . \tag{5.33}$$

Present decomposition gives some additional information. An interesting result is that l_{NC}, the non circulatory lift, only contributes to C_{l_τ}. l_{NC} with its second order time derivative terms is interpreted as an *added mass* and is all taken into account by the time variation of the hydrodynamic impulse on the body. In addition, it gives the possibility to decouple the effects of α, $\dot{\alpha}$ and $\ddot{\alpha}$ as shown in the next section.

5.3 Definition of the dynamic force derivatives $C_{l\alpha}$, $C_{l\dot{\alpha}}$ and $C_{l\ddot{\alpha}}$ in nonlinear flows

Equation (5.27) decomposes Theodorsen's function, the coefficient of the circulatory part, in three contributions, respectively associated with the vortex force on the body ($D(k)$), the wake ($\mathrm{i}kD(k)$) and body impulse variation ($\mathrm{i}kE(k)$). The complex nature of $C(k)$ is important because it highlights a lag between the obtained force and its cause.

$D(k)$, $\mathrm{i}kD(k)$, $\mathrm{i}kE(k)$ and $\tilde{C}(k) = D(k) + \mathrm{i}kD(k)$ are compared with $C(k)$ in figure 5.1. In particular $\tilde{C}(k)$, providing the contribution and lag due to l_ℓ and $l_{S_{far}}$, tends to $C(k)$ as $k \to 0$. The local behavior for $k \to 0$ is

$$\tilde{C}(k) = C(k) \approx \frac{2\mathrm{i}}{\pi k(H_1(k) + \mathrm{i}H_0(k)} . \tag{5.34}$$

Figure 5.1 confirms this behavior, being $\tilde{C}(k)$ very close to $C(k)$ in the range $0 <$

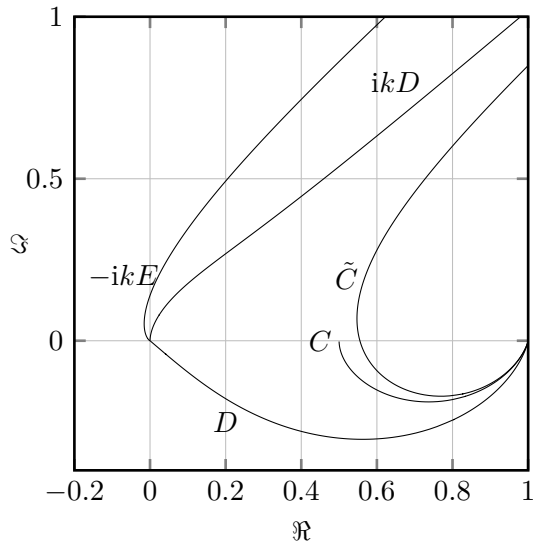

Figure 5.1 Diagrams of $C(k)$, $\tilde{C}(k)$, $D(k)$, i$kD(k)$, i$kE(k)$ in the complex plane.

$k < 0.1$. This aspect is further evidenced by analysing individually the real $\tilde{F}(k)$ and imaginary part $\tilde{G}(k)$ of $\tilde{C}(k)$, see figure 5.2. Both $\tilde{F}(k)$ and $\tilde{G}(k)$ are indistinguishable from their corresponding terms in Theodorsen's function $F(k)$ and $G(k)$ up to $k \approx 0.25$. Moreover the real part $\Re(\mathrm{i}kE)$ is very small when compared with $\tilde{F}(k)$ implying that $\tilde{F}(k)$ well approximates $F(k)$ up to $k \approx 1$.

This result can be exploited to propose a new definition of the dynamic force derivatives. Indeed, the dynamic force derivatives are usually computed by experiments or by nonlinear numerical analysis imposing a small periodic time variation of α or h and performing a Fourier analysis of the obtained forces and moments. This analysis provides a separation between *in-phase* and *out-of-phase* contributions, but the effects of the in-phase perturbations (for instance α and $\ddot{\alpha}$) cannot be completely decoupled. In particular, the relation between the result of the Fourier analysis of $C_l(t)$ (with an overbar) and the exact values is

$$\bar{C}_{l\alpha} = C_{l\alpha} - k^2 C_{l\ddot{\alpha}} \ , \qquad \bar{C}_{l\dot{\alpha}} = C_{l\dot{\alpha}} \tag{5.35}$$

as well described by Da Ronch et al. [82], among others.

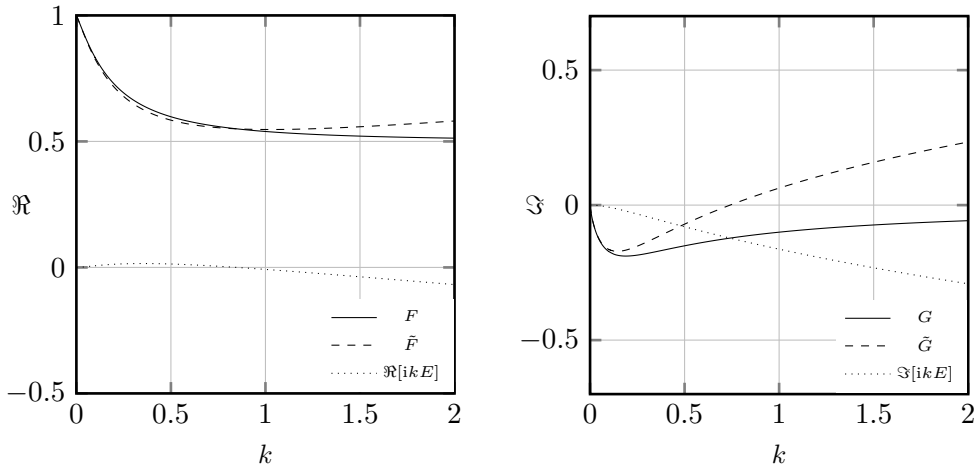

Figure 5.2 Real (left) and imaginary (right) parts of $C(k)$, $\tilde{C}(k)$ and $ikE(k)$ against reduced frequency k.

This limit can be overcome by present decomposition. Indeed, in case of oscillating inviscid plate the correct value is known: $C_{l\alpha} = 2\pi F(k)$ and is very well approximated by $2\pi\tilde{F}(k)$ up to $k = 1$ as shown in figure 5.3. In the same figure $\bar{C}_{l\alpha}$, as obtained by the analytic solution, is also plotted; it approximates $C_{l\alpha}$ in the quasi-steady regime only ($k < 0.05$).

The α derivative of the vortex force and of the wake contribution , denoted respectively $C_{l_{\ell\alpha}}$ and $C_{l_{S_{far}\alpha}}$, can be obtained by standard Fourier analyses of the case $a = 1/2$ since C_{l_ℓ} and $C_{l_{S_{far}}}$ do not depend on $\dot{\alpha}$ (for $a = 1/2$) and $\ddot{\alpha}$ as evidenced by equations (5.31) and (5.32). Therefore, $C_{l_{\ell\alpha}}$ and $C_{l_{S_{far}\alpha}}$ can be obtained without interference with $\ddot{\alpha}$ effects and a decoupled value of $C_{l\alpha}$ can be recovered:

$$C_{l\alpha} \equiv C_{l_{\ell\alpha}} + C_{l_{S_{far}\alpha}} \ . \tag{5.36}$$

It is exactly given by $2\pi\tilde{F}(k)$ in case of inviscid oscillating plate. The computation of the dynamic derivatives can be completed, since $C_{l\dot{\alpha}}$ is correctly obtained by the Fourier analysis, whereas $C_{l\ddot{\alpha}}$ can be recovered by the first of equations (5.35) being $\bar{C}_{l\alpha}$ and $C_{l\alpha}$ already known.

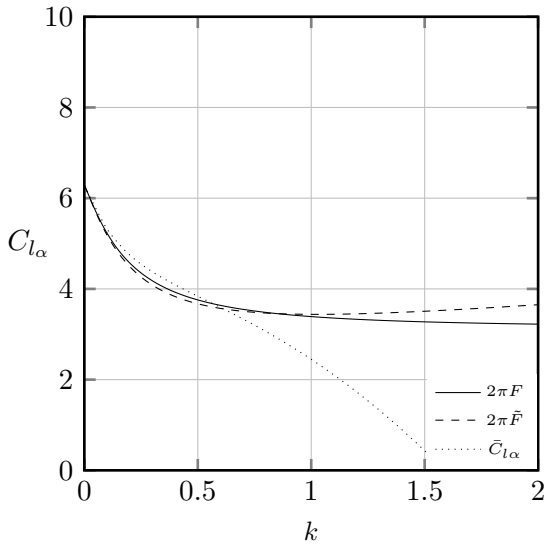

Figure 5.3 Comparison of the different definitions of dynamic force derivative $C_{l\alpha}$ against reduced frequency k.

5.4 Numerical analysis of an incompressible oscillating flat plate flow

Two-dimensional unsteady simulations of an oscillating flat plate flow have been performed by the flow solver FLOWer [68], already presented in section 4.1.3. The time integration method and the numerical schemes are the same. Imposed freestream Mach number is $M_\infty = 0.1$ in all calculations which have been performed by a moving grid method. A cartesian mesh strongly refined near the plate has been adopted. Specifying with N the number of grid cells around the plate, $N/2$ cells were used along the wake and $N/4$ in the direction orthogonal to the plate, with the far field boundary distant approximately 100 airfoil chords from the body.

The flow post-processing has been performed with an ad-hoc Fortran code, which input is the structured FLOWer solution, and gives as output the force decomposition. The numerical integration method is the same presented in section (4.1.3).

A grid convergence study was carried out analyzing a steady simulation ($\alpha = 30°$ and

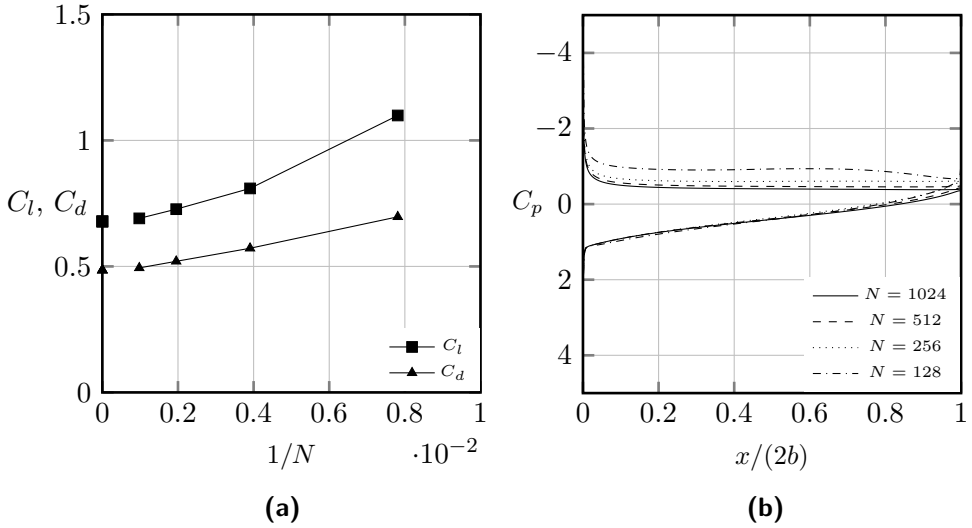

Figure 5.4 Flat plate, $M_\infty = 0.1$, $Re_\infty = 300$, $\alpha = 30°$. Lift, drag and pressure coefficient versus grid density.

$Re_\infty = 300$). Figure 5.4 confirms the convergence as the mesh is refined by showing computed near field lift and drag coefficients versus $1/N$ together with Richardson's extrapolation to zero mesh size and associated pressure coefficient distributions on the plate.

The validation of the unsteady simulations has been performed comparing the computed time evolution of the near field lift coefficient with the result of Liu et al. [76]. Figure 5.5 (T is the time period) proposes a sub-stall case for a pitching and plunging plate at $k = 0.06\pi$ and $Re_\infty = 300$. Present near field lift coefficient perfectly agrees with the solution of Liu et al. already with the grid with $N = 256$. On the contrary, some discrepancies are present in case of dynamic stall which is characterized by a much more complex unsteady flow field, see figure 5.6. Therefore calculations performed with the refined grid with $N = 512$ were also repeated halving time step ($\Delta t = T/400$). The secondary peaks proposed by the reference solution also appear in the refined solution, suggesting convergence while reducing both mesh size and time step. In order to reduce computational costs, all unsteady simulations were subsequently performed with the grid with $N = 256$. They are sufficient for our purposes since, even if they still have some

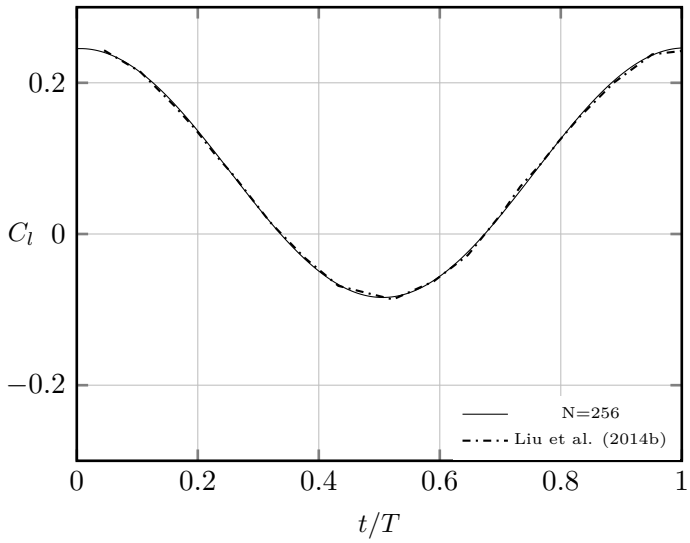

Figure 5.5 Pitching and plunging flat plate. $\alpha = 1^\circ + 3^\circ \cos(kV_\infty t/b)$, $h/(2b) = 0.025 \sin(kV_\infty t/b)$, $k = 0.06\pi$, $Re_\infty = 300$. Comparison of computed lift coefficients with near field calculation of Liu et al. [76].

discrepancies with the 0-mesh size extrapolation results, our main interest is here for the analysis of the force breakdown and comparisons with the near field force computation. Strict convergence to a very low residual has been obtained in all calculations, adopting 200 time steps for each time period and 1000 sub-iterations in the dual time stepping time integration method.

Subscripts a and c have been adopted respectively to specify aerodynamic coefficients obtained by equations (3.1) and (5.6). Computed lift and drag coefficients are reported; subscripts again specify the decomposition according to the nomenclature defined in equations (3.1) and (5.6). Integrations have been performed assuming a constant value in each grid cell for volume integrals and on each cell face for surface integrals. The sensitivity to the adopted integration domain $\mathcal{V}$ has been preliminarily investigated. Indeed the accuracy in the computation of the volume and surface integrals can be largely affected, in particular when the integration domain increases also including flow regions with a poorly refined grid. A rectangular integration domain has been used with the front edge two chords ahead of the airfoil and the two side edges placed at two chords from the plate. The

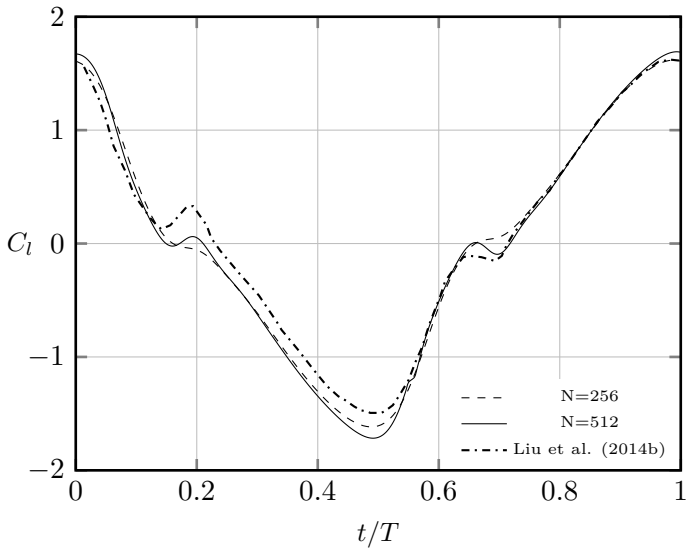

Figure 5.6 Pitching and plunging flat plate. $\alpha = 30° \cos(kV_\infty t/b)$, $h/(2b) = 0.25 \sin(kV_\infty t/b)$, $k = 0.06\pi$, $Re_\infty = 300$. Comparison of computed lift coefficients with near field calculation of Liu et al. [76].

aerodynamic coefficients have been computed changing the wake plane position $x_S/(2b)$. The results obtained by equation (5.6) are compared with the near field result in figure 5.7. The pitching case $k = 0.05$, $Re = 300$ and $\bar{\alpha} = 5°$ is reported at time $t/T = 0.25$ when the plate is at $\alpha = 5°$. The agreement with the near field results is excellent for both equations and the sensitivity to the adopted $\mathcal{V}$ is very weak as far as the grid is sufficiently refined, first discrepancies appear in the computed lift for $x_S/(2b) > 2$. All results presented in what follows have been obtained adopting $x_S/(2b) = 1.005$, because excluding the wake from the integration domain we obtain a straightforward comparison with the analytical inviscid results and separation of the effects of the bound and free vorticity.

The contribution to lift (C_{l_μ}) and drag (C_{d_μ}) of the term explicitly depending on viscosity $\boldsymbol{\Delta}_\mu$ have been analyzed in both sub-stall and dynamic stall cases. As expected they are negligible when the boundary layer hypothesis is fulfilled (sub-stall case) being $|C_{l_\mu}| < 0.0005$ and $|C_{d_\mu}| < 0.002$. Even in the dynamic stall case, characterized by

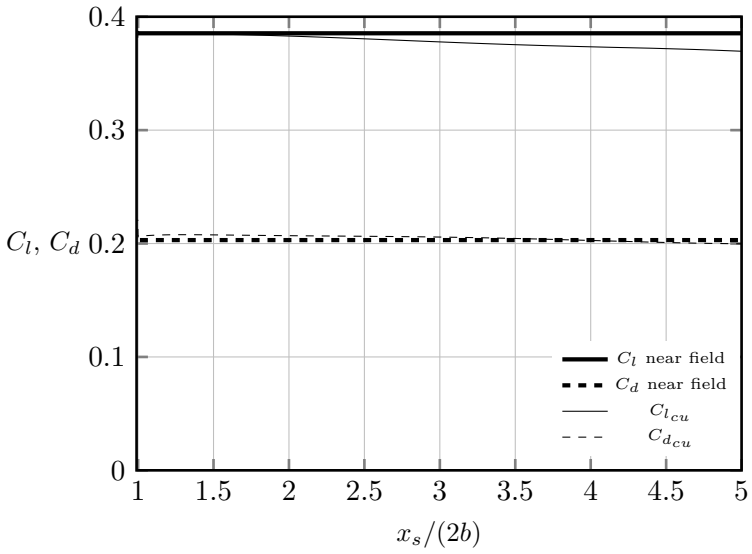

Figure 5.7 Pitching flat plate, $\bar{\alpha} = 5°$, $k = 0.05$, $Re_\infty = 300$, $t/T = 0.25$. Lift and drag computations by equation (5.6) against wake plane position. $x_s/(2b) = 1$ specifies plate trailing edge.

large regions of separated flow, $\boldsymbol{\Delta}_\mu$ is a minor contribution to the aerodynamic force ($|C_{l_\mu}| < 0.08$ and and $|C_{d_\mu}| < 0.02$), however in the following it will always be included in all figures when the total lift and drag coefficients will be reported.

In what follows the analysis has been performed separating pitching and plunging cases thus obtaining a more clear comparison with the analytical inviscid results.

5.4.1 Pitching motion

5.4.1.1 Low Reynolds number case

The numerical simulations were performed at Reynolds number $Re_\infty = 300$. A sub-stall ($\bar{\alpha} = 5°$) and a dynamic stall condition ($\bar{\alpha} = 30°$) were studied, both for $k = 0.05$ and $k = 0.5$ with the rotation center placed at $a = -1/2$. The pitching law is $\alpha(t) = \bar{\alpha}\sin(\bar{\omega}t)$. Four snapshots of the non dimensional vorticity field (ω^*) for the case $k = 0.05$, $\bar{\alpha} = 30°$ are shown in figure 5.8. The typical leading edge vortex formation and its downstream convection is shown.

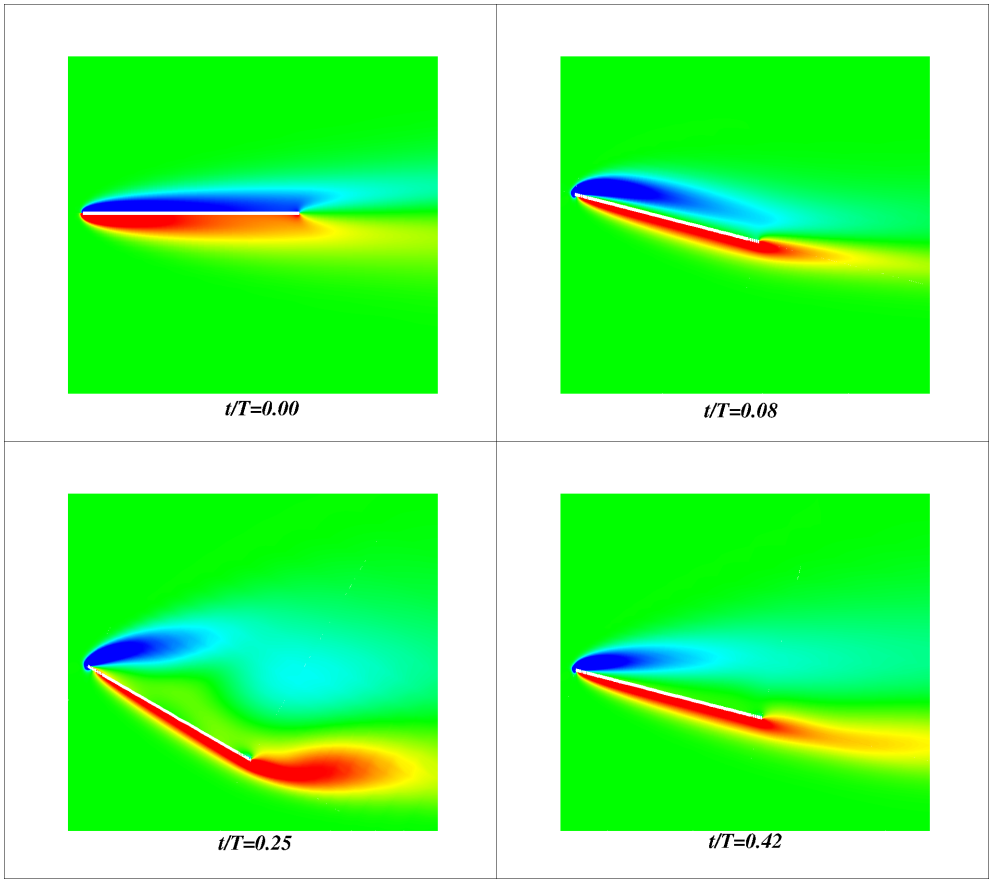

Figure 5.8 Pitching flat plate, $\bar{\alpha} = 30°$, $k = 0.05$, $Re_\infty = 300$. Vorticity contours snapshots at different times, $\Delta\omega^* = 0.3$.

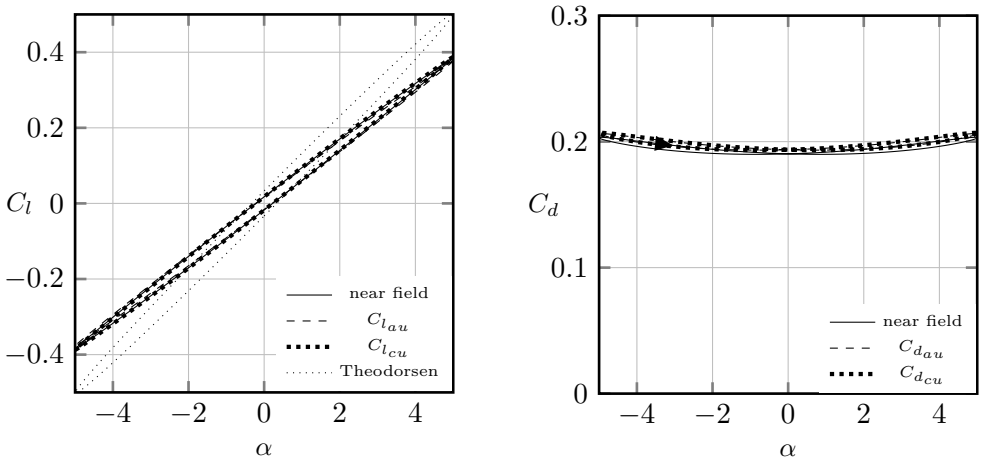

Figure 5.9 Pitching flat plate, $\bar{\alpha} = 5°$, $k = 0.05$, $Re_\infty = 300$. Comparison between near field and mid-field calculations of lift and drag coefficients.

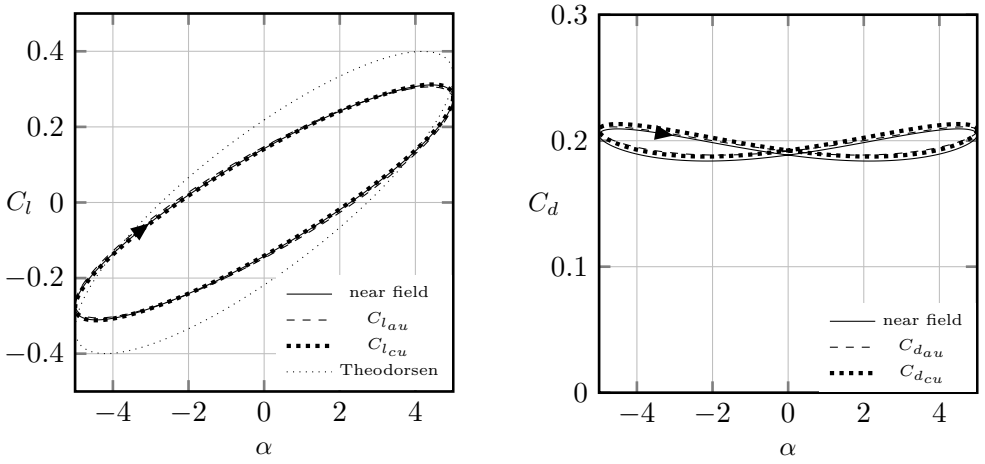

Figure 5.10 Pitching flat plate, $\bar{\alpha} = 5°$, $k = 0.5$, $Re_\infty = 300$. Comparison between near field and mid-field calculations of lift and drag coefficients.

The comparison with the reference near field results for all simulations are presented in the $C_l - \alpha(t)$ and $C_d - \alpha(t)$ diagrams, figures 5.9-5.12. The mixed inertial-non inertial formula $\boldsymbol{F}_{cu}$ is in agreement with the near field results in all the tests for lift and drag contributions. The inertial formula $\boldsymbol{F}_{au}$ has some small discrepancies in the lift coefficient at the highest incidences in the cases $\bar{\alpha} = 30°$ and more marked differences appear for the

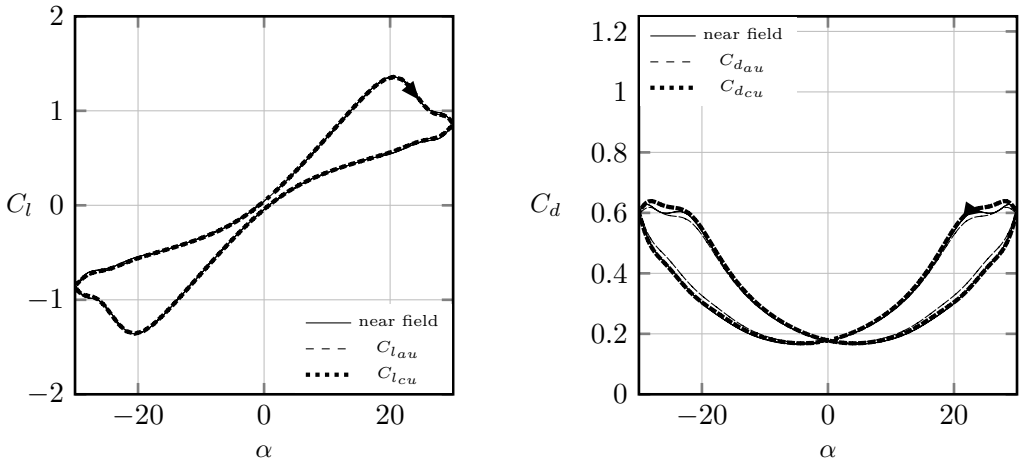

Figure 5.11 Pitching flat plate, $\bar{\alpha} = 30°$, $k = 0.05$, $Re_\infty = 300$. Comparison between near field and mid-field calculations of lift and drag coefficients.

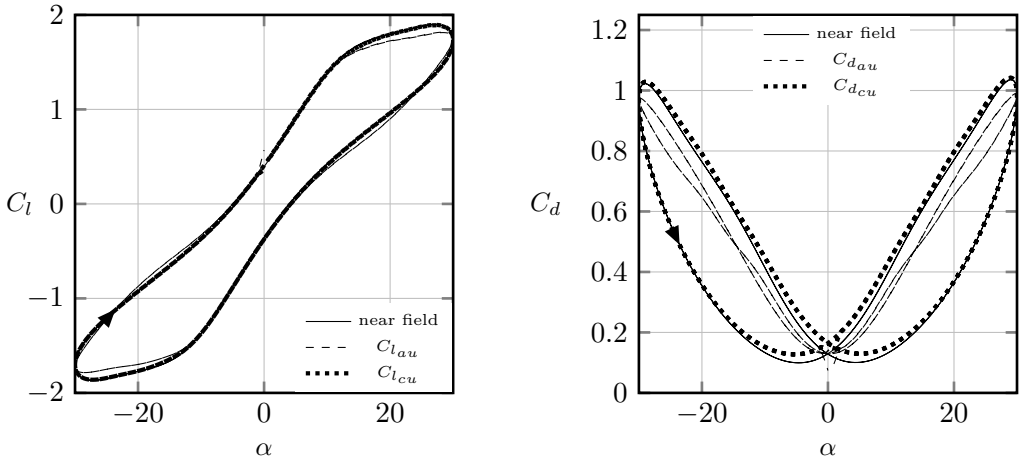

Figure 5.12 Pitching flat plate, $\bar{\alpha} = 30°$, $k = 0.5$, $Re_\infty = 300$. Comparison between near field and mid-field calculations of lift and drag coefficients.

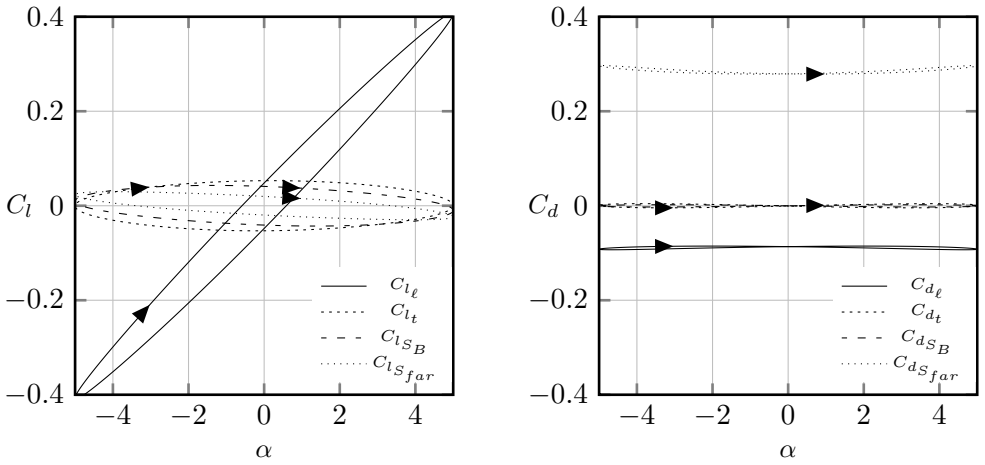

Figure 5.13 Pitching flat plate, $\bar{\alpha} = 5°$, $k = 0.05$, $Re_\infty = 300$. Lift and drag decomposition by equation (3.1) ($\boldsymbol{F}_{au}$).

drag computation. The unacceptable results for drag obtained by inertial formula $\boldsymbol{F}_{au}$ should be noted in the case $\bar{\alpha} = 30°$, $k = 0.5$. They are due to the more complex and less accurate calculation of the Eulerian time derivative in an inertial reference in the case of a moving grid, see equation (5.4).

The shown hysteresis cycles highlight the lag between instantaneous angle of attack and force variations (the arrows in the plots specify the direction of increasing time). The dynamic stall phenomenon with the associated lift enhancement for $\bar{\alpha} = 30°$ is evident, taking into account that the computed static stall angle is $\alpha_s = 14°$ with a corresponding maximum lift coefficient $C_{l_{max}} = 0.75$ (computations not shown).

The force decomposition obtained by equations (3.1) and (5.6) in the case $\bar{\alpha} = 5°$, $k = 0.05$ are proposed in figures 5.13 and 5.14.

It can be noted that $C_{l_{\ell'}} \approx C_{l_\ell}$ and $C_{l_{S'_{far}}} \approx C_{l_{S_{far}}}$. This result depends on identity (D.8) taking into account that the lift contribution of $\boldsymbol{F}_{\ell_T}$ is clearly zero in case of plunging motion and is negligible in case of small pitching oscillations since it is obtained by integration of a term of order $\alpha\dot{\alpha}V_\infty/b$.

The essential contribution to drag is given by the wake term $C_{d_{S_{far}}}$ in equation (3.1) or $C_{d_{S'_{far}}}$ in equation (5.6), whereas bound vortex force contribution C_{d_ℓ} and $C_{d_{\ell'}}$

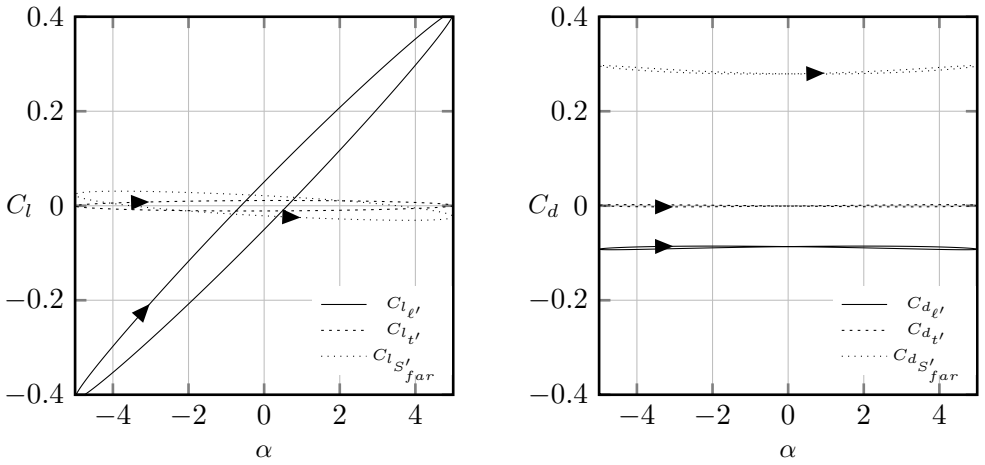

Figure 5.14 Pitching flat plate, $\bar{\alpha} = 5°$, $k = 0.05$, $Re_\infty = 300$. Lift and drag decomposition by equation (5.6) ($\boldsymbol{F}_{cu}$).

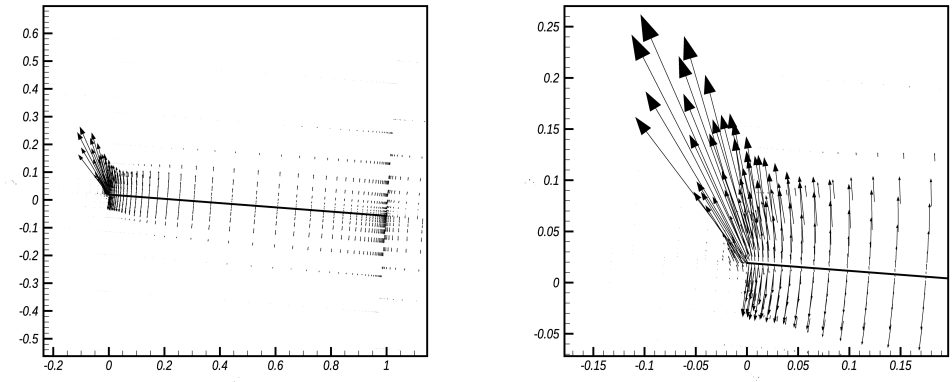

Figure 5.15 Pitching flat plate, $\bar{\alpha} = 5°$, $k = 0.5$, $Re_\infty = 300$, $t/T = 0.25$. $-\boldsymbol{\ell}$ vector field around the plate (left) with an enlargement of the leading edge region (right).

interestingly provides a significant and nearly constant thrust. Again, as for lift, $C_{d_{\ell'}} \approx C_{d_\ell}$ and $C_{d_{S'_{far}}} \approx C_{d_{S_{far}}}$. The generation of the thrust force is evidenced in figure 5.15 where a snapshot of the vector field $-\boldsymbol{\ell}$ is plotted ($\alpha = 5°$, $k = 0.5$). Thrust is clearly generated on the suction side of the plate leading edge; on most of the plate $-\boldsymbol{\ell}$ essentially contributes to lift; it is vanishing outside of the boundary layer.

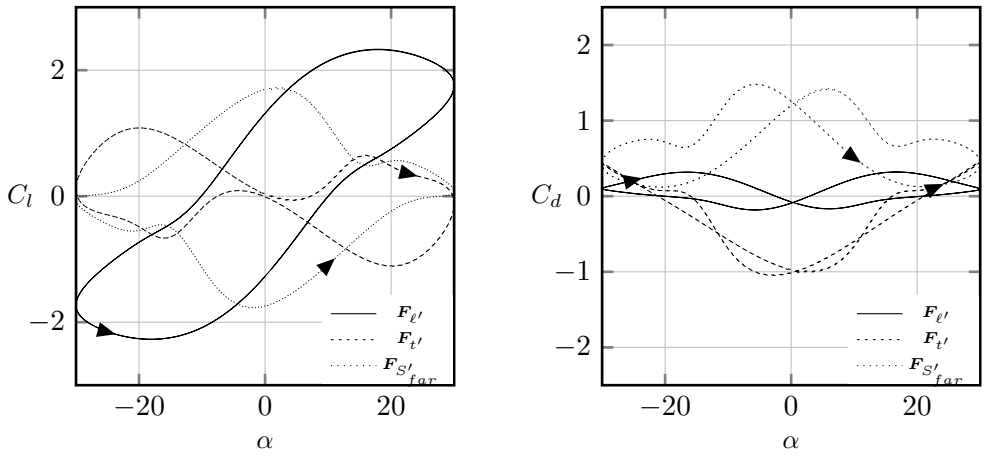

Figure 5.16 Pitching flat plate, $\bar{\alpha} = 30°$, $k = 0.5$, $Re_\infty = 300$. Lift and drag decomposition by equation (5.6) ($\boldsymbol{F}_{cu}$).

The force decomposition for a dynamic stall case is presented in figure 5.16. As anticipated, in this case ($\bar{\alpha} = 30°$, $k = 0.5$) only $\boldsymbol{F}_{cu}$ formula provided accurate results. The different contributions have a much more complex behavior. In this stalled condition, the thrust component of the vortex force is oscillating around zero.

The analytical lift coefficient formula of Theodorsen & Mutchler is also plotted in figures 5.9-5.10. Despite of a qualitative agreement, differences are remarkable even in these sub-stall conditions evidencing the significant impact of nonlinearities at low Reynolds numbers.

5.4.1.2 High Reynolds number case

A more interesting comparison with the inviscid analytical solution requires a high Reynolds number analysis which has been performed solving the Unsteady Reynolds Averaged Navier-Stokes (URANS) equations. Calculations were obtained by the same solver adopting the standard $\kappa - \omega$ SST turbulence model and a refined grid in the boundary layer and wake. Different tests were analyzed at $Re_\infty = 1 \cdot 10^6$ and $M_\infty = 0.1$ and $a = -1/2$. Diagrams $C_l - \alpha(t)$ and $C_d - \alpha(t)$ for $\bar{\alpha} = 3°$ and $k = 0.05$ are presented in figure 5.17.

The results of inertial formula (3.1) are characterized by strong oscillations and are

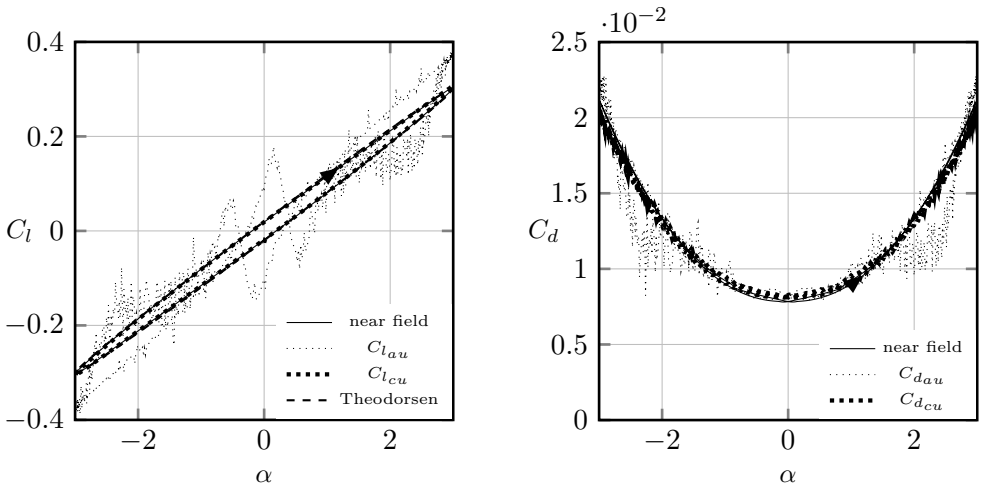

Figure 5.17 Pitching flat plate, $\bar{\alpha} = 3°$, $k = 0.05$, $Re_\infty = 1 \cdot 10^6$. Comparison between near field and mid-field calculations of lift and drag coefficients.

clearly unacceptable, whereas the mixed inertial non-inertial formula (5.6) is again in excellent agreement with near field result. As already discussed, the problem is given by the poor accuracy in the computation of $\boldsymbol{F}_{t_T}$ which depends on $\boldsymbol{\nabla}\omega$. Anyway, the decomposition by $\boldsymbol{F}_{au}$ formula can be recovered by an indirect calculation of $\boldsymbol{F}_{t_T}$ thanks to the identity (D.8).

For this high Reynolds number case, it is also interesting to compare the computed lift decomposition (indirect calculation of $\boldsymbol{F}_{au}$) with analytical formulae, imaginary part of equations (5.31), (5.32) and (5.33). The comparison is presented in figure 5.18, where the lift coefficient contributions are plotted against time. The computed results are in very good agreement with the theoretical values.

These results led to the numerical computation of the dynamic force derivative $C_{l\alpha}$ by equation (5.36), with contributions $C_{l_{\ell\alpha}}$ and $C_{l_{S_{far}{}^\alpha}}$ computed by Fourier analysis as discussed in section 5.3. The results are compared with expected inviscid theoretical value in figure 5.19. Flow calculations were performed at $Re_\infty = 1 \cdot 10^6$ and $Re_\infty = 300$ ($\bar{\alpha} = 3°$, $a = 1/2$). The agreement for $Re_\infty = 1 \cdot 10^6$ is impressive such as the advantage of following present numerical computation of $C_{l\alpha}$ with respect to classical $\bar{C}_{l\alpha}$ computation in case of high values of k (see figure 5.3). The nonlinear effects are evidenced in the case

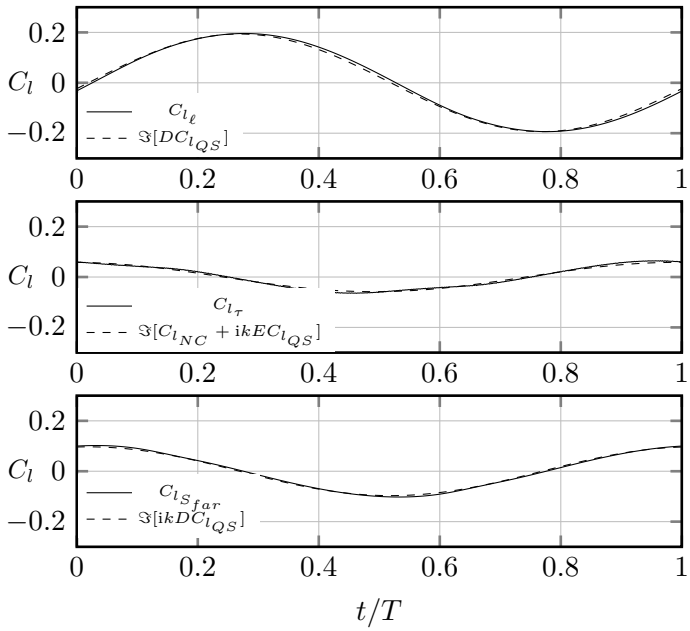

Figure 5.18 Pitching flat plate, $\bar{\alpha} = 3°$, $k = 0.5$, $Re_\infty = 1 \cdot 10^6$. Comparison of Lamb vector based lift decomposition with inviscid theoretical result of Theodorsen and Mutchler [79].

$Re_\infty = 300$, characterized by a significant lower value of $C_{l\alpha}$.

Figures 5.20 and 5.21 present the same comparison for $C_{l\dot{\alpha}}$ and $C_{l\ddot{\alpha}}$. The reference analytical equations are:

$$kC_{l\dot{\alpha}} = \pi k + 2\pi kF(k)\left(\frac{1}{2} - a\right) + 2\pi G(k) \ , \qquad k^2 C_{l\ddot{\alpha}} = -a\pi k^2 + 2\pi kG(k)\left(\frac{1}{2} - a\right) \ . \tag{5.37}$$

5.4.2 Plunging motion

5.4.2.1 Low Reynolds number case

The plunging motion of the plate was also studied. The results for $\bar{h}/(2b) = 0.025$, $k = 0.05$ and $Re_\infty = 300$ are here presented. The plunging motion imposed is $h = \bar{h}\sin(\bar{\omega}t)$.

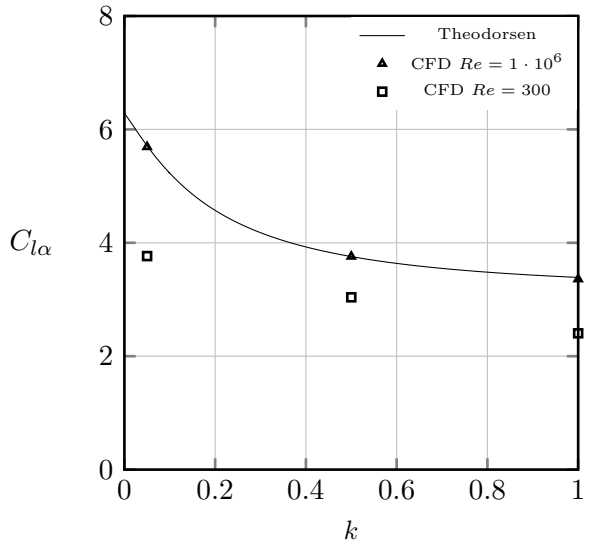

Figure 5.19 Pitching flat plate, $a = 0.5$, dynamic force derivative $C_{l\alpha}$. Computed values vs reference analytical inviscid values.

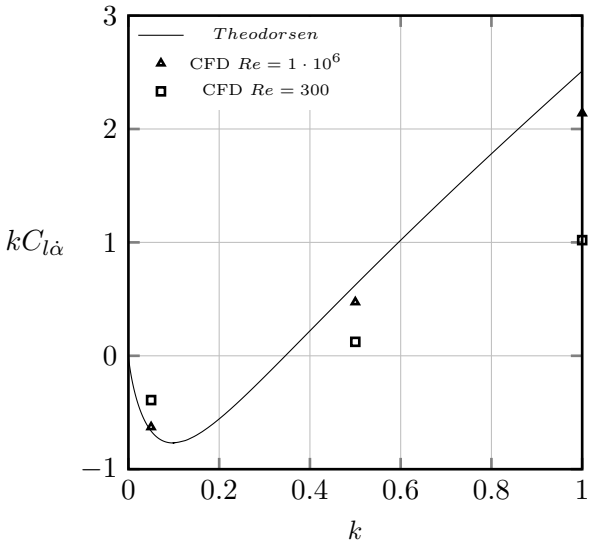

Figure 5.20 Pitching flat plate, $a = 0.5$, dynamic force derivative $C_{l\dot{\alpha}}$. Computed values vs reference analytical inviscid values.

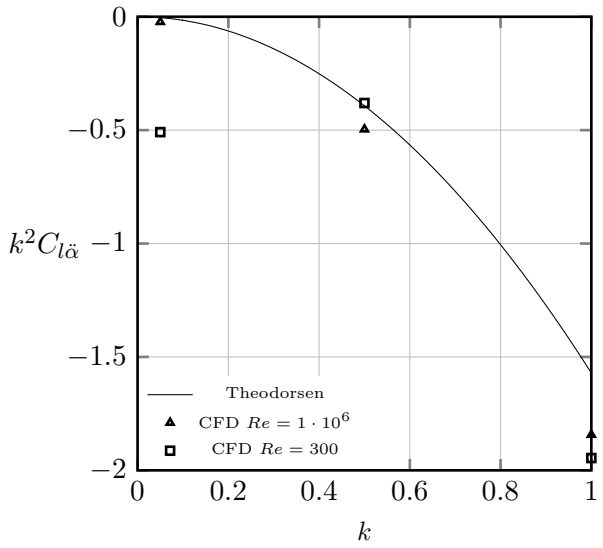

Figure 5.21 Pitching flat plate, $a = 0.5$, dynamic force derivative $C_{l\ddot{\alpha}}$. Computed values vs reference analytical inviscid values.

Figure 5.22 proposes the comparison with the near field force, whereas figures 5.23 and 5.24 respectively propose the decomposition of $\boldsymbol{F}_{au}$ and $\boldsymbol{F}_{cu}$. The results of the pitching motion analysis are substantially confirmed, since $C_{d_\ell} \approx C_{d_{\ell'}}$, $C_{d_{S_{far}}} \approx C_{d_{S'_{far}}}$, and the vortex force gives a nearly constant thrust contribution, while $C_{d_{S_{far}}}$ is the essential contribution to drag. In this case of small plunging amplitude the results of equations (3.1) and (5.6) are in perfect agreement; again a nearly constant thrust contribution due to $\boldsymbol{F}_\ell$ or equivalently to $\boldsymbol{F}_{\ell'}$, is evidenced.

5.4.2.2 High Reynolds number case

As for the pitching motion, in case of high Reynolds numbers, the agreement of the computed lift coefficient with the analytical expression of Theodorsen & Mutchler is very good, as shown in figure 5.25 for the case $\bar{h}/(2b) = 0.025$, $k = 0.5$ and $Re_\infty = 1 \cdot 10^6$. Again, accurate results were only obtained by $\boldsymbol{F}_{cu}$ formula.

The comparison of the computed lift decomposition with analytical expressions (5.31), (5.32) and (5.33) in case of plunging motion is proposed in figure 5.26. The agreement is

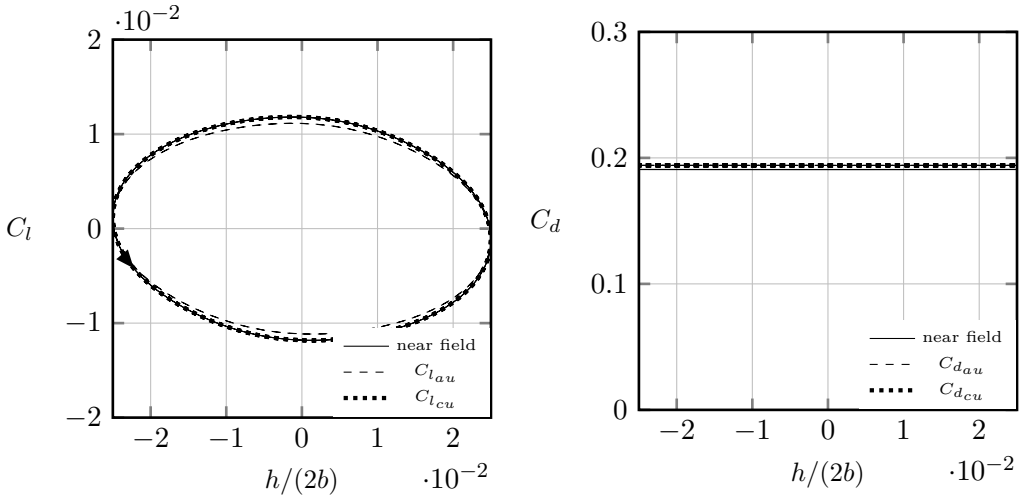

Figure 5.22 Plunging flat plate, $\bar{h}/(2b) = 0.025$, $k = 0.05$, $Re_\infty = 300$. Comparison between near field and mid-field calculations of lift and drag coefficients.

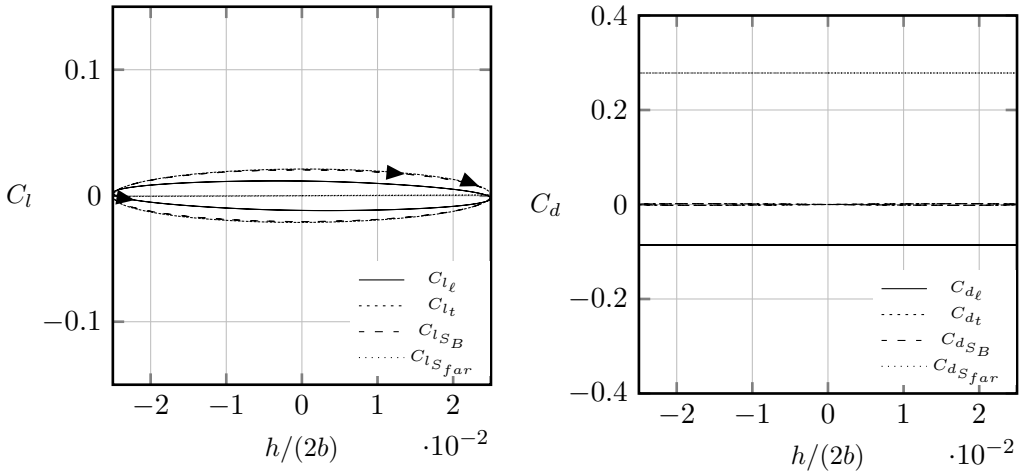

Figure 5.23 Plunging flat plate, $\bar{h}/(2b) = 0.025$, $k = 0.05$, $Re_\infty = 300$. Lift and drag decomposition by equation (3.1) ($\boldsymbol{F}_{au}$).

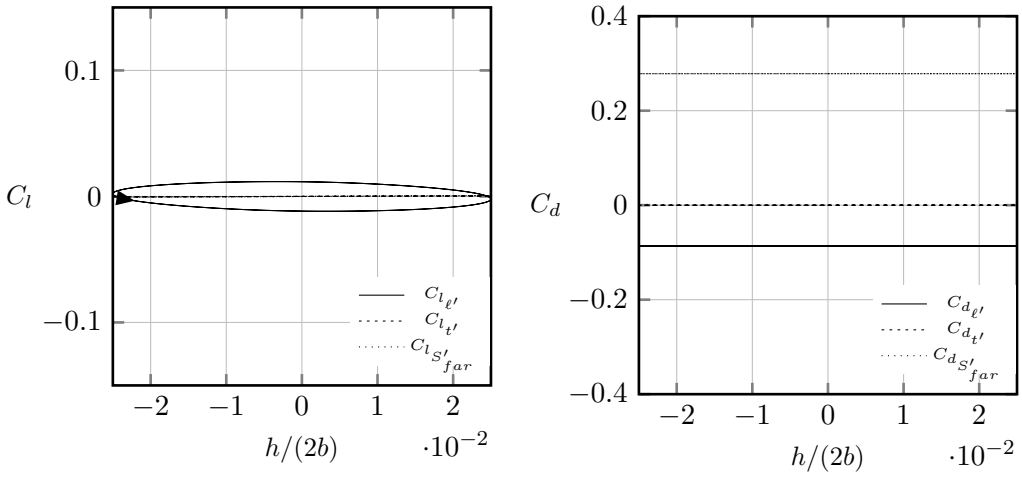

Figure 5.24 Plunging flat plate, $\bar{h}/(2b) = 0.025$, $k = 0.05$, $Re_\infty = 300$. Lift and drag decomposition by equation (5.6) ($\boldsymbol{F}_{cu}$).

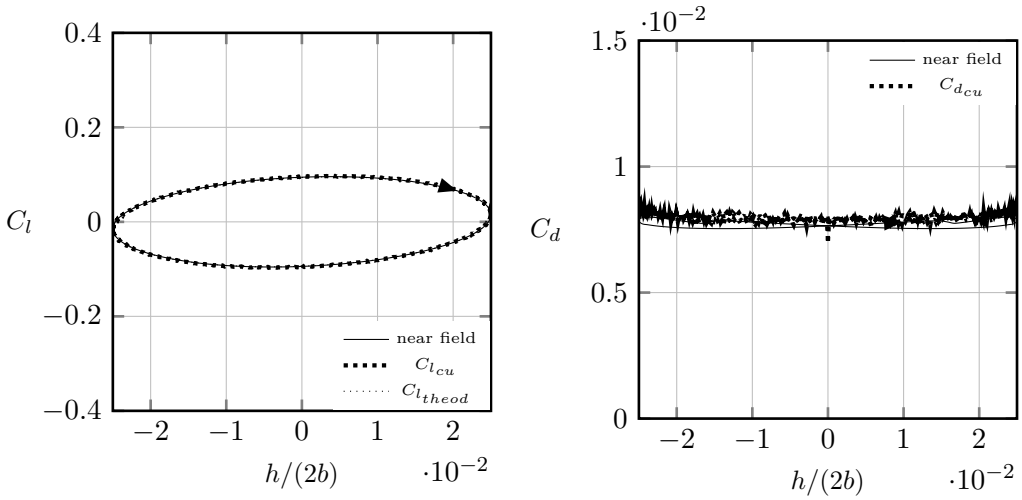

Figure 5.25 Plunging flat plate, $\bar{h}/(2b) = 0.025$, $k = 0.5$, $Re_\infty = 1 \cdot 10^6$. Comparison between near field and mid-field calculations of lift and drag coefficients. Dotted line is the inviscid analytical solution of Theodorsen and Mutchler [79].

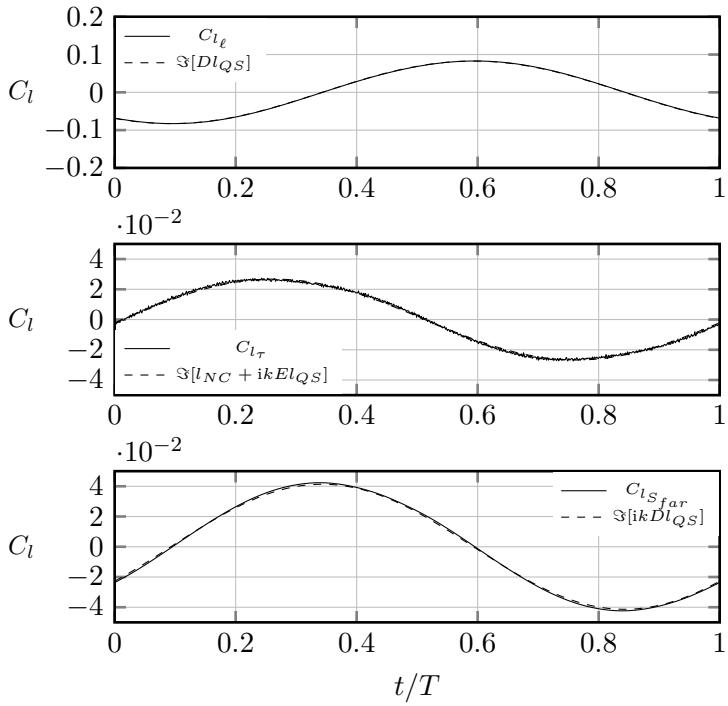

Figure 5.26 Plunging flat plate, $\bar{h}/(2b) = 0.025$, $k = 0.5$, $Re_\infty = 1 \cdot 10^6$. Comparison of Lamb vector based lift decomposition with inviscid theoretical result of Theodorsen and Mutchler [79].

also confirmed in this case.

5.5 The analysis of two-dimensional compressible flows

The link between inviscid theories and present incompressible aerodynamic force formula discussed in section 5.2 is here rearranged in order to introduce a new force breakdown first of all in incompressible flows. Aerodynamic force is decomposed in a reversible part, which in the limit of inviscid flows it returns exactly inviscid formulae, and an irreversible one. An extension of this decomposition is then proposed in compressible flows. A numerical application on the subsonic pitching airfoil flow simulation already proposed by Toubin et al. [48], briefly discussed in section 2.2.5, is then discussed. Present force breakdown is then compared with Toubin et al. drag breakdown results.

5.5.1 Link with inviscid theories

5.5.1.1 A force breakdown in incompressible flows

Considering a two dimensional incompressible inviscid flow around a flat plate, of length $2b$, centered at $x = 0$, and integrating the pressure loading Δp from $-b$ to x_w, where $x_w > b$ is an arbitrary point along the wake, and taking into account that Δp is 0 on the wake, equation (5.9) can be rewritten as

$$l = -\int_{-b}^{x_w} \Delta p(x,t)\mathrm{d}x = \rho V_\infty \int_{-b}^{x_w} \gamma(\xi,t)\mathrm{d}x + \rho \frac{d}{dt}\int_{-b}^{x_w} (x_w - \xi)\,\gamma(\xi,t)\mathrm{d}\xi \ , \tag{5.38}$$

where γ is the concentrated vorticity distribution over the flat plate, and on the wake.

Similarly, for a viscous flow, taking into account of identity (5.2), valid for incompressible flows, equation (5.1) gives:

$$\boldsymbol{F} = -\rho \int_{\mathcal{V}} \boldsymbol{\ell}\mathrm{d}\mathcal{V} - \frac{\mathrm{d}}{\mathrm{d}t}\int_{\mathcal{V}} \boldsymbol{r}\times\boldsymbol{\omega}\mathrm{d}\mathcal{V} - \rho \int_{S_{far}} \boldsymbol{r}\times\boldsymbol{n}\times\boldsymbol{\ell}\mathrm{d}S \ . \tag{5.39}$$

This formula is valid for an arbitrary choice of the pole. Considering S_{far} composed by a wake plane S_w orthogonal to the wake and adopting as pole for the moment calculations the wake center on S_w ($\boldsymbol{x}_w$), we have

$$\boldsymbol{F} = -\rho \int_{\mathcal{V}} \boldsymbol{\ell}\mathrm{d}\mathcal{V} - \frac{\mathrm{d}}{\mathrm{d}t}\int_{\mathcal{V}} (\boldsymbol{r}-\boldsymbol{x}_w)\times\boldsymbol{\omega}\mathrm{d}\mathcal{V} - \rho \int_{S_{far}} (\boldsymbol{r}-\boldsymbol{x}_w)\times\boldsymbol{n}\times\boldsymbol{\ell}\mathrm{d}S \ . \tag{5.40}$$

The last term of equation (5.40) is only a drag contribution [58]. Furthermore, integration by part of this term gives the momentum defect on the wake [57], therefore it takes into account for viscous effects, and is the irreversible contribution to the aerodynamic force:

$$\boldsymbol{F}_{irr} = -\rho \int_{S_{far}} (\boldsymbol{r}-\boldsymbol{x}_w)\times\boldsymbol{n}\times\boldsymbol{\ell}\mathrm{d}S \ . \tag{5.41}$$

The reversible part of the aerodynamic force is given by the remaining term, the respon-

sible for the lift generation:

$$\begin{aligned}\boldsymbol{F}_{rev} &= -\rho \int_{\mathcal{V}} \boldsymbol{\ell} \mathrm{d}\mathcal{V} + \rho \frac{\mathrm{d}}{\mathrm{d}t} \int_{\mathcal{V}} (\boldsymbol{x}_w - \boldsymbol{r}) \times \boldsymbol{\omega} \mathrm{d}\mathcal{V} = \\ &= -\rho \int_{\mathcal{V}} \boldsymbol{\ell} \mathrm{d}\mathcal{V} + \rho \int_{\mathcal{V}} (\boldsymbol{x}_w - \boldsymbol{r}) \times \frac{\partial \boldsymbol{\omega}}{\partial t} \mathrm{d}\mathcal{V} + \rho \int_{S_b} (\boldsymbol{x}_w - \boldsymbol{r}) \times \boldsymbol{n} \times \boldsymbol{\ell} \mathrm{d}S \ .\end{aligned} \tag{5.42}$$

Equation (5.42) is the perfect counterpart of equation (5.38) in viscous flows. With some algebra, we can obtain this equivalent formula for $\boldsymbol{F}_{irr}$:

$$\boldsymbol{F}_{irr} = -\rho \int_{S_{far}} \boldsymbol{r} \times \boldsymbol{n} \times \boldsymbol{\ell} \mathrm{d}S - \rho \int_{\mathcal{V}} \boldsymbol{x}_w \times \frac{\partial \boldsymbol{\omega}}{\partial t} \mathrm{d}\mathcal{V} + \rho \int_{S_b} \boldsymbol{r}_w \times \boldsymbol{n} \times \boldsymbol{\ell} \mathrm{d}S \ . \tag{5.43}$$

The definition of $\boldsymbol{F}_{rev}$ and $\boldsymbol{F}_{irr}$ is rigorous as far as the definition of $\boldsymbol{x}_w$ is clear. Indeed, in a real viscous flow x_w cannot be chosen in the near wake, i.e. the zone where boundary layer vorticity is still relevant.

5.5.1.2 An extension to compressible flows

Differently from the incompressible case, in compressible flows there is not a direct link between Mele and Tognaccini aerodynamic force formula (3.1) and the inviscid theories. This is due to the different definition, in compressible flows, of the hydrodynamic impulse. There is currently no theoretical link between $\boldsymbol{F}_t$ and $\boldsymbol{F}_{S_b}$, even if they are surely related. So here it is proposed an extension of the definition of reversible and irreversible force components in the compressible regime, which tries to generalize the incompressible link with inviscid theories.

$$\boldsymbol{F}_{rev} = \boldsymbol{F}_{\ell} + \boldsymbol{F}_{m_\rho} + \boldsymbol{F}_{t*} \ , \tag{5.44}$$

$$\boldsymbol{F}_{irr} = -\int_{S_{far}} \tilde{\boldsymbol{r}} \times \boldsymbol{n} \times \rho \boldsymbol{\ell} \mathrm{d}S + \int_{\mathcal{V}} \tilde{\boldsymbol{r}}_w \times \frac{\partial \rho \boldsymbol{\omega}}{\partial t} \mathrm{d}\mathcal{V} + \int_{S_b} \tilde{\boldsymbol{r}}_w \times \boldsymbol{n} \times \rho \boldsymbol{\ell} \, \mathrm{d}S \ , \tag{5.45}$$

where $\boldsymbol{F}_{t*}$:

$$\boldsymbol{F}_{t*} = -\int_{\mathcal{V}} \tilde{\boldsymbol{r}} \times \boldsymbol{\nabla} \times \rho \frac{\partial \boldsymbol{V}}{\partial t} \mathrm{d}\mathcal{V} + \int_{\mathcal{V}} \tilde{\boldsymbol{r}}_w \times \frac{\partial \rho \boldsymbol{\omega}}{\partial t} \mathrm{d}\mathcal{V} + \int_{S_b} (\tilde{\boldsymbol{r}}_w - \tilde{\boldsymbol{r}}) \times \boldsymbol{n} \times \rho \boldsymbol{\ell} \, \mathrm{d}S \ . \tag{5.46}$$

It can be easily shown that the compressible breakdown is consistent with the incompressible one.

5.5.2 Numerical analysis of the subsonic picthing airfoil flow

The numerical solution around a pitching NACA 0012 airfoil analyzed is the same performed by Toubin and Bailly [48], here briefly described. Simulations were performed with ONERA *elsA* code [75]. The pitching law is sinusoidal, with an oscillation between $-5°$ and $+5°$. The freestream Mach number is $M_\infty = 0.3$, the Reynolds number $Re_\infty = 6.6 \cdot 10^6$, the reduced frequency $k = 0.1$. 9000 timesteps for each time period have been set. Spalart-Almaras turbulence model and Jameson numerical scheme have been chosen. The grid presents about 530000 cells, with 568 body points. The farfield is set to 20 chords distance in the downstream direction, and 25 chords in the others.

In figure 5.27 computed lift coefficient has been analyzed. Equation (3.1) and near field computation show a perfect agreement. Furthermore, a good agreement has been found between $C_{l_{rev}}$ and the near field result. Please note that the method Toubin and Bailly [48] method can not deal with aerodynamic lift computation. In figure 5.28 is proposed the computed drag coefficient by eqs. (2.23) and (3.1). Both formulae are in excellent agreement with the near field computation.

Proposed drag breakdown needs a proper identification of the parameter x_w along the wake. In figure 5.29 is proposed a method to find the right value of x_w, which is chosen at the end of the near wake. This figure shows the distribution of $\boldsymbol{F}_\ell \cdot \boldsymbol{i}_x$, the vortex drag, along the wake, at two different timesteps. $x_w = 0$ is the body TE. Since the vortex force is directly proportional to the vorticity, the near wake here is considered finished when the vortex drag starts to have a periodic behavior in space (inviscid theories indeed show a periodic behavior of the wake vortex sheet in space and time, see equation (5.17)).

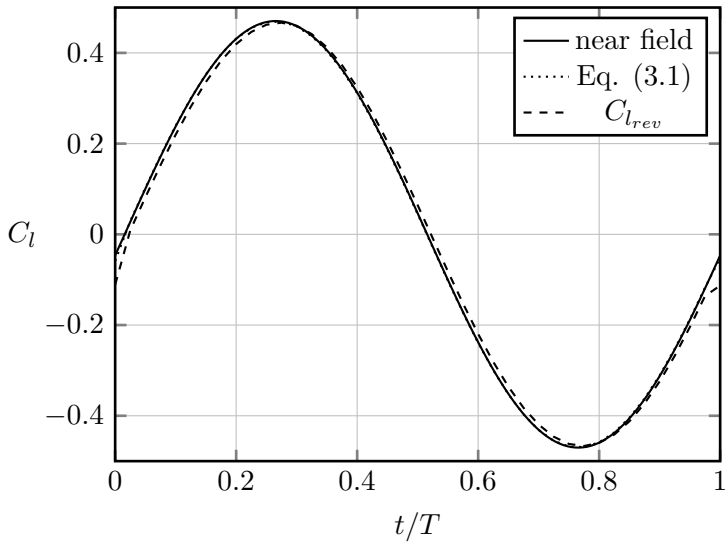

Figure 5.27 Pitching NACA 0012, $Re_\infty = 6.6{\cdot}10^6$, $M_\infty = 0.3$, $\bar{\alpha} = 5°$, $k = 0.1$. Computed aerodynamic lift coefficients.

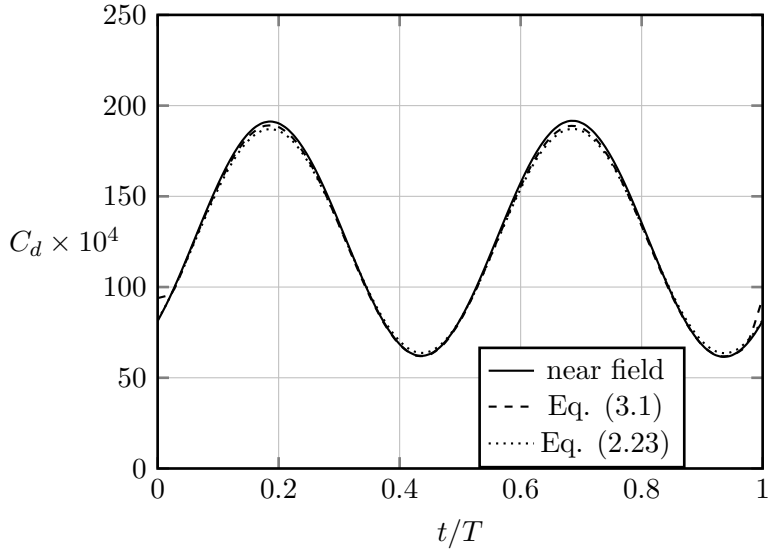

Figure 5.28 Pitching NACA 0012, $Re_\infty = 6 \cdot 10^6$, $M_\infty = 0.3$, $\bar{\alpha} = 5°$, $k = 0.1$. Computed aerodynamic drag coefficient.

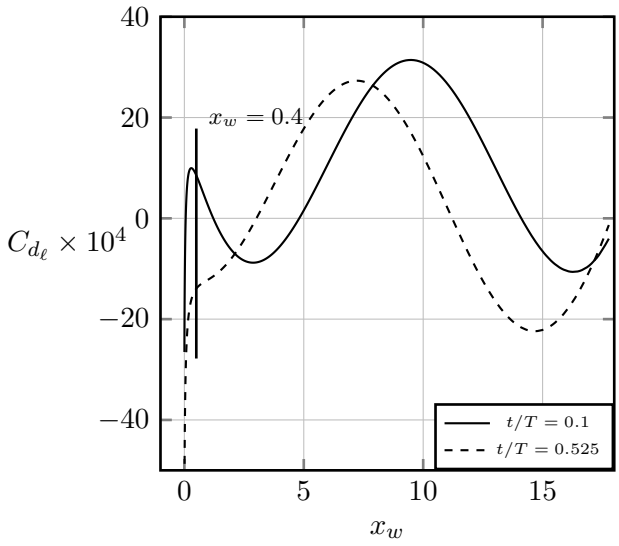

Figure 5.29 Pitchin NACA 002, $Re_\infty = 6 \cdot 10^6$, $M_\infty = 0.3$, $k = 0.1$. Vortex drag distribution along the wake at different timesteps.

This periodic behavior starts at $x_w \approx 0.4$. Before the periodic zone, vortex force shows a sudden increase, due to the TE vorticity production, already found in steady flows (see for example figure 4.8). In the steady case, the periodic wake turns into a symmetric wake along the wake axis ($\boldsymbol{F}_\ell = 0$). The same analysis at different timesteps shows a slightly different value of x_w. In the following it will be assumed $x_w = 0.4$.

Proposed drag breakdowns are compared in figure 5.30. The decomposition performed by equation (2.23) is the one found by Toubin and Bailly [48]. C_{d_v} and $C_{d_{irr}}$ values are similar, with a difference of about 10 counts (about the 10% of difference). The agreement between $C_{d_{ui}}$ and $C_{d_{rev}}$ is more satisfactory. Please note that, while Toubin and Bailly results are weakly sensitive to the integration domain choosen [48], proposed reversible and irreversible drag coefficients are much more sensitive. This is due to the sensitivity to the choice of x_w.

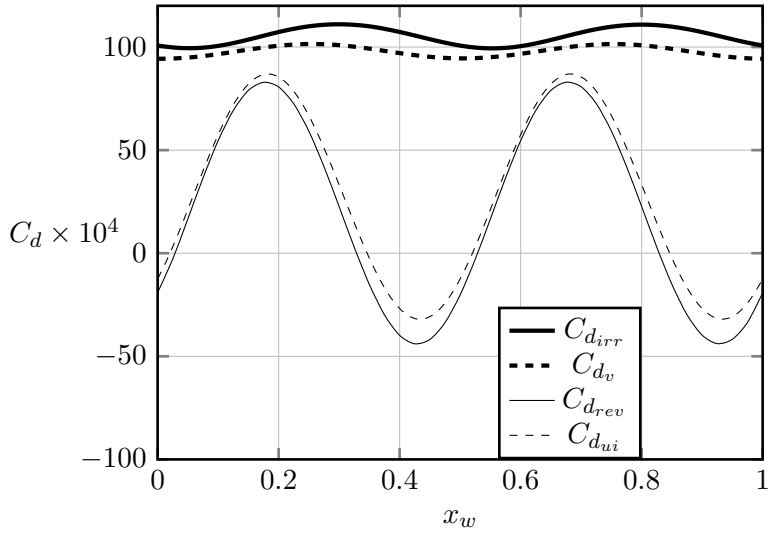

Figure 5.30 Pitching NACA 0012, $Re_\infty = 6 \cdot 10^6$, $M_\infty = 0.3$, $k = 0.1$. Comparison between proposed drag components.

CONCLUSIONS

In this work an unconventional method for the analysis, the computation and the breakdown of the aerodynamic force has been presented. The theory has been particularized to the analysis of steady and unsteady flows. Findings and implications are hereafter discussed:

Aerodynamic force in steady flows The analysis of compressible flows by means of a Lamb-vector based theory, previously derived by Mele and Tognaccini [58] and validated for two-dimensional flows, has been firstly extended to tree-dimensional flows. Present method has been validated on elliptic wing flows in subsonic and transonic conditions. Furthermore, a rigorous definition of lift-induced drag in a real compressible flow has been derived, thus introducing a drag breakdown in profile and lift-induced components. The application on elliptic wing flows revealed an accurate prediction of each drag component. Lift-induced drag in each test-case resulted coincident with classical Prandtl formula, even in transonic flow conditions. The analysis of the behavior of each lift component with the freestream Mach number gave the possibility to introduce scaling laws intimately linked with classical Prandtl and Glauert compressibility correction.

A new exact aerodynamic force formula has been then derived, to account for the numerical loss of accuracy encountered in two-dimensional high transonic flows by Mele and Tognaccini [58]. Furthermore, a viscous wave profile drag breakdown is proposed, underlying its potential discrepancy with previous profile drag breakdown methods [6, 7]. Analyses on NACA 0012 and elliptic wing flows validated the robustness of the new method in high transonic regimes and the validity of viscous-wave profile drag breakdown compared with previous method. Theory has been also successfully applied to a realistic transonic aircraft configuration. Aerodynamic force computation revealed to be accurate. A spurious drag contribution has also been identified, revealing the potentiality of present method. Some discrepancies between present wave drag computation and previous method have been encountered. These are due to the fact that present defini-

tion doesn't take into account for boundary layer entrainment that occurs after the shock waves.

Finally, a new wave drag definition by means of Lamb vector volume integrals is proposed, with a validation on a NACA 0012 transonic flow simulation.

Aerodynamic force in unsteady flows Wu et al. [50] aerodynamic force theory in incompressible flows, valid in an inertial reference frame, is revisited. The same theory has been adapted to non-inertial frames, where it loses the midfield property that characterizes Wu et al. formula. This property has been recovered with the derivation of a new exact formula, with a mixed inertial-non inertial approach. This formula was found to be more accurate than Wu et al. one when applied to numerical simulations around oscillating flat plates at low and high Reynolds number, obtained by moving rigid grid methods. An analysis of classical Theodorsen and Mutchler [79] and Karman and Sears [80] inviscid theories showed to have a direct link with the present theory. Thanks to this link, a new definition of dynamic force derivatives in airfoil flows has been derived. The application to high Reynolds number flows returned the inviscid Theodorsen and Mutchler reference values. Furthermore, an application to low-Reynolds number flows has been proposed.

Thanks to the link with the inviscid theories, a new definition of reversible and irreversible parts of the aerodynamic force is derived in incompressible flows. This definition has been possible thanks to the hydrodinamic force definition in incompressible flows, intimately linked with the present theory. This breakdown has been extended to compressible flows. The theory has been validated with a pitching airfoil simulation in subsonic conditions, already proposed by Toubin et al. [48], for their unsteady drag breakdown method validation. Present force breakdown has been compared with Toubin et al. results. The reversible part of the force computes the whole aerodynamic lift. Total drag is correctly computed by Lamb vector theory. Drag breakdown results gave a satisfactory agreement with Toubin et al. analyses.

Potentiality and future of present aerodynamic force theory The aerodynamic force theory presented in this dissertation revealed many potentialities:

- It is an exact formula valid in compressible real flows. It has no limits of applicability. It could become a valid design tool, potentially, in any industrial application which requires aerodynamic force analysis and prediction.
- It has shown significant accuracy. In steady flows it gave the possibility to cancel the majority of the spurious drag. Computed drag results thus are in excellent agreement with its correct value. This is an aspect that could be crucial for industrial applications.
- It can be particularized for the analysis of different problems. With the same theory it has been discussed the drag breakdown in steady and unsteady flows.
- Potentially the method can also be applied to experimental applications. The only input is the velocity field, and its derivatives. No pressure term appears in the force definition. The major issues which could present some difficulties are probably the boundary layer resolution, that is typically low in PIV applications, or the accuracy of PIV measurements, that affects farfield integrations.

The following step on this theory is the analysis of the drag-thrust bookkeeping. The issue, born in the aeronautical contest, where, in CFD applications, there is typically no separation between the thrust and drag, is becoming now relevant on new industrial and research demands regarding the natural flight. Present method has in his inner nature the potentiality to decompose drag and thrust contributions of any fluid-based propulsion system. First promising applications have been recently presented [66].

A

DERIVATIVE MOMENT TRANSFORMATIONS

Let $\mathcal{V}$ be a subset of $\mathbb{R}^d$, where $d = 2, 3$ is the space dimension, having a regular boundary $\partial\mathcal{V}$, and $\boldsymbol{f}$ a vector field defined in $\mathcal{V}$. The following integral relations are applicable (see Wu et al. [51]):

$$\int_{\mathcal{V}} \boldsymbol{f}\,\mathrm{d}\mathcal{V} = \int_{\mathcal{V}} \boldsymbol{r} \times (\boldsymbol{\nabla} \times \boldsymbol{f})\,\mathrm{d}\mathcal{V} - \int_{\partial\mathcal{V}} \boldsymbol{r} \times (\boldsymbol{n} \times \boldsymbol{f})\,\mathrm{d}S\ , \tag{A.1}$$

where $\boldsymbol{r} = \boldsymbol{x}/(d-1)$ is the modified vector position.

For a potential function ϕ, the following identity is also applicable:

$$\int_{S} \phi\boldsymbol{n}\mathrm{d}S = -\int_{S} \boldsymbol{r} \times \boldsymbol{n} \times \boldsymbol{\nabla}\phi\,\mathrm{d}S + \oint_{\partial S} \phi\boldsymbol{r} \times \mathrm{d}\boldsymbol{x}\ . \tag{A.2}$$

where $S = \partial\mathcal{V}$. Last term is exactly 0 when $\mathcal{V}$ has no open surfaces.

B

DIMENSIONAL ANALYSIS OF THE FORCE BREAKDOWN

Marongiu et al. [55] proposed a dimensional analysis of the force components of equation (3.1) in the incompressible steady regime, in the hypothesis of boundary layer flow. Here is proposed their analysis.

Considering a boundary layer flow, all the velocity components are $\approx \mathcal{O}(1)$, except the component normal to the wall (v), that is of order $\approx \mathcal{O}(\delta)$, with δ the nondimensional magnitude of the boundary layer thickness, that is of order $\approx \mathcal{O}(1/\sqrt{Re})$. Furthermore the normal velocity derivatives are of order $\approx \mathcal{O}(1/\delta)$ $\left(\frac{\partial u}{\partial y}\right)$. Being a boundary layer flow, $\boldsymbol{F}_{S_{far}}$ is a wake integral, $S_{far} \to S_w$, already defined in figure 3.2, with $\boldsymbol{n} = (1, 0)$. Taking into account that $\mathcal{V} = L_{ref}^2 \delta \mathcal{V}^*$, $S_w = L_{ref} \delta S_w^*$, $y = L_{ref} y^* = L_{ref} \delta \bar{y}$, $v = V_\infty v^* = V_i nfty \delta \bar{v}$, and of the stress tensor non-dimensional form, it's easy to find that

$$\ell_x^* = -\bar{v}\delta \left(\delta \frac{\partial \bar{v}}{\partial x^*} - \frac{1}{\delta} \frac{\partial u^*}{\partial \bar{y}} \right), \qquad \ell_y^* = u^* \left(\delta \frac{\partial \bar{v}}{\partial x^*} - \frac{1}{\delta} \frac{\partial u^*}{\partial \bar{y}} \right) , \tag{B.1}$$

$$\frac{\boldsymbol{F}_\ell}{0.5 \rho_\infty V_\infty^2 L_{ref}} \approx - \left[\delta \int_{\mathcal{V}^*} \bar{v} \frac{\partial u^*}{\partial \bar{y}} \mathrm{d}\mathcal{V}^* \boldsymbol{i}_x \right] + \left[\int_{\mathcal{V}^*} u^* \frac{\partial u^*}{\partial \bar{y}} \mathrm{d}\mathcal{V}^* \right] \boldsymbol{i}_y , \tag{B.2}$$

$$\frac{\boldsymbol{F}_{S_{far}}}{0.5 \rho_\infty V_\infty^2 L_{ref}} \approx \left[\delta \int_{S_w^*} n_x \bar{y} u^* \frac{\partial u^*}{\partial \bar{y}} \mathrm{d}S^* \right] \boldsymbol{i}_x - \left[\int_{S_w^*} n_x x^* u^* \frac{\partial u^*}{\partial \bar{y}} \mathrm{d}S^* \right] \boldsymbol{i}_y , \tag{B.3}$$

$$\frac{\boldsymbol{\Delta}_\mu}{0.5\rho_\infty V_\infty^2 L_{ref}} \approx \frac{1}{2}\left[\delta^2 \int\limits_{S_w^*} n_y \left(\frac{\partial u^*}{\partial \bar{y}} - \bar{y}\frac{\partial^2 u^*}{\partial \bar{y}^2}\right) \mathrm{d}S^*\right] \boldsymbol{i}_x + \\ - \frac{1}{2}\left[\delta \int\limits_{S_w^*} n_y x^* \frac{\partial^2 u^*}{\partial \bar{y}^2} \mathrm{d}S^*\right] \boldsymbol{i}_y \ . \tag{B.4}$$

Drag components of $\boldsymbol{F}_\ell$ and $\boldsymbol{F}_{S_{far}}$ are of order $\mathcal{O}(\delta)$, while $\boldsymbol{\Delta}_\mu$ drag component is of order $\mathcal{O}(\delta^2)$. At the same way, lift components are respectively of order $\mathcal{O}(1)$ and $\mathcal{O}(\delta)$. Being $\delta << 1$ when $Re \to \infty$, $\boldsymbol{\Delta}_\mu$ becomes negligible, exactly 0 when $n_y = 0$. It's easy to extend this analysis to three-dimensional flows, with the same results.

C

FREE VORTICITY AND BOUND VORTICITY DECOMPOSITION

Let us consider a three-dimensional incompressible flow, at moderately high Reynolds number. With a particular choice of the integration domain, it is possible to split free vorticity and bound vorticity contributions.

Following the scheme proposed in figure C.1, we choose an integration volume that ends at the body trailing edge. $\boldsymbol{\Delta}_\mu$ contribution is negligible (0 if $n_y = n_z = 0$). In this way, all the force is given by the sum of $\boldsymbol{F}_\ell$, $\boldsymbol{F}_{S_{far}}$ and $\boldsymbol{F}_t$. We can extend the integration domain further than the TE, for example to a station x_w with an orthogonal plane $S_W \neq S_{TE}$. If we call $\boldsymbol{F}_1$ the force computed in the first volume Ω, $\boldsymbol{F}_2$ the force computed in $\Omega \bigcup W$, and $\boldsymbol{F}_{12}$ the force computed in the volume W, we have

$$\boldsymbol{F}_1 = \boldsymbol{F}_2 \qquad \rightarrow \qquad \boldsymbol{F}_{12} = 0 \tag{C.1}$$

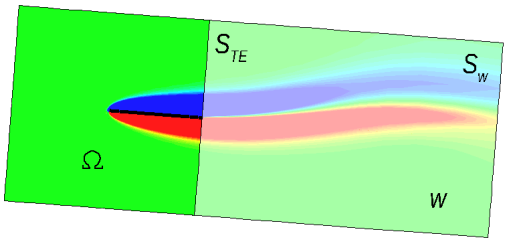

Figure C.1 Definition of the integration domain for the free and bound vorticity splitting.

since total force does not depend on the integration domain. Expressing with the subscript 12 force components in the volume W, it results

$$\boldsymbol{F}_{S_{far_{12}}} = -\boldsymbol{F}_{\ell_{12}} - \boldsymbol{F}_{t_{12}} \ . \tag{C.2}$$

On the lateral surface of W, as on the lateral surface of Ω, $\boldsymbol{F}_{S_{far}}$ is 0 since Lamb vector is 0, supposing volumes are large enough. Only orthogonal planes S_{TE} and S_W give contributions. Equation (C.2) becomes

$$\boldsymbol{F}_{S_W} + \boldsymbol{F}'_{S^W_{TE}} = -\boldsymbol{F}_{\ell_{12}} - \boldsymbol{F}_{t_{12}} \ , \tag{C.3}$$

where $\boldsymbol{F}'_{S^W_{TE}} = -\boldsymbol{F}_{S^\Omega_{TE}}$, where with the superscripts Ω and W we indicate S_{TE} as boundary of Ω or W, that have opposite normal vector. The RHS of equation (C.2) is function of the vorticity just after the TE, i.e. the free vorticity. So $\boldsymbol{F}_{S_{far}} = \boldsymbol{F}_{S_W}$ takes into account of the free vorticity, while $\boldsymbol{F}_{\ell_1}$ and $\boldsymbol{F}_{t_1}$ take into account for the bound vorticity contributions. Identity (C.2) can be generalized for every volume Ω and W, provided them both contain body boundary layer.

D

DERIVATION OF MIXED INERTIAL-NON INERTIAL AERODYNAMIC FORCE FORMULA

Taking into account for equations (5.3) and (5.4), equation (3.1) becomes:

$$\boldsymbol{F}_a = \boldsymbol{F}'_\ell + \boldsymbol{F}_{\ell_T} + \boldsymbol{F}_{t'} + \boldsymbol{F}_{t_T} + \boldsymbol{F}_{S_{far'}} + \boldsymbol{F}_{S_T} + \boldsymbol{F}_{S_b} + \boldsymbol{F}_{t_b} + \boldsymbol{\Delta}_\mu \ , \tag{D.1}$$

where

$$\boldsymbol{F}_{\ell'} = -\rho \int_{\mathcal{V}} \boldsymbol{\ell}' \mathrm{d}\mathcal{V} \ , \ \boldsymbol{F}_{\ell_T} = -\rho \int_{\mathcal{V}} \boldsymbol{\omega} \times \boldsymbol{V}_T \mathrm{d}\mathcal{V} \ , \tag{D.2}$$

$$\boldsymbol{F}_{t'} = -\rho \int_{\mathcal{V}} \boldsymbol{r} \times \frac{\partial \boldsymbol{\omega}}{\partial t'} \mathrm{d}\mathcal{V} \ , \ \boldsymbol{F}_{t_T} = \rho \int_{\mathcal{V}} \boldsymbol{r} \times (\boldsymbol{V}_T \cdot \boldsymbol{\nabla}\boldsymbol{\omega}) \mathrm{d}\mathcal{V} \ , \tag{D.3}$$

$$\boldsymbol{F}_{S'_{far}} = -\rho \int_{S_{far}} \boldsymbol{r} \times (\boldsymbol{n} \times \boldsymbol{\ell}') \mathrm{d}S \ , \ \boldsymbol{F}_{S_T} = -\rho \int_{S_{far}} \boldsymbol{r} \times [\boldsymbol{n} \times (\boldsymbol{\omega} \times \boldsymbol{V}_T)] \mathrm{d}S \ . \tag{D.4}$$

This equation holds for $\boldsymbol{\Omega}$ parallel to $\boldsymbol{\omega}$, i.e. for two-dimensional flows. Taking into account for the identity[50]

$$\int_{\mathcal{V}} \boldsymbol{b} \mathrm{d}\mathcal{V} = \int_{\mathcal{V}} \boldsymbol{r} \times \boldsymbol{\nabla} \times \boldsymbol{b} \mathrm{d}\mathcal{V} - \int_{\partial\mathcal{V}} \boldsymbol{r} \times (\boldsymbol{n} \times \boldsymbol{b}) \mathrm{d}S \tag{D.5}$$

we have

$$\boldsymbol{F}_{\ell_T} = -\rho \int_{\mathcal{V}} \boldsymbol{r} \times [\boldsymbol{\nabla} \times (\boldsymbol{\omega} \times \boldsymbol{V}_T)] \, \mathrm{d}\mathcal{V} + \int_{\partial\mathcal{V}} \boldsymbol{r} \times [\boldsymbol{n} \times (\boldsymbol{\omega} \times \boldsymbol{V}_T)] \, \mathrm{dS} \ . \tag{D.6}$$

Due to continuity equation: $\boldsymbol{\nabla} \times (\boldsymbol{\omega} \times \boldsymbol{V}_T) = \boldsymbol{V}_T \cdot \boldsymbol{\nabla}\boldsymbol{\omega}$, therefore

$$\begin{aligned} \boldsymbol{F}_{\ell_T} &= -\rho \int_{\mathcal{V}} \boldsymbol{r} \times (\boldsymbol{V}_T \cdot \boldsymbol{\nabla}\boldsymbol{\omega}) \, \mathrm{d}\mathcal{V} + \int_{\partial\mathcal{V}} \boldsymbol{r} \times [\boldsymbol{n} \times (\boldsymbol{\omega} \times \boldsymbol{V}_T)] \, \mathrm{dS} \\ &= -\boldsymbol{F}_{t_T} - \boldsymbol{F}_{S_T} + \int_{S_b} \boldsymbol{r} \times [\boldsymbol{n} \times (\boldsymbol{\omega} \times \boldsymbol{V}_T)] \, \mathrm{d}S \ . \end{aligned} \tag{D.7}$$

On the body $\boldsymbol{V}' = 0$ and $\boldsymbol{\omega} \times \boldsymbol{V}_T = \boldsymbol{\ell}$, hence

$$\boldsymbol{F}_{\ell_T} + \boldsymbol{F}_{t_T} + \boldsymbol{F}_{S_T} + \boldsymbol{F}_{S_b} = 0 \ . \tag{D.8}$$

Taking into account for this identity, equation (D.1) reduces to

$$\boldsymbol{F}_c = \boldsymbol{F}_{\ell'} + \boldsymbol{F}_{t'} + \boldsymbol{F}_{S'_{far}} + \boldsymbol{F}_{t_b} + \boldsymbol{\Delta}_\mu \ . \tag{D.9}$$

E

LINK WITH THE LINEAR INVISCID THEORY

E.1 Inviscid flow equations

Let us consider an incompressible unsteady two-dimensional inviscid flow around a flat plate assuming small plunging and pitching oscillations with a constant freestream velocity $\boldsymbol{V}_\infty$ aligned with the x-axis. The plate length is $2b$ with its center placed at $x = 0$. Denoting with φ the potential of the perturbation velocity $\boldsymbol{v} = (u, w)^T$, φ is solution of the problem

$$\nabla^2\varphi = 0 \,, \tag{E.1}$$

$$\lim_{\boldsymbol{r}\to\infty} \boldsymbol{\nabla}\varphi = 0 \,, \tag{E.2}$$

$$-b \le x \le b : \qquad w(x,0,t) = \frac{\partial z_a}{\partial t} + V_\infty \frac{\partial z_a}{\partial x} = w_a(x,t) \,, \tag{E.3}$$

$$x > b : \qquad \frac{\partial \Delta\varphi}{\partial t}(x,0,t) + V_\infty \frac{\partial \Delta\varphi}{\partial x}(x,0,t) = 0 \,; \tag{E.4}$$

where $\Delta\varphi = \varphi(x,0^+) - \varphi(x,0^-)$ and $z_a(t)$ is the instantaneous geometry of the plate given by

$$z_a(x,t) = -h(t) - \alpha(t)(x - ab) \,. \tag{E.5}$$

In this equation $h(t)$ specifies the plunging motion ($h > 0$ for $z_a < 0$) and $\alpha(t)$ the pitching motion around a rotation center placed at $x = ab$ ($\alpha > 0$ if clockwise). The velocity on the plate, given by equation (E.3), is therefore:

$$w_a(x,t) = -V_\infty\alpha - \dot{h} - \dot{\alpha}(x - ab) \,. \tag{E.6}$$

The only physically relevant solution is identified by satisfying the Kutta condition (continuous velocity at plate trailing edge). Pressure can be finally obtained by the linearized unsteady Bernoulli equation

$$p = p_\infty - \rho V_\infty u - \rho \frac{\partial \varphi}{\partial t} \ , \tag{E.7}$$

where p_∞ is the freestream pressure value.

The analytic solution in case of periodic oscillations has been obtained by Theodorsen and Mutchler [79], see Bisplinghoff [81, pp. 251-281] for a more detailed description.

The flow can be solved with a bound vorticity distribution γ_b along the plate, where $\gamma_b > 0$ for a clockwise induced flow, and a free vorticity distribution $\gamma_w(x,t)$ along the wake $z = 0$, $x > b$.

From the linearized Bernoulli equation (E.7) the pressure loading along the plate is:

$$-\Delta p(x,t) = \rho \frac{\partial \Delta\varphi}{\partial t} + \rho V_\infty \frac{\partial \Delta\varphi}{\partial x} \ . \tag{E.8}$$

Since $\frac{\partial \phi}{\partial x} = u$ and $\Delta u = \gamma_b$, the integration along the plate provides

$$l = -\int_{-b}^{b} \Delta p(x,t) \mathrm{d}x = \rho V_\infty \Gamma - \rho \frac{d}{dt} \int_{-b}^{b} x \gamma_b(x,t) \mathrm{d}x - \rho V_\infty b \gamma_w(b,t) \ , \tag{E.9}$$

Therefore:

$$l = l_\ell + l_\tau + l_{S_{far}} \ , \tag{E.10}$$

where

$$l_\tau = -\rho \frac{d}{dt} \int_{-b}^{b} x \gamma_b(x,t) \mathrm{d}x \ , \qquad l_{S_{far}} = -\rho V_\infty b \gamma_w(b,t) \ .$$

Due to Kelvin theorem:

$$\Gamma(t) + \int_{b}^{\infty} \gamma_w(x,t) \mathrm{d}x = 0 \ , \qquad \gamma_w(b,t) = -\frac{1}{V_\infty} \frac{d\Gamma}{dt} \tag{E.11}$$

and $l_{S_{far}}$ is also given by

$$l_{S_{far}} = \rho b \frac{d\Gamma}{dt} \ . \tag{E.12}$$

E.2 von Karman & Sears formula

The bound vorticity is given by[81, p. 217]

$$\gamma_b(x,t) = \frac{2}{\pi}\sqrt{\frac{b-x}{b+x}} \fint_{-b}^{b} \sqrt{\frac{b+\xi}{b-\xi}} \frac{[w_a(\xi,t) - \lambda(\xi,t)]}{x-\xi} \mathrm{d}\xi \ , \tag{E.13}$$

where w_a is defined by equation (E.3), whereas λ is the velocity induced by the free vorticity of the wake γ_w:

$$\lambda(x,t) = -\frac{1}{2\pi} \fint_{b}^{\infty} \frac{\gamma_w(\eta,t)\mathrm{d}\eta}{x-\eta} \ . \tag{E.14}$$

von Karman & Sears introduced a particular decomposition $\gamma_b(x,t) = \gamma_0(x,t) + \gamma_1(x,t)$, where:

$$\gamma_0(x,t) = \frac{2}{\pi}\sqrt{\frac{b-x}{b+x}} \fint_{-b}^{b} \sqrt{\frac{b+\xi}{b-\xi}} \frac{w_a(\xi,t)}{x-\xi} \mathrm{d}\xi \ , \tag{E.15}$$

$$\gamma_1(x,t) = -\frac{2}{\pi}\sqrt{\frac{b-x}{b+x}} \fint_{-b}^{b} \sqrt{\frac{b+\xi}{b-\xi}} \frac{\lambda(\xi,t)}{x-\xi} \mathrm{d}\xi \ . \tag{E.16}$$

γ_0 is the *quasi-steady* vorticity, i.e. "vorticity which would be produced, according to the thin airfoil theory, by the motion of the airfoil, if the wake had no effect", whereas γ_1 is "the vorticity which is induced by the wake". Taking into account for equations (E.14) and (E.16),

$$\int_{-b}^{b} \gamma_1(x,t)\mathrm{d}x = \int_{b}^{\infty} \gamma_w(\eta,t) \left(\sqrt{\frac{\eta+b}{\eta-b}} - 1 \right) \mathrm{d}\eta \ , \tag{E.17}$$

thus, the first integral in the RHS of equation (E.10) provides:

$$\rho V_\infty \int_{-b}^{b} \gamma_b(x,t)\mathrm{d}x = \rho V_\infty \int_{-b}^{b} \gamma_0(x,t)\mathrm{d}x + \rho V_\infty \int_{b}^{\infty} \gamma_w(\eta,t)\left(\sqrt{\frac{\eta+b}{\eta-b}}-1\right)\mathrm{d}\eta \ . \tag{E.18}$$

von Karman & Sears also found:

$$\int_{-b}^{b} x\gamma_1(x,t)\mathrm{d}x = \int_{b}^{\infty} \gamma_w(\eta,t)\left(\sqrt{\eta^2-b^2}-\eta\right)\mathrm{d}\eta \ , \tag{E.19}$$

$$\begin{aligned}\frac{d}{dt}\int_{-b}^{b} x\gamma_1(x,t)\mathrm{d}x =& V_\infty \int_{b}^{\infty} \gamma_w(\eta,t)\left(\sqrt{\frac{\eta+b}{\eta-b}}-\frac{b}{\sqrt{\eta^2-b^2}}-1\right)\mathrm{d}\eta + \\ &- V_\infty b\gamma_w(b,t) \ ,\end{aligned} \tag{E.20}$$

then the second integral in the RHS of equation (E.10) becomes:

$$\begin{aligned}&\rho\frac{d}{dt}\int_{-b}^{b} x\gamma_b(x,t)\mathrm{d}x = \\ &\rho\frac{d}{dt}\int_{-b}^{b} x\gamma_0(x,t)\mathrm{d}x + \rho V_\infty \int_{b}^{\infty} \gamma_w(\eta,t)\left(\sqrt{\frac{\eta+b}{\eta-b}}-\frac{b}{\sqrt{\eta^2-b^2}}-1\right)\mathrm{d}\eta - \rho b V_\infty \gamma_w(b,t) \ .\end{aligned} \tag{E.21}$$

Therefore equation (E.10) reduces to

$$l = \rho V_\infty \int_{-b}^{b} \gamma_0(x,t)\mathrm{d}x - \rho\frac{d}{dt}\int_{-b}^{b} x\gamma_0(x,t)\mathrm{d}x + \rho b V_\infty \int_{b}^{\infty} \frac{\gamma_w(\eta,t)}{\sqrt{\eta^2-b^2}}\mathrm{d}\eta \ , \tag{E.22}$$

which is exactly the expression found by von Karman & Sears.

BIBLIOGRAPHY

[1] Flechner, S. G., Jacobs, P. F., and Whitcomb, R. T., "A High Subsonic Speed Wind-Tunnel Investigation of Winglets on a Representative Second-Generation Jet Transport Wing," Technical Note TN D-8264, NASA, Langley Research Center, 1976.

[2] Davidson, D. L., "The Role of Computational Fluid Dynamics in Process Industries," *The Bridge - National Academy of Engineering*, Vol. 32, 2002.

[3] Adrian, R. J., "Particle-Imaging Techniques for Experimental Fluid Mechanics," *Annual Review of Fluid Mechanics*, Vol. 23, No. 1, 1991, pp. 261–304.

[4] Kutta, M. W., "Auftriebskräfte in Stroömenden Flüssigkeiten," *Illustrierte Aeronautische Mitteilungen*, Vol. 6, 1902, pp. 133.

[5] Joukowskij, N. E., "Sur les Tourbillons Adjoints," *Traraux de la Section Physique de la Societe Imperiale des Amis des Sciences Naturales*, Vol. 13, No. 2, 1906.

[6] Paparone, L. and Tognaccini, R., "Computational Fluid Dynamics-Based Drag Prediction and Decomposition," *AIAA Journal*, Vol. 41, No. 9, Sept. 2003, pp. 1647–1657.

[7] Destarac, D. and Van der Vooren, J., "Drag/thrust analysis of jet-propelled transonic transport aircraft; Definition of physical drag components," *Aerospace Science and Technology*, Vol. 8, No. 6, 2004, pp. 545–556.

[8] Noca, F., Shiels, D., and Jeon, D., "Measuring Instantaneous Fluid Dynamic Forces on Bodies, using unly Velocity Fields and their Derivatives," *Journal of Fluids and Structures*, Vol. 11, No. 3, 1997, pp. 345 – 350.

[9] Noca, F., Shiels, D., and Jeon, D., "A Comparison of Methods for Evaluating Time-Dependent Fluid Dynamic-Forces on Bodies, using only Velocity Fields and their Derivatives," *Journal of Fluids and Structures*, Vol. 13, No. 5, 1999, pp. 551 – 578.

[10] Prandtl, L., "Tragflügeltheorie." *Nachrichten von der Gesellschaft der Wissenschaften zu Göttingen*, Vol. Geschäeftliche Mitteilungen, Klasse, 1918, pp. 451–477.

[11] Prandtl, L., "Application of Modern Hydrodynamics to Aeronautics in Two Parts," NACA Technical Report 116, 1921.

[12] van Dam, P., C., "Recent experience with different methods of drag prediction," *Progress in Aerospace Sciences*, Vol. 35, No. 8, Nov. 1999, pp. 751–798.

[13] Meredith, P. T., "Viscous phenomena affecting high-lift systems and suggestions for future CFD development." *High-Lift System Aerodynamics*, Vol. AGARD CP 315, Sept. 1993, pp. 19–1–8.

[14] Slooff, J. W., "Computational Drag Analysis and Minimization; Mission Impossible?" *Proceedings of the Aircraft Drag Prediction and Minimization Symposium*, edited by AGARD, Vol. Addendum 1, 1986.

[15] Spalart, P. R., "On the far wake and induced drag of aircraft," *Journal of Fluid Mechanics*, Vol. 603, 2008, pp. 413–430.

[16] Mele, B., Ostieri, M., and Tognaccini, R., "Vorticity Based Breakdown of the Aerodynamic Force in Three-Dimensional Compressible Flows," *AIAA Journal*, Vol. 54, No. 4, April 2016, pp. 1198–1208.

[17] Mele, B., Ostieri, M., and Tognaccini, R., "Aircraft Lift and Drag Decomposition in Transonic Flows," *Journal of Aircraft*, May 2017, pp. 1–12.

[18] Ostieri, M., Mele, B., and Tognaccini, R., "Linear and nonlinear decomposition of the aerodynamic force acting on an oscillating plate," *AIAA Journal*, Nov. 2017, Article in advance.

[19] Ostieri, M., Tognaccini, R., Bailly, D., and Destarac, D., "Two alternative drag breakdowns in unsteady flows," AIMETA - XXIII Conference - The Italian Association of Theoretical and Applied Mechanics, Salerno, 4th - 7th September, 2017.

[20] Ostieri, M., Tognaccini, R., Bailly, D., and Destarac, D., "Aerodynamic force and Lamb vector field in compressible unsteady flows," AIAA SciTech 2018, 8th - 12th January, Kissemme, Florida, USA, 2018.

[21] Betz, A., "A method for the direct determination of wing-section drag," NACA Technical Report 337, Washington, 1925.

[22] Jones, B., "Measurement of Profile Drag by the Pitot-Transverse Method," Technical Report 1688, British ARC R&M, 1936.

[23] Maskell, E., "Progress towards a method for the measurement of the components of the drag of a wing of finite span," RAE Technical Report 72232, United Kingdom, 1972.

[24] Kusunose, K., *A wake integration method for airplane drag prediction*, Vol. 3 of *The 21st century COE Program International COE of Flow dynamics Lecture Series*, Tohoku University Press, 2005.

[25] Oswatitsch, K., *Gas Dynamics*, Academic Press, New York, US, 1956.

[26] Destarac, D., "Far-Field Drag in Transonic Potential Flow: Analysis and Optimisation," *Recent Developments and Applications in Aeronautical CFD*, No. paper 25 in Royal Aeronautical Society European Forum, Bristol, Unighted Kingdom, 1993.

[27] Destarac, D., *Far-Field / Near-field drag balance and applications of drag extraction in CFD*, CFD-based aircraft drag prediction and reduction, Von Karman Institute Lecture Series, Jan. 2003.

[28] Van der Vooren, J. and W. Slooff, J., "CFD-Based Drag Prediction: State of the Art, Theory, Prospects," Lecture Notes, AIAA Professional Studies Series, Course on Drag-Prediction and Measurement, Dutch Aerospace Lab., NLR TP 90246, 1990.

[29] Lanzetta, M., Mele, B., and Tognaccini, R., "Advances in aerodynamic drag extraction by far field methods," *Journal of Aircraft*, Vol. Article in advance (on-line), 2015.

[30] Méheut, M., "Thrust and torque far-field analysis of propeller and Counter Rotating Open Rotor configurations," *31st AIAA Applied Aerodynamics Conference*, 2013.

[31] Kiock, R., "The Alvast Model of DLR," *DLR IB*, Vol. 129, No. 96, 1996, pp. 22.

[32] Destarac, D., "Spurious Far-Field-Boundary Induced Drag in Two-Dimensional Flow Simulations," *Journal of Aircraft*, Vol. 48, No. 4, July 2011, pp. 1444–1455.

[33] Destarac, D., "Investigating Negative Drag in Grid Convergence for Two-Dimensional Euler Solutions," *Journal of Aircraft*, Vol. 48, No. 4, July 2011, pp. 1468–1470.

[34] Levy, D. W., Zickuhr, T., Vassberg, J., Agrawal, S., Wahls, R. A., Pirzadeh, S., and Hemsch, M. J., "Data Summary from the First AIAA Computational Fluid Dynamics Drag Prediction Workshop," *Journal of Aircraft*, Vol. 40, No. 5, Sept. 2003, pp. 875–882.

[35] Laflin, K. R., Klausmeyer, S. M., Zickuhr, T., Vassberg, J. C., Wahls, R. A., Morrison, J. H., Brodersen, O. P., Rakowitz, M. E., Tinoco, E. N., and Godard, J.-L., "Data Summary from Second AIAA Computational Fluid Dynamics Drag Prediction Workshop," *Journal of Aircraft*, Vol. 42, No. 5, Sept. 2005, pp. 1165–1178.

[36] Vassberg, J., Tinoco, E., Mani, M., Brodersen, O., Eisfeld, B., Wahls, R., Morrison, J., Zickuhr, T., Laflin, K., and Mavriplis, D., "Summary of the Third AIAA CFD Drag Prediction Workshop," Aerospace Sciences Meetings, American Institute of Aeronautics and Astronautics, Jan. 2007.

[37] Vassberg, J., Tinoco, E., Mani, M., Rider, B., Zickuhr, T., Levy, D., Brodersen, O., Eisfeld, B., Crippa, S., Wahls, R., Morrison, J., Mavriplis, D., and Murayama, M., "Summary of the Fourth AIAA CFD Drag Prediction Workshop," Fluid Dynamics and Co-located Conferences, American Institute of Aeronautics and Astronautics, June 2010.

[38] Levy, D., Laflin, D., Tinoco, E., Vassberg, J., Mani, M., Rider, B., Rumsey, C., Wahls, R., Morrison, K., Brodersen, O., Crippa, S., Mavriplis, D., and Murayama, M., "Summary of Data from the Fifth AIAA CFD Drag Prediction Workshop." *AIAA Paper 2013-0046*, Jan. 2013.

[39] Tinoco, E. N., Brodersen, O., Keye, S., and Laflin, K., "Summary of Data from the Sixth AIAA CFD Drag Prediction Workshop: CRM Cases 2 to 5," AIAA SciTech Forum, American Institute of Aeronautics and Astronautics, Jan. 2017.

[40] Vassberg, J., Dehaan, M., Rivers, M., and Wahls, R., "Development of a Common Research Model for Applied CFD Validation Studies," Guidance, Navigation, and Control and Co-located Conferences, American Institute of Aeronautics and Astronautics, Aug. 2008.

[41] Hue, D. and Esquieu, S., "Computational Drag Prediction of the DPW4 Configuration Using the Far-Field Approach," *Journal of Aircraft*, Vol. 48, No. 5, 2011, pp. 1658–1670.

[42] Hue, D., "CFD Investigations on the DPW-5 Configuration with Measured Experimental Wing Twist using the elsA Solver and the Far-Field Approach." *AIAA Paper 2013-2508*, Jun. 2013.

[43] Hue, D., "Fifth Drag Prediction Workshop: Computational Fluid Dynamics Studies Carried Out at ONERA," *Journal of Aircraft*, Vol. 51, No. 4, July 2014, pp. 1295–1310.

[44] Tognaccini, R., *Methods for drag decomposition, Thrust-drag bookkeeping from CFD calculations*, CFD-based aircraft drag prediction and reduction, Von Karman Institute Lecture Series, Nov. 2003.

[45] Ueno, M., Yamamoto, K., Tanaka, K., Murayama, M., and Tognaccini, R., "Far-field drag analysis of NASA Common Research Model simulation," *Journal of Aircraft*, Vol. 50, No. 2, 2013, pp. 388–397.

[46] Tognaccini, R., "Drag Computation and Breakdown in Power-on Conditions," *Journal of Aircraft*, Vol. 42, No. 1, 2005, pp. 245–252.

[47] Gariépy, M., Trépanier, J., and Malouin, B., "Generalization of the Far-Field Drag Decomposition Method to Unsteady Flows," *AIAA Journal*, Vol. 51, No. 6, 2013, pp. 1310–1319.

[48] Toubin, H. and Bailly, D., "Development and Application of a New Unsteady Far-Field Drag Decomposition Method," *AIAA Journal*, Vol. 53, No. 11, 2015, pp. 3414–3429.

[49] Toubin, H., Bailly, D., and Costes, M., "Improved Unsteady Far-Field Drag Breakdown Method and Application to Complex Cases," *AIAA Journal*, Vol. 54, No. 6, 2016, pp. 1907–1921.

[50] Wu, J.-Z., Lu, X.-Y., and Zhuang, L., "Integral force acting on a body due to local flow structures," *Journal of Fluid Mechanics*, Vol. 576, 2007, pp. 265–286.

[51] Wu, J.-Z., Ma, H.-Y., and Zhou, M.-D., *Vortical Flows*, Springer, 2006.

[52] Yang, Y.-T., Zhang, R.-K., An, Y.-R., and Wu, J.-Z., "Steady vortex force theory and slender-wing flow diagnosis," *Acta Mechanica Sinica*, Vol. 23, No. 6, Dec 2007, pp. 609–619.

[53] von Karman, T. and Burgers, J., "General Aerodynamic Theory - Perfect fluids," *Aerodynamic Theory*, edited by W. Durand, Springer, Berlin, Germany, 1935.

[54] Saffman, P. G., *Vortex Dynamics*, Cambridge Monographs on Mechanics, Cambridge University Press, 1993.

[55] Marongiu, C., Tognaccini, R., and Ueno, M., "Lift and Lift-Induced Drag Computation by Lamb Vector Integration," *AIAA Journal*, Vol. 51, No. 6, 2013, pp. 1420–1430.

[56] Marongiu, C. and Tognaccini, R., "Far-Field Analysis of the Aerodynamic Force by Lamb Vector Integrals," *AIAA Journal*, Vol. 48, No. 11, Nov. 2010, pp. 2543–2555.

[57] Wu, J. C., "Theory for Aerodynamic Force and Moment in Viscous Flows," *AIAA Journal*, Vol. 19, No. 4, April 1981, pp. 432–441.

[58] Mele, B. and Tognaccini, R., "Aerodynamic force by Lamb vector integrals in compressible flow," *Physics of Fluids*, Vol. 26, No. 5, 2014, pp. 056104.

[59] Xu, C.-Y., Chen, L.-W., and Lu, X.-Y., "Large-eddy simulation of the compressible flow past a wavy cylinder," *Journal of Fluid Mechanics*, Vol. 665, 2010, pp. 238–273.

[60] Liu, L.-Q., Wu, J.-Z., Shi, Y.-P., and Zhu, J.-Y., "A dynamic counterpart of Lamb vector in viscous compressible aerodynamics," *Fluid Dynamics Research*, Vol. 46, No. 6, 2014, pp. 061417.

[61] Liu, L.-Q., Shi, Y.-P., Zhu, J.-Y., Su, W.-D., Zou, S.-F., and Wu, J.-Z., "Longitudinal–transverse aerodynamic force in viscous compressible complex flow," *Journal of Fluid Mechanics*, Vol. 756, 2014, pp. 226–251.

[62] Liu, L. Q., Zhu, J. Y., and Wu, J. Z., "Lift and drag in two-dimensional steady viscous and compressible flow," *Journal of Fluid Mechanics*, Vol. 784, 2015, pp. 304–341.

[63] Filon, L. N. G., "The Forces on a Cylinder in a Stream of Viscous Fluid," *Proceedings of the Royal Society of London. Series A*, Vol. 113, No. 763, 1926, pp. 7–27.

[64] Lagerstrom, P. A., Cole, J. D., and Trilling, L., *Problems in the theory of viscous compressible fluids*, California Institute of Technology, 1949.

[65] Mao, F., Shi, Y. P., and Wu, J. Z., "On a general theory for compressing process and aeroacoustics: linear analysis," *Acta Mechanica Sinica*, Vol. 26, No. 3, June 2010, pp. 355–364.

[66] Russo, L., Ostieri, M., and Tognaccini, R., "Link between thrust and vorticity in steady and unsteady flows," AIMETA - XXIII Conference - The Italian Association of Theoretical and Applied Mechanics, Salerno, 4th - 7th September, 2017.

[67] Wilcox, D., *Turbulence Modeling for CFD*, DCW Industries, Incorporated, 1994.

[68] Raddatz, J. and Fassbender, J., *Block structured Navier-Stokes solver FLOWer*, Vol. 89 of *Notes on Numerical Fluid Mechanics and Multidisciplinary Design*, Springer Berlin, 2005, pp. 27-44.

[69] Poirier, D., Allmaras, S., McCarthy, D., Smith, M., and Enomoto, F., "The CGNS system," Fluid Dynamics and Co-located Conferences, American Institute of Aeronautics and Astronautics, June 1998.

[70] Kroo, I., "Drag due to lift: concepts for prediction and reduction," *Annual Review Fluid Mechanics*, Vol. 33, 2001, pp. 587–617.

[71] Vassberg, J., "A Unified Baseline Grid about the Common Research Model Wing-Body for the Fifth AIAA CFD Drag Prediction Workshop." *AIAA Paper 2011-3508*, Jun. 2011.

[72] Rivers, M. and Dittberner, A., "Experimental Investigations of the NASA Common Research Model in the NASA Langley National Transonic Facility and NASA Ames 11-Ft Transonic Wind Tunnel (Invited)." *AIAA Paper 2011-1126*, Jan. 2011.

[73] Rivers, M., Hunter, C., and Campbell, R., "Further Investigation of the Support System Effects and Wing Twist on the NASA Common Research Model." *AIAA Paper 2012-3209*, Jun. 2012.

[74] Gariépy, M., Malouin, B., Trépanier, J.-Y., and Laurendeau, E., "Far-Field Drag Decomposition Applied to the Drag Prediction Workshop 5 Cases," *Journal of Aircraft*, Vol. 50, No. 6, 2013, pp. 1822–1831.

[75] Cambier, L. and Gazaix, M., "ElsA: An efficient object-oriented solution to CFD complexity," *40th AIAA Aerospace Sciences Meeting and Exhibit*, 2002.

[76] Liu, T., Wang, S., Zhang, X., and He, G., "Unsteady Thin-Airfoil Theory Revisited: Application of a Simple Lift Formula," *AIAA Journal*, Vol. 53, No. 6, 2014, pp. 1492–1502.

[77] Wang, S., Zhang, X., He, G., and Liu, T., "Evaluation of Lift Formulas Applied to Low-Reynolds-Number Unsteady Flows," *AIAA Journal*, Vol. 53, No. 1, January 2015, pp. 161–175.

[78] Pedlosky, J., *Geophysical Fluid Dynamics*, Springer, 1st ed., 1979.

[79] Theodorsen, T. and Mutchler, W., "General Theory of Aerodynamic Instability and the Mechanism of Flutter," Tech. Rep. 496, NACA Technical Report, 1935.

[80] Karman, T. H. V. and Sears, W. R., "Airfoil Theory for Non-Uniform Motion," *Journal of the Aeronautical Sciences*, Vol. 5, No. 10, Aug. 1938, pp. 379–390.

[81] Bisplinghoff, R., Ashley, H., and Halfman, R., *Aeroelasticity*, Dover Books on Aeronautical Engineering Series, Dover Publications, 1955.

[82] Da Ronch, A., Vallespin, D., Ghoreyshi, M., and Badcock, K. J., "Evaluation of dynamic derivatives using Computational Fluid Dynamics," *AIAA Journal*, Vol. 50, No. 2, 2012, pp. 470–484.

PUBLICATIONS

In the following it is reported a list of all the journal articles, conferences and conference papers in which the author participated or contributed.

Journal articles

- Mele, B., Ostieri, M. and Tognaccini, R., "Vorticity based breakdown of the aerodynamic force in three-dimensional compressible flows", AIAA Journal, Vol. 54, No. 4 (2016), pp. 1198-1208.
- Mele, B., Ostieri, M. and Tognaccini, R., "Aircraft lift and drag decomposition in transonic flows" , Journal of Aircraft, Vol. 54, No. 5 (2017), pp. 1933-1944.
- Ostieri, M., Mele, B., Tognaccini, R., "Linear and nonlinear decomposition of the aerodynamic force acting on an oscillating plate", AIAA Journal, (2017). Article in advance.

Conference papers

Papers in which the author name is underlined have been presented by the author himself.

- Mele, B., Ostieri, M. and Tognaccini, R., AIAA Paper, AIAA Scitech 2015, 5-9 January 2015, Kissimmee, Florida, USA, "Vortex force and lift-induced drag in compressible flows", AIAA 2015-1272.
- Mele, B., Ostieri, M. and Tognaccini, R., AIAA Paper, AIAA Aviation 2016, 13-17 June 2016, Washington D.C., USA, "A novel mid-field breakdown of the aerodynamic force in compressible flows", AIAA 2016-3429.
- Mele, B., Ostieri, M. and Tognaccini, R., AIAA Paper, AIAA Scitech 2017, 9-13 January 2017, Grapevine, Texas, USA, "Exact aerodynamic force decomposition and dynamic force derivatives in non linear flows", AIAA 2017-0950

- Ostieri, M., Tognaccini, R., Bailly, D. and Destarac, D., AIAA Paper, AIAA Scitech 2018, 8-12 January 2018 (extended abstract accepted), Kissemmee, Florida, USA, "Aerodynamic force and Lamb vector field in compressible unsteady flows".
- Ostieri, M., Tognaccini, R., Bailly, D. and Destarac, D., XXIII AIMETA congress, 4-7 September 2017, Salerno, Italy, "Two alternative drag breakdowns in unsteady flows".
- Russo, L., Ostieri, M. and Tognaccini, R., XXIII AIMETA congress, 4-7 September 2017, Salerno, Italy, "Link between thrust and vorticity in steady and unsteady flows".

Conferences (book of abstracts only)

- Ostieri, M., Mele, B. and Tognaccini, R., XXII AIMETA congress, 14-17 September 2015, Genoa, Italy, "Aerodynamic force and Lamb vector field in an oscillating flat plate flow".
- Ostieri, M., Tognaccini, R. and Mele, B., EFMC11, 11^{th} European Fluid Mechanics Conference, 12-16 September 2016, Sevilla, Spain, "Comparison of linear and non linear analyses of the aerodynamic force acting on an oscillating plate".

ACKNOWLEDGEMENTS

I would like to thank Prof. Angelo Iollo and Prof. Andrea Ianiro for their really kind revisions of this dissertation. I really appreciated your words and your suggestions.

I would like to express my gratitude to Prof. Renato Tognaccini for his perseverance, dedication, for all the efforts he made to grow me up as a professional and for the opportunity he gave me with this research. I would also like to thank Dr. Benedetto Mele (we hope Prof. as soon as possible!). His wise suggestions, his great help and his technical skills helped me a lot, giving me the possibility to improve my capabilities.

I would like to thank the Professors of the X floor. It is also thanks to them that I loved fluid dynamics, and I really appreciated the moments spent together at the department.

I would like to thank Didier Bailly and Daniel Destarac for the great support, for the fruitful discussions and for the opportunity they gave me at ONERA, that helped me gaining awareness and stronger technical skills. I would also like to thank Antoine Dumont, my roommate at ONERA, for his kindness and availability.

I would like to thank my colleagues as well as friends, with which I passed always happy and funny moments. I will not forget all the moments passed laughing or discussing about whatever. I would like also to thank all my friends. In particular I would like to thank my "historical" friends, the "KTM". During these years the time I had for them has become always and always smaller. But they are always in my heart, and I will not forget the moments passed together. I would also like to thank my new group, the "Caciotte", with which I always passed funny moments, build strong relationships, and for the help they gave me in every situation.

I would like to thank my family, for their constant support, for their willingness and efforts to try to help me in every situation, and for the love they gave me.

Finally, I would like to thank my beloved Elena. She made me wiser, she helped me with her kindness, she guided me with her love, and she made me a better man. This work has also her mark. I am really lucky to have her by my side.